NASA Contractor Report 4079

The Effects of Inlet Turbulence and Rotor/Stator Interactions on the Aerodynamics and Heat Transfer of a Large-Scale Rotating Turbine Model

I—Final Report

R. P. Dring, M. F. Blair, H. D. Joslyn,
G. D. Power, and J. M. Verdon
United Technologies Research Center
East Hartford, Connecticut

Prepared for
Lewis Research Center
under Contract NAS3-23717

National Aeronautics
and Space Administration

**Scientific and Technical
Information Office**

1987

C O N T E N T S

VOLUME I - FINAL REPORT

C O N T E N T S (Concluded)

LIST OF SYMBOLS

B_x	airfoil axial chord
C_f	skin friction $(\tau_w^*/\rho_\infty^2\ U_2^{*2})$
C_{f_n}	magnitude of nth Fourier component of C_f
C_p	specific heat at constant pressure
C_P	turbine pressure coefficient (based on turbine inlet total pressure and Q_{Um})
CP	airfoil pressure coefficient (based on airfoil incident total pressure, P01, and airfoil exit static pressure, P2)
C_{Tot}	absolute flow speed normalized by U_m
C_x	axial flow speed
Fr	Froessling number (based on incident flow speed and leading edge diameter)
k	grid stretching factor
L_{ref}	reference length
M	Mach number
N	Number of airfoils in a row
P	static pressue
P_n	magnitude of nth Fourier component of P
Q_{Um}	dynamic pressure based on U_m
q	surface heat flux
Re	Reynolds number (based on airfoil axial chord and exit flow speed)
Re_θ	Reynolds number (based on momentum thickness and local flow speed)
R_N	airfoil leading edge radius

S	surface arc length from trailing edge
St	Stanton number (based on airfoil exit flow speed)
St_n	magnitude of nth Fourier component of St
T	static temperature
t	time
U	unsteadiness (T:total, R:random, and P:periodic), figure 26
U	streamwise velocity
U	stage inlet flow velocity
U_m	rotor wheel speed at midspan
W_{Tot}	relative flow speed normalized by U_m
x	streamwise distance
X	axial distance
α	absolute flow angle from axial
β	relative flow angle from axial
ρ	density
τ	shear stress
ϕ_{c_f}	phase angle of 1st Fourier component of C_f
ϕ_{p_n}	phase angle of nth Fourier component of P
ϕ_{st}	phase angle of 1st Fourier component of St
ω	frequency
σ	standard deviation

Superscripts

*	dimensional quantity
-	time average

1	first stator inlet
2	first stator exit
3	rotor exit
4	second stator exit
T	total
R	random
P	periodic

Subscripts

e	value at edge of boundary layer
TE	value at trailing edge
w	value at wall
∞	value in free-stream (upstream of leading edge)

THE EFFECTS OF INLET TURBULENCE AND ROTOR/STATOR INTERACTIONS ON THE AERODYNAMICS AND HEAT TRANSFER OF A LARGE-SCALE ROTATING TURBINE MODEL

I - Final Report

Robert P. Dring
Michael F. Blair
H. David Joslyn
Gregory D. Power
Joseph M. Verdon

SUMMARY

A combined experimental and analytical program was conducted to examine the effects of inlet turbulence on airfoil heat transfer. The experimental portion of the study was conducted in a large-scale (approximately 5X engine), ambient temperature, rotating turbine model configured in both single stage and stage-and-a-half arrangements. Heat transfer measurements were obtained using low-conductivity airfoils with miniature thermocouples welded to a thin, electrically heated surface skin. Heat transfer data were acquired for various combinations of low or high inlet turbulence intensity, flow coefficient (incidence), first-stator/rotor axial spacing, Reynolds number and relative circumferential position of the first and second stators. Aerodynamic measurements obtained as part of the program include distributions of the mean and fluctuating velocities at the turbine inlet and, for each airfoil row, midspan airfoil surface pressures and circumferential distributions of the downstream steady state pressures and fluctuating velocities. Analytical results include airfoil heat transfer predictions produced using existing two-dimensional boundary layer computation schemes and an examination of solutions of the unsteady boundary layer equations. The results of this program are reported in four separate volumes. All four have a common report title and the following volume subtitles:

REPORT TITLE: THE EFFECTS OF INLET TURBULENCE AND ROTOR/STATOR INTERACTIONS ON THE AERODYNAMICS AND HEAT TRANSFER OF A LARGE-SCALE ROTATING TURBINE MODEL

VOLUME TITLES:	VOLUME I:	UTRC - R86-956480-1	FINAL REPORT
	VOLUME II:	UTRC - R86-956480-2 (NASA CR 179467)	HEAT TRANSFER DATA TABULATION 15% AXIAL SPACING
	VOLUME III:	UTRC - R86-956480-3 (NASA CR 179468)	HEAT TRANSFER DATA TABULATION 65% AXIAL SPACING
	VOLUME IV:	UTRC - R86-956480-4 (NASA CR 179469)	AERODYNAMIC DATA TABULATION

INTRODUCTION

The accurate prediction of gas turbine airfoil exterior convective heat load distributions is recognized throughout the industry to be an exceedingly difficult yet important problem. A wide variety of factors are known to contribute to the complexity of airfoil passage flows and heat transfer, e.g., high levels of flow field turbulence and unsteadiness, extreme accelerations and decelerations, velocities ranging from low subsonic to supersonic, important secondary flows produced by high turning - low aspect ratio airfoils, nonuniform time-mean total pressure and temperature distributions, strong surface curvature, film cooling/boundary layer interactions, rotational effects, airfoil row interactions (rotor/stator and stator/stator), local flow separations, and shock-boundary layer interactions. The difficulties of incorporating this formidable list of effects into design systems have been compounded by an ever widening gap between rising turbine inlet gas flow temperatures and the more slowly rising allowable airfoil metal temperatures.

The gas turbine community has expended a great deal of effort to develop analytical tools for airfoil boundary layer computation, and in particular, for heat transfer predictions. In order of increasing mathematical complexity these tools include (1) correlations corrected for design-specific velocity distributions, curvature, turbulence etc., (2) finite-difference and integral boundary layer computation schemes using velocity distributions computed from airfoil row potential flow codes, and finally (3) three-dimensional Navier-Stokes flow field solutions. A variety of empirically adjusted analytical turbulence and transition models have been incorporated into these computation schemes.

Instrumentation and testing techniques are not currently available for the documentation of both the surface heat transfer distributions and the unsteady velocity and temperature fields in the extremely hostile environment of operating gas turbines. For this reason the assessment of the relative merits of the predictive techniques has relied on comparisons with experimental data gathered in cascades and turbine-simulation models. Each of these experimental approaches has been designed to examine the isolated impact on the heat transfer of certain specific effects. Excellent reviews of the best available existing published data along with comparisons to the state-of-the-art predictive schemes are given by Han, Chait, Boyee and Rapp (ref. 1), Hylton, Mihelc, Turner, Nealy and York (ref. 2) and Rae, Taulbee, Civinskas and Dunn (ref. 3).

As might be expected for any collection of experiments covering such a large number of complex variables, there are numerous apparent discrepancies between the various data sets. Because different experimental techniques were

employed by the various investigators and since the thoroughness of the flow field documentation varied widely, there presently exists considerable uncertainty as to the role and importance of some of the factors believed to affect turbine heat transfer. For example, the data of Lokay and Trushin (ref 4) indicate that airfoil rotation may strongly increase heat transfer levels raising a question as to the validity of using cascade data for the design of a rotating blade row. Other examples are the uncertainties regarding the roles of periodic unsteadiness (wake chopping and potential flow field interactions) and broad-band turbulence on airfoil heat transfer.

The present experiment was specifically designed to examine the combined effects of broad-band (grid generated) turbulence and airfoil interactions (periodic unsteadiness) on a rotating turbine model. These tests were conducted in a low-speed, large-scale turbine model. This model made possible the accurate documentation of the mean and fluctuating flow fields at both the inlet of the turbine and downstream of each airfoil row. Data were obtained for three airfoil rows, a first stator, first rotor, and a second stator for a range of Reynolds numbers. The effects of changing rotor incidence (flow coefficient), inlet turbulence level, and airfoil axial and circumferential spacing were documented. One feature of this investigation was that detailed cascade heat transfer distribution data already existed for the rotor airfoil (ref. 5) presenting an opportunity for a comparison between similar rotating and nonrotating heat transfer distributions. The present study, then, examined the impact of rotation, inlet turbulence and periodic unsteadiness on turbine heat transfer. In addition it provides the companion aerodynamic data required to evaluate the performance of existing airfoil heat transfer prediction techniques. Two companion analytical programs were also included as part of this effort. The first employed a steady boundary layer analysis and the second employed an unsteady boundary layer analysis developed specifically for this program. Comparisons of both analyses with the measured data are included in this report.

This volume only presents the highlights of the program. The detailed tabular and graphical presentations of all of the heat transfer and aerodynamics data are presented in Volumes II, III, and IV.

OBJECTIVES

The first program objective was to obtain a detailed set of heat transfer coefficients along the midspan of a stator and a rotor in a rotating turbine stage. The experimental program was designed such that the rotor data could be compared directly with data taken in a static cascade. The data are compared to a standard analysis of blade boundary layer heat transfer which is widely available today. In addition to providing this all-important comparison between rotating and stationary data, this experiment provides important insight to the more elaborate fully three-dimensional programs being proposed for future research. A second program objective was to obtain a detailed set of heat transfer coefficients along the midspan of a stator located in the wake of an upstream turbine stage. Particular focus here was on the relative circumferential location of the first and second stators. Both program objectives were carried out at two levels of inlet turbulence. The low level was on the order of 1 percent while the high level of approximately 10 percent is more typical of combustor exit turbulence intensity. The final program objective was to improve the analytical capability to predict the experimental data.

EXPERIMENTAL EQUIPMENT

1. Turbine Facility

All experimental work for this program was conducted in the United Technologies Research Center Large Scale Rotating Rig (LSRR). This test facility was designed for conducting detailed experimental investigations of flow within turbine and compressor blading. Primary considerations were to provide a rig which would: (1) be of sufficient size to permit a high degree of resolution of three dimensional flows, (2) possess a high degree of test configuration flexibility and (3) enable measurements to be made directly in the rotating frame of reference.

The facility is of the open circuit type with flow entering through a 12-ft diameter inlet. A 6 in. thick section of honeycomb is mounted at the inlet face to remove any cross flow effects. The inlet smoothly contracts the cross section to 5 ft. diameter. Flow is then passed through a series of three fine mesh screens to reduce the turbulence level. Immediately downstream of the screen is a seven foot long section which slides axially and permits access to the test section. The test section consists of a series of constant diameter casings enclosing the turbine, compressor or, fan model assemblies. The casings are wholly or partially transparent, which facilitates flow visualization and laser-Doppler-velocimeter studies. The rotor shaft is cantilevered from two downstream bearings thus providing a clean flow path at the model inlet. Axial length of the test section is 36 in. The rotor is driven or braked by a hydraulic pump and motor system which is capable of maintaining shaft speeds up to 890 rpm. Downstream of the test section flow passes through an annular diffuser into a centrifugal fan and is subsequently exhausted from the rig. A vortex valve is mounted at the fan inlet face for flow rate control.

For the present program the turbine facility (fig. 1) was assembled in both single stage (stator 1/rotor) and 1 1/2 stage (stator 1/rotor/stator 2) configurations with various axial spaces between adjacent rows. The following table lists the various geometric combinations for which heat transfer data were obtained.

GEOMETRIES TESTED

	SINGLE STAGE CONFIGURATION	1 1/2 STAGE CONFIGURATION
AXIAL SPACE BETWEEN STATOR 1 AND ROTOR	15% Bx and 65% Bx	65% Bx
AXIAL SPACE BETWEEN ROTOR AND STATOR 2	----------	63% Bx
TURBULENCE GRID	IN and OUT	IN and OUT

As indicated in the table a turbulence generating grid, to be described in detail in a later section, was installed upstream of the first stator for selected test cases (fig. 1).

The general features of the turbine test section geometry are shown in figures 1 through 3. Figure 1 presents a sketch of the test section arranged in the 1 1/2 stage configuration with the upstream turbulence grid installed. As indicated in figure 1, the turbine model has 22 first stage stator airfoils, 28 first stage rotor airfoils and 28 second stage stator airfoils. Figure 2 shows a radial view of the single stage configuration at midspan at the 15% axial spacing. A photograph of the facility showing the rotor and second stator rows installed in the test section is presented in figure 3.

2. Airfoil Coordinates and Surface Nomenclature

The surface hub, midspan, and tip coordinates (x,y) of the three airfoil rows (stator 1, rotor and stator 2) are given in Tables 1, 2 and 3 respectively.

The locations of all heat transfer data presented in this report are given in terms of a distance along the respective airfoil surface(s) as measured from a reference (s = 0) location. To achieve high experimental location accuracy the s = 0 location for each airfoil was determined using a geometric criterion instead of the location of the aerodynamic stagnation point. This geometrical "zero" was defined as the point on the leading edge, at midspan, tangent to a straight line which was also tangent to the trailing edge radius. This definition is illustrated for the rotor airfoil in figure 4. During the fabrication and instrumentation procedures the s = 0 location was precisely determined for each airfoil using a simple straight-edge. As shown in figure 4, the distance "S" is defined as increasing positive along the suction surface and increasing negative along the pressure surface.

3. Flowpath Steady Aerodynamic Instrumentation

The time-mean aerodynamic measurements in this program were carried out in two separate stages. Prior to the measurement of any of the heat transfer data, airfoil midspan pressure distributions and hub and casing flow path static pressure distributions were obtained for all three airfoil rows. These pressure distribution data were obtained both with the turbulence generating grid in and out. In addition, surveys of the inlet flow total pressure were obtained at four pitchwise locations, 23% B_x upstream of the first stator leading edge both with and without the turbulence grid installed. These total pressure surveys, together with hub and outer casing flowpath static pressures measured upstream of the first stator leading edge plane, provided the inlet mass flow (flow coefficient) calibration for the turbine model.

One airfoil from each row (first stator, rotor, second stator) was instrumented with twenty two static pressure taps distributed around the perimeter to provide the airfoil surface static pressure distributions. Flowpath static pressures on the hub and casing were acquired downstream of each airfoil row. Arrays of twenty taps distributed over two airfoil pitches at the hub and casing provided airfoil-to-airfoil static pressure distributions. Arrays of ten static pressure taps distributed circumferentially around both the hub and casing provided static pressure distributions around the entire annulus. The axial location of these static pressure taps coincided with the locations where both steady and unsteady aerodynamic traverse measurements were made. Except for the static pressure taps on the rotor and on the rotor hub, all hub and casing flowpath static pressure taps and the first and second stator static pressure taps were connected to five computer controlled 48 port Scanivalves (Model 48J9-1290) mounted in the stationary frame pressure acquisition system. A rotating frame pneumatic instrumentation package mounted on the rotor axis contained a single 48 port Scanivalve (Model 48J9-1290) to which the rotor and the rotor hub static pressure taps were connected. The calibration of both the stationary and rotating frame Scanivalve transducers (1 psia Druck Model PDCR 22) is computer controlled as will be discussed below.

Following the completion of the heat transfer testing, aerodynamic traverse measurements were obtained downstream of each of the three airfoil rows. These measurements include midspan circumferential traverses of the total and static pressures and the flow yaw and pitch angles. The first stage stator wake was documented approximately 17% of axial chord downstream of the stator trailing edge. The rotor wake was documented in the rotating frame of reference approximately 32% of axial chord downstream of its trailing edge. The axial gap separating the first stage rotor and stator during this testing was approximately 50% of the rotor axial chord. The second stage stator wake was documented 14% of axial chord downstream of its trailing edge. These measurements define the inlet and exit aerodynamic conditions for each airfoil row.

United Sensor five hole pneumatic probes (USC-F-152) were traversed in the stationary and rotating frames of reference to document the stator and rotor wakes. A detailed description of this type of probe and its calibration is presented in reference 6. The 0.09 in. diameter probe tip is small relative to the stator and rotor midspan pitch (approximately 1.5% of pitch). The stationary frame traverse system is described in reference 7. For the stationary traverse, the probes are mounted in a traverse device located external to the model. They enter the flowpath through sealed slots in the casing and can be traversed radially from hub to tip and circumferentially over two airfoil pitches. The probe pressure ports are connected by computer controlled pneumatic fluid switches to 1 psia Druck (Model PDCR 22) transducers located in the stationary frame pressure acquisition system. The rotating traverse system (ref. 8) mounted inside the rotor hub can traverse probes radially from hub to tip and circumferentially over two rotor pitches. Pressure ports of the rotating frame probes are connected by computer controlled fluid switches to 1 psia Druck (Model PDCR 22) differential transducers mounted in the rotating instrumentation package close to the rotor axis. Both the stationary and rotating frame probes are automatically nulled in yaw by computer control.

A dedicated online Perkin Elmer (PE 8/16E) minicomputer controls the radial and circumferential positioning and the yaw nulling of both the stationary and rotating frame probes. Electrical communication with the rotating frame instrumentation package, transducers and traverse system is through a Fabricast (Model 1273) slip-ring assembly mounted on the rotor drive shaft. On-line calibration of all transducers, both stationary and rotating, is controlled by the computer. Various combinations of reference pressures supplied by five Ametek (Model RK-300WC) dead weight testers are applied to all rotating and stationary transducers to generate a five point calibration covering the appropriate pressure range for each test. The dead weight testers are accurate to ±0.005 inches of water. The calibration pressures and reference pressure (inlet absolute total pressure) are brought onto the rotating frame through a two channel rotary union. This permits on line calibration of the rotating frame transducers with the rig in operation (rotating). Overall, the repeatibility of the entire data acquisition system is typically 1% of reading.

4. High-Response Aerodynamic Measurements and Instrumentation

Design of the Turbulence Generating Grid. - As part of the present investigation the effects of high levels of freestream turbulence on the heat transfer distributions through the LSRR turbine blading were to be examined. These heat transfer data were to be obtained for a turbine inlet turbulence intensity of approximately 10%, a level representative of the turbulence measured at the exit of aircraft gas turbine combustors (ref. 9). For

purposes of airfoil to airfoil consistency (circumferential uniformity) and so that the present results could be compared with other data on the effects of turbulence on heat transfer, the turbulence generated for these tests was required to be spatially uniform, nearly isotropic, and temporally steady (over time scales long when compared to the turbulent fluctuations). In addition, the test turbulence had to be generated in a manner such that there was a reasonably high intensity through the 1 1/2 stages of the turbine, i.e., the streamwise decay of the turbulence had to be similar to that in an engine.

Immediately downstream of any coarse turbulence generating device there exists a short length of turbulence development followed by a much longer region of high but rapidly decreasing turbulence intensity. Two considerations in the selection of a device for generating turbulence for a particular test application are (1) that the "development" region terminate upstream of the test zone, and (2) that the rate of decay through the test zone be acceptable. Numerous studies have been conducted by earlier investigators to examine the physical processes associated with the near-grid region of high intensity, rapidly decaying turbulence (the "initial decay period" of Batchelor and Townsend, ref. 10). These studies have revealed that the dominant phenomenon of this phase of the decay process is the transfer of energy from the larger to smaller dissipating eddies (the "energy cascade"). From this general characteristic of turbulent flows it follows that the rate of decay of a given level of turbulent energy decreases with increasing turbulence integral scale. The larger the integral scale of a turbulent flow the lower proportion of the turbulent energy is contained in the dissipating wavenumber range. These effects were clearly demonstrated by Sato (ref. 11) (see Hinze, ref. 12) who showed that with increasing distance (x) from a turbulence source, high wavenumber turbulence decayed as $x^{-5/2}$ while the total kinetic energy decayed as x^{-1}. The conclusion that can be reached from this principle is that the only avenue available to influence the decay rate of a given turbulence intensity is to choose a method of turbulence production which generates a field with a sufficiently large integral scale.

A wide variety of flow control devices have been employed by other investigators to generate high intensity turbulence, e.g., monoplane or biplane square or rectangular lattices, uni-directional bar arrays, grids with injection, perforated plates, and honeycombs. Of these devices, the square array-biplane lattice of square cross-section bars has been consistently shown by many independent investigators to be the most reliable and predictable generator of uniform, steady turbulence (e.g., refs. 13 through 16). Studies documenting the performance of this type of grid have shown that, providing the bars are uniformly spaced and the open area is 60 percent or greater, the turbulence produced will be homogeneous. In addition, the turbulence can be expected to have a spectral distribution in good agreement with the von Karman one-dimensional isotropic spectrum and that there will be near equality of the

various turbulence components (u', v' and w' will be equal to within about 20%) (refs. 14 through 16). With this type of turbulence generator the level of turbulence intensity and the streamwise decay rate (the scale of the turbulence) are determined by the choice of bar size/mesh combination.

Alternative turbulence generators considered for use in the present application included uni-directional bar arrays, grids with injection, and perforated plates. Uni-directional bar arrays, although extremely simple and economical to construct, were rejected on the grounds that they generate an anisotropic field (refs. 15 and 17). The available documentation on blown grids (refs. 18 and 19) contains contradictory information on the magnitude of the effects of injection on turbulence. For this reason it was decided that there was an unacceptable level of uncertainty associated with the design and application of such a generating device. The use of perforated plates was also considered due to their simplicity and low cost. However, perforated plates have been shown to produce highly intense turbulence with unacceptably high decay rate (ref. 20) (small scale turbulence) and were rejected for this application.

Based upon the above reasoning the technique selected for generating high levels of turbulence for these tests was the biplane grid. The turbulence generator selected consisted of a nearly square array lattice of three rings spaced uniformly in the radial direction with 80 evenly spaced radial bars. Both the rings and radial bars are of square 1/2 inch cross-section. The mesh spacing of the bar is 2.1 inches radially and 4.5 degrees (2.1 in. at mid-annulus) circumferentially. The correlation of reference 13 indicates that with this grid located 15 inches upstream of the blading the turbulence intensity could be expected to drop from 10 percent to 5 percent between the first vane leading edge and the second vane trailing edge.

Turbulence Measurements at the Turbine Model Inlet. - Detailed measurements of the streamwise component of the fluctuating velocity were obtained just upstream of the turbine model inlet. These data were obtained both with and without the turbulence grid installed. Traverses of the inlet turbulence were measured at four pitchwise locations (0, 25, 50 and 75 percent pitch) at 12 spanwise locations each (an array of 48 locations) over a plane 1.35 inches (23% chord) upstream of the first stator leading edge. In addition, turbulence data were obtained at 12 spanwise stations at 50 percent pitch at the axial station of the first stator leading edge. Turbulence intensity measurements were obtained at all the above locations while measurements of the local turbulent length scale and the spectral distribution of the fluctuations were documented at four spanwise locations for each traverse. All of these measurements were obtained using a TSI model 1210-20 cylindrical hot film probe, a TSI Model 1050 Constant Temperature Anemometer and a TSI Model 1052 4th order polynomial linearizer. Autocorrelations of the linearized hot-film

signals were generated using a Saicor Model SAI-42 Correlator and Probability Analyzer. Spectral distributions were determined using a Spectral Dynamics Model SD 340 MICRO FFT narrow band analyzer. A block diagram of the instrumentation arrangement is presented in figure 5.

High-Response Inter-Row Velocity Measurements. - High response inter-row velocity measurements were acquired circumferentially over two first stator pitches at midspan locations downstream of each airfoil row with the turbine model in the 1 1/2 stage configuration. These locations, denoted as Sta 2, 3 and 4 in figure 1, are at the same axial distances downstream of the first stator, rotor and second stator respectively at which the five hole pneumatic probe traverse data were acquired. The traverse measurements were made with a Thermo Systems Inc. (TSI) Model 1211 -20 hot film probe which has a single radially oriented sensor. The probe was mounted in the same stationary frame traverse system used for the steady pneumatic five hole probe traversing. The probe was calibrated over a range of velocities from 40 to 200 feet per second in ambient temperature air and was powered by a TSI Model 1050 anemometer. The anemometer output was conditioned by a TSI Model 1052 linearizer which provided a 0 - 10 volt output to the data acquisition system. A single thermocouple probe used to measure the inlet flow temperature was installed upstream of the turbulence grid location. This permitted a temperature correction to be applied to the measured linearized hot film voltage during data reduction.

Hot film probe positioning and data acquisition was controlled by the PE 8/16E minicomputer. A schematic of the high response instrumentation and data acquisition system configured for phase lock average (PLA) acquisition is shown in figure 6. Although only two channels of data (hot film and thermocouple) were acquired in the present program, the acquisition system is capable of simultaneously acquiring up to four channels of data (ref. 7). The acquisition of the linearized hot film voltage and the inlet thermocouple voltage was initiated once every rotor revolution by a reference signal generated by an Optron Model OPB 253 optical photo-sensor focused on a reference rotor blade tip that was highly polished. At each stationary frame circumferential traverse location (typically 60 per traverse), high response data were acquired at three hundred rotor positions over three consecutive rotor pitches. One hundred sets of high response (instantaneous) data (300 per revolution for 100 revolutions) were acquired and digitized at each traverse location and recorded on magnetic tape for detailed off-line analysis.

5. Airfoil Heat Transfer Measurements

Description of the Technique. - Boundary layers on aircraft gas turbine airfoils never remain laminar over the entire chord but pass through transition to or toward turbulent flow before reaching the trailing edge. These developing boundary layers are subjected to strong streamwise pressure gradients, both favorable and adverse, and they may even locally separate from and reattach to the airfoil surface. All these phenomenon combine to produce very strong streamwise variations in the rate of convective heat transfer. The experimental techniques employed in this investigation were selected to obtain accurate measurements of heat transfer rates in the presence of such strong local variations.

Of the numerous phenomena that influence turbine convective heat transfer rates the most important effects (first order effects) are a consequence of local flow conditions. Examples of aerodynamic phenomenon which have extremely large effects on turbine convective heat transfer rates are the transition of a boundary layer from laminar to turbulent flow, separation or reattachment, and strong velocity gradients. These "first order" heat transfer effects can be experimentally simulated without reproducing the large temperature differences present in the gas turbine environment but by employing only very small levels of surface heat flux. These small heat flux levels generate proportionally small fluid temperature gradients and result in flows of near constant density. For such near-constant density flows the absolute direction of convective heat flux, whether to or from the solid surface, is immaterial. In numerous earlier experiments (e.g., refs. 21 through 23) electrical resistive heating of surface metal foils has proved to be a highly practical method for generating low levels of uniform surface heat flux. Recently this basic experimental method has been significantly improved through a series of technique development programs at UTRC. Of primary importance has been the development of techniques for using rigid cast urethane foam as the construction material for test aerodynamic models. Rigid urethane has an extremely low thermal conductivity (8×10^{-5} gm-cal/cm-s K) which nearly eliminates errors in heat transfer measurements due to conduction in the airfoil away from the surface heating foil. Techniques have also been developed for attaching metal foil to the urethane foam models using extremely thin layers of adhesive. Use of these new construction techniques results in uniform surface heat flux test models with negligible (less than 1 percent) back-losses and minimal transverse "smearing" through conduction. Calculations indicate that, even in a region with a lateral gradient of heat transfer coefficient of 100 percent per inch, local heat transfer coefficients can be measured within an accuracy of 5 percent using these construction materials and techniques. References 5, 24 and 25 present examples of the use of these heat transfer measurement techniques.

Instrumented Airfoil Construction Technique. - As described in the preceding section, heat transfer measurements were obtained in this study using low conductivity rigid foam castings of the test airfoils. A uniform heat flux was generated on the surface of the foam test airfoils using electrically heated metal foil strips attached to the model surface. Local heat transfer coefficients around the airfoils were determined using thermocouples to measure the temperature difference between the heated metal skin and the free stream.

Photographs of the first stage rotor model at various steps of fabrication are presented in figure 7. The first stage of the fabrication process consisted of developing a metal "master airfoil". An aluminum rotor blade, chosen at random from the LSRR rotor, was carefully inspected to determine locations with surface waviness. These slight deviations from a perfectly "developable" surface (a surface with no compound curvature) are an inherent characteristic of the "multiple radial station contour tracing" machining process used to manufacture the aluminum airfoils. Despite the fact that this surface waviness only consists of depressions a few thousandths of an inch deep at their maximum, they do present a problem unique to this method of instrumentation. The metal foil which is to be glued to the exterior surface of the airfoil is extremely intolerant of surface waviness. Even miniscule depressions on the airfoil translate to "wrinkles" or "lumps" on the finished, assembled airfoil surface. For this reason it was necessary that any depressions be filled to produce as nearly a "developable" surface as possible. This filling procedure consisted of a trial-and-error/inspection iteration towards the finished airfoil. An airfoil was accepted as a "master" only after a completely wrinkle-free "test" metal foil could be glued to its entire surface. An inviscid flow computation of the velocity distribution around the finished "master" airfoil indicated that the maximum change in local velocity produced by the surface filling (measured Maximum filling thickness) was only 1/4 percent. A photograph of the completed "metal master airfoil" is presented in figure 7. The next step in the model fabrication process (not shown in fig. 7) consisted of casting a concrete mold of the master airfoil. Special low shrinkage gypsum cement (USG Hydrocal) was used to produce a smooth airfoil surface and a precise geometrical reproduction.

A steel skeleton (fig. 7) was fabricated for each of the test airfoils to ensure adequate strength to endure both the aerodynamic forces and, for the rotor, the centrifugal forces of the test environment. The skeleton provided a secure location to attach the foam airfoil to either the rotor hub or the stator case. The photograph of the first stage rotor skeleton presented in figure 7 shows the attachment "button" for fastening the blade to the hub.

The airfoils were cast in rigid foam with the steel skeleton mounted in the concrete mold. A special fixture ensured that the mounting button on the skeleton was precisely located at the same position relative to the concrete

mold as was the button on the original "metal master airfoil". Photographs of the suction and pressure surfaces of the cast foam rotor blade are shown in figure 7. For this particular model the suction surface was instrumented and the pressure surface was the "backside" through which the instrumentation was routed. The suction surface view shows the pattern of holes to be used for installation of the thermocouples. The holes in the suction surface were evenly spaced at one inch increments at the midspan location. The pressure surface view shows the trenches cut into that surface for routing of thermocouple leads, the copper buss bars for connecting to the foil skin and the electric power leads. The copper buss bars ensure that the voltage along each end of the foil strip is uniform, producing a uniform current over the entire foil surface.

The rate of heat transfer varies strongly with location near the leading edge of an airfoil. Measurement of these extreme gradients in heat transfer requires a dense grid of thermocouples in this region. In an attempt to obtain accurate measurements in the leading edge region for the present test airfoils, a new high density thermocouple installation technique was developed. Shown in figure 8 is a photograph of the leading edge array installed in this particular rotor model. The photograph shows the backside of the leading edge region of the foil before it was installed on the airfoil. Also shown are a specially fabricated template for accurately locating thermocouple beads and a thin "transfer template" which is shown attached directly to the backside of the foil. This "transfer template" was removed following the completion of the thermocouple installation. Shown in the photograph are 20 thermocouples located at 0.050 in. apart within an estimated variation of $\pm$ 0.005 in.

The next photograph of figure 8 shows the rotor model with the heater foil installed on the suction surface only. In this photograph the thermocouples have been welded to the backside of the heater foil and routed through the trenches to the support button. The third photograph of figure 8 shows the model with the foil attached to the pressure surface and connected to the buss bars. At this stage the instrumentation cavity was refilled with urethane foam to conform to the original pressure surface contour. The final photograph of figure 8 shows the completed test model coated with flat black paint. This paint coating ensures a uniform, known emissivity so that a small ($\sim$ 3 percent) but accurate radiation correction can be incorporated into the data reduction routine.

Heat Transfer Instrumentation. - The heat transfer instrumentation plans for the first stator, the rotor and the second stator are presented in figures 9, 10, and 11 respectively. Each figure shows the airfoil midspan contour and the TC locations around its perimeter. The TC locations are also tabulated below in terms of (1) axial distance (X) from the leading edge (minimum X location) normalized by airfoil axial chord (B_X) and (2) arc length (S')

moving counterclockwise from the trailing edge (maximum X location), also normalized by the airfoil axial chord. At three locations on the airfoil suction and pressure surfaces (indicated by *) TCs are also located at ± 8.3%, ± 16.6% and ± 25% span from midspan. All the rest of the TCs are located at midspan. Note, however, that the dense leading edge arrays of TCs were obtained by staggering adjacent TCs slightly above and below midspan (± 1% of span). Figures 9, 10 and 11 each represent a composite of the instrumentation on two airfoils, one instrumented along the suction surface and the other along the pressure surface. The dense leading edge TC arrays are duplicated on both the airfoils with the suction surface instrumentation and on the airfoils with the pressure surface instrumentation. Thus, although there are (on the average) 95 TC sites on each contour, each instrumented airfoil has (on the average) 58 TCs or 116 per airfoil row, which offers a reassuring redundancy in the measurements.

As previously noted the steady state heat transfer boundary condition on the airfoil heated surfaces was nominally one of constant convective heat flux. Slight corrections to the constant-convective-heat-flux condition resulting from surface radiation, heat conduction through the foam and local variations in strip resistance produced by local metal temperature differences were included in the data reduction procedures.

The thermocouple leads from the stator models were connected directly to Uniform Temperture Reference (UTR) blocks (Kaye Instruments, UTR-48N). The rotor model thermocouple leads were connected through a Wendon Co. 212 ring slip ring unit to another set of stationary frame UTR blocks. A photograph of the Wendon slip ring unit installed in the rig is shown in figure 12. This photo shows an important feature of this slip ring, the stationary and rotating connection points are in close proximity assuring that any secondary voltages generated at these connections are extremely small. Data were recorded using a Hewlett-Packard 300 channel data aquisition unit (3497A/3498A), and an ice point reference (Kaye Instruments, K140-4). Reduction of the thermocouple signals to temperature and engineering heat transfer units was accomplished using an LSI 11/03 minicomputer. Data were recorded on double-density floppy disks.

The freestream temperatures used to compute the airfoil Stanton numbers were determined using both stationary and rotating frame thermocouples. The stationary temperature measurements were obtained using thermocouples located just upstream of the grid at eight equally spaced circumferential locations. A second measure of the freestream temperature was obtained using the array of thermocouples on the leading edge of whichever rotor model was unheated in a particular test run. These rotating frame temperature measurements, then, represent a circumferential average of the rotor recovery temperature. The freestream temperature measurements were required to meet two conditions: (1)

All eight upstream temperatures and the unheated rotor temperature (corrected for rotor wheel speed had to agree within ±1 1/2°F. (2) The inlet temperature had to be below 65°F. These criteria were intended to assure that there would be both an adequate temperature difference between the heated surfaces and the freestream and that the temperature of the flow entering the turbine was uniform.

Standard error analysis techniques (see ref. 5) indicate that the corrected heat transfer coefficients were accurate to within ± 4 percent (See Table 6).

TEST CONDITIONS

The steady and unsteady aerodynamic data presented in this section represent only a brief summary of the aerodynamic data acquired during this program. The complete body of aerodynamic data is presented in Volume IV of this report entitled "Aerodynamic Data Tabulation", UTRC-R86-956480-4, NASA CR 179469.

1. Steady Aerodynamics

The aerodynamic documentation of the turbine model indicated that all parameters were very close to data obtained during prior testing with this turbine model (ref. 26). As an example, the midspan pressure distributions for the first stator, rotor and second stator are shown in figures 13, 14a-14c and 15a-15c, respectively. The measured data are represented by the symbols and the results of a two dimensional calculation (ref. 27) are represented by the curves. Since the inlet flow speed to the first stator was held nearly constant at 75 ft/second, the first stator midspan pressure distributions, e.g., figure 13, were nearly identical at the three flow coefficients at which tests were conducted. Figures 14a-14c and 15a-15c, respectively, show the rotor and second stator midspan pressure distributions at flow coefficients of 0.68, 0.78, and 0.96. The parameters required as input to the calculation and for calculating pressure coefficients (C_p) for each airfoil row were (1) the streamtube contraction and loss estimated from an axisymmetric through flow calculation, (2) the airfoil inlet total pressure deduced from the measured airfoil pressure surface static pressure (ref. 26), and (3) the airfoil exit static pressure calculated from the free vortex distribution between the measured hub and outer casing flowpath static pressures. The airfoil inlet and exit flow angles were varied to obtain the best agreement of the calculation with the measured airfoil surface pressure distributions. As seen in figures 13-15, agreement between the two dimensional potential flow calculation and the measured pressures at midspan is excellent. Surface velocity distributions computed with this potential flow analysis were used as input to the boundary layer claculations presented later in this report.

The flow at midspan on the first stator (fig. 13) is well behaved. On the pressure surface, the flow accelerates smoothly from the leading edge to the trailing edge. On the suction surface, there is an overspeed near the leading edge followed by an acceleration to the throat. From the throat, the flow decelerates smoothly to the trailing edge without separating. Flow visualization studies (ref. 26) conducted previously on this airfoil showed the flow on both the suction and pressure surfaces to be nearly two-dimensional and free of any regions of local separation. For the 15% stator 1/rotor axial spacing at all three flow coefficients with the grid in and out, a first stator exit flow angle of 22° measured from tangential resulted in the

best match between the calculated and measured pressure distributions. At the larger axial spacing (X/B_x = 0.5), an exit flow angle of 22.5° resulted in the best match. Overall, the first stator steady pressure distribution was invariant with rotor speed (flow coefficient) and inlet turbulence. The variation due to stator 1/rotor axial spacing was on the order of the experimental accuracy.

On the rotor, for both axial spacings with the grid in and out and at flow coefficients of 0.68, 0.78 and 0.96, a rotor exit flow angle of 25.25° resulted in the best match between the calculated and measured pressures (figs. 14a, b and c). At the 15% axial spacing with the grid in and out, rotor relative inlet angles of 45°, 40° and 35° resulted in the best match with the data at flow coefficients of 0.68, 0.78 and 0.96 respectively. At the larger axial spacing, rotor relative inlet flow angles of 46°, 41° and 35° resulted in the best match with the measured data. At a specific flow coefficient, for both the 15% and 50% axial spacings with the grid in and out, the rotor pressure distributions were nearly identical.

At the 0.96 flow coefficient (fig. 14c), the flow on the suction surface undergoes a strong overspeed near the leading edge and decelerates to the trailing edge. The suction surface overspeed results from the inlet flow being at nearly 5° positive incidence relative to that at the nominal design flow coefficient (0.78). At the 0.68 and 0.78 flow coefficients (figs. 14a and 14b), there is a slight overspeed in the flow near the leading edge on both the pressure and suction surfaces. The pressure surface leading edge overspeed is more pronounced at 0.68 where the inlet flow is at 5° negative incidence relative to that at the nominal design flow coefficient (0.78). Overall, the steady state flow over the rotor is weakly dependent on axial spacing and inlet turbulence. There is, however, a strong dependence on the relative inlet flow angle (flow coefficient). The absence of midspan boundary layer separation on both the pressure and suction surfaces has been demonstrated previously by extensive flow visualization (ref. 26).

Midspan pressure distributions were obtained on the second stator with the turbine model in the one and one-half stage configuration and with a first stator/rotor axial spacing of 50%. Overall, the match between the potential flow calculation and the measured results is good except in the region aft of the throat on the suction surface (figs. 15a, b and c). Distributions with the grid in and out are virtually identical. An exit flow angle of 26° resulted in the best match between the calculated distributions and the measured data at flow coefficients of 0.68, 0.78 and 0.96. Second stator absolute inlet flow angles of 65°, 62° and 51° gave the best match with the data at flow coefficients of 0.68, 0.78 and 0.96, respectively. Overall, the flow on both the pressure and suction surfaces is well behaved. On the pressure surface there is a very pronounced overspeed in the flow near the leading edge at all three flow coefficients. This is not surprising since

relative to the second stator inlet metal angle, the inlet flow is nearly at 18° of negative incidence at the 0.68 flow coefficient and at 5° of negative incidence at the 0.96 flow coefficient.

Other documentation of the turbine model steady aerodynamics included the hub and outer casing flowpath static pressures measured downstream of each airfoil row and circumferential distributions of total and static pressures and flow yaw and pitch angles measured downstream of each airfoil row with the traverse probes at midspan. Circumferential distributions of flow velocity and speed were calculated from these parameters. Due to mechanical constraints, all steady and unsteady circumferential traverse measurements were made with a first stator/rotor axial spacing of 50%.

Circumferentially averaged hub and casing flowpath static pressures for all three airfoils operating at the design flow coefficient (0.78) and with the grid out are shown in figure 16. Also shown are (1) a free vortex static pressure distribution calculated from the measured hub and casing flowpath static pressures and (2) the circumferentially averaged static pressure measured at midspan with the five hole probe. The free vortex calculation agrees with the traverse probe results at midspan and was used in the two dimensional potential flow comparisons in the calculation of the airfoil pressure coefficients for the measured data (figs. 13 through 15). The measured hub and casing flowpath static pressures for flow coefficients of 0.68, 0.78 and 0.96 with the grid in and out are tabulated in Volume IV (UTRC-R86-956480-4) along with the calculated free vortex values of static pressure at midspan.

Examples of the circumferential distributions of flow angle and velocity measured downstream of each airfoil row (at Sta. 2, 3 and 4, fig. 1) with the five hole traverse probe are shown in figures 17, 18 and 19. These results were acquired at the design flow coefficient (0.78) and with the grid out. All of the midspan traverse data (total and static pressures, flow yaw and pitch angles and velocity) acquired at each of the three flow coefficients with the grid out and in are presented in Volume IV of this report (UTRC-R86-956480-4). For each flow coefficient and with the grid both in and out, except for a level shift in the total and static pressure, the five hole probe circumferential traverse measurements obtained were nearly identical. The shift in pressure level is due to the reference pressure (inlet total) being located upstream of the turbulence grid location. By accounting for the total pressure loss across the grid, the measured total and static pressure distributions for the grid-in configuration can be made to match the grid-out distributions. Circumferential distributions of flow yaw angle and speed for the grid out (figs. 17, 18 and 19) are virtually identical to the results obtained with the grid in. Overall, the addition of the turbulence grid did not significantly alter the circumferential distributions of measured steady flow properties.

The circumferential variations in flow yaw angle and speed outside the first stator wakes (fig. 17) are predominantly due to potential flow effects and can be predicted at this axial traverse location using a two-dimensional potential flow calculation (e.g. ref. 27). Downstream of the rotor and second stator, however, strong three-dimensional secondary flow mechanisms are responsible for much of the circumferential variation in flow properties (figs. 18 and 19).

A comparison of the inlet and exit angles determined from the five hole probe traverse with those inferred from the potential flow calculation is shown in Table 4 for each airfoil row at the design flow coefficient with the grid out. Keep in mind that the potential flow calculation does not account for the axial gaps between airfoil rows. The assumption in the calculation is that the rows are sufficiently far apart that they do not affect each other. Overall the flow yaw angles deduced from the two dimensional potential flow calculation are in good agreement with the circumferentially averaged traverse measurements. The exception occurs at the rotor exit where the yaw angle obtained from the traverse is nearly six degrees greater than that deduced from the potential flow calculation. This underturning indicated by the traverse data is due to the fact that the traverse was conducted nearly 36% of axial chord downstream of the rotor trailing edge plane where the two counter-rotating rotor passage vortices do in fact result in an underturning of the flow (ref. 28). This three dimensional flow mechanism appears to have only had a very weak impact on the rotor midspan pressure distributions since they are in such good agreement with the two dimensional calculation.

Documentation of the time-mean velocity distributions at the inlet to the turbine model was accomplished using the previously described hot-film anemometer system. These time-mean velocity data were obtained at four pitch locations (0, 25, 50 and 75 percent pitch) at a plane 1.35 inches (23% chord) upstream of the first vane leading edge. The resulting mean velocity distributions, obtained both with and without the turbulence grid installed, are presented in figures 20a and 20b. As shown in figure 20a for each pitch location the mean velocity was quite uniform over the central 80% of the span with variations of less than about 5%. The inlet flow was uniform for both the no grid configuration and with the grid installed indicating that the grid blockage was very evenly radially distributed. In figure 20b the spanwise averaged velocities measured at the various pitchwise locations are compared to a potential flow prediction for the first stator row. As indicated in figure 20b the local measured velocities, both with and without the grid, are in excellent agreement with the potential flow prediction. At this station (X/B_x = -23%), then, both the prediction and data indicate that a ± 10% pitchwise variation in the mean flow field was induced by the first stator row. The potential flow prediction also indicated (not shown) that this upstream influence did not extend very far upstream of the stator leading edge station. For example, at X/B_x = -0.8 the pitchwise variation in mean velocity was predicted to be less than ± 1%.

2. Unsteady Velocity Measurements

Turbine Model Inlet Turbulence (Grid-Out). - Examination of the spectral distribution of the turbulence measured near the turbine inlet (grid-out) indicated that the hot film signal contained a number of narrow bands with very strong contributions to the total power spectrum. A sample grid-out unfiltered hot-film power spectrum from 0 to 500 Hz is presented in figure 21 with the narrow "spikes" of very high power density labeled A through I. Identification of the probable sources of each of these narrow bands was accomplished by process of elimination. First the turbine model was operated at a number of rotation speeds to determine which spikes were contributed by the model itself and which originated from other sources. All the remaining non-turbine-model bands were identified from known disturbance frequencies (e.g. the main blower blade passing frequency) or as predictable acoustic resonance lengths in the test facility. The specific frequency and probable source of each of the narrow bands is listed in figure 21. These "spikes" in the unfiltered signal almost certainly do not result from velocity fluctuations (turbulence) in the flow but are either the result of the probe shaking relative to the flow (A-fig. 21) or acoustic waves in the flowpath. Acoustic waves contribute to a hot film or hot wire signal because these sensors respond to the instantaneous sensor Reynolds number. An acoustic disturbance passing across the hot film produces an instantaneous density fluctuation and a contribution to the overall unsteady signal. These acoustic contributions to the signal (approximately 30% of the total signal) must be subtracted to determine the turbulence level. It should be mentioned that the possibility was explored that band F was not an acoustic disturbance but was indeed a periodic velocity fluctuation induced upstream of the rotor. This possibility was discounted because a potential flowfield computation indicated that at the hot-film sensor location the velocity fluctuations produced by the passing rotor blades would have been less than 1/10% of the mean velocity. The spanwise distributions of the measured turbine inlet turbulence intensity are presented in figure 22 for four pitchwise locations. These data represent the streamwise component of the turbulence computed by subtracting bands A through I (fig. 21) from the total local signal. As shown in figure 22, in the midspan region the turbulence intensity was slightly greater than 1/2% with much higher levels (as high as 10% near the case) in the endwall boundary layers.

Turbine Model Inlet Turbulence (Grid-In). - The spanwise distributions of the turbulence intensity measured at X = -1.35 inches (X/B_x = -23%) with the turbulence grid installed are presented in figures 23a and 23b. These figures present the streamwise RMS fluctuating velocities nondimensionalized by the local and mean-passage velocities respectively. The pitchwise variation of turbulence intensity was very much less for figure 23b than 23a indicating that the absolute value of the velocity fluctuations produced by the grid were relatively uniform. The pitchwise variations indicated by figure 23a resulted from the pitchwise variations of mean inlet flow field (see fig. 20). The average value of the turbulence intensity in the midspan region with the

turbulence grid in was 9.8% with a standard deviation of 0.46%. Note that there is a difference between the results shown in figure 23 (grid-in) and those presented in figure 22 (grid-out), both of which were obtained at the same axial station. Although the results shown in figure 20b confirm that the same pitchwise variation in local mean velocity existed for the grid-in and grid-out configurations the grid out turbulence intensities based on the local velocity collapsed to a single narrow band. That the low turbulence (grid out) intensities agreed when nondimensionalized on local velocity while the high turbulence (grid-in) intensities agreed when based on mean passage velocity is a consequence of the radically different wavenumber distributions for the two disturbance spectra. The grid generated turbulence had practically all its energy in eddys about the size of the grid bars while most of the energy for the no grid natural turbulence was in the very low wavenumber range (see fig. 21). This very long wavelength natural turbulence is an inherent consequence of drawing air from the outside with huge scale (>100') atmospheric fluctuations. The difference, then, between the grid-in and grid-out conditions is that while the grid generated turbulent eddys are small relative to the stator pitch the important eddy scale of the natural turbulence is immense compared to these same dimensions. The grid generated turbulence can be considered "frozen" after at encounters the stator potential flow field effects and so the relatively uniform velocity fluctuations translate to a uniform turbulence intensity based on a single mean passage velocity. The huge scale portion of the natural turbulence, on the other hand, appears as an unsteady flow field to the entire stator row. The entire potential flow fluctuates with the unsteadiness and hence turbulence intensities based on local mean velocities agree.

A comparison of the present grid-in turbulence results with the classic biplane grid study of Baines and Peterson (ref. 13) is presented in figure 24. Turbulence measurements obtained at midspan at X = -1.35 inches (X/B_x = -23%) and at X = 0 are shown as the solid symbols in the figure. Agreement between both the absolute level and the decay rate of these present results and the data of reference 13 was excellent.

In addition to the above measurements of turbulence intensity distribution both the integral length scale and the power spectral density of the streamwise component of the turbulence were recorded at selected stations. Measurement of turbulent length scales was accomplished by generating autocorrelations of the signals with a Saicor Model SAI-42 Correlator and Probability Analyzer. A correlator unit such as the Saicor SAI 42 generates the autocovariance of a fluctuating signal. For some input signal, E(t), the autocovariance is defined as

$$R_E(\tau) \equiv \overline{E(t) \times E(t + \tau)} \qquad (1)$$

where τ is a variable "delay" time and the product is averaged over time (t).

The autocovariance is usually written as a dimensionless quantity and is referred to as the autocorrelation coefficient. For our case, with the signal from the hot-film sensor, E(t) proportional to U(t) the autocorrelation coefficient of interest was

$$R_U(\tau) = \frac{\overline{U(t) \times U\ (t+\tau)}}{\overline{U'^2}} \qquad (2)$$

A single time scale characteristic of the longest correlation distance in the entire fluctuating turbulent field can be extracted from such autocorrelation data. This time scale, the "Eulerian Longitudinal (streamwise) Integral Time Scale" (J_{UX}), is defined as

$$J_{UX} \equiv \int_{\tau=0}^{\tau=\infty} R_U(\tau)\, d\tau \qquad (3)$$

The following sketch represents a typical freestream turbulence autocorrelation coefficient plot such as those produced by the SAICOR Correlator/Plotter unit used for these measurements (see fig. 5).

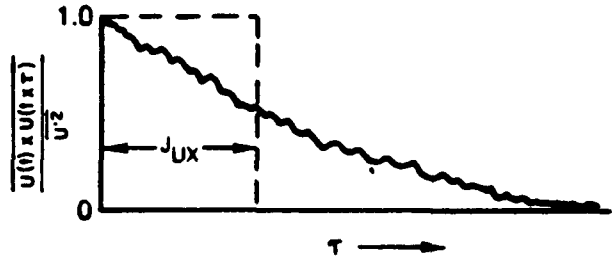

Integration of such curves was accomplished using a planimeter with the area (of unit length) being the longitudinal integral scale.

From Taylor's hypothesis (see Hinze, ref. 12), if $U'/U \ll 1$ then the turbulent eddies retain an approximately constant shape as they pass by the fixed hot-film sensor. The autocorrelation, then, is approximately equal to a space correlation with separation $-U\tau$ in the X direction.

$$R(X) = R(-\tau\bar{U}) \qquad (4)$$

Using equations (3) and (4), a "characteristic" length scale, the Longitudinal (streamwise) Integral Scale (Λ_f), can be determined for a given turbulent flow.

$$\Lambda_f = \bar{U}\, J_{UX} \tag{5}$$

The fluctuating velocities in a turbulent flow can be examined to determine the distribution, as a functiuon of frequency, of the various contributions to the overall turbulence level. For the present program, these frequency related data were obtained using a Spectral Dynamics Model SD 340 MICRO FFT Analyzer (see fig. 5). A spectral analyzer, such as the SD 340, processes a signal to determine the fluctuation level within particular intervals or bandwidths of frequency. The distribution of these narrow band fluctuation levels over a wide range of frequencies is referred to as the spectrum. The contribution of the square of the fluctuation levels within particular unit bandwidths to the overall fluctuation level squared is called the power spectral density. Knowing the overall level, the spectral analyzer output can be used to construct a power spectral density distribution (power spectrum).

Power spectral density distributions are usually presented in dimensionless form with the Dimensionless Spectrum, $\bar{U}\, U'^2(f)/(\overline{U'^2})\Lambda_f$, as a function of the Dimensionless Wavenumber, $\Lambda_f f/U$. In addition to previously defined symbols, these expressions contain U'(f), the fluctuating velocity within a bandwidth of 1 Hz, and the frequency f (Hz). The following sketch represents a typical free-stream turbulence power spectral density distribution.

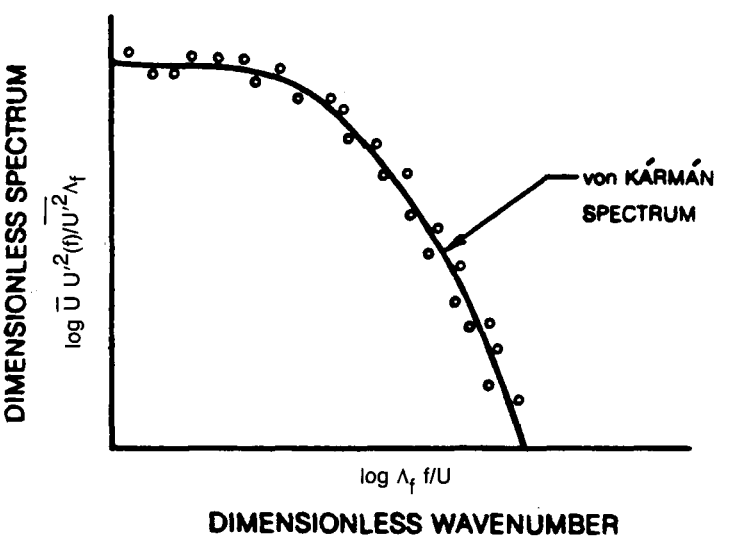

Included in the above sketch is the von Karman theoretical spectrum for one-dimensional isotropic turbulence, the form of turbulence expected to result in the flow "far" from the turbulence generating grids. A presentation of the analysis used to predict this spectrum can be found in Hinze (ref. 12).

The power spectral density distributions measured at five locations near the first stator leading edge are presented in figure 25. Also given in figure 25 are the local values of the mean and turbulent velocities and the measured local integral scale. As can be seen from an examination of figure 25, the spectral distributions at all five locations were in excellent agreement with the von Karman theoretical spectrum for one-dimensional isotropic turbulence.

Measurements of the local integral scale were obtained at twenty locations. These results indicated that the streamwise integral scale was relatively uniform with a mean value of $\Lambda_f = 0.80$ inches and a standard deviation for the 20 samples of $\sigma = 0.09$ inches.

The conclusion that has been reached from an examination of figures 23 through 25 are that in the midspan region: (1) the grid generated turbulence is relatively uniform with a mean value of $U'/U = 9.8\%$ at $X/B_x = -23\%$, (2) the performance of the present turbulence generating grid is in excellent agreement with the performance of similar biplane grids (ref. 13), (3) the spectral distribution of the grid generated turbulence was in excellent agreement with the von Karman spectrum, a result typical of fully developed grid generated turbulence.

Inter-row Velocity and Unsteadiness. - This section will present the results of the high response hot-film probe traverses carried out downstream of each airfoil row at midspan. Since one of the objectives of this program was to characterize the random, periodic and total unsteadiness levels between airfoil rows, the digitized hot-film probe data obtained during each rotor revolution at each circumferential traverse location was reduced to the instantaneous flow speed on an instant-by-instant basis (300 per revolution over three blade passing periods). This is illustrated in figure 26 where the instantaneous flow speed, $V_k(t)$, for one rotor passing period and one revolution is shown to be composed of a random component, $v_k(t)$, superimposed on the periodic, $\bar{V}_k(t)$, or phase lock averaged (PLA) component. The PLA speed at a particular circumferential traverse location is obtained by averaging the 100 sets (revolutions) of instantaneous speed data acquired at that location. A timewise integration of the PLA speed over the three rotor blade passing periods results in the time average (steady) flow speed, V_o. It must be kept in mind that since only a single, radially oriented, hot film probe was used in this experiment the probe output is a measure of flow speed (magnitude) and not flow velocity (direction).

Circumferential distributions over two first stator pitches of the time average speed downstream of all three airfoil rows at midspan are shown at the 0.78 flow coefficient with the grid out in figures 27a, 28a and 29a, respectively. The results with the grid in are presented in figures 27b, 28b and 29b. Note that the unsteadiness in these figures has been presented in terms of its square root. Hence, since $\overline{U}_T = \overline{U}_R + \overline{U}_P$ (fig. 26), the square root of the average of the total unsteadiness (TOT AVG) is the square root of the sum of the squares of the averages of the random and periodic unsteadinesses (RAN AVG, and PER AVG). The addition of the grid resulted only in relatively small changes in the circumferential distributions of flow speed downstream of each airfoil row (Sta's. 2, 3 and 4). The maximum difference in the pitch average speed due to the addition of the grid was 2.7% and this occurred at the second stator exit (Sta. 4) where the wake defect with the grid in (fig. 29b) was slightly less than that with the grid out (fig. 29a). For traverses made in the stationary frame, e.g., at Sta. 2 and 4, the circumferential distributions of flow speed measured with the hot film probe (figs. 27a and 29a) are nearly identical to those measured with the five hole probe (figs. 17b and 19b). No direct comparison can be made for the rotor since the pneumatic data (fig. 18b) was acquired in the rotating frame of reference and the hot film data (fig. 28a) was acquired in the stationary frame. In the hot film data at the rotor exit, low speed regions spaced one first stator pitch apart are evident for both the grid out and in (figs. 28a and 28b). These low speed regions are the chopped and highly bowed first stator wakes that have diffused as they were convected through the rotor passage. For both the grid in and out, the pitch averages of the circumferential distributions of the time average speed at all three measurement stations are in excellent agreement with the pneumatic five hole probe traverse results. Overall, the pitch average steady flow speed measured with the hot film and five hole probes differ by no more than ± 1.5%.

The time average total, $\overline{U}_T$, periodic, $\overline{U}_P$, and random, $\overline{U}_R$ unsteadiness levels at each circumferential traverse location were calculated independently using the relations shown in figure 26. Unsteadiness as defined here is based on flow speed fluctuations and not velocity (vector) fluctuations (ref. 29). The reference speed, V_{ref}, used in the calculations was the pitch average steady flow speed at the exit of the appropriate airfoil row. The relation shown by the last equation of figure 26 was used to check the data reduction, i.e., the total unsteadiness is equal to the sum of the periodic and random unsteadiness. Circumferential distributions of the square root of $\overline{U}_T$, $\overline{U}_P$, and $\overline{U}_R$ downstream of each airfoil row are shown in figures 27 through 29 for the turbine model operating at the design flow coefficient and for both the grid out and in. By presenting the square root of the unsteadiness the results are in a format similar to the typical representation of turbulence, i.e. a speed fluctuation. Also shown are the corresponding distributions of the time average (steady) speed discussed earlier. The pitch averages of the flow speed and the total, random and periodic unsteadiness are included on each

figure. Results obtained at the off-design flow coefficients (C_x/U = 0.68 and 0.96) with the grid out and in are presented in Volume IV (R86-956480-4) of this report. The high total unsteadiness peaks at Sta. 2 (figs. 27a and 27b) are due primarily to the random unsteadiness in the first stator wakes. The peak in periodic unsteadiness in the wake (figs. 27a and 27b) may be related to periodic vortex shedding from the first stator trailing edge. A reduction in periodic unsteadiness occurred both in and outside the first stator wakes when the turbulence grid was added (fig. 27b). Also, the addition of the grid resulted in an increase in random unsteadiness primarily in the potential core flow region between the wakes.

At the rotor exit (Sta. 3), for both the grid-out (fig. 28a) and the grid-in (fig. 28b), the peaks in total unsteadiness are nearly coincident with the low speed regions associated with the first stator wakes. With the grid out, peaks in both random and periodic unsteadiness nearly coincide with these low speed regions. The addition of the grid results in a smoothing of the total, random and periodic unsteadiness distributions. This can be seen by comparing figure 28a (grid-out) with figure 28b (grid-in) and is attributed to the enhanced mixing of the first stator wakes by the increased random unsteadiness produced by the grid.

As seen by comparing figures 29a and 29b, at the second stator exit (Sta. 4), the addition of the grid resulted only in very slight changes in the circumferential distributions of total, random and periodic unsteadiness. The peak levels of total, random and periodic unsteadiness nearly coincide with the second stator wakes (figs. 29a and 29b). These results are similar in what was observed at the first stator exit (Sta. 2).

The pitch average of the square root of the total, random and periodic unsteadiness distributions downstream of each airfoil row (figs. 27-29) are summarized in Table 5 for the design flow coefficient. Results for both the grid-out and grid-in configurations are presented. As seen in Table 5, there is an increase in total unsteadiness at the first stator exit when the turbulence grid is installed. This increase is primarily an increase in random unsteadiness outside of the stator wakes due to the addition of the turbulence grid (fig. 27b vs. 27a). The pitch averaged periodic unsteadiness at the first stator exit for both the grid-out and grid-in configurations is nearly the same. At the exit of both the rotor and second stator the pitch averaged total unsteadiness is unaffected by the addition of the turbulence grid. However, at the rotor exit, the addition of the grid results in a small increase in the pitch averaged random unsteadiness and a decrease in the pitch averaged periodic unsteadiness. At the second stator exit, neither the pitch average random nor the periodic unsteadiness is appreciably altered by the addition of the grid. The total unsteadiness is also unaffected by the addition of the grid.

These results indicate that the random unsteadiness introduced into the flow by the addition of the turbulence grid upstream of the first stator has nearly decayed to the grid-out level at the first stator exit (Sta. 2). At the rotor exit and at second stator exit, grid generated unsteadiness is barely discernible. The addition of the grid and the resulting unsteadiness at the inlet to the rotor had only a slight impact on the rotor midspan heat transfer. Also the addition of the grid resulted in a barely discernible increase in the second stator midspan heat transfer. These results will be discussed in greater detail later in this report.

EXPERIMENTAL RESULTS

1. Characteristics of the Turbine Model

As previously discussed this experiment was conducted in a large-scale rotating turbine model configured either as a single stage (stator 1/rotor) or as one-and-one-half stages (stator 1/rotor/stator 2). The turbine model simulates a relatively heavily loaded machine with a hub/tip radius ratio of 0.8. All three airfoil rows have solidities and aspect ratios very near unity. When operating at design conditions the turbine (at midspan) has a flow coefficient of 0.78, a stage loading coefficient of 2.8 and 34% static pressure reaction. The axial spacing between the first stator and the rotor was varied from 15% to 65% of the average of the first stage stator and rotor axial chords (B_x). Typical engine spacing is about 25% to 50% B_x. In the stage and a half configuration the axial spacing between the rotor and the second stator was held at a constant 63% B_x. The rotor tip clearance was 0.090 inches or 1.5% span which is typical for current engine design. Rotor incidence angle was varied widely with the flow coefficient (C_x/U) set from 54% to 123% of the design value. Rotor and second stator incidence changes are illustrated in figure 30 which shows a radial view of the turbine model in the one and one-half stage, grid-in configuration. The first stator/rotor axial spacing is 50%. Rotor inlet and exit velocity triangles for three values of flow coefficient (C_x/U = 0.68, 0.78 and 0.96) are also shown.

2. Format of the Data Presentation

This report (Volume I, UTRC-R86-956480-1) presents heat transfer data, summary curves, comparisons between various sets of these data and, finally, comparisons of the data with analytical predictions. Tabulations of the heat transfer data are available in Volume II, UTRC-R86-956480-2 (NASA CR-179467) (15% axial spacing) and in Volume III, UTRC-R86-956480-3 (NASA CR-179468) (65% axial spacing and the 1 1/2 stage configuration) while the aerodynamic data are tabulated in Volume IV, UTRC-R86-956480-4 (NASA CR-179469). Included in the heat transfer data tabulations are the specific test conditions for each data set. These test conditions, in particular the turbine inlet temperature, spanned a significant range (from 28°F to 60°F) since experimental testing extended over a period of many months.

Because of limitations in the number of thermocouple data channels available only two test airfoils could be monitored at any time (more precisely four models, a pressure and a suction surface instrumented airfoil for each of two airfoil rows.) For this reason when the turbine model was configured as a single stage both the first stator and the rotor could be simultaneously monitored while for the stage-and-a-half configuration only the data from the rotor and the second stage stator were obtained. It has been assumed, and borne out by the stator 1/rotor and rotor/stator 2 interaction tests, that the

effects of the second stator on the first stator heat transfer distribution were negligible. The stage-and-a-half configuration data, then, are presented as consolidated sets. In reality the first stator heat transfer data for these stage-and-a-half sets were obtained with the turbine model configured as a single stage.

The distributions of heat transfer along the various airfoil surfaces are presented as Stanton numbers based upon the specific test exit velocity and density for the particular airfoil. The Stanton numbers are plotted as a function of surface distance from the reference location (fig. 4) nondimensionalized by the axial chord. On each heat transfer distribution figure the location of the airfoil trailing edge is indicated as TE. In addition, for each distribution a data code of six (6) digits appears: R__P__ giving two (2) digit RUN (R) and POINT (P) numbers for the data set. These run and point numbers provide a cross-reference between the present summary report and Volumes II and III where the individual data points are tabulated. Included in each figure are the specific flow coefficient and axial spacing for the data set and a note indicating whether the upstream turbulence generating grid was IN or OUT.

3. Baseline Airfoil Heat Transfer Distributions

Midspan heat transfer distributions for all three airfoil rows of the turbine are presented in figures 31a, 31b and 32 for the design operating point (Cx/U = 0.78). The purpose of presenting these three figures is to introduce the general features of the measured heat transfer distributions for a relatively simple test case. This particular test condition, designated as the "baseline" case, was selected because it combined airfoil spacings, a flow coefficient and Reynolds numbers near typical design values with a low flow turbulence level at the model inlet. For this "baseline" case the stator 1/rotor spacing was 65% Bx. The rotor/stator 2 spacing was 63% Bx. The flow coefficient (C_x/U) was 0.78. There was no upstream grid so the inlet turbulence level was approximately 1/2%.

For each of the three figures the experimental data are compared to heat transfer distributions predicted by the UTRC two-dimensional finite difference boundary layer code (ABLE, refs. 30 and 31). For figures 31a and 31b predictions for both fully laminar (L) flow and fully turbulent (T) flow (Cebeci-Smith, ref. 32) are included. Only the fully turbulent (T) prediction was presented for figure 32. Each of these finite-difference boundary layer computations employed the respective computed airfoil velocity distribution of figures 13 through 15 as input.

For the first stator (fig. 31a) the two-dimensional prediction provided an excellent description of the measured heat transfer distribution. For nearly the entire pressure surface and for the upstream half of the suction

surface the agreement between the heat transfer data and the laminar prediction was excellent. At $S/B_x \sim 1$ the data indicate that the suction surface boundary layer passed through transition downstream of which the heat transfer slightly exceeded the level predicted for fully turbulent flow. This local post-transition "overshoot" of the heat transfer level was probably a result of the low local boundary layer momentum thickness Reynolds number (Re_θ). The predicted growth rate of the laminar portion of the suction surface boundary layer was considerably lower than the predicted growth rate of the fully turbulent portion. At $S/B_x = 0.9$ the laminar boundary layer calculation predicted $Re_\theta = 490$ while the fully turbulent computation predicted $Re_\theta = 1510$. For this reason at $S/B_x \sim 1$, where the boundary layer actually passed through transition, the test boundary layer Re_θ was considerably smaller than that predicted for fully turbulent flow. The local measured heat transfer then locally exceeded the predicted fully turbulent value. Downstream of the "overshoot" the rapid growth rate of the post-transitional boundary layer brought the measured heat transfer into close agreement with the fully turbulent prediction.

In contrast to the accuracy of the two-dimensional boundary layer predictions for the first stator the comparisons between the predictions and the data for the rotor, figure 31b, showed considerably greater disagreement. The rotor airfoils, of course, were exposed to a much more disturbed flow than the first stator since they were passing through both the wakes and the potential flows generated by the first stators (ref. 26). As can be seen from an examination of figure 31b the measured heat transfer distribution indicates that the only region of laminar flow on the entire rotor was in the immediate vicinity of the stagnation region. On the suction surface there appears to be about one-third of a chord of transitional flow followed by fully turbulent two-dimensional heat transfer. On the pressure surface the measured heat transfer rates exceeded the two-dimensional fully turbulent level by as much as 50%. Pressure surface heat transfer rates well in excess of two-dimensional fully turbulent levels were measured for many of the test cases in this study. This phenomenon was observed for certain test conditions for each of the three airfoil rows and will be discussed in detail in later sections.

An examination of figure 32 indicates that for the second stator the two-dimensional analysis had little relationship to the measured results. This result was probably a consequence of the intense turbulence, unsteadiness and secondary flows, e.g. the rotor tip leakage vortex, generated by the first stage rotor. Note that for both the pressure and suction surfaces the measured heat transfer rates were well in excess of the predicted levels.

The important observation to be made from figures 31a, 31b and 32 is that there was a progressive and significant increase in the complexity of the flow as it proceeded through the turbine. At the first stator the measured heat transfer distribution was very well described by two-dimensional laminar and turbulent boundary layer predictions. These predictions worked reasonably

well for the leading edge region and suction surface of the rotor but quite poorly for the rotor pressure surface and for both surfaces of the second stator. Secondary flows, unsteadiness and turbulence generated at each successive airfoil row appears to have made the flow less and less well described by a two-dimensional boundary layer analysis.

4. Effect of Stator 1/Rotor Spacing

The extent to which turbine airfoil heat transfer rates are affected by stator-rotor aerodynamic interactions is not currently known. Although it is virtually certain that the periodic unsteadiness, turbulence and secondary flows generated in the stator row affect the downstream rotor heat transfer, it is not known whether the rotor influences the upstream stator heat transfer through potential flow field interactions. One factor which may influence the magnitude of stator-rotor interaction effects is the size of the axial separation between the stator trailing edge and the rotor leading edge. Although periodic potential (inviscid) flow field interaction effects diminish rapidly with increasing separation, the influence of increasing separation is much slower for effects related to stator wakes and secondary flows. The impact of these viscous and secondary flow phenomenon on the rotor flow field is extremely complex and the role played by airfoil axial spacing is currently unknown.

The effects on airfoil heat transfer produced by changing stator-rotor spacing were examined in the present study using two model configurations. The test configurations consisted of stator 1/rotor axial separations of 15% and 65% B_x. Heat transfer distributions measured on both the first stator and on the rotor for both spacings are given in figure 33. The 65% B_x data and the theoretical laminar and turbulent predictions are the "baseline" results presented previously in figure 31. For both spacings of figure 33 the flow coefficient was 0.78 and the turbulence grid was out. An examination of figure 33 reveals that, at least for this turbine model, even this relatively large change in axial spacing did not materially change either the stator or the rotor heat transfer distributions. This result is in conflict with data published by Dring, et al., reference 26 which were measured in an earlier study in this same facility. The data of reference 26 indicated that changing the axial separation had produced a significant difference in the stator suction side heat transfer. Since these earlier data were obtained (1) using a considerably less accurate thermocouple monitoring system than used for the present system, and (2) using a far less exhaustive documentation of the temperature field at the inlet to the turbine model (see the discussion at the end of EXPERIMENTAL EQUIPMENT, 5. Airfoil Heat Transfer Measurements), the present results are believed to be far more accurate. The conclusion drawn from this test, then, is that changes to the stator-rotor axial spacing produced negligible effects on the heat transfer distirbutions on either the stator or the rotor. The same conclusion was also reached with the turbulence grid in as will be discussed below in Section 7.

5. Effect of Reynolds Number with Low Inlet Turbulence

The next series of figures (34, 35a and 35b) display the effects of airfoil Reynolds number on the first stage heat transfer distributions. These data were all obtained with a near-design flow coefficient ($C_x/U = 0.78$) upstream turbulence grid out and 15% axial spacing. The heat transfer distributions for the first stator for Re (based on axial chord and exit conditions) = 41 to 65 x 10^4 are presented in figure 34. Each of the measured data sets is shown compared to the predicted two-dimensional heat transfer distribution for that particular Reynolds number. On the pressure surface, agreement with the fully laminar prediction was excellent for all three Reynolds numbers. Evidence of possible boundary layer transition near the pressure surface trailing edge progressively decreased with decreasing Reynolds number. On the suction surface the agreement between the laminar prediction and upstream half of the data was also excellent in all cases. A careful examination of the data near $S/B_x = 1$ indicates that transition moved progressively, albeit slightly, downstream as Re decreased. Finally for $S/B_x > 1$ both the highest and lowest Re data agreed very well with the two-dimensional fully turbulent prediction. For Re = 52 x 10^4 an anamolous discrepancy of about 10% between theory and data is present for this region. One possible explanation for this difference is that an undetected shift in model heat flux occured during the process of data acquisition.

The primary conclusion reached from figure 34 is that the facility, turbine model and instrumentation system all behaved as expected. As the Reynolds number changed for this relatively clean first stator flow the data and the theory remained in excellent agreement.

The rotor heat transfer distributions for this test configuration (15% gap, grid-out) are presented in figures 35a & 35b for Re = 23-58 x 10^4. Each data set is again shown compared with the two-dimensional prediction for that particular Re. On the suction surface there was an increasingly significant, both in size and heat transfer level, transitional region as the Reynolds number dropped. For all cases, however, the suction surface heat transfer data agreed reasonably well with the two-dimensional, fully turbulent boundary layer prediction in the trailing edge region.

The pressure surface heat transfer distributions shown in figure 35 reveal a strong dependence on the Reynolds number. At the largest Reynolds number the pressure surface heat transfer is significantly higher (by 50 to 80%) than the fully turbulent prediction. As the Reynolds number drops the data approach the turbulent predictions. As mentioned previously, elevated levels of pressure surface heat transfer were observed for numerous airfoil-flow condition combinations in this investigation. Discussion of the phenomenon will follow as more examples are presented.

6. Effect of High Inlet Turbulence Level

A primary objective of this program was to examine the effects of high levels of broad band inlet turbulence on the airfoil heat transfer distributions. High levels of inlet turbulence were produced for these experiments using a coarse generating grid installed upstream of the turbine model. As established by the data presented in the section describing the test conditions the turbulence produced by this grid was homogeneous and near isotropic. With the grid in, the average turbulence intensity just upstream of the first stator leading edge was 9.8% while the "grid-out" (baseline) turbulence was 1/2%. The effects on the airfoil heat transfer distributions produced by raising the inlet turbulence intensity are shown in figures 36 and 37. The single stage (stator 1/rotor) heat transfer distributions are given in figure 36 while the rotor/stator 2 distributions for the stage-and-a-half configuration are presented in figure 37. The flow coefficient and Reynolds number were very similar for the two cases. It is expected that the first stator distribution shown in figure 36a was not changed by the installation of the second stator so these first stator data apply to both the single and the stage-and-a-half configurations.

As indicated by the results shown in figure 36a the impact of the high inlet turbulence on the first stator distribution was dramatic with significant increases of heat transfer on the leading edge and along both the suction and pressure surfaces. On the suction surface the increased turbulence moved the location of transition well upstream from $S/B_x \approx 1.0$ to $S/B_x \approx 0.3$. For this high level of turbulence, then, transition occured in a region of accelerating flow instead of near the minimum pressure point (see fig. 13). Another effect of the turbulence on the first stator suction surface distribution was to produce considerably enhanced heat transfer in the fully turbulent portion of the flow.

The effect of the higher turbulence level was also very evident along the first stator pressure surface. For the low turbulence case the heat transfer was essentially laminar while with high turbulence the measured heat transfer was as much as 60% greater than the two-dimensional fully turbulent prediction. The data of figure 36a constitute another example of an airfoil-flow condition combination for which the measured pressure surface heat transfer far exceeded fully turbulent levels.

On the rotor, figure 36b, the effects produced by increasing the inlet turbulence were much less dramatic than for the first stator. A much smaller change to the heat transfer resulted for the rotor because even the baseline (low inlet turbulence) rotor flow is highly disturbed by the first stator wakes. The incremental change in the unsteadiness level produced by installing the grid was much less for the rotor than for the first stator. On the rotor suction surface, transition appears to have moved upstream to $S/B_x \sim 0.2$

with the increased turbulence level. Changes downstream of transition in the fully turbulent region were negligible. The only region of the rotor pressure surface which showed any effects from the increased turbulence was close to the leading edge ($-0.5 < S/B_x < 0$).

The data presented in figure 37a were obtained on the rotor with the second stator installed in the turbine model. The data of figure 36b (single-stage) and 37a (stage-and-a-half) were measured for the same dimensionless running conditions on test dates about five months apart. Because this test facility draws air from the outside there was a significant difference in inlet temperatures (about 25°F) between the test sets. Despite this difference and the time separation (wear on the slip-ring unit) the data of figures 36b and 37a are in excellent agreement. The only significant difference between the data sets was for the aft region of the pressure surface for no grid. In this region the single-stage and the stage-and-a-half data differed by about 10%, a difference which may be a real stator 2/rotor interaction effect or simply an experimental anamoly.

The impact of changing the inlet turbulence level on the stator 2 heat transfer is shown in figure 37b. These results indicate that the impact of the inlet turbulence was negligible, an effect which was expected as the baseline second stator flow field was so highly disturbed even in the absence of the turbulence grid.

7. Combined Effects of Inlet Turbulence and Stator 1/Rotor Spacing

In Section 4 above it was concluded that for the low inlet turbulence configuration the impact on heat transfer of changing the stator 1/rotor spacing was negligible. To confirm that there was no amplification between the periodic stator 1/rotor interaction effects and the addition of broad based inlet turbulence these axial separation tests were repeated with the grid installed (figs. 38a and 38b). These results confirm the conclusion reached earlier with no grid, i.e. axial spacing does not materially impact either the first stator or rotor heat transfer.

8. Effect of Reynolds Number with High Inlet Turbulence

The next series of figures (39a & b and 40a & b) displays the impact of Reynolds number on the first stator and rotor heat transfer distributions with high inlet turbulence. The first stator distributions are given for seven Reynolds numbers ranging from 2.4 to 6.4 x 10^5 in figures 39a and 39b. The Reynolds numbers decrease from the top to the bottom of each figure, two separate figures are being used to avoid crowding. On the first stator suction surface figures 39 show an orderly, progressive downstream movement of the

transition zone with decreasing Reynolds number. As the Reynolds number decreased the length of the near-laminar heat transfer zone increased and the length of the fully turbulent zone contracted. On the pressure surface the data sets can be separated into two groups. For $Re \geq 4.0 \times 10^5$ the measured heat transfer exceeded each fully turbulent prediction while for $Re \leq 4.0 \times 10^5$ there was near agreement between the data sets and the respective two-dimensional predictions.

Results similar to those of the first stator are shown in figures 40a and 40b for the rotor. On the suction surface, for the highest Reynolds number, the data and fully turbulent prediction agree for the entire chord. As Reynolds number decreased a progressively growing zone of transitional flow developed and the region of fully turbulent heat transfer decreases. On the pressure surface the sharp rise in heat transfer near the trailing edge steadily decreased with the Reynolds number. Although the differences between the fully turbulent predictions and the respective pressure surface data decreased with falling Reynolds number there was no case which provided good agreement along the entire suction surface. Specifically, the data in the region around $S/B_x = -0.4$ was always about 40% above the prediction.

9. Pressure Surface Heat Transfer

There have now been a large number of examples presented in which the pressure surface heat transfer rates significantly exceeded the two-dimensional, fully turbulent predictions. For the first stator heat transfer rates in excess of fully turbulent were demonstrated for high Reynolds numbers and high inlet turbulence (fig. 39a). For the rotor, very high pressure surface heat transfer was documented for high Reynolds number-low inlet turbulence flow (fig. 35a) and for all Reynolds numbers with high inlet turbulence (figs. 40a and 40b). These results indicate that there can be an interaction between the effects of concave surface curvature, Reynolds number and the level of free-stream disturbance that may produce heat transfer enhancement to levels far in excess of fully turbulent. The variation of the Reynolds number for these tests affected both the surface momentum thickness distributions and the local boundary layer acceleration parameter, $K = \nu/U^2 \, \partial U/\partial x$. For a fixed location on a particular airfoil there was a reduction in Re_θ and an increase in K as the Reynolds number dropped. One possibility is that for certain critical combinations of concave surface curvature, Re_θ, K and free-stream disturbance level, important Goertler vortex systems are produced in the boundary layer. Perhaps the development of these systems is surpressed for sub-critical situations and two-dimensional, fully turbulent flow results. Whatever the physical cause of this phenomenon, similar effects have been observed by other investigators. Both Consigny and Richards (ref. 33) and Daniels and Browne (ref. 34) reported pressure surface heat transfer rates well in excess of fully turbulent values.

10. Effect of Flow Coefficient (Rotor Incidence)

All of the data presented up to this point were obtained with the turbine model operating at the design flow coefficient ($C_x/U = 0.78$). To examine the effects of flow coefficient (rotor incidence) on the airfoil heat transfer, test data were obtained for a range of off-design conditions. Flow coefficient variations were produced by holding the facility through-flow velocity (C_x) constant and adjusting the rotor speed (U). Although the rotor inlet relative velocity was a function of the flow coefficient, the rotor exit relative velocity was to first order invariant. All of the Stanton number distributions presented in this report are based upon airfoil exit conditions so it is possible to make a comparison between heat transfer distributions obtained at different flow coefficients. To avoid crowding only the design flow coefficient theoretical heat transfer distribution is presented for each airfoil.

The following table lists the flow coefficients at which data were acquired. It also lists the rotor inlet relative flow angle (from tangential, β), and the change in rotor incidence from the nominal design condition (Δi).

C_x/U	β	Δi
0.96	35°	+5°
0.78	40°	0
0.68	45°	-5°
0.56	55°	-15°
0.50	65°	-25°
0.45	75°	-35°
0.42	85°	-45°

It had been observed in previous flow visualization tests with this rotor (ref. 35) that the airfoil had attached boundary layers over the flow coefficient range from 0.96 down to 0.56. At 0.50 and below a separation bubble appeared on the rotor pressure surface near the leading edge. This bubble grew with further reductions in flow coefficient. At 0.42 the bubble had grown to about midchord.

First stator and rotor heat transfer distributions obtained over a relatively small range of flow coefficient are presented in figure 41 for the low inlet turbulence condition and in figure 42 for high inlet turbulence. An examination of figure 41 indicates that changing the flow coefficient had no significant impact on the first stator heat transfer. On the rotor (fig. 41b)

the data indicate that: 1) the heat transfer rates near the trailing edge on both the pressure and suction surfaces were nearly independent of flow coefficient, 2) the peak stagnation region ($S/B_x = 0$) heat transfer depended on the flow coefficient as a consequence of the changing relative inlet velocity and 3) there were local effects on both the pressure and suction sides near the stagnation region which were dependent on the flow coefficient (i.e. incident flow speed and angle). Note the effects on the rotor suction surface near $S/B_x = 0.3$. As C_x/U increased, a region of very high local Stanton number resulted at this location. The basic cause of this spike in heat transfer is the suction surface overspeed (fig. 14c), the strength of which is a function of the flow coefficient. At $C_x/U = 0.68$ there is only a slight overspeed followed by a favorable pressure gradient to midchord (fig. 14a) while for $C_x/U = 0.96$ the suction surface overspeed location has by far the highest velocity on the airfoil and is followed by a strong adverse pressure gradient (fig. 14c). For $C_x/U_m = 0.96$ the boundary layer is apparently unable to negotiate the adverse pressure gradient, separates, passes through a very short transition and reattaches as a high-speed fully-turbulent layer. For $C_x/U = 0.68$ the boundary layer experiences an extended transition length through the favorable pressure gradient to near midchord. A much subdued version of this same phenomenon can be seen on the pressure surface where the most severe overspeed ($S \sim 1/2$ inch) occurs for $C_x/U = 0.68$ (fig. 14a).

Stator 1 and rotor heat transfer distributions obtained for the same three flow coefficients with the turbulence grid are presented in figures 42a and 42b. As for the low free-stream turbulence case the first stator heat transfer data, figure 41a, indicate no impact from the variation in flow coefficient. On the rotor the addition of free-stream turbulence tended to reduce the relative importance of the flow coefficient effects. With the high inlet turbulence nearly the entire suction surface has fully turbulent heat transfer rates while the pressure surface distributions have nearly collapsed to a single curve.

Rotor heat transfer distributions obtained for an extremely wide range of flow coefficients are presented in figure 43. These rotor data were obtained for the stage-and-a-half configuration and no turbulence grid. Data are presented for seven flow coefficients ranging from 0.96 to 0.42 with the results plotted in two separate figures to avoid crowding. Note that the data for $C_x/U = 0.96$ are given in both figures 43a and 43b for purposes of comparison. These results reflect operation at severe-off-design (negative incidence) conditions and are included to demonstrate the impact on heat transfer for such extreme excursions.

On the suction surface, for $S/B_x < 0.7$, the local Stanton numbers decreased with C_x/U for the four test conditions of figure 43a until they approached laminar heat transfer rates. Further decreases in C_x/U, shown in figure 43b, produced nearly identical, near laminar, heat transfer rates in

this region. For reasons of economy the suction surface thermocouples downstream of $S/B_x = 0.7$ were not utilized during this phase of the experiment (as seen in figure 43b). On the pressure surface there was a continuous, systematic increase in Stanton numbers through the entire range of test flow coefficients. The appearance of the distributions suggests that for $C_x/U < 0.5$ the flow was separated from the pressure surface. At these extreme negative incidence values the heat transfer was evidently dominated by a large, possibly unsteady, pressure surface separation bubble observed to start at $C_x/U = 0.50$ and to grow in chordal extent as (C_x/U) was reduced (ref. 35).

11. Second Stator Heat Transfer Distributions

The flow field entering the second stator row fluctuates temporally at the rotor blade passing frequency. The effects generated by the first stator remain sufficiently coherent while passing through the rotor, such that a circumferential variation with the pitch of the first stator is present in the second stator inlet flow field (ref. 29). For this reason, the possibility that the second stator heat transfer was dependent upon circumferential location relative to the first stator was examined as part of this program. The second stator heat transfer was determined with the first stator located at five circumferential positions. The first stator row was indexed circumferentially in five increments of 25% of the first stator pitch so that the first and last locations were geometrically similar. The heat transfer distributions measured for the five index locations are given in figure 44a with no inlet turbulence grid and in figure 44b with the grid installed. The value (L) given for each data set indicates the stator 1/stator 2 relative circumferential position in fractions of a pitch.

Probably the most striking feature of the second stator heat transfer distributions, both for the grid-in and grid-out are the very high values of Stanton number relative to the two-dimensional turbulent boundary layer prediction. On the pressure surface the heat transfer data are 50-100% above the prediction. This result is in general agreement with most of the first stator (grid in) and rotor pressure surface measurements. On the suction surface, however, the second vane heat transfer is entirely different from the first stage results. Not only are the suction surface heat transfer data well in excess of the two-dimensional prediction but the data and theory are diverging with increasing distance. It appears that by the second stator the flow field has become so contaminated by secondary flow that a two-dimensional prediction is inappropriate.

The effects associated with stator 1/stator 2 relative location appear to have been minor. For both grid-in and grid-out the suction surface data obtained at L = 0.0, 0.25, 0.50, and 1.0 were in good agreement with only the data at L = 0.75 falling about 10% below the other four sets. On the pressure

surface the data for all five index locations were virtually identical, both with and without the grid. These results indicate that the strong circumferential gradients from the first stator have spread across most of the channel by the second stator leading edge to the extent that their impact on heat transfer is minimal. Finally, the absolute differences between the data of figures 44a and 44b (grid in VS out) were very small indicating that the influence of turbulence at the turbine inlet is restricted to the first stage.

12. Heat Transfer Distributions in the Leading Edge Region

First Stator. - Detailed distributions of the heat transfer measured in the leading edge region of the first stator are given in figures 45 and 46. The data of figure 45 were obtained with the upstream turbulence grid out and for figure 46 with the grid in. For these figures the heat transfer data are presented in the form of the Froessling number $Nu/\sqrt{Re_o}$ where the Reynolds number is based on the diameter of the leading edge and the incident flow speed. Locations for these detailed leading edge plots are given as S/R_N, the surface distance divided by the nose radius. Included in each figure is a simple prediction of the laminar heat transfer distribution. No enhancement due to the incident free-stream turbulence has been employed. As in all earlier plots S = 0 corresponds to a geometrical location (fig. 4) and not to the stagnation point. The stagnation point predicted by a potential flow computation (ref. 27) is given by the solid dot on the theoretical curve. Note that, unlike a cylinder in crossflow, the heat transfer distribution is not symmetrical about the stagnation point. In addition, since the flow acceleration is very much stronger in the direction of the suction surface, the maximum predicted heat transfer rate is not at the stagnation point but is displaced toward the suction surface. For both figures 45 and 46 data are presented for a range of Reynolds numbers. The scatter of all the data taken at each location is indicated by range bars.

The grid-out results of figure 45 indicate that the first stator leading edge results were very well predicted by the laminar theory. In addition the data bear out the asymetrical leading edge heat transfer distribution predicted by the potential flow and boundary layer solutions. The data taken with the upstream grid installed are given in figure 46. In these cases the data were about 20% higher than the laminar prediction and, again, bear out the predicted asymetrical distribution. The results of figure 46 are quite surprising in that the change in first stator inlet turbulence from 1/2% to 9.8% produced such a small change in Froessling number. Data taken in a number of studies of cylinders in cross flow have indicated that freestream turbulence has a very strong effect on the stagnation region heat transfer (see Lowery and Vachon, ref. 36). It may be that the effects of freestream turbulence are much larger for free cylinders than for cylindrical leading edges of airfoils. For the cylinder there may be interactions between the

unsteady wake flow and the free-stream turbulence which produce enhancement of the leading edge heat transfer due to the unsteadiness. There is also the possibility that the difference may be related to the scale of the turbulence involved or to some other feature of the flow.

Rotor. - Froessling number distributions for the rotor leading edge with the grid-out and grid-in are given in figures 47 and 48 respectively. For these rotor plots the Reynolds numbers are based on the approach relative velocity and they, as well as the stagnation point location, are dependent on the flow coefficient. Theoretical laminar heat transfer distributions are given for three flow coefficients C_x/U = 0.68, 0.78, 0.96. Note that the theoretical location of the stagnation line is indicated for each curve showing the shift towards the pressure surface as C_x/U increases. Figure 47 includes seven sets of data (actually 14 sets since the leading edge data are composites from the two test airfoils) which cover a factor of 3 in nose Reynolds number. Agreement between the theoretical laminar predictions and this data with the grid out is very good. Again, this result is surprising in that the rotor is chopping through the stator wakes apparently without the enhancement one might have expected for a cylinder in cross flow.

The influence of the upstream grid on the rotor leading edge heat transfer is shown in figure 48. Differences between figures 47 and 48 were small (10-20%).

Second Stator. - Data and theoretical predictions for the second stator leading edge, grid-out and grid-in, are given in figures 49 and 50. Again the measured and predicted results are asymetrical. The data and the laminar theory are in good agreement and the effect of the upstream grid was small. That the second stator leading edge data was substantially in agreement with the laminar theory is quite remarkable considering how disturbed the flow is at this station. There was considerable disagreement between theory and data everywhere else on this airfoil (fig. 44) but in the leading edge region the agreement is excellent.

13. Comparison of Rotor and Plane Cascade Data

Surface heat transfer distribution data were obtained in an earlier investigation in a cascade with the same rotor airfoil geometry used in this present program. The earlier data were obtained in a large-scale plane cascade and were published by Graziani et al. (ref. 5). In brief, the cascade test airfoils had an axial chord of 11.08 inches and an aspect ratio and solidity near unity. The cascade inlet angle was 44.6° so the airfoil incidence was nearly identical to that for the cases in the present study with flow coefficient of 0.68. The cascade heat transfer data were obtained for an exit Reynolds number of 8.8×10^5 and for two values of endwall boundary layer thickness. The heat transfer data of the cascade study were measured using an electrically-heated-wall/thermocouple system similar in principle to that used

for the present study. Only a very limited number of data points were obtained in the leading edge region of the cascade. A detailed description of the cascade experiment is given in (ref. 5).

The airfoil midspan heat transfer data of reference 5 are presented in figure 51 in the coordinates used for the present program. Data are given for the cases with a very thin (δ < 1 inch) and a relatively thick (δ > 2 inches) endwall boundary layers, both of which had an inlet turbulence level of 1%. Laminar and turbulent heat transfer distributions predicted by the same analysis used in all of the previous comparisons (refs. 30 through 32) are included in figure 51. On the suction surface the data for the thin endwall boundary layer indicate that the flow was well modeled by the two-dimensional theory. Evidently the boundary layer remained laminar from the stagnation line to about $S/B_x = 0.4$, passed through transition and behaved as a fully turbulent, two-dimensional flow from $S/B_x \sim 1$ to the airfoil trailing edge. The thick-endwall-boundary-layer suction surface data appears to indicate that transition occurred somewhat upstream of the location for the thin boundary layer case. Following transition the heat transfer measured for the thick endwall boundary layer fell significantly below the fully turbulent prediction. Sharma and Graziani (ref. 37) have demonstrated that the reduced suction surface, aft-region heat transfer of the thick endwall boundary layer case resulted from the flow convergence produced by the passage secondary flow vortices. On the pressure surface the thick and thin endwall boundary layer cases were in close agreement at a nearly constant level of heat transfer matching neither the laminar nor the turbulent predictions.

A comparison of the heat transfer distribution measured in the cascade with thin endwall boundary layers, with the data obtained in the rotor of the present study is presented in figure 52. These two data sets were obtained at somewhat different Reynolds numbers so the predicted heat transfer distributions are given for both conditions. An examination of figure 52 indicates that, on the suction surface, transition was somewhat earlier for the rotating case than for the blade cascade. This result is not surprising as the disturbance level for the rotating blade was considerably higher than the 1% turbulence level at the entrance of the cascade. When allowance is made for the effect of Reynolds number, the post-transitional ($S/B_x > 0.8$) results for the rotating and cascade tests were practically identical. There was, however, a significant difference between the heat transfer distributions measured on the pressure surface with the cascade data falling well below the set from the rotating blade. This provides an additional piece of evidence which indicates that strong enhancement of fully turbulent, concave surface heat transfer may only occur for high levels of free-stream disturbance. Whatever the cause, the major difference between the rotating and non-rotating airfoil midspan heat transfer distributions was the considerably higher levels of free-stream turbulence on the pressure surface of the rotating airfoil.

The heat transfer data mesured in the leading edge region of the cascade airfoils are presented in figure 53. Included in figure 53 are the predicted laminar distributions for this airfoil as well as the comparable leading edge data from the rotating cases (grid out). Note that for laminar flow the Froessling number is independent of Reynolds number. Because of the different instrumentation techniques employed the experimental uncertainty is considerably greater for the cascade leading edge data than for the rotating airfoil data. Despite the data scatter associated with the cascade model it is still clear that the stagnation region heat transfer was reasonably well predicted by the laminar model. There was no evidence that the moderate (~ 1%) free-stream turbulence in the cascade tunnel substantially enhanced the heat transfer in the leading edge region of the airfoil.

14. Spanwise Distributions of the Heat Transfer

As discussed in the "Heat Transfer Instrumentation" section, spanwise variations of the Stanton number were determined using spanwise rows of thermocouples. Each of the test airfoils was instrumented with six spanwise rows consisting of seven thermocouples spaced at 1/2 inch increments (spanwise locations were midspan, ±1/2 inch, ±1 inch and ±1 1/2 inch). The specific streamwise locations of the spanwise rows are given in figures 9, 10, and 11.

Plots of the spanwise distributions of the heat transfer are presented for all test cases in Vols. II and III of this report. Spanwise distributions are given for both the suction and pressure surfaces of each airfoil. An examination of the first stator pressure surface distributions indicates that for all test cases and streamwise locations the heat transfer was uniform over the entire width of the spanwise instrumentation pattern (the central 50% of the span). On the first stator suction surface the central 40% of the span showed spanwise uniform heat transfer for all locations. The outboard (±25%) thermocouples at the furthest downstream row ($S/B_x \sim 1$), however, indicated that the heat transfer at the 25% and 75% span locations was consistently higher than the measured midspan values.

The spanwise distributions obtained on the rotor pressure surface indicate that for all test cases the heat transfer was spanwise uniform. On the rotor suction surface, however, there were two indications of spanwise nonuniformity: (1) At the first spanwise row of thermocouples ($S/B_x \sim .3$) the Stanton number measured near the blade tip was consistently higher than the midspan value. (2) At the last spanwise row of thermocouples ($S/B_x \sim 1.26$) the region of midspan uniformity had shrunk to a width of only ±10% span with distinctly higher heat transfer at locations near the hub and tip.

The second stator transverse distributions indicated that the heat transfer was spanwise uniform over the central 40% of the span on both the suction and pressure surfaces. This result was surprising in light of the fact that the streamwise distributions of the heat transfer on the second stator were in marked disagreement with two dimensional predictions.

These spanwise distributions will require extensive examination and comparison with other data before conclusions can be reached as to their significance.

ANALYTICAL PROGRAM

1. Steady Boundary Layer Analysis

Background. - The boundary layers on the airfoils of typical aircraft gas turbines are transitional, subject to high levels of both random and periodic unsteadiness, affected by surface curvature, and are subject to very strong adverse as well as favorable pressure gradients. In addition, the very high free stream gas temperatures to which the airfoils are subjected demand that airfoil surface heat transfer coefficients be predicted with high accuracy. Failure in this regard would result in either an unacceptably short airfoil life or a significant performance penalty due to the inefficient use of airfoil cooling air. The purpose of the present section is to demonstrate the degree to which the heat transfer results presented in the previous sections can be predicted by one specific boundary layer analysis. The most important aspect of this comparison will be the degree to which the analysis can predict the transitional nature of the boundary layer and the way in which transition is affected by different levels of free stream turbulence. Keep in mind that transition can occupy a major portion of the airfoil surface and that in some cases it can dominate the entire boundary layer from just downstream of the stagnation point all the way to the trailing edge of the airfoil. In order to provide some perspective a very abbreviated survey of some of the many previous analytical/experimental comparisons for turbine airfoil heat transfer will be presented in the following paragraphs along with the major conclusions drawn in each study.

McDonald and Fish (ref. 38), in their analysis of boundary layer transition, carried out comparisons with heat transfer measurements obtained on a cascade of turbine airfoils having transitional boundary layers. This data, obtained by Turner (ref. 39), was for both the suction and pressure surfaces of the airfoil and it was acquired at two levels of free stream turbulence, 0.5% and 6.0%. Generally speaking the agreement between the measured and computed results was good, however, there were local areas where agreement was poor.

Daniels and Brown (ref. 34) compared the predictions of five different analytical models with heat transfer data acquired from a cascade of airfoils in a light piston tunnel. The data were acquired at two levels of free stream turbulence, 0.4% and 4.0%. They concluded - "Comparisons between the experimental data and the predictions showed with certain exceptions good agreement for the laminar leading edge region and for the fully turbulent region on the suction surface. The transition region on the suction surface was not well predicted. On the pressure surface the agreement between the predictions and the data was generally poor."

Consigny and Richards (ref. 33) also carried out measurements of heat transfer on a cascade of turbine rotor airfoils in a light piston tunnel. Their experimental variables included Mach number, Reynolds number, incidence and free stream turbulence (varying from 0.8% to 5.0%). Their boundary layer predictions were based on a two-equation closure model. They concluded - "The results were found to be encouraging although some fundamental discrepancies were observed. In particular, the calculation coped poorly with the variation of heat transfer in the transition region and in the prediction of the turbulent boundary layer downstream of separation bubbles."

Hylton et al. (ref. 2) presented comparisons of predictions based on a special version of STAN5 (ref. 40) with three data sets taken from the open literature as well as with additional data sets acquired from two turbine first stator airfoils in a steady state cascade operated at simulated engine conditions. They concluded - "In general, commonly available transition process models (origin, length, and path [intermittency]) were found to be inadequate for providing a consistent representation of experimental results."

Rae et al. (ref. 3) presented analytical/experimental comparisons based on heat transfer data obtained in the rotating rig testing of two complete turbine first stages (first stator and rotor) in a shock tunnel. Their analysis was based on a version of STAN5 as modified by Gaugler (ref. 41). In general their agreement ranged from "not too bad" to "poor." However, for some of the comparisons there were large and unexplained differences between the measured and computed results.

In considering the various analytical/experimental assessments discussed in the preceeding paragraphs a point that should be kept in mind is that in all probability some of the data is inaccurate and that some of the experiments probably include inadvertant three dimensional effects. Both of these possibilities would confuse the assessment of even the best of predictions. However, the picture that emerges from this overview is far from encouraging, especially with respect to the onset and length of transition. It can safely be anticipated that this will be a serious shortcoming in the comparisons with the present data where the effects of transition on the suction surface are also pronounced, e.g. figures 34 and 35. Other features of the present data that can be expected to present difficulties to most current boundary layer turbulence and transition models are the very high Stanton numbers on the airfoil pressure surfaces. Recall that this phenomena occurred when the free stream turbulence and the Reynolds number were both high, e.g. figures 36 and 37.

The boundary layer analysis chosen for the present assessment is the "ABLE" code of Carter, Edwards and Werle (refs. 30 and 31). This is an efficient and versatile calculation that includes models for laminar, transitional, and turbulent flow. The ABLE code contains a number of options for the transition and turbulence models that are employed. In the present

assessment two such models have been evaluated. The first was the algebraic turbulence model of Cebici and Smith (ref. 32). It is this model which was used to generate the fully turbulent predictions in figures 19 through 32, as indicated by the "T" in each figure. The other model that will be evaluated in the present section is that of McDonald et al. (refs. 38 and 42). This analysis includes physical models for both transitional and turbulent flow, both of which are functions of the free stream turbulence imposed. With this model the level of free stream turbulence controls both the onset and the length of transition. It should be pointed out, however, that the turbulent Prandtl number profile used in the present comparison was not that of McDonald and Kreskovsky (ref. 42) but rather a profile based on the measurements of Blair (ref. 43) was used in its place. The effect of this modified turbulent Prandtl number profile was to increase the predicted Stanton numbers slightly beginning in the transitional region and through the turbulent region. The increase was typically 6% in the turbulent region.

Results. - The analytical/experimental comparisons for this assessment are shown in figures 54, 55, and 56 for the first stage stator, rotor, and the second stage stator respectively. The comparisons are all for the 0.78 flow coefficient. Comparisons were also made at 0.68 and 0.96 but the conclusions drawn were no different than those at 0.78. The comparisons are all for the data acquired in the 65% axial gap configuration. Recall that changing the axial gap from 15% to 65% had little effect on the measured results (see fig. 33). All of the comparisons are for the high Reynolds number cases, i.e. Reynolds numbers in the range of 600,000. Finally, the comparisons are with the data acquired with both the grid in and with the grid out. With the grid out the stage inlet turbulence was 0.5% and with the grid in it was typically 10%. Each of the figures includes a laminar prediction up to laminar separation indicated by "L", a fully turbulent prediction (using the Cebici, Smith model, ref. 32) indicated by "T", and a family of transitional predictions (using the model of McDonald and Kreskovsky, ref. 42 and the turbulent Prandtl number profile of Blair, ref. 43) indicated by the level of the free stream turbulence used in each calculation. On the pressure surfaces the transitional predictions for free stream turbulences up to 10% were generally very close to the laminar predictions. On the suction surfaces increasing the free stream turbulence produced a monotonic upstream movement of transition.

On the pressure surfaces of the three airfoils reasonable agreement between the measured and the computed results was only obtained on the first stator with the grid out. With the grid in the measured data were far above even the fully turbulent prediction. Similarly the pressure surface data for the rotor and the second stator were far above the fully turbulent predictions for the grid both in and out. Recall that in the discussion of the data in an earlier section of this report it was observed that the high pressure surface Stanton numbers occurred when the inlet unsteadiness was high (due to either turbulence or the passing of an upstream airfoil row) and when the Reynolds number was high. At lower Reynolds numbers the Stanton numbers reduced to the fully turbulent level (figs. 35, 39, and 40).

On the suction surfaces of the three airfoils the agreement between the measured and computed results was generally unsatisfactory for both the cases with the grid in and with the grid out. The best agreement was obtained on the rotor for the case with the grid in. In this case after transition the data were in good agreement with the fully turbulent prediction. On the first stator the transition predictions were in poor agreement with the data in spite of the relatively benign inflow condition, i.e. without an upstream airfoil row. On the rotor the transition predictions were also poor. This may be related to the wakes of the upstream stator but recall that the rotor Stanton number distribution varied only slightly as the stator/rotor axial gap was changed from 15% to 65% with the grid both out and in (fig. 33b with the grid out and fig. 38b with the grid in). The analytical/experimental agreement for the second stator is poor but this is at least in part due to three dimensional effects present in the flow over this airfoil. This possibility had been raised earlier in the discussion of figure 44.

As with the results of the previous analytical/experimental comparisons discussed in the background section above, the present comparisons do not look encouraging. Doubtless any analytical model can be adjusted until it can predict some of the available data but none of the models appear to be able to predict all of the available data.

2. Unsteady Boundary Layer Analysis

Background. - In this section solutions to the unsteady, two-dimensional, compressible boundary-layer equations are presented. A derivation of these equations can be found in many references including the text by Schlichting (ref. 44). The governing equations consist of the continuity equation, the streamwise momentum equation, and the energy equation in total enthalpy form along with the equation of state, Sutherland's viscosity-temperature law, the definition of total enthalpy, and the Cebeci-Smith turbulence model (ref. 32). Werle and Verdon (ref. 45) introduced a turbulent, compressible generalization of the Levy-Lees transformation for the boundary-layer equations. Through this transformation the growth of the boundary layer in computational space is minimized and the density is eliminated as a dependent variable. In the present analysis, this turbulent Levy-Lees transformation is extended to unsteady flow, in particular, periodic unsteady flow. A difference approximation to the transformed partial differential equation set is obtained using first-order backward differences in the streamwise (x) direction and in time (t) and second order central differences in the normal direction. The resulting algebraic equations are quasi-linearized and marched implicitly first in time and then in the streamwise direction such that a block tridiagonal matrix equation is solved at each step in t and x. The no-slip boundary condition is applied at the surface along with either a prescribed temperature or heat transfer rate. At the initial time step, the time

dependent terms are set to zero so that a steady boundary-layer solution results. The unsteady solution is then determined over several periods to eliminate the error in assuming an initially steady flow. At the first upstream station, which is chosen to be close to the stagnation point, the transformed streamwise derivatives of the dependent variables are set to zero resulting in a self-similar, time-dependent solution.

To determine a solution to the boundary-layer equations the specifications of the edge velocity and enthalpy along with the derivatives of these quantities with respect to time and the surface coordinate are required. The available experimental data consists of the time-averaged (mean) pressure distribution and the Fourier coefficients of the fluctuating pressure. In order to determine the edge-condition information required for the boundary-layer calculation from the pressure measurements, a surface Euler solution was determined. Here, the Euler equations, i.e., the inviscid streamwise momentum and energy equations, are solved along the body surface to determine velocity and enthalpy distributions arising from a given pressure distribution using a finite difference method. This method is similar to that applied in the boundary-layer calculation, except that at each step only a 2x2 matrix, rather than a block tridiagonal matrix, must be inverted. The initial temporal solution is once again obtained by assuming steady flow and the upstream boundary condition is obtained from a solution of the surface Euler equations in the vicinity of the stagnation point.

The boundary-layer analysis described above was developed to predict the behavior of the unsteady viscous flow along rotor and stator surfaces, which is induced by the aerodynamic interaction between the adjacent rows. This type of analysis should provide insight into a phenomenon in which heat transfer rate is enhanced by unsteady effects (ref. 4). The perturbation analyses carried out by Telionis (ref. 46) indicate that the nonlinearities in the equations of motion produce a contribution to the mean or steady-state heat transfer rate which is caused by the unsteadiness. This contribution, termed acoustic streaming, is a higher order phenomenon so that it will be negligible if the unsteady fluctuations are small. However, such fluctuations can be quite large near the leading edge of a rotor so that the acoustic streaming phenomenon can be important in this region. Since streaming effects are a consequence of the time dependence of the flow and the nonlinearity of the governing equations, a time-dependent nonlinear viscous analysis, rather than a quasi-steady or linearized unsteady one is required to analyze them. This analysis was first applied to several simple flow cases, of which two are reported here, to test its accuracy. The first case involved the steady flow past a flat plate with variable heat transfer rate; the second, which has been studied previously by numerous authors, involved an oscillating free-stream flowing over a flat plate. In the second case both laminar and turbulent flows were considered. Once the accuracy of the present unsteady viscous analysis was verified, this analysis was applied to predict the boundary-layer

flows along the turbine rotor and stator investigated experimentally by Dring et al. (ref. 26) in the UTRC large-scale rotating rig. Note that in the following discussion dimensional quantities are denoted by the star superscript. Non-dimensional quantities are given by:

$$U = U^*/U^*_\infty$$

$$P = P^*/\rho^*_\infty U^{*2}_\infty$$

$$X = X^*/L^*_{ref}$$

$$t = t^* U^*_\infty/L^*_{ref}$$

$$\omega = \omega^* L^*_{ref}/U^*_\infty$$

corresponding to velocity, pressure, length, time, and frequency, respectively.

Test Cases. - flow past a symmetric flat plate airfoil: For the first case, the steady flow past a flat plate airfoil was analyzed to assess the ability of the present code to predict accurately the wall temperature when a wall heat transfer distribution is prescribed. This flow was studied experimentally by Blair, et al. (ref. 16) and numerically by Edwards, et al. (ref. 47). Figure 57 shows the input and results for this case. The specified wall heat transfer rate and the flow conditions external to the boundary layer are shown in figure 57a indicating an unheated length over a forward part of the plate. The flow is laminar and was calculated using a finite difference grid having 100 constant streamwise steps of .0078 m. and a 101 normal steps with a spacing of .025 in the transformed coordinate at the wall and a stretching factor k = 1.02 where k is the ratio of adjacent grid spacings. The computed results for the Stanton number are shown in figure 57b along with the experimental measurements of reference 16 and the theoretical results of reference 47. The agreement is quite good thus verifying that the present analysis gives accurate predictions of laminar heat transfer effects.

A second test case was analyzed to determine the ability of the code to accurately predict unsteady skin friction and heat transfer effects. Here the unsteady viscous flow over a flat plate airfoil is excited by an oscillating free-stream with velocity

$$U_e = U_o(1 + B \cos \omega t) \qquad (1)$$

where U_e is the velocity at the edge of the boundary layer, U_o is the time-average of this velocity and $U_o B$ and ω are the amplitude and frequency, respectively, of the unsteady velocity component. The laminar problem was first considered by Lighthill (ref. 48) who developed approximate analytical solutions for low and high reduced frequencies (i.e., $\omega x/U_o$ where x is the distance along the flat plate measured from the leading edge). For $U_o = 1$, Lighthill's solutions indicate that the oscillatory wall shear stress leads the prescribed edge velocity by a phase angle which increases nearly linearly with reduced frequency at low reduced frequencies and by a phase angle which asymptotically approaches 45 deg. at high reduced frequencies. Since Lighthill's original paper, these results have been verified numerically by many investigators including Cebeci (ref. 49), Telionis and Romaniuk (ref. 50), Ackerberg and Phillips (ref. 51), and McCroskey and Philippe (ref. 52).

For the specific case considered here, we set $B = 0.15$, $U_o^* = U_\infty^* = 17.1$ m/sec and $\omega^* = 234.55$ rad/sec. Calculations were performed over two temporal periods of the oscillation using forty (40) uniform time steps per period. The steady flow corresponding to $B = 0.0$ was used as an initial condition for this calculation, and it was found that transient unsteady response behavior disappeared after approximately 40 time steps or one period of the oscillation. The skin friction based on the mean edge velocity can be written in the form:

$$C_f = \frac{\tau_\omega^*}{\frac{1}{2}\rho_\infty^* U_\infty^{*2}} = \overline{C}_f + C_{f_1} \cos(\omega t + \phi_{c_f}) + \ldots \qquad (2)$$

where τ_ω^* is the surface shear stress and the dots refer to the terms of higher frequency. In Lighthill's analysis, the higher order terms are assumed to be negligible. Predictions for the amplitude $\overline{C}_f$ and phase angle ϕ_{c_f} of the skin friction fluctuations for the laminar case are shown in figure 58 along with Lighthill's approximate solutions for low and high reduced frequency. The present numerical results are in very good agreement with the asymptotic results at the extremes of the reduced frequency range considered. Furthermore, the present numerical results are in very close agreement with those obtained by Cebeci (ref. 49) for incompressible, unsteady boundary layers.

The turbulent version of the foregoing problem has been studied numerically by several investigators such as McCroskey and Philippe (ref. 52) and Cebeci (ref. 49) and experimentally by Karlsson (ref. 53). For the specific turbulent case considered in the present study, we set $U_o^* = U_\infty^* = 5.33$ m/sec, $B = 0.352$, and $\omega^* = 25.13$ rad/sec. Predictions for the amplitude

and phase angle of the fluctuating skin friction are shown in figure 59 along with results obtained earlier by McCroskey and Philippe (ref. 52) and Cebeci (ref. 54). The Cebeci-Smith turbulence model with an unsteady correction to the pressure gradient term (ref. 54) was used in each of the analyses. The agreement between the numerical solutions is qualitatively good over the range of the reduced frequencies considered. These results show that a much smaller phase shift occurs in the turbulent than in the laminar case. The experimental data of Karlsson (not shown) also indicates this trend; however, the numerical results do not match the experimental measurements. The lack of agreement between numerical prediction and experimental measurement is probably due, in part, to experimental uncertainties as well as to an inadequate turbulence model.

Lighthill (ref. 48) also studied the effect of unsteady edge velocity on laminar heat transfer characteristics. As in the case of the wall shear, the Stanton number can be expressed as a Fourier series, i.e.,

$$S_t = \frac{q_w^*}{\rho_\infty^* U_\infty^* C_p (T_w^* - T_\infty^*)} = \bar{S}_t + S_{t_1} \cos(\omega t + \phi_{St}) + \ldots \qquad (3)$$

where q_w^* is the heat flux at the wall, ρ_∞^* is the free-stream fluid density, U_∞^* is the free-stream velocity, C_p is the specific heat at constant pressure, T_w^* is the specified wall temperature, and T_∞^* is the temperature upstream of the body. Lighthill found that as the reduced frequency approaches zero the phase angle, ϕ_{St}, also approaches zero and that as the reduced frequency approaches infinity, the phase angle approaches -90 deg.

For the specific case considered in the present work, we set B = 0.10 and ω^* = 4.19 rad/sec. The mean edge velocity was specified to be a function of distance from the leading edge such that:

$$U_o = \frac{1 - bx}{1 - b} \qquad (4)$$

with b = .0025. This case was considered previously by Telionis (ref. 45) using a small perturbation, incompressible, boundary-layer analysis. Our present results for the behavior of St_1 vs. $\omega x/U_o$ agree qualitatively with those of Telionis as shown in figure 60a. Although the quantitative agreement between the results is quite good at low frequencies, the two theoretical predictions deviate from each other at the higher frequencies. Lighthill (ref. 55) provided the criterion

$$\frac{\omega x}{U_o} M << 1 \qquad (5)$$

where M is the free-stream Mach number for neglecting compressibility effects in the calculation of unsteady viscous flows. Thus, at high reduced frequency compressibility effects are important even at low Mach numbers, and the results determined with a compressible boundary-layer analysis can be expected to deviate from those determined with an incompressible analysis when the reduced frequency is sufficiently high. In accordance with Lighthill's predictions, the present results show a phase angle which is zero at a reduced frequency of zero and becomes close to the asymptotic value of -90 deg as the reduced frequency becomes large as shown in figure 60b. The discrepancy at high frequency occurs because Lighthill's analysis also applied only to incompressible flows. Note that the computed results for the amplitude and phase angle of the first Fourier term oscillate with reduced frequency, a phenomenon noted previously by Telionis and by Ackerberg and Phillips (ref. 51).

In the preceding sections, an unsteady, compressible boundary layer analysis was introduced in which the equations are written in similarity type variables to capture the growth of the boundary layer. This analysis was shown to compare quite well with previous steady and unsteady numerical results for skin friction and heat transfer rate distributions for laminar flow. Turbulent flow results indicate the same trends as those obtained by previous investigators; however, the results do not compare quantitatively. This lack of agreement points to the need for a turbulence model which is applicable to unsteady boundary-layer flows. In the following sections, this analysis is applied to rotor and stator flow fields and the results are compared to experimental data.

Results. - In this section, results for heat transfer rate distributions on turbine rotor and stator airfoil surfaces are presented. The calculations are based on experimental unsteady pressure distributions determined by Dring et al. (ref. 26). The experiment, as with the present experiment, was performed in the United Technologies Research Center (UTRC) Large Scale Rotating Rig No. I (fig. 3). The test configuration consisted of a row of 22 fixed stators followed by a row of 28 rotating rotors with axial gaps between adjacent rows of 15% and 65% of airfoil axial chord. The suction and pressure surfaces of the rotor and stator were instrumented to measure pressure and heat transfer characteristics. Some of the pressure taps were designed to measure the time-averaged or mean pressure while other high response pressure transducers were designed to measure the fluctuating pressure. The latter measurements were represented and tabulated as a series of Fourier coeffi-

cients. There was an insufficient number of transducers to determine fully the pressure gradient along the entire stator and rotor surfaces for use in the boundary-layer calculation. However, theoretical results which were determined using the steady potential flow analysis of reference 27 were found to compare quite well with the available mean pressure data over the entire surfaces of the rotor and stator. Therefore, the pressure distributions determined from the inviscid analysis were used to provide the mean surface pressure distributions required for the boundary-layer calculations. The experimental Fourier coefficients of the fluctuating pressures were spline fit to provide estimates of the unsteady pressure distributions over the entire airfoil surface. These estimates were then superimposed on the mean pressure distributions to provide the unsteady pressure distributions used in the unsteady viscous calculations.

Results for the suction and pressure surfaces of the stator and rotor are presented below for the 15% gap case. The following free-stream and reference conditions were specified for the stator blade:

$$M_\infty = 0.0704$$

$$P^*_\infty = 100{,}979 \text{ N/m}$$

$$T^*_\infty = 288.1 \text{ °K}$$

$$L^*_{ref} = .15066 \text{ m}$$

$$Re_\infty = 247{,}156$$

where M_∞ is the Mach number, P^*_∞ is the static pressure, and T^*_∞ is the static temperature upstream of the leading edge. Re_∞ is based on the upstream conditions and the axial chord, L^*_{ref}. In addition, the wall heat transfer was specified to be .00503 kW/m^2. The calculation grid was constructed with variable normal and streamwise grid spacings to resolve the large gradient regions of the flow. In the normal direction the first point off the wall in the transformed coordinate system, the stretching factor and the maximum number of points across the layer were 0.002, 1.2, and 41, respectively, where the stretching is defined as the ratio of adjacent step sizes. In the streamwise direction the first points from the stagnation point, non-dimensionalized by the reference length, were specified to be 0.0007 for the suction surface calculations and 0.0006311 for the pressure surface calculations. In addition, the stretching factor and the maximum number of grid points were specified to be 1.05 and 100, respectively, for both the suction and pressure surface calculations. These calculations were performed over 3 temporal

periods using 50 time-steps per period. The rotor passing frequency was 1202.6 rad/sec which corresponds to the rotor rotating at 410 rpm with 28 rotors passing each stator during one revolution.

The free-stream and reference conditions for the rotor were given as:

$$M_\infty = 0.1065$$

$$P^*_\infty = 100{,}500 \text{ N/m}$$

$$T^*_\infty = 288.2 \text{ °K}$$

$$L^*_{ref} = .16105 \text{ m}$$

$$Re_\infty = 397{,}667$$

where quantities are based on conditions upstream of the rotor. The heat transfer rate was specified to be .00503 kW/m^2. In this case the rotor is rotating at the same speed as before, 410 rpm, but there are only 22 stators so that the stator passing frequency is 943.7 rad/sec. The normal grid was constructed with the same parameters as those used for the stator calculations and the streamwise grid was constructed using the same stretching factor and number of grid points. The initial streamwise step-size for the suction and pressure surface calculations were 0.000666 and 0.0005178, respectively. As in the stator cases, the calculations were performed over 3 temporal periods using 50 time-steps per period. In the following discussion the pressure coefficient (C_p) is defined as the local pressure minus the pressure at the trailing edge divided by the dynamic pressure at the trailing edge. Bars over quantities indicate that they are time-averaged values.

Stator suction surface: Results for the stator suction surface, including mean and fluctuating surface pressure and Stanton number distributions are shown in figure 61. As mentioned above, the measured mean pressures compare quite well with the predicted inviscid pressure distributions so that the latter were used as the mean pressure input to the boundary-layer analysis and are shown in figure 61a along with the data. The unsteady pressure distribution can be expressed in the form:

$$C_p = \overline{C}_p + \sum_{n=1}^{\infty} P_n \cos(n\omega t + \phi_{p_n}) \qquad (6)$$

The amplitudes of the first three terms of this series, which were determined by spline fitting the measured Fourier coefficients, are shown in figure 61b. Note that unsteady effects on the stator are caused by potential flow variations associated with the downstream rotor. Since these attenuate rapidly with axial distance upstream of the rotor, unsteady effects on the stator blade are most pronounced near the trailing edge. In addition, the amplitudes of the second and third Fourier components of the fluctuating pressure are quite small over the entire suction surface.

In order to compare the predicted and measured heat transfer rates, it was first necessary to specify a transition region for the boundary-layer calculation which required a knowledge of the beginning and end of the transition region. Estimates of x = 0.85 and 1.05 for the beginning and end of the transition region were obtained from hot film measurements and the measured Stanton numbers. The results from the unsteady boundary-layer calculations are shown in figures 61c and 61d. Figure 61c contains a plot of the mean Stanton number and the corresponding unsteady envelope along with the measured mean data. The envelope was constructed by adding to and subtracting from the mean Stanton number the sum of all the amplitudes of the Fourier coefficients. As such, this envelope is an approximation to the envelope which would be constructed from the maximum and minimum Stanton number at each streamwise station. There are several observations which can be made at this point. First, the agreement between the calculated mean Stanton number and the measured data is quite good in the laminar region. This agreement is less satisfactory in the transition region, but the calculated results do approach the measured data near the trailing edge of the blade where the flow is fully turbulent. Discrepancies between the predictions and measurements are most likely due to the use of inadequate transition and turbulence models for unsteady flow with heat transfer and uncertainties about the actual location of the transition region. A second observation is that both the calculations and the data indicate that the maximum value of Stanton number occurs slightly downstream from the stagnation point. Also note that the magnitudes of the Fourier coefficients normalized by the mean Stanton number (fig. 61d) indicate that the unsteady effects are concentrated at the trailing edge of the stator blade. The results in figure 61d also indicate that the Fourier amplitudes decrease rapidly with n and hence a linearized unsteady viscous analysis might provide a useful description of the flow.

Previous experimental (ref. 4) and theoretical (ref. 45) investigations indicate that unsteady effects could increase the mean heat transfer rate along airfoil surfaces over the rate which occurs for the same airfoil operating in a steady flow. In order to test this hypothesis for the present case, a steady calculation was performed using the mean pressure distributions as input. It was found that the Stanton number distributions determined from this steady calculation differed only slightly from the mean Stanton number distributions determined from the unsteady calculation. This indicates that

the unsteady pressures do not cause a noticeable increase in the mean heat transfer rate along the stator suction surface and the experimental measurements bear this out in that the Stanton number was very insensitive to the rotor/stator axial gap (figs. 33 and 38).

Stator pressure surface: The results for the stator pressure surface are shown in figure 62. Again the measured mean pressures compare quite well with the results of the potential flow analysis so that the predicted pressure distribution shown in figure 62a was used as input into the unsteady boundary-layer analysis. The amplitudes of the first three Fourier terms which are the result of spline fitting the experimental values are shown in figure 62b. Here, the unsteady fluctuations are even more concentrated near the trailing edge than for the stator suction surface. As before the magnitude of the Fourier components decrease rapidly with increasing frequency. Based on comparison with data, the transition region on the stator-blade pressure surface was specified to extend from $x = 0.85$ to 2.5 indicating a large region of transitional flow.

The results of the calculations are shown on figures 62c and 62d. The calculated mean Stanton number versus the streamwise distance from the stagnation point is shown along with the measured data in figure 62c. The unsteady pressure fluctuations had an insignificant effect on the heat transfer rate distributions along the pressure surface; therefore no envelope is shown in figure 62c. The calculated results compare very well with the measured data over the entire pressure surface. This result implies that the transition and turbulence models used in the calculation lead to good predictions if the unsteady disturbances are very small. The Fourier coefficients of the Stanton number are shown in figure 62d. Note that the maximum value of the first coefficient is less than 0.5% of the mean value of pressure indicating that there is very little effect of the moving downstream rotor on the viscous layers on the pressure surfaces of the stator. As in the case of the stator suction surface, the Stanton number distribution calculated with the steady boundary layer analysis using the mean pressure distribution as input was identical to the mean Stanton number distribution calculated with the unsteady boundary layer analysis.

Rotor suction surface: The rotor encounters a much more complicated unsteady flow field than the stator. While the fluctuations affecting the stator consist mainly of potential flow disturbances from the passing rotor, the rotor is affected primarily by the viscous wakes coming off of the stator. Thus each rotor sees pockets of high free-stream turbulence as well as time-dependent total pressure fluctuations. However, a comparison of the measured mean pressures with the inviscid predictions indicates that the mean pressure distribution is not greatly affected by the incoming wakes (ref. 45). Therefore, the boundary-layer analysis was conducted in the same manner as in the case of the stator. The pressures input into this analysis consisted of the

spline-fit measured Fourier coefficients superimposed on the calculated inviscid pressures. The mean pressure distribution on the suction surface and the first three Fourier coefficients are shown in figures 63a and 63b. Note that the unsteady effects are most severe near the leading edge. In addition, the magnitudes of the fluctuations are generally much greater than those for the stator.

The results of the viscous calculations are shown on figures 63c and 63d. A determination of the location of the transition from the data was difficult. The experimental data indicated a large transition region; therefore, for calculation purposes, the locations of the beginning and end of transition were chosen to be x = 0.01 and 1.00, respectively. The calculated mean Stanton number and the unsteady envelope which indicates the approximate maximum and minimum Stanton number are shown on figure 63c along with the measured data. The mean Stanton number compares quite well with the data in the leading edge region where the flow is laminar and at the trailing edge where the flow is fully turbulent. However, the correlation between theory and experiment is not so good in the relatively long transition region. Besides the fact that the transition model used in the calculation does not account for unsteady effects, another explanation for the discrepancies between measured and predicted Stanton numbers is that the location of the beginning and end of the transition region may vary considerably with time whereas in the calculations these locations were assumed to be stationary. Another observation is that although the unsteady pressure fluctuations die out as the trailing edge is approached, the Stanton number fluctuations persist so that there is a finite unsteady envelope at the trailing edge. This can also be seen in figure 63c which contains a plot of the Fourier coefficients of the unsteady Stanton number. As for the stator suction surface the amplitudes of the second and third Fourier terms are quite small over the rotor blade suction surface (see fig. 63d).

Rotor - pressure surface: the mean pressure and the spline-fit Fourier coefficients for the rotor-blade pressure surface are shown on figures 64a and 64b, respectively. Again, unsteady effects are predominant over the forward portion of the blade and the amplitudes of the fluctuations decrease with increasing n. The data indicates that the flow is fully turbulent over most of the pressure surface so that an instantaneous transition at the leading edge was specified for the unsteady boundary-layer calculations.

The skin friction distribution calculated using the steady boundary-layer analysis and the mean pressure distribution of figure 64a is shown in figure 64c. The flow does not separate although the skin friction does dip down toward zero near the leading edge. If the unsteady envelope for the skin friction is such that the minimum skin friction is negative then an instantaneous flow reversal would occur although the mean skin friction would indicate that the flow was attached. This was the case for the unsteady

boundary-layer calculations along the rotor pressure surface. Figure 64d shows a plot of skin friction versus time at the streamwise station upstream of the point at which an unsteady flow reversal was first encountered. It can be seen that, although the mean skin friction is much greater than zero, the instantaneous value dips almost to zero. At the next station the value dipped below zero indicating flow separation and forcing termination of the unsteady portion of the calculations. This result implies that the actual flow may contain a small region of reversed flow during part of a cycle. The steady calculations show reasonably good agreement with measured heat transfer data as shown in figure 64e which is a plot of the calculated Stanton number based on the mean pressure distribution. Once again the uncertain location of the transition region may be responsible for some of the discrepancy between theory and experiment. In the region up to the point where flow reversal was encountered, the unsteady calculations indicated no difference in the mean Stanton number compared to the Stanton number calculated with the steady analysis.

General Comments. - The foregoing calculations were performed assuming that the effect of the wake impinging on the rotor blades was confined to pressure fluctuations, i.e. no increase in free-stream turbulence or change in total temperature were assumed at the edge of the boundary layer. And, in fact, a comparison with the measured data indicates that the neglect of these unknown variables does not significantly affect the agreement between the calculated results and the data, at least as far as the mean flow is concerned. Also the pressure fluctuations were found to have a more pronounced effect on skin friction than on heat transfer rate. This perhaps results from the fact that the influence of the pressure on the temperature profiles is an indirect one, while the pressure has a direct effect on the streamwise velocity in the low momentum region near the wall. Finally, it was found that the comparisons between the heat transfer rates calculated with the unsteady boundary-layer analysis and those calculated using the steady analysis showed very little differences in all cases, indicating that if there is enhanced heat transfer due to unsteady effects, these effects are outside of the unsteady pressure effects which were studied in the present investigation.

CONCLUSIONS

A combined experimental and analytical program has been conducted to examine the impact of a number of variables on the midspan heat transfer coefficients of the three airfoil rows in a one and one-half stage large scale turbine model. These variables included:

- stator 1/rotor axial spacing (15% and 65%)
- Reynolds number (flow speed)
- turbine inlet turbulence (0.5% and 10%)
- flow coefficient (airfoil incidence)
- relative stator 1/stator 2 circumferential position
- rotation (rotor vs. cascade)

Heat transfer data were acquired on the suction and pressure surfaces of the three airfoils. High density data were also acquired in the leading edge stagnation regions. In addition to the heat transfer data, extensive documentation of the steady and unsteady aerodynamics was also acquired. Finally, the heat transfer data were compared with both a steady and an unsteady boundary layer analysis. Specific conclusions in each of these areas were as follows.

Steady Aerodynamics

The following conclusions are based on the steady aerodynamic measurements which included circumferential distributions of hub and casing flowpath static pressures, distributions of airfoil midspan static pressures and circumferential distributions of total and static pressures and flow yaw and pitch angles obtained by traversing a five hole pneumatic probe downstream of each of the three rows of airfoils.

The major conclusions are as follows. It was observed that the airfoil midspan pressure distributions were in good agreement with two dimensional potential flow and that they were essentially unaffected by either the turbulence generating grid or the axial gaps between the airfoil rows. It was also observed that the turbulence generating grid had no significant impact on the circumferential distributions of flow speed downstream of each row of airfoils. The conclusion reached here was that the midspan aerodynamics in this experiment were well behaved and that the heat transfer results would be typical of those of a well-designed turbine. Specific conclusions are listed below.

1. The aerodynamic documentation of the turbine model, and in particular the airfoil midspan pressure distributions, indicated that the relevant aerodynamic parameters for this model were very close to data obtained previously.

2. The airfoil midspan pressure distributions predicted with a two dimensional potential flow calculation agree very closely with the measured pressure distributions.

3. For each of the three airfoils, the exit midspan static pressure obtained from a calculated free-vortex distribution between the measured hub and casing flowpath static pressures was in excellent agreement with the circumferentially averaged midspan pneumatic five hole probe traverse data.

4. The first stator midspan pressure distribution was invariant with rotor speed (flow coefficient) and inlet unsteadiness (grid-out vs. grid-in). The variation in the pressure distribution due to stator 1/rotor axial spacing was very small.

5. The rotor midspan pressure distribution was weakly dependent on axial spacing and inlet unsteadiness. However, over the forward portion of the airfoil ($0 \leq X/B_x \leq 0.4$) there was a strong dependence on the relative inlet flow angle.

6. The second stator midspan pressure distribution was invariant with unsteadiness. However, over the forward portion of the airfoil ($0 \leq X/B_x) \leq 0.4$) there was a strong dependence on the absolute inlet flow angle.

7. The addition of the turbulence grid did not significantly alter the circumferential distributions of the aerodynamic properties measured with the five hole probe traversed at midspan downstream of each of the three airfoil rows.

8. For all three airfoil rows the inlet and exit flow yaw angles deduced from a two dimensional potential flow calculation were in good agreement with the circumferentially averaged five hole probe traverse measurements. The exception occurred at the rotor exit where, due to three dimensional secondary flow effects, the flow yaw angle obtained from the traverse data was nearly six degrees greater than that deduced from the potential flow calculation.

Unsteady Aerodynamics

The following conclusions are based on the unsteady aerodynamic measurements made by traversing a single element hot film probe (oriented radially) at midspan in the absolute frame of reference downstream of each of the three airfoil rows.

The major conclusions are as follows. It was observed that the turbulence generating grid produced the desired level of turbine inlet turbulence (approximately 10%) and that the grid produced a large increase in total unsteadiness at the first stator exit. At the rotor exit and at the second stator exit, however, the change in unsteadiness level due to the grid was insignificant. The major conclusion reached here was that combustor-generated unsteadiness would strongly affect the flow over the first stator of a turbine but that downstream rows would be dominated by turbine-generated unsteadiness. Specific conclusions are listed below.

1. The addition of the turbulence grid resulted only in relatively small changes in the circumferential distributions of flow speed.

2. Where five hole and hot film probes were traversed in the same frame of reference, e.g., the stationary frame downstream of the two stator rows, the resulting circumferential distributions of flow speed measured with each type of probe were nearly identical.

3. Overall, the circumferentially averaged flow speeds measured with the hot film probe and with the five hole probe were in good agreement. They differed by no more than 1.5%.

4. The addition of the turbulence grid resulted primarily in a large increase in total unsteadiness at the first stator inlet and a relatively small increase in total unsteadiness at the first stator exit (rotor inlet). At both the rotor exit and second stator exit, the addition of the grid did not significantly increase the total unsteadiness in the flow.

5. The increase in total unsteadiness due to the addition of the turbulence grid was due to an increase in random unsteadiness, not periodic unsteadiness. In fact, the addition of the grid resulted in a decrease in the periodic unsteadiness measured in the absolute frame downstream of all three airfoil rows.

6. Measurements of the streamwise fluctuating component of the turbine inlet velocity were obtained just upstream of the first stator leading edge with a single-element hot-film anemometer. The turbulence intensity measured at midspan was 0.5% without the turbulence generating grid and 9.8% with the grid installed.

Heat Transfer

The following conclusions are based on the midspan heat transfer measurements carried out on the suction and pressure surfaces of the first stator, the rotor, and the second stator.

The major conclusions are as follows. It was observed that a combination of unsteadiness, high Reynolds number and concave curvature could produce pressure surface heat transfer distributions well in excess of fully turbulent levels. It was shown that large boundary layer separation bubbles produced by severe incidence angles could also cause large increases in heat transfer. Finally, it was demonstrated that while turbine inlet turbulence can have a very strong impact on the first stator heat transfer, its impact on downstream rows is minimal. The major conclusion reached here was that pressure surface heat transfer could be well in excess of design predictions due to both combustor- and turbine-generated unsteadiness and that this is an area where additional research is sorely needed. Specific conclusions are listed below.

1. The heat transfer distributions measured on the first stator, rotor and second stator for the design flow coefficient and with no turbulence grid indicate that there was a progressive and significant increase in the complexity of the flow as it proceeded through the turbine. At the first stator the measured heat transfer distribution was very well described by two-dimensional laminar and turbulent boundary layer predictions. These predictions worked reasonably well for the leading edge region and suction surface of the rotor but quite poorly for the rotor pressure surface and for both surfaces of the second stator. Secondary flows, unsteadiness and turbulence generated by each successive airfoil row appears to have made the flow less and less well described by a two-dimensional boundary layer analysis.

2. Changes to the stator-rotor axial spacing produced negligible effects on the heat transfer distributions on both the stator and the rotor. This same insensitivity to spacing resulted for both the grid-in and grid-out test conditions.

3. Heat transfer distributions were measured on the first stator with no turbulence grid and over a range of Reynolds numbers. On the suction surface these data indicate that there was an increasingly significant transitional region as the Reynolds number dropped. For all cases, however, the suction surface heat transfer data agreed reasonably well with two-dimensional, fully turbulent boundary layer predictions in the trailing edge region.

4. The impact of high inlet turbulence on the first stator heat transfer distribution was dramatic with significant increases of heat transfer on the leading edge and along both the suction and pressure surfaces. On the suction surface the increased turbulence moved the location of transition well upstream from $S/B_x \approx 1.0$ to $S/B_x \approx 0.3$. For this high level of turbulence, then, transition occurred in a region of accelerating flow instead of near the minimum pressure. The effect of the higher turbulence level was also very evident along the first stator pressure surface. For the low turbulence case the heat transfer was essentially laminar while with high turbulence the measured heat transfer was as much as 60% greater than the two-dimensional fully turbulent prediction.

5. On the rotor the effects produced by increasing the inlet turbulence were much less dramatic than for the first stator. On the rotor suction surface, transition appears to have moved upstream to $(S/B_x) \approx 0.2$ with the increased turbulence level. Changes downstream of transition in the fully turbulent region were negligible. The only region of the rotor pressure surface which showed any effects from the increased turbulence was close to the leading edge $(-0.5 < S/B_x < 0)$.

6. The impact of changing the turbine inlet turbulence level on the stator 2 heat transfer was negligible. This was expected since the baseline second stator flow field was so highly disturbed even in the absence of the turbulence grid.

7. The first stator and first rotor pressure surface heat transfer distributions for certain regimes of the test matrix indicate that there can be an interaction between the effects of concave surface curvature, Reynolds number and the level of free-stream disturbance that can produce heat transfer enhancement to levels far in excess of fully turbulent. One possibility is that for certain critical combinations of concave surface curvature, Re_θ, acceleration and free-stream disturbance level, important Goertler vortex systems are produced in the boundary layer.

8. Rotor heat transfer distributions obtained over a relatively small (near design) range of flow coefficients (incidence) indicate that: 1) the heat transfer rates near the trailing edge on both the pressure and suction surfaces were independent of flow coefficient, 2) the peak stagnation region $(S/B_x = 0)$ heat transfer dependent on the flow coefficient as a consequence of the changing relative inlet velocity and 3) there were local effects on both the pressure and suction sides near the stagnation region which were dependent on the flow coefficient (i.e., incident flow speed and angle).

9. Rotor heat transfer distributions obtained for extremely low values of flow coefficient (C_x/U) indicated that for $(C_x/U) < 0.5$ the flow was separated from the pressure surface. At these extreme negative incidence values the heat transfer was evidently dominated by a large, possibly unsteady, pressure surface separation bubble observed to start at $(C_x/U) = 0.50$ and to grow in chordal extend as (C_x/U) was reduced.

10. The effects associated with stator 1/stator 2 relative location appear to have been minor. The data for all five index locations were virtually identical, both with and without the turbulence grid installed. These results indicate that the strong circumferential gradients from the first stator have spread across most of the channel by the second stator leading edge to the extent that their impact on heat transfer is minimal.

11. Heat transfer distributions measured in the stagnation region of the first stator, rotor, and second stator were in excellent agreement with laminar theory for all test Reynolds numbers and flow coefficients. Enhancement of the leading edge heat transfer from turbulence effects was modest (about 20%).

12. The rotor heat transfer distributions obtained in the present program were compared with data obtained for the same airfoil section in a plane cascade. This comparison indicated that if the rotating and non-rotating tests had been conducted at the same Reynolds number and inlet turbulence levels the heat transfer distributions would have been nearly identical.

13. For the flow coefficient (0.78), hub/tip ratio (0.8), and relative exit flow angle (25°) of the present rotor the correlation of Lokay and Trushin (ref. 4) suggests that the effects of rotation would increase the averaged rotor heat transfer by 25% relative to an equivalent nonrotating case. The preceding conclusion (#12) suggests that this increase is due to the turbulence environment in a turbine and not to anything fundamentally related to rotation, such as centrifugal or Coriolis effects.

Steady Boundary Layer Analysis

The boundary layer transition and turbulence models examined in this assessment (refs. 32, 38, 42 and 43) did not provide accurate predictions of either the transitional nature of the suction surface boundary layers or the very high heat transfer observed on the pressure surfaces (figs. 54 and 55). Although only one transition and turbulence model was assessed here the major conclusion is consistent with many previous assessments of other models. This conclusion is that these models are not yet capable of consistently predicting many of the important features of the heat transfer on turbine airfoils and that actual engine designs will probably, have to rely, at least in part, on a correlative approach.

Unsteady Boundary Layer Analysis

An unsteady, compressible boundary layer analysis was developed to study the effects of rotor/stator interaction on the heat transfer rate at the blade surfaces. The analysis was applied to several steady and unsteady test cases. For laminar flow the theoretical results were shown to compare quite well with available experimental data and previous analytical solutions for skin friction and heat transfer rate. The turbulent results showed good qualitative agreement with those of previous investigators; however, due to the lack of an appropriate turbulence model for unsteady flow, the various turbulent flow predictions do not agree quantitatively.

The unsteady, compressible boundary layer analysis was also applied to the present rotor/stator configuration using the measured pressure distributions as input to the boundary layer calculations. The major conclusion drawn for these calculations was that the time averaged effect of unsteadiness on heat transfer was small since the time average of the unsteady heat transfer predictions differed only slightly from the heat transfer calculated for a steady prediction. Specific conclusions are listed below.

1. The agreement between the calculated and measured mean Stanton numbers was quite good in laminar regions. The agreement was less satisfactory in the transition regions; however the calculated results approach the measured data near the trailing edge of the blades where the flow was fully turbulent. The discrepancies between the predictions and the measurements are most likely due to inadequate transition and turbulence models and uncertanties about transition locations.

2. Both the calculations and the data indicated that the maximum value of Stanton number occurs slightly downstream of the stagnation point on the suction surface. In addition, they both indicated that the Fourier amplitudes of Stanton number decrease rapidly with increasing frequency and hence a linearized unsteady viscous analysis might provide a useful description of the flow.

3. It was found that the Stanton number distributions determined from a steady boundary layer calculation differed only slightly from the mean Stanton number distributions determined from the unsteady boundary layer calculation. This result indicates that the unsteady pressure fluctuations studied in the present investigation do not significantly enhance the mean heat transfer at a blade surface.

RECOMMENDATIONS

As a result of the information that has been generated in this program many questions have been answered, but as is often the case, many more have been generated. The following list of recommended future research activities reflects these questions.

(1) The very high levels of pressure surface heat transfer that occur when the unsteadiness level and the Reynolds number are high need to be understood and modeled analytically.

(2) Considerable additional effort needs to be focused on improved predictions of boundary layer transition.

(3) With the present exhaustive treatment of midspan heat transfer completed the next logical step would be to carry out similar full span measurements which would include the hub and tip endwalls. It is likely that the unsteady effects of rotor/stator interaction on airfoil aerodynamics and heat transfer will be stronger near the endwalls due to the more enduring nature of the airfoil secondary flows and wakes in these regions.

(4) To the extent that turbine designers may observe heat transfer on turbine airfoils in actual engines that cannot be reconciled with the present data, attention should be focused on the effects of the temporal and spatial nonuniformities of the flow produced in the combustor and the impact that these nonuniformities might have on turbine heat transfer.

REFERENCES

1. Han, L. S., Chait, A., Boyee, W. F. and Rapp, J. R.: Heat Transfer on Three Turbine Airfoils, AFWAL-TR-82-2124, Aero Propulsion Laboratory, Air Force Wright Aeronautical Laboratories, Air Force Systems Command, Wright-Patterson Air Force Base, Ohio 45433, January 1, 1982.

2. Hylton, L. D., Mihelc, M. B., Turner, E. R., Nealy, D. A. and York, R. E.: Analytical and Experimental Evaluation of the Heat Transfer Distribution Over the Surfaces of Turbine Vanes, NASA CR 168015, Final Report for Contract No. NAS3-22761, May 1983.

3. Rae, W. J., Taulbee, D. B., Civinskas, K. C. and Dunn, M. G.: Turbine-Stage Heat Transfer: Comparison of Shock-Duration Measurements With State-of-the-Art Prediction, AIAA Paper No. AIAA-86-1465, submitted to the AIAA Journal of Propulsion and Power.

4. Lokay, V. I., and Trushin, V. A.: Heat Transfer from the Gas and Flow-Passage Elements of a Rotating Gas Turbine. Heat Transfer - Soviet Research, Vol. 2, No. 4, July, 1970.

5. Graziani, R. A., Blair, M. F., Taylor, J. R. and Mayle, R. E.: An Experimental Study of Endwall and Airfoil Surface Heat Transfer in a Large Scale Turbine Blade Cascade, ASME Journal of Eng. for Power, Vol. 102, April 1980, pp. 257-267.

6. Dring, R. P., Joslyn, H. D. and Hardin, L. W.: Experimental Investigation of Compressor Rotor Wakes, AFAPL-TR-79-2107, Air Force Aero Propulsion Laboratory, Technology Branch, Turbine Engine Division (TBX), Wright-Patterson AFB, OH.

7. Joslyn, H. D., Dring, R. P. and Sharma, O. P.: Unsteady Three-Dimensional Turbine Aerodynamics, Trans. ASME, Journal of Engineering for Power, Vol. 105, April 1983, pp. 322-331.

8. Dring, R. P., and Joslyn, H. D.: Measurements of Turbine Rotor Blade Flows, Trans. ASME, Journal of Engineering for Power, Vol. 103, No. 2, April 1981, pp. 400-405.

9. Zimmerman, D. R.: Laser Anemometry Measurements at the Exit of a T630-C20 Combustor, NASA CR-159623, DDC RN 79-4, April, 1979.

10. Batchelor, G. K. and Townsend, A. A.: Decay of Isotropic Turbulence in the Initial Period, Proc. Royal Society of London, Vol. 193A, pp. 539-558.

11. Sato, H.: Experimental Study of the Spectrum of Isotropic Turbulence, I and II, Journal of the Physical Society of Japan, Vol. 6, 1951, pp. 387-392, Vol. 7, 1952, pp. 392-396.

12. Hinze, J. O.: Turbulence, McGraw-Hill, New York, 1975, pp. 259-278.

13. Baines, W. D. and Peterson, E. G.: An Investigation of Flow Through Screens, Trans. ASME, Vol. 73, 1951, pp. 467-480.

14. Compte-Bellot, G. and Corrsin, S.: The Use of a Contraction to Improve Isotropy of Grid Generated Turbulence, JFM, Voo. 25, 1966, pp. 657-682.

15. Hancock, P. E.: Effect of Free-Stream Turbulence on Turbulent Boundary Layers, Ph.D. Thesis, Imperial College, University of London, 1980.

16. Blair, M. F., Bailey, D. A. and Schlinker, R. H.: Development of a Large-Scale Wind Tunnel for the Simulation of Turbomachinery Airfoil Boundary Layers, ASME J. of Eng. for Power, Vol. 103, 1981, pp. 678-687.

17. Huffman, G. D., Zimmerman, D. R. and Bennett, W. A.: The Effect of Free-Stream Turbulence Level on Turbulent Boundary Layer Behavior, AGARD AG164, pp. 91-115.

18. Gad-el-Hak, M. and Corrsin, S.: Measurements of the Nearly Isotropic Turbulence Behind a Uniform Jet Grid, JFM, Vol. 62, 1974, pp. 115-143.

19. Tassa, Y. and Kamotani, Y.: Experiments in Turbulence Behind a Grid with Jet Injection in Downstream and Upstream Direction, The Physics of Fluids, Vol. 18, No. 4, 1974, pp. 411-414.

20. Loehrke, R. I. and Nagib, J. M.: Experiments in Management of Free-Stream Turbulence, AGARD Report No. 598, AD-749891, 1972.

21. Reynolds, W. C., Kays, W. M. and Kline, S. J.: Heat Transfer in the Turbulent Incompressible Boundary Layer, III Arbitrary Wall Temperature and Heat Flux, NASA Memo 12-3-58W, 1958.

22. Ota, T. and Kon, N.: Heat Transfer in the Separated and Reattached Flow in a Blunt Flat Plate, ASME Journal of Heat Transfer, November 1974, pp. 459-462.

23. Subramanian, C. S. and Antonia, R. A.: Effect of Reynolds Number on a Slightly Heated Turbulent Boundary Layer, Int. J. of Heat and Mass Transfer, Vol. 24, No. 11, 1981, pp. 1833-1846.

24. Blair, M. F.: Influence of Free-Stream Turbulence on Turbulent Boundary Layer Heat Transfer and Mean Profile Development, ASME Journal of Heat Transfer, Vol. 105, February 1983, pp. 33-47.

25. Blair, M. F.: Heat Transfer in the Vicinity of a Large-Scale Obstruction in a Turbulent Boundary Layer, to be presented at AIAA Thermophysics Conference, Snowmass, CO, June 1984.

26. Dring, R. P., Joslyn, H. D., Hardin, L. W. and Wagner, J. H.: Turbine Rotor-Stator Interaction. ASME J. Eng. for Power, Vol. 104, pp. 729-742, October, 1982.

27. Caspar, J. R., Hobbs, D. E. and Davis, R. L.: Calculation of Two-Dimensional Potential Cascade Flow Using Finite Area Methods, AIAA Journal, Vol. 18, January 1980, p. 103-109.

28. Joslyn, H. D. and Dring, R. P.: An Experimental and Analytical Study of Turbine Temperature Profile Attenuation, AFOSR Contract No. F49620-86-C-0020, completion date: August 1988.

29. Sharma, O. P., Butler, T. L., Joslyn, H. D. and Dring, R. P.: Three-Dimensional Unsteady Flow in an Axial Flow Turbine, AIAA Journal of Propulsion and Power, Vol. 1, No. 1, January-February 1985, pp. 29-38. (Presented in expanded form as AIAA Paper No. AIAA-83-1170).

30. Carter, J. E., Edwards, D. E. and Werle, M. J.: Coordinate Transformation for Laminar and Turbulent Boundary Layers, AIAA Journal, Vol. 20, No. 2, February 1982, pp. 282-284.

31. Edwards, E. E., Carter, J. E. and Werle, M. J.: Analysis of the Boundary Layer Equations Including a Coordinate Transformation--The ABLE Code, UTRC81-30, 1981.

32. Cebeci, T. and Smith, A. M. O.: Analysis of Turbulent Boundary Layers, Academic Press, 1974.

33. Consigny, H. and Richards, B. E.: Shock Duration Measurements of Heat Transfer Rate to a Gas Turbine Rotor Blade, 81-GT-146, Trans. ASME, Jour. Engineering for Power, Vol. 104, No. 3, July 1982, pp. 542-551.

34. Daniels, L. D. and Browne, W. B.: Calculation of Heat Transfer Rates to Gas Turbine Blades, International Journal of Heat and Mass Transfer, Vol. 24, No. 1, 1981, pp. 871-879.

35. Joslyn, H. D. and Dring, R. P.: Negative Incidence Flow Over a Turbine Rotor Blade, ASME Paper No. 83-GT-23, presented at the 1983 Gas Turbine Conference in Phoenix, AZ. (Based on USAF Report No. AFWAL-TR-81-2114).

36. Lowery, G. W. and Vachon, R. I.: The Effect of Turbulence on the Heat Transfer from Heated Cylinders, Int. J. Heat Mass Transfer, Vol. 18, 1975, pp. 1229-1242.

37. Sharma, O. P. and Graziani, R. A.: Influence of Endwall Flow on Airfoil Suction Surface Mid-Height Boundary Layer Development in a Turbine Cascade, ASME Paper No. 82-GT-127, ASME Gas Turbine Conference, 1982.

38. McDonald, H. and Fish, R. W.: Practical Calculation of Transitional Boundary Layer. International Journal of Heat and Mass Transfer, Vol. 16, No. 9, 1973, pp. 1729-1744.

39. Turner, A. B.: Local Heat Transfer Measurements on a Gas Turbine Blade, Jour. Mech. Eng. Sci., Vol. 13, No. 1, 1971.

40. Crawford, M. E. and Kays, W. M.: STAN5 - A Program for Numerical Computation of Two-Dimensional Internal and External Boundary Layer Flows, NASA CR-2742, 1976.

41. Gaugler, R. E.: Some Modifications to, and Operating Experiences with, the Two-Dimensional Finite Difference, Boundary Layer Code STAN5, ASME Paper No. 81-GT-89, March 1981.

42. McDonald, H. and Kreskovsky: Effect of Free-Stream Turbulence on the Turbulent Boundary Layer, Int. J. of Heat and Mass Transfer, Vol. 17, 1974.

43. Blair, M. F. and Edwards, D. E.: The Effects of Free-Stream Turbulence on the Turbulence Structure and Heat Transfer in Zero Pressure Gradient Boundary Layers, final report for AFOSR Contract No. F49620-81-C-0053, AFOSR TR-83-0149, Gov't Acc. No. ADA 126465, November 1982.

44. Schlichting, H.: Boundary-Layer Theory. 6th Ed., McGraw-Hill Co., Inc., New York, 1978.

45. Werle, M. J. and J. M. Verdon: Viscid/Inviscid Interaction Analysis for Symmetric Trailing Edges. UTRC report R79-914493-5, January 1980.

46. Telionis, D. P.: Unsteady Viscous Flows. Springer Series in Computational Physics, Springer-Verlag, New York, 1981.

47. Edwards, D. E., J. E. Carter, and M. J. Werle: Analysis of the Boundary Layer Equations Including a New Composite Coordinate Transformation - The ABLE Code. UTRC report 81-30, May 1982.

48. Lighthill, M. J.: The Response of Laminar Skin Friction and Heat Transfer to Fluctuations in the Stream Velocity. Proc. Roy. Soc., 224A, PP. 1-23, 1954.

49. Cebeci, T.: Calculation of Laminar and Turbulent Boundary Layers for Two-Dimensional Time-Dependent Flows. NASA CR-2820, July 1977.

50. Telionis, D. P. and M. S. Romaniuk: On the Response of Skin Friction and Heat Transfer to Fluctuating Boundary Layers. AIAA paper No. 77-235, 1977.

51. Ackerberg, R. C. and J. H. Phillips: The Unsteady Laminar Boundary Layer on a Semi-Infinite Flat Plate Due to Small Fluctuations in the Magnitude of the Free-Stream Velocity. J. Fluid Mech., Vol. 51, p. 137-157, 1972.

52. McCroskey, W. J. and J. J. Philippe: Unsteady Viscous Flow on Oscillating Airfoils. AIAA J., Vol. 13, p. 71-79, 1975.

53. Karlsson, S. K. F.: An Unsteady Turbulent Boundary. J. Fluid Mech., Vol. 5, p. 622-636,1959.

54. Cebeci, T. and H. B. Keller: On the Computation of Unsteady Turbulent Boundary Layers, in Recent Research on Unsteady Boundary Layers, E. A. Eichelbrenner (Ed.), II, Academic Press, New York, 1970.

55. Lighthill, M. J.: In Laminar Boundary Layers, ed. Rosenhead, L., Oxford Press, London and New York.

APPENDIX

A HISTORY OF RELATED TURBINE RESEARCH ACTIVITIES IN THE UTRC/LSRR

In an effort to provide additional background for the aerodynamics and heat transfer results of the present program summaries are presented in the following paragraphs of the various published research activities that have been conducted on the turbine model in the UTRC/LSRR. These activities include studies of film cooling, rotating frame measurement techniques, three dimensional aerodynamics, and unsteady aerodynamics both on airfoil surfaces as well as throughout the flow field. These activities are presented here in a more or less chronological order.

Dring, R. P., Blair, M. F. and Joslyn, H. D.: An Experimental Investigation of Film Cooling on a Turbine Rotor Blade, Trans. ASME, Journal of Engineering for Power, Vol. 102, No. 1, January 1980, pp. 81-87. (Based on USAF Report No. AFAPL-TR-78-63)

Film cooling has been studied on the rotor blade of a large scale (low speed) model of a high pressure turbine first stage. Film coolant was discharged from single holes on the pressure and suction surfaces of the airfoil. For each blowing site the coolant to free stream mass flux ratio and density ratio were varied from 0.5 to 1.5 and from 1.0 to 4.0 respectively. Both surface flow visualization and local film cooling adiabatic effectiveness data were obtained. The observation was made that although it can have a strong radial component, the trajectory of the film coolant was very insensitive to coolant flow conditions. The existence of the radial component of the film coolant trajectory was found to have a strong impact on the nature of the effectiveness distribution. The data have been compared with data taken by other investigators on flat surfaces and in plane cascades. Agreement between the flat plate data and the suction surface data was reasonably good. However, the pressure surface results showed a much faster decay of the effectiveness than did the flat plate data due to effects thought to be related to both curvature and radial flow.

Dring, R. P., and Joslyn, H. D.: Measurements of Turbine Rotor Blade Flows, Trans ASME, Journal of Engineering for Power, Vol. 103, No. 2, April 1981, pp. 400-405.

Measurement methods for obtaining various types of experimental data on a turbine rotor blade are discussed in this paper. A variety of different types of measurements have been taken in the rotating frame of reference, including:

airfoil surface static pressure distributions, the radial distribution of total pressure in the incident flow, flow visualization of surface streamlines, and radial-circumferential traversing of a pneumatic probe aft of the rotor. Typical results are presented showing interesting flow phenomena present on the rotor. In particular, results are shown which demonstrate the various viscous and inviscid mechanisms that give rise to strong radial flows.

Dring, R. P., Joslyn, H. D., Hardin, L. W. and Wagner, J. H.: Turbine Rotor-Stator Interaction, Trans. ASME, Journal of Engineering for Power, Vol. 104, No. 4, October 1982, pp. 729-742. (Based on USAF Report No. AFWAL-TR-81-2114)

The aerodynamic interaction between the rotor and stator airfoils of a large scale axial turbine stage have been studied experimentally. The data included measurements of the time averaged and instantaneous surface pressures and surface thin film gage output on both the rotor and stator at midspan. The data was acquired with rotor-stator axial gaps of 15 and 65 percent of axial chord. The upstream potential flow influence of the rotor on the stator was seen as well as the downstream potential flow and wake influences of the stator on the rotor. The time averaged rotor and stator pressure distributions were in excellent agreement with potential flow and were also very insensitive to rotor-stator axial gap. Unsteady pressure on the stator and rotor were as high as ±15% and ±80% respectively of the local time averaged dynamic pressure. The stator unsteadiness was primarily due to the rotor potential field but the rotor unsteadiness was heavily influenced by the stator wake. Although a natural boundary layer transition process was occurring on the stator the rotor was typically undergoing periodic variation between laminar and turbulent behavior.

Dring, R. P. and Joslyn, H. D.: The Relative Eddy in Axial Turbine Rotor Passages, ASME Paper No. 83-GT-22, presented at the 1983 Gas Turbine Conference in Phoenix, AZ. (Based on USAF Report No. AFWAL-TR-81-2114)

It has been observed that strong radially outward flow can be present on the pressure surface of an axial turbine rotor blade. This paper demonstrated that the relative eddy plays a major role in producing this radial flow. An analysis of the relative eddy indicated that it can explain observed trends both with blade incidence as well as with spanwise location on the blade. Suggestions are offered as to how the turbine designer might exercise some control over this aerodynamic mechanism.

Joslyn, H. D. and Dring, R. P.: Negative Incidence Flow Over a Turbine Rotor Blade, ASME Paper No. 83-GT-23, presented at the 1983 Gas Turbine Conference in Phoenix, AZ. (Based on USAF Report No. AFWAL-TR-81-2114)

The operation of variable cycle gas turbines at negative incidence can result in highly three dimensional separated flows on the turbine rotor pressure surface. These flows can impact both performance and durability. This program was conducted to experimentally study the behavior of surface flow on a large scale axial flow turbine rotor with incidence varying up to and including negative incidence separation. Fullspan pressure distributions and surface flow visualization were acquired over a range of incidence. The data indicate that at large negative incidence, pressure surface separation occurred and extended to 60 percent chord at midspan. These separated flows were simulated at midspan by applying potential flow theory to match the measured pressure distributions.

Joslyn, H. D., Dring, R. P. and Sharma, O. P.: Unsteady Three-Dimensional Turbine Aerodynamics, Trans. ASME, Journal of Engineering for Power, Vol. 105, April 1983, pp. 322-331.

High response aerodynamic measurements were made in a large scale, axial, flow turbine model to study the unsteadiness and three dimensionality of the flow. High response velocity vector and total pressure data were acquired. A comparison was made of the results of phase lock averaging both raw and reduced data (voltages and velocities). The velocity vector measurements showed that there were strong radial flows present as well as significant periodic changes in the flow field due to relative rotor and stator positions. Random, periodic, and total unsteadiness levels were computed from the instantaneous and phase lock averaged velocity data. Time averaged data were compared with an inviscid two-dimensional calculation. A comparison was also made of time averaged total pressure measurements obtained from high response and low response (steady-state) probes.

Sharma, O. P., Butler, T. L., Joslyn, H. D. and Dring, R. P.: Three-Dimensional Unsteady Flow in an Axial Flow Turbine, AIAA Journal of Propulsion and Power, Vol. 1, No. 1, January-February 1985, pp. 29-38. (Presented in expanded form as AIAA Paper No. AIAA-83-1170)

The results of an experimental program directed at understanding the unsteady mean and turbulent flow in a large-scale 1-1/2 stage research turbine are presented. High response instrumentation and the phase-locked averaging data reduction techniques were utilized to acquire data having high spatial and temporal resolution. These data included the unsteady three-dimensional distribution of mean and turbulent velocities and total and static pressures.

The data between the guide vane and the rotor and downstream of the rotor are presented. The flow downstream of the vane was found to be essentially steady and was dominated by large Reynolds stresses in the wakes and secondary flow regions. In contrast, the flow downstream of the rotor was highly unsteady. Two different rotor exit flow regimes were identified, corresponding to maximum and minimum interaction of the rotor leading edges with the upstream vane wakes. During the maximum interaction, the vane wakes merged with the rotor wakes, the midchannel flow was fairly uniform, and two strong secondary flow vortices were present. During minimum interaction, the vane wakes entered the rotor passages between the airfoils, the midchannel flow was nonuniform, and the secondary flow vortices were less well defined.

Joslyn, H. D., Caspar, J. R., and Dring, R. P.: Inviscid Modeling of Turbomachinery Wake Transport, AIAA Journal of Propulsion and Power, Vol. 2, No. 2, March-April 1986, pp. 175-180.

The problem of unsteady wake-airfoil interaction and wake transport is of importance in nearly all fluid mechanical devices that involve rotating machinery. In this study, an inviscid airfoil-to-airfoil potential flow analysis is used to predict the transport of the wakes of upstream stators through both rotating compressor and turbine airfoil passages. The dependence of wake rotation on airfoil lift and the dependence of wake distortion on airfoil geometry are both shown. Flow visualization results obtained in both a large scale compressor and a large scale turbine rig show good comparison with the predictions of the inviscid model.

Joslyn, H. D. and Dring, R. P.: Surface Indicator and Smoke Flow Visualization in Rotating Machinery, presented at the First International Symposium on Transport Phenomena, Honolulu, HI, 1985, Heat Transfer and Fluid Flow in Rotating Machinery ed. Wen-Jei Yang, Hemisphere Publishing Co., pp. 156-169.

Historically, the observation of fluid motion has unveiled complex flow phenomena, verified concepts and aided in the development of analytical models. Flow visualization was the first and, in many instances, the only experimental technique available to study complex fluid dynamics problems. Currently, there is little information in the open literature to demonstrate the value and application of flow visualization in rotating turbomachinery research. Since 1977 the United Technologies Research Center Large Scale Rotating Rig (LSRR-1) has been committed to studying in detail the complex, three dimensional flow fields of rotating axial flow compressors and turbines. As is shown in this paper, the capability to conduct flow visualization studies on the rotating airfoil and endwall surfaces and in the rotating airfoil passages is a valuable aide in not only identifying the aerodynamic

mechanisms present, but also in understanding their impact on the various parameters used by engineers to characterize turbomachinery flow fields. Specific applications of the surface indicator technique include studies of turbine film cooling, three dimensional flows on turbine airfoils, analytical modeling of turbine pressure surface flows and compressor suction surface flows, and compressor hub corner stall/blockage effects. Smoke flow visualization results from a preliminary study of wake-airfoil interaction are also presented.

Butler, T. L., Sharma, O. P., Joslyn, H. D. and Dring, R. P.: Redistribution of an Inlet Temperature Distortion in an Axial Flow Turbine Stage, AIAA Paper No. AIAA-86-1468, presented at the Twenty-Second Joint Propulsion Conference, Huntsville, AL, June 1986.

Results of an experimental program aimed at determining the extent of the redistribution of an inlet temperature distortion in an axial flow turbine stage are presented. The experiments were performed in a large scale, low speed turbine where fluid seeded with CO_2, was introduced upstream of the guide vane and its progress through the turbine was tracked by sensing CO_2 concentration at various locations inside the stage. Data were obtained both with and without the inlet temperature distortion. CO_2 concentration contours obtained downstream of the vane showed very little change with heating, indicating that the vane flow field remains relatively unaffected by the introduction of the temperature distortion. Inside the rotor passage however, fairly dramatic changes in the CO_2 contours on the airfoil surfaces were observed for the temperature distortion case. A segregation of hot and cold fluid was observed with the higher CO_2 concentration, higher temperature fluid migrating to the rotor pressure side and the lower CO_2 concentration, lower temperature fluid migrating to the rotor suction side. Significant increases in spanwise flow migration were also observed. Two separate physical mechanisms are postulated which tend to enhance one another to explain the observed experimental trends. Calculations were performed using a three dimensional Euler solver for the vane and rotor for both test cases. Results show that the calculation is able to qualitatively simulate the experimental results.

Joslyn, H. D., Butler, T. J. and Dring, R. P.: Trace Gas Measurements of Spanwise Mixing in a Turbine Stage, submitted for presentation at the 1987 ASME Gas Turbine Conference in Anaheim, CA.

The problem of predicting turbine temperature profile attenuation, i.e., the radial redistribution of the combustor exit gas temperature profile by spanwise mixing through the turbine has been and continues to be of major concern in the industry. Without this predictive capability, optimal cooling, increased performance and increased durability cannot be achieved except by

long and costly development test programs. An experimental technique using a trace gas to simulate an axisymmetric turbine inlet temperature profile in a single stage turbine is demonstrated. Spanwise mixing (attenuation) of the simulated inlet profile by three-dimensional aerodynamic mechanisms is determined from trace gas concentration measurements made in a single stage turbine model. Trace gas concentration contours are consistent with pitch angle measurements downstream of the stator and with flow visualization on the rotor airfoil surfaces and hub endwall.

Joslyn, H. D. and Dring, R. P.: An Experimental and Analytical Study of Turbine Temperature Profile Attenuation, AFOSR Contract No. F49620-86-C-0020, completion date: August 1988.

An experimental and analytical program is being carried out to gain an understanding of the underlying three dimensional aerodynamic mechanisms that influence turbine inlet temperature profile attenuation. In particular, the experimental effort is designed to first, define by detailed measurements the aerodynamic mechanisms that drive the attenuation, and second, to determine the degree to which the various mechanisms distort (attenuate) a simulated turbine inlet temperature profile as it proceeds through a one and one-half stage turbine model. The analytical portion of the program has been formulated to narrow the gap that exists between current analytical capabilities which are limited to stationary turbine passage flows and the requirements of the design engineer for an accurate method to predict the heat transfer on a rotating turbine blade with strong three dimensional secondary flows and Coriolis forces. The results will (1) provide guidance for the further development of accurate three dimensional codes to predict turbine gas path temperature distributions that result from the redistribution (attenuation) of the turbine inlet temperature profile, and (2) provide a rationale to the turbine designer for the optimization of turbine hot section cooling schemes.

TABLE 1a
AIRFOIL GEOMETRY

AIRFOIL: FIRST STATOR (HUB)
PITCH (ins.): 6.88865

	LEADING EDGE	TRAILING EDGE
RADIUS (ins.)	0.44485	0.10988
METAL ANGLE (degr.)	90.00395	22.44246
WEDGE ANGLE (degr.)	31.79000	6.85000

	X(ins.)	Y_L(ins.)	Y_U(ins.)
1	0.00000	5.98844	5.98844
2	0.05932	5.76650	6.21038
3	0.11864	5.68598	6.29089
4	0.17796	5.63254	6.34433
5	0.23728	5.59498	6.38189
6	0.29660	5.56902	6.40786
7	0.35592	5.55114	6.42556
8	0.41524	5.53364	6.44182
9	0.47456	5.51555	6.45743
10	0.53388	5.49688	6.47239
11	0.59320	5.47760	6.48668
12	0.74150	5.42681	6.51919
13	0.88980	5.37219	6.54678
14	1.03810	5.31366	6.56894
15	1.18640	5.25111	6.58508
16	1.33470	5.18440	6.59454
17	1.48300	5.11341	6.59667
18	1.63130	5.03800	6.59063
19	1.77960	4.95798	6.57559
20	1.92790	4.87318	6.55065
21	2.07620	4.78339	6.51481
22	2.22450	4.68839	6.46704
23	2.37280	4.58791	6.40627
24	2.52110	4.48160	6.33143
25	2.66940	4.36922	6.24143
26	2.81770	4.25033	6.13530
27	2.96600	4.12450	6.01210
28	3.11430	3.99119	5.87111
29	3.26260	3.84973	5.71175
30	3.41090	3.69938	5.53366
31	3.55920	3.53930	5.33677
32	3.70750	3.36863	5.12118
33	3.85580	3.18656	4.88723
34	4.00410	2.99229	4.63534
35	4.15240	2.78525	4.36603
36	4.30070	2.56517	4.07986
37	4.44900	2.33245	3.77749
38	4.59730	2.08792	3.45958
39	4.74560	1.83271	3.12684
40	4.89390	1.56797	2.78000
41	5.04220	1.29464	2.41981
42	5.19050	1.01365	2.04697
43	5.33880	0.72592	1.66229
44	5.39812	0.60905	1.50524
45	5.45744	0.49120	1.34645
46	5.51676	0.37243	1.18596
47	5.57608	0.25271	1.02380
48	5.63540	0.13213	0.86004
49	5.69472	0.01077	0.69471
50	5.75404	-0.08624	0.52783
51	5.81336	-0.10952	0.35947
52	5.87268	-0.09755	0.18966
53	5.93200	0.00001	0.00001

TABLE 1b
AIRFOIL GEOMETRY

AIRFOIL: FIRST STATOR (MIDSPAN)
PITCH (ins.): 7.71118

	LEADING EDGE	TRAILING EDGE
RADIUS (ins.)	0.44484	0.10987
METAL ANGLE (degr.)	90.00000	21.42000
WEDGE ANGLE (degr.)	31.80000	6.84000

	X(ins.)	Y_L(ins.)	Y_U(ins.)
1	0.00000	6.80766	6.80766
2	0.05932	6.44830	7.15365
3	0.11864	6.43405	7.17319
4	0.17796	6.41912	7.19210
5	0.23728	6.40354	7.21034
6	0.29660	6.38729	7.22791
7	0.35592	6.37035	7.24476
8	0.41524	6.35273	7.26089
9	0.47456	6.33441	7.27624
10	0.53388	6.31540	7.29080
11	0.59320	6.29568	7.30453
12	0.74150	6.24325	7.33502
13	0.88980	6.18623	7.35957
14	1.03810	6.12447	7.37758
15	1.18640	6.05781	7.38835
16	1.33470	5.98603	7.39114
17	1.48300	5.90896	7.38513
18	1.63130	5.82633	7.36940
19	1.77960	5.73787	7.34300
20	1.92790	5.64326	7.30490
21	2.07620	5.54212	7.25403
22	2.22450	5.43404	7.18927
23	2.37280	5.31852	7.10949
24	2.52110	5.19498	7.01363
25	2.66940	5.06273	6.90066
26	2.81770	4.92096	6.76967
27	2.96600	4.76873	6.61989
28	3.11430	4.60490	6.45078
29	3.26260	4.42825	6.26202
30	3.41090	4.23771	6.05354
31	3.55920	4.03254	5.82550
32	3.70750	3.81279	5.57826
33	3.85580	3.57948	5.31230
34	4.00410	3.33397	5.02816
35	4.15240	3.07798	4.72650
36	4.30070	2.81269	4.40803
37	4.44900	2.53937	4.07350
38	4.59730	2.25873	3.72369
39	4.74560	1.97172	3.35942
40	4.89390	1.67884	2.98147
41	5.04220	1.38062	2.59066
42	5.19050	1.07737	2.18773
43	5.33880	0.76951	1.77352
44	5.39812	0.64517	1.60482
45	5.45744	0.52020	1.43448
46	5.51676	0.39451	1.26252
47	5.57608	0.26816	1.08901
48	5.63540	0.14117	0.91397
49	5.69472	0.01364	0.73745
50	5.75404	-0.11456	0.55950
51	5.81336	-0.24329	0.38014
52	5.87268	-0.37263	0.19943
53	5.93200	0.00000	0.00000

TABLE 1c
AIRFOIL GEOMETRY

AIRFOIL: FIRST STATOR (TIP)
PITCH (ins.): 8.53371

	LEADING EDGE	TRAILING EDGE
RADIUS (ins.)	0.44487	0.10986
METAL ANGLE (degr.)	90.00401	0.25751
WEDGE ANGLE (degr.)	31.79000	6.79000

	X(ins.)	Y_L(ins.)	Y_U(ins.)
1	0.00000	7.57702	7.57702
2	0.05932	7.35507	7.79897
3	0.11864	7.27456	7.87949
4	0.17796	7.22112	7.93293
5	0.23728	7.18355	7.97049
6	0.29660	7.15759	7.99646
7	0.35592	7.13967	8.01409
8	0.41524	7.12193	8.02987
9	0.47456	7.10338	8.04449
10	0.53388	7.08402	8.05803
11	0.59320	7.06383	8.07044
12	0.74150	7.00967	8.09615
13	0.88980	6.95010	8.11406
14	1.03810	6.88487	8.12374
15	1.18640	6.81377	8.12465
16	1.33470	6.73650	8.11627
17	1.48300	6.65274	8.09803
18	1.63130	6.56207	8.06935
19	1.77960	6.46407	8.02955
20	1.92790	6.35817	7.97793
21	2.07620	6.24376	7.91381
22	2.22450	6.12004	7.83635
23	2.37280	5.98609	7.74477
24	2.52110	5.84072	7.63818
25	2.66940	5.68263	7.51566
26	2.81770	5.51023	7.37624
27	2.96600	5.32200	7.21892
28	3.11430	5.11693	7.04264
29	3.26260	4.89526	6.84631
30	3.41090	4.65850	6.62883
31	3.55920	4.40859	6.38910
32	3.70750	4.14741	6.12648
33	3.85580	3.87650	5.84072
34	4.00410	3.59714	5.53208
35	4.15240	3.31031	5.20125
36	4.30070	3.01688	4.84935
37	4.44900	2.71730	4.47775
38	4.59730	2.41223	4.08802
39	4.74560	2.10214	3.68183
40	4.89390	1.78726	3.26080
41	5.04220	1.46798	2.82654
42	5.19050	1.14458	2.38047
43	5.33880	0.81723	1.92403
44	5.39812	0.68529	1.73880
45	5.45744	0.55272	1.55219
46	5.51676	0.41958	1.36422
47	5.57608	0.28587	1.17502
48	5.63540	0.15177	0.98458
49	5.69472	0.01698	0.79299
50	5.75404	-0.08620	0.60033
51	5.81336	-0.10950	0.40661
52	5.87268	-0.09754	0.21192
53	5.93200	0.00001	0.00001

TABLE 2a
AIRFOIL GEOMETRY

AIRFOIL: FIRST ROTOR (HUB)
PITCH (ins.): 5.41251

	LEADING EDGE	TRAILING EDGE
RADIUS (ins.)	0.34867	0.19000
METAL ANGLE (degr.)	39.56323	25.97078
WEDGE ANGLE (degr.)	31.19000	5.31000

	X(ins.)	Y_L(ins.)	Y_U(ins.)
1	0.00000	2.86604	2.86604
2	0.06341	2.66555	3.08102
3	0.12682	2.59706	3.21151
4	0.19023	2.55545	3.33187
5	0.25364	2.53057	3.44343
6	0.31705	2.51881	3.54722
7	0.38046	2.51882	3.64406
8	0.44387	2.53062	3.73464
9	0.50728	2.55553	3.81950
10	0.57069	2.59558	3.89912
11	0.63410	2.63747	3.97388
12	0.79262	2.73147	4.14166
13	0.95115	2.81137	4.28528
14	1.10967	2.87832	4.40773
15	1.26820	2.93322	4.51126
16	1.42672	2.97676	4.59755
17	1.58525	3.00948	4.66791
18	1.74377	3.03180	4.72339
19	1.90230	3.04408	4.76477
20	2.06082	3.04653	4.79267
21	2.21935	3.03939	4.80757
22	2.37787	3.02278	4.80981
23	2.53640	2.99681	4.79963
24	2.69492	2.96157	4.77715
25	2.85345	2.91708	4.74242
26	3.01197	2.86339	4.69537
27	3.17050	2.80050	4.63584
28	3.32902	2.72831	4.56359
29	3.48755	2.64670	4.47823
30	3.64607	2.55547	4.37924
31	3.80460	2.45445	4.26599
32	3.96312	2.34348	4.13761
33	4.12165	2.22234	3.99304
34	4.28017	2.09081	3.83080
35	4.43870	1.94860	3.64903
36	4.59722	1.79535	3.44572
37	4.75575	1.63070	3.21968
38	4.91427	1.45405	2.97070
39	5.07280	1.26487	2.69996
40	5.23132	1.06245	2.40938
41	5.38985	0.84595	2.10143
42	5.54837	0.61435	1.77875
43	5.70690	0.36649	1.44378
44	5.77031	0.26245	1.30685
45	5.83372	0.15541	1.16841
46	5.89713	0.04543	1.02861
47	5.96054	-0.06777	0.88753
48	6.02395	-0.16117	0.74527
49	6.08736	-0.19892	0.60194
50	6.15077	-0.20989	0.45759
51	6.21418	-0.19908	0.31233
52	6.27759	-0.16158	0.16622
53	6.34100	-0.01989	-0.01989

TABLE 2b
AIRFOIL GEOMETRY

AIRFOIL: FIRST ROTOR (MIDSPAN)
PITCH (ins.): 6.05879

	LEADING EDGE	TRAILING EDGE
RADIUS (ins.)	0.34872	0.19000
METAL ANGLE (degr.)	42.18646	25.97093
WEDGE ANGLE (degr.)	31.24000	5.31000

	X(ins.)	Y_L(ins.)	Y_U(ins.)
1	0.00000	3.41970	3.41970
2	0.06341	3.21919	3.62774
3	0.12682	3.15069	3.74347
4	0.19023	3.10908	3.84906
5	0.25364	3.08419	3.94593
6	0.31705	3.07242	4.03518
7	0.38046	3.07243	4.11769
8	0.44387	3.08422	4.19414
9	0.50728	3.10912	4.26511
10	0.57069	3.14694	4.33106
11	0.63410	3.18401	4.39238
12	0.79262	3.26583	4.52752
13	0.95115	3.33349	4.63984
14	1.10967	3.38822	4.73220
15	1.26820	3.43094	4.80674
16	1.42672	3.46228	4.86506
17	1.58525	3.48271	4.90837
18	1.74377	3.49248	4.93760
19	1.90230	3.49176	4.95347
20	2.06082	3.48053	4.95652
21	2.21935	3.45868	4.94712
22	2.37787	3.42596	4.92555
23	2.53640	3.38201	4.89193
24	2.69492	3.32633	4.84632
25	2.85345	3.25830	4.78863
26	3.01197	3.17735	4.71868
27	3.17050	3.08283	4.63616
28	3.32902	2.97433	4.54063
29	3.48755	2.85162	4.43151
30	3.64607	2.71488	4.30799
31	3.80460	2.56463	4.16905
32	3.96312	2.40136	4.01334
33	4.12165	2.22577	3.83912
34	4.28017	2.03852	3.64406
35	4.43870	1.84022	3.42595
36	4.59722	1.63139	3.18387
37	4.75575	1.41252	2.91861
38	4.91427	1.18402	2.63221
39	5.07280	0.94623	2.32774
40	5.23132	0.69955	2.00832
41	5.38985	0.44403	1.67680
42	5.54837	0.18008	1.33571
43	5.70690	-0.09214	0.98699
44	5.77031	-0.20337	0.84573
45	5.83372	-0.31578	0.70359
46	5.89713	-0.42949	0.56065
47	5.96054	-0.54448	0.41698
48	6.02395	-0.63800	0.27261
49	6.08736	-0.67575	0.12765
50	6.15077	-0.68673	-0.01791
51	6.21418	-0.67591	-0.16397
52	6.27759	-0.63841	-0.31052
53	6.34100	-0.49672	-0.49672

TABLE 2c
AIRFOIL GEOMETRY

AIRFOIL: FIRST ROTOR (TIP)
PITCH (ins.): 6.70506

	LEADING EDGE	TRAILING EDGE
RADIUS (ins.)	0.34881	0.19000
METAL ANGLE (degr.)	46.66805	25.96767
WEDGE ANGLE (degr.)	31.26000	5.31000

	X(ins.)	Y_L(ins.)	Y_U(ins.)
1	0.00000	3.97348	3.97348
2	0.06341	3.77294	4.17548
3	0.12682	3.70443	4.27381
4	0.19023	3.66280	4.36353
5	0.25364	3.63790	4.44573
6	0.31705	3.62612	4.52127
7	0.38046	3.62611	4.59084
8	0.44387	3.63787	4.65499
9	0.50728	3.66275	4.71419
10	0.57069	3.69488	4.76883
11	0.63410	3.72462	4.81924
12	0.79262	3.78887	4.92848
13	0.95115	3.83974	5.01637
14	1.10967	3.87814	5.08539
15	1.26820	3.90472	5.13737
16	1.42672	3.91989	5.17369
17	1.58525	3.92388	5.19537
18	1.74377	3.91674	5.20321
19	1.90230	3.89838	5.19778
20	2.06082	3.86851	5.17950
21	2.21935	3.82665	5.14862
22	2.37787	3.77210	5.10529
23	2.53640	3.70385	5.04954
24	2.69492	3.62049	4.98122
25	2.85345	3.52015	4.90012
26	3.01197	3.40033	4.80585
27	3.17050	3.25903	4.69788
28	3.32902	3.09581	4.57543
29	3.48755	2.91352	4.43757
30	3.64607	2.71577	4.28296
31	3.80460	2.50562	4.10990
32	3.96312	2.28505	3.91608
33	4.12165	2.05587	3.69853
34	4.28017	1.81890	3.45544
35	4.43870	1.57520	3.18730
36	4.59722	1.32521	2.89675
37	4.75575	1.06966	2.58780
38	4.91427	0.80884	2.26420
39	5.07280	0.54319	1.92951
40	5.23132	0.27306	1.58629
41	5.38985	-0.00136	1.23664
42	5.54837	-0.27975	0.88207
43	5.70690	-0.56201	0.52368
44	5.77031	-0.67597	0.37945
45	5.83372	-0.79046	0.23478
46	5.89713	-0.90562	0.08974
47	5.96054	-1.02119	-0.05569
48	6.02395	-1.11481	-0.20147
49	6.08736	-1.15257	-0.34753
50	6.15077	-1.16355	-0.49387
51	6.21418	-1.15274	-0.64045
52	6.27759	-1.11524	-0.78728
53	6.34100	-0.97355	-0.97355

TABLE 3a

AIRFOIL GEOMETRY

AIRFOIL: SECOND STATOR (HUB)
PITCH (ins.): 5.41251

	LEADING EDGE	TRAILING EDGE
RADIUS (ins.)	0.34999	0.19000
METAL ANGLE (degr.)	41.01068	4.98619
WEDGE ANGLE (degr.)	29.91000	8.91000

	X(ins.)	Y_L(ins.)	Y_U(ins.)
1	0.00000	3.68263	3.68263
2	0.06452	3.48015	3.89472
3	0.12904	3.41120	4.01869
4	0.19356	3.36955	4.13494
5	0.25808	3.34493	4.24410
6	0.32260	3.33372	4.34672
7	0.38712	3.33462	4.44324
8	0.45164	3.34773	4.53408
9	0.51616	3.37461	4.61958
10	0.58068	3.41583	4.70006
11	0.64520	3.45739	4.77578
12	0.80650	3.55269	4.94580
13	0.96780	3.63560	5.09069
14	1.12910	3.70599	5.21287
15	1.29040	3.76376	5.31424
16	1.45170	3.80880	5.39634
17	1.61300	3.84106	5.46037
18	1.77430	3.86048	5.50735
19	1.93560	3.86704	5.53806
20	2.09690	3.86072	5.55317
21	2.25820	3.84153	5.55319
22	2.41950	3.80950	5.53852
23	2.58080	3.76468	5.50948
24	2.74210	3.70714	5.46629
25	2.90340	3.63698	5.40908
26	3.06470	3.55430	5.33790
27	3.22600	3.45921	5.25273
28	3.38730	3.35188	5.15348
29	3.54860	3.23245	5.03995
30	3.70990	3.10111	4.91189
31	3.87120	2.95802	4.76892
32	4.03250	2.80339	4.61058
33	4.19380	2.63745	4.43628
34	4.35510	2.46037	4.24527
35	4.51640	2.27244	4.03662
36	4.67770	2.07384	3.80928
37	4.83900	1.86483	3.56222
38	5.00030	1.64569	3.29479
39	5.16160	1.41663	3.00662
40	5.32290	1.17789	2.69784
41	5.48420	0.92975	2.36890
42	5.64550	0.67246	2.02068
43	5.80680	0.40629	1.65431
44	5.87132	0.29738	1.50296
45	5.93584	0.18710	1.34900
46	6.00036	0.07548	1.19252
47	6.06488	-0.03748	1.03361
48	6.12940	-0.13608	0.87238
49	6.19392	-0.17738	0.70890
50	6.25844	-0.18997	0.54327
51	6.32296	-0.17996	0.37560
52	6.38748	-0.14267	0.20595
53	6.45200	0.00000	0.00000

TABLE 3b
AIRFOIL GEOMETRY

AIRFOIL: SECOND STATOR (MIDSPAN)
PITCH (ins.): 6.05879

	LEADING EDGE	TRAILING EDGE
RADIUS (ins.)	0.34999	0.19000
METAL ANGLE (degr.)	45.66800	25.00000
WEDGE ANGLE (degr.)	27.50000	6.50000

	X(ins.)	Y_L(ins.)	Y_U(ins.)
1	0.00000	4.10291	4.10291
2	0.06452	3.47786	4.30650
3	0.12904	3.52885	4.40610
4	0.19356	3.57793	4.50013
5	0.25808	3.62510	4.58895
6	0.32260	3.67035	4.67285
7	0.38712	3.71368	4.75210
8	0.45164	3.75508	4.82695
9	0.51616	3.79454	4.89760
10	0.58068	3.83206	4.96425
11	0.64520	3.86762	5.02707
12	0.80650	3.94796	5.16834
13	0.96780	4.01599	5.28865
14	1.12910	4.07162	5.38963
15	1.29040	4.11482	5.47259
16	1.45170	4.14552	5.53859
17	1.61300	4.16371	5.58849
18	1.77430	4.16934	5.62296
19	1.93560	4.16244	5.64258
20	2.09690	4.14298	5.64778
21	2.25820	4.11101	5.63888
22	2.41950	4.06655	5.61615
23	2.58080	4.00965	5.57973
24	2.74210	3.94037	5.52972
25	2.90340	3.85879	5.46611
26	3.06470	3.76498	5.38882
27	3.22600	3.65906	5.29771
28	3.38730	3.54111	5.19255
29	3.54860	3.41127	5.07300
30	3.70990	3.26967	4.93863
31	3.87120	3.11644	4.78891
32	4.03250	2.95172	4.62316
33	4.19380	2.77568	4.44053
34	4.35510	2.58849	4.24001
35	4.51640	2.39030	4.02052
36	4.67770	2.18130	3.78134
37	4.83900	1.96166	3.52218
38	5.00030	1.73160	3.24330
39	5.16160	1.49128	2.94535
40	5.32290	1.24090	2.62941
41	5.48420	0.98064	2.29682
42	5.64550	0.71074	1.94914
43	5.80680	0.43141	1.58790
44	5.87132	0.31707	1.43996
45	5.93584	0.20126	1.29018
46	6.00036	0.08400	1.13867
47	6.06488	-0.03471	0.98552
48	6.12940	-0.15484	0.83080
49	6.19392	-0.27639	0.67459
50	6.25844	-0.39934	0.51699
51	6.32296	-0.52368	0.35805
52	6.38748	-0.64939	0.19786
53	6.45200	0.00000	0.00000

TABLE 3c
AIRFOIL GEOMETRY

AIRFOIL: SECOND STATOR (TIP)
PITCH (ins.): 6.70506

	LEADING EDGE	TRAILING EDGE
RADIUS (ins.)	0.35006	0.19000
METAL ANGLE (degr.)	50.49115	24.98778
WEDGE ANGLE (degr.)	25.12000	4.09000

	X(ins.)	Y_L(ins.)	Y_U(ins.)
1	0.00000	4.53429	4.53429
2	0.06452	4.33178	4.73679
3	0.12904	4.26282	4.81836
4	0.19356	4.22116	4.89463
5	0.25808	4.19652	4.96641
6	0.32260	4.18530	5.03396
7	0.38712	4.18619	5.09751
8	0.45164	4.19929	5.15728
9	0.51616	4.22602	5.21343
10	0.58068	4.25762	5.26613
11	0.64520	4.28729	5.31552
12	0.80650	4.35297	5.42538
13	0.96780	4.40647	5.51708
14	1.12910	4.44777	5.59199
15	1.29040	4.47683	5.65117
16	1.45170	4.49364	5.69551
17	1.61300	4.49819	5.72567
18	1.77430	4.49045	5.74219
19	1.93560	4.47047	5.74550
20	2.09690	4.43822	5.73590
21	2.25820	4.39375	5.71360
22	2.41950	4.33706	5.67874
23	2.58080	4.26823	5.63135
24	2.74210	4.18728	5.57140
25	2.90340	4.09426	5.49876
26	3.06470	3.98924	5.41323
27	3.22600	3.87229	5.31449
28	3.38730	3.74348	5.20215
29	3.54860	3.60289	5.07566
30	3.70990	3.45062	4.93435
31	3.87120	3.28675	4.77738
32	4.03250	3.11139	4.60366
33	4.19380	2.92465	4.41196
34	4.35510	2.72666	4.20118
35	4.51640	2.51749	3.97077
36	4.67770	2.29731	3.72077
37	4.83900	2.06620	3.45177
38	5.00030	1.82436	3.16495
39	5.16160	1.57187	2.86176
40	5.32290	1.30889	2.54389
41	5.48420	1.03553	2.21304
42	5.64550	0.75199	1.87091
43	5.80680	0.45841	1.51902
44	5.87132	0.33818	1.37585
45	5.93584	0.21639	1.23140
46	6.00036	0.09302	1.08577
47	6.06488	-0.03190	0.93902
48	6.12940	-0.13607	0.79122
49	6.19392	-0.17738	0.64244
50	6.25844	-0.18996	0.49272
51	6.32296	-0.17995	0.34214
52	6.38748	-0.14267	0.19073
53	6.45200	0.00000	0.00000

TABLE 4

AIRFOIL INLET AND EXIT FLOW ANGLES DETERMINED FROM 5 HOLE PROBE TRAVERSE (TRAV) AND POTENTIAL FLOW CALCULATION (T862) AT THE DESIGN FLOW COEFFICIENT, (Cx/Um) = 0.78

1st STATOR	ROTOR	2nd STATOR
α_1 (T862) = 90°	β_2 (T862) = 41°	α_3 = (T862) = 62°
	β_2 (TRAV) = 40.6°	α_3 (TRAV) = 64°
α_2 (T862) = 22.5	β_3 (T862) = 25.25°	α_4 (T862) = 26°
α_2 (TRAV) = 22.4°	β_3 (TRAV) = 31.7°	α_4 (TRAV) = 23.7°

TABLE 5

PITCH AVERAGED UNSTEADINESS RESULTS AT Cx/Um = 0.78

	TOTAL $\sqrt{\overline{U_T}}$	RANDOM $\sqrt{\overline{U_R}}$	PERIODIC $\sqrt{\overline{U_P}}$
1st STATOR EXIT			
• GRID OUT	0.030	0.022	0.019
• GRID IN	0.036	0.031	0.017
ROTOR EXIT			
• GRID OUT	0.155	0.120	0.096
• GRID IN	0.155	0.137	0.069
2nd STATOR EXIT			
• GRID OUT	0.061	0.058	0.020
• GRID IN	0.061	0.058	0.017

TABLE 6

EXPERIMENTAL UNCERTAINTY

Flow angles	$\pm 0.5^{o}$
Flow coefficient (C_x/U_m)	$\pm$ 1%
Flow speed	$\pm$ 2%
Pressure coefficient (C_P)	$\pm$ 2%
Rotor wheel speed (U_m)	$\pm$ 0.1%
Wheel speed dynamic head (Q_{Um})	$\pm$ 0.5%
Reynolds number	$\pm$ 2%
Temperature (an individual reading)	$\pm 0.5\ F^{o}$
Free-stream temperature	$\pm 1.5\ F^{o}$
Stanton Number	$\pm$ 4%
Thermocouple location	
- absolute	$\pm$ 0.020 ins.
- relative in stagnation region	$\pm$ 0.005 ins.

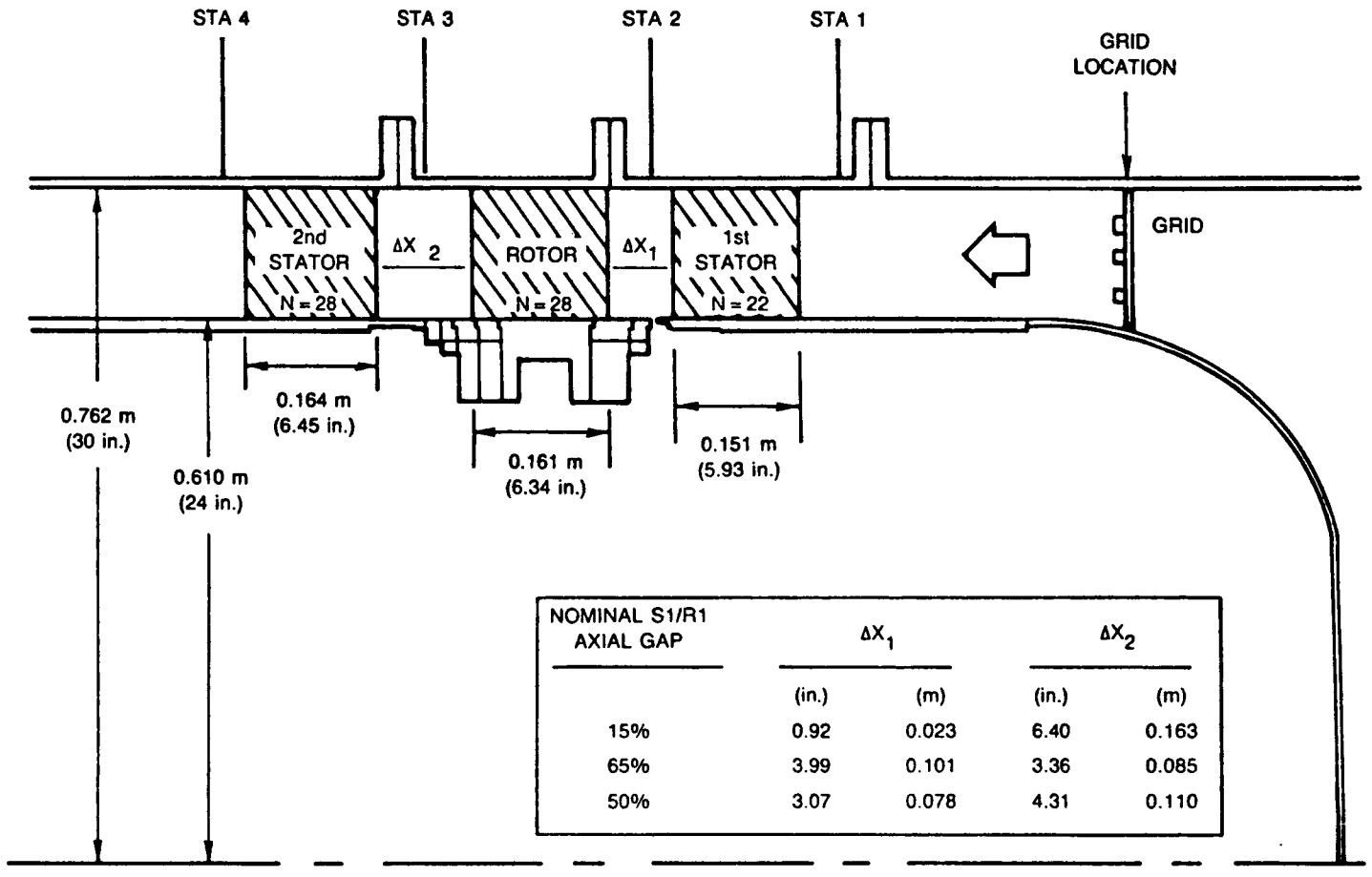

NOMINAL S1/R1 AXIAL GAP	ΔX_1		ΔX_2	
	(in.)	(m)	(in.)	(m)
15%	0.92	0.023	6.40	0.163
65%	3.99	0.101	3.36	0.085
50%	3.07	0.078	4.31	0.110

Fig. 1 United Technologies Research Center Large Scale Rotating Rig

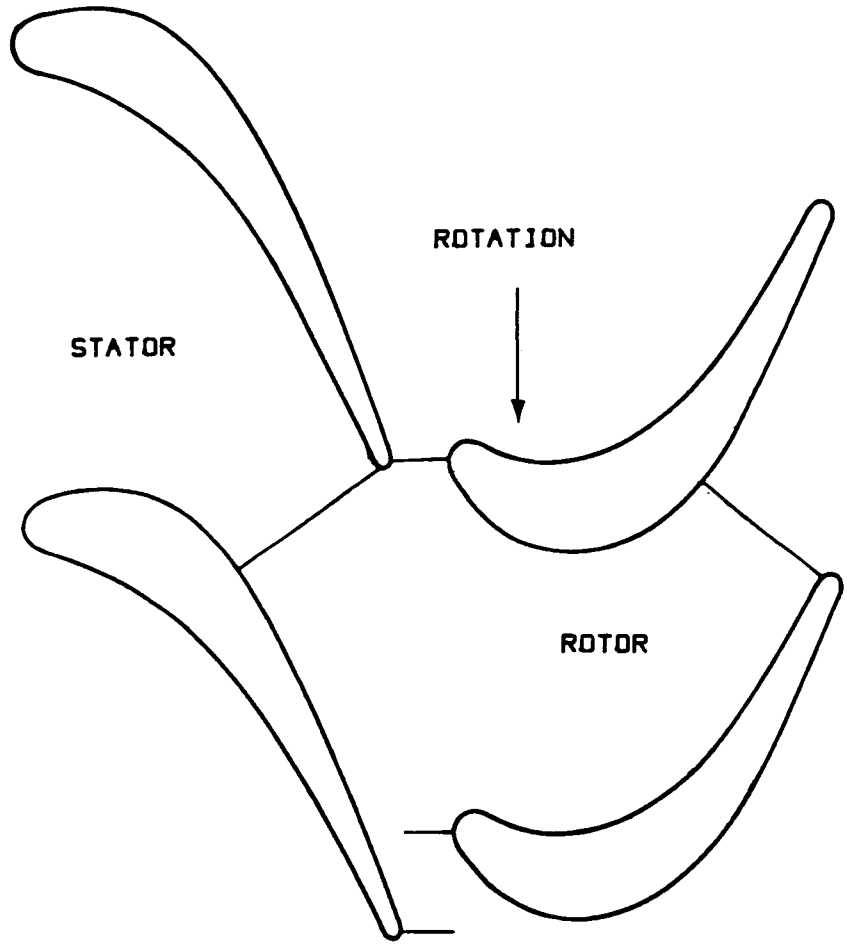

FIG. 2 TURBINE STAGE AT 15% AXIAL GAP

(FIRST VANE AND ROTOR CASE REMOVED)

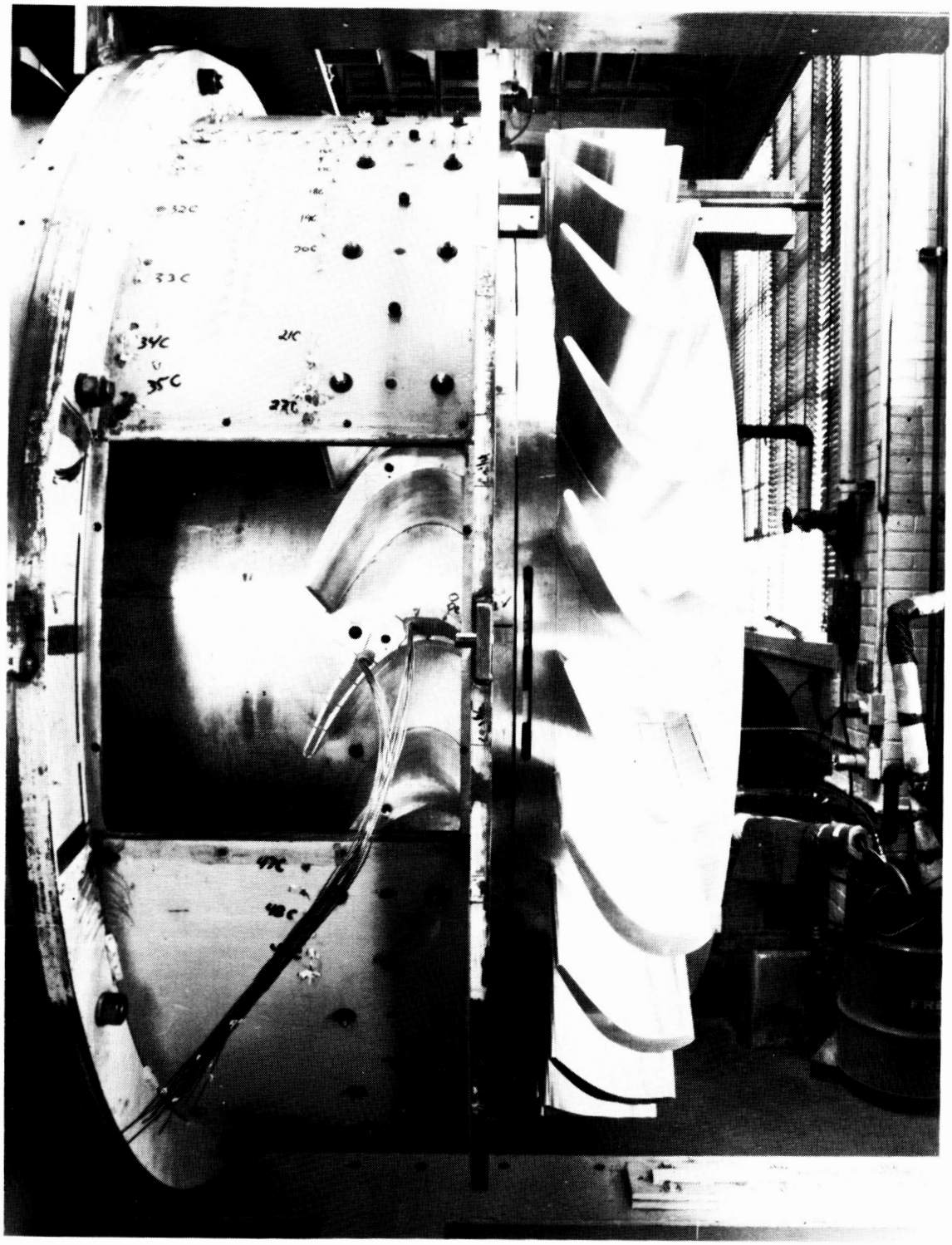

FIG. 3 LARGE SCALE ROTATING RIG 1 1/2 STAGE TURBINE CONFIGURATION

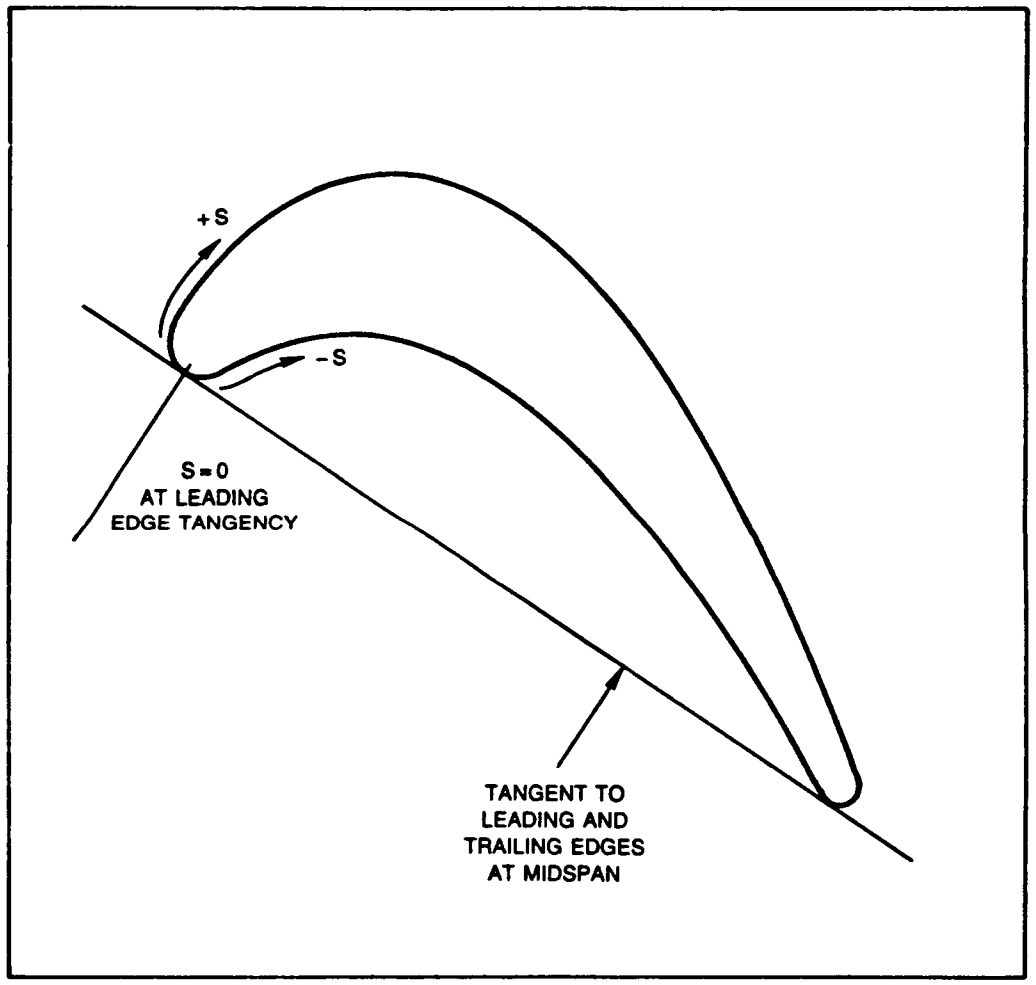

FIG. 4 DIAGRAM OF SURFACE DISTANCE (S) NOMENCLATURE

86-6-40-1

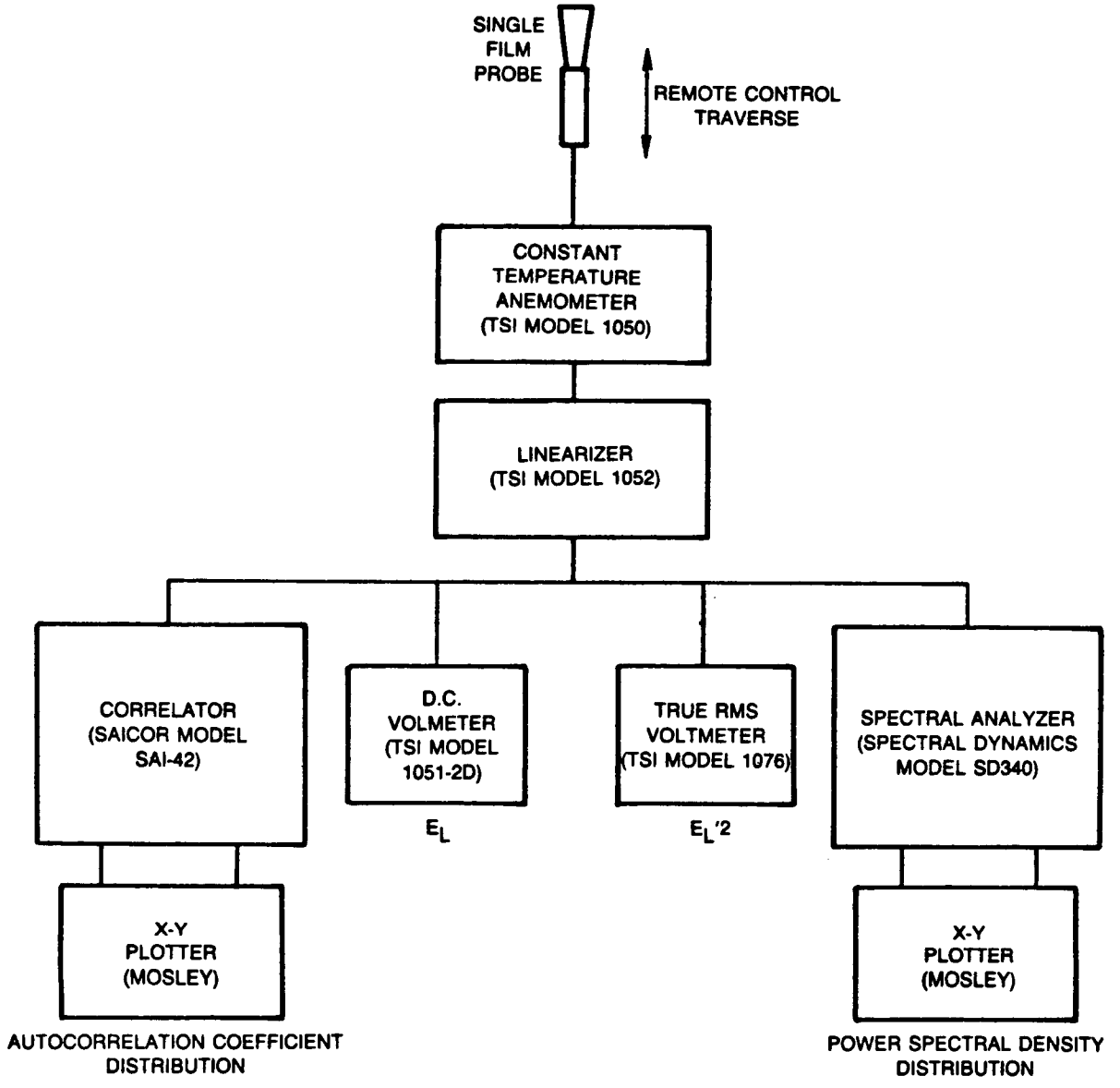

FIG. 5 BLOCK DIAGRAM OF INSTRUMENTATION ARRANGEMENT FOR OBTAINING LENGTH SCALE AND SPECTRAL DISTRIBUTION DATA

86—6—84—4

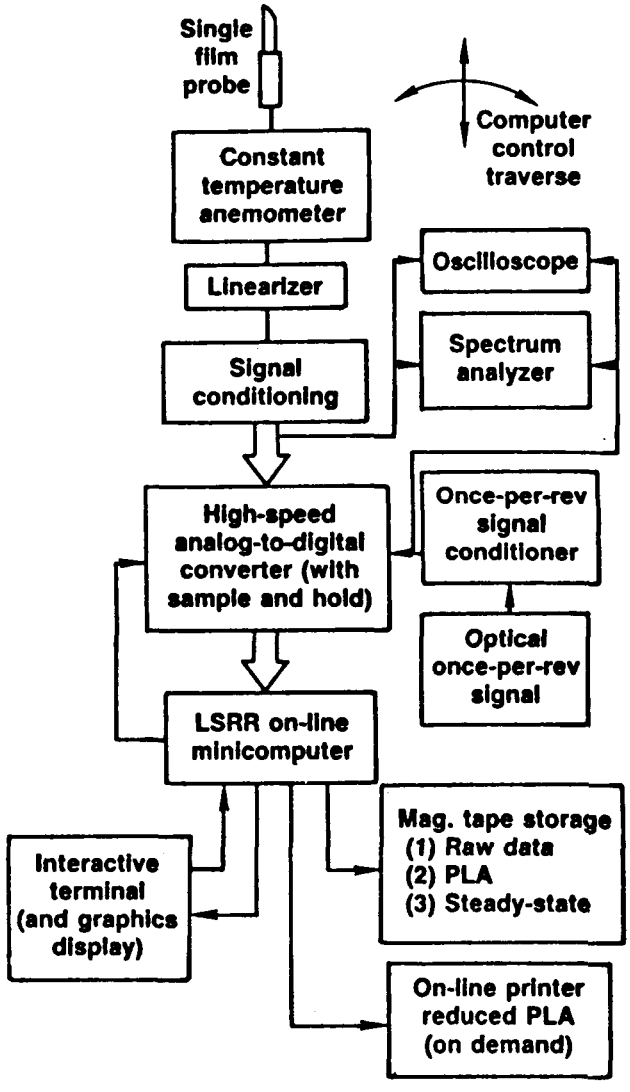

FIG. 6 INSTRUMENTATION AND DATA ACQUISITION SYSTEM FOR VELOCITY AND UNSTEADINESS DATA

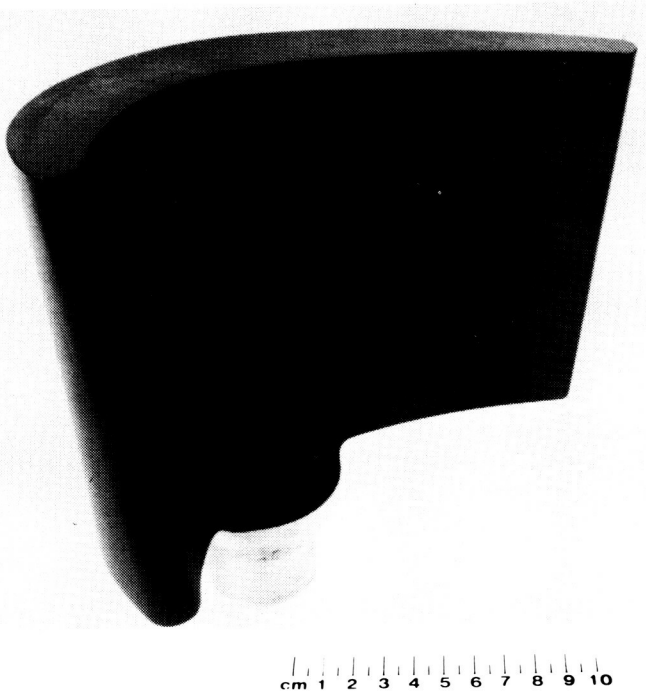

METAL MASTER AIRFOIL

STEEL SKELETON

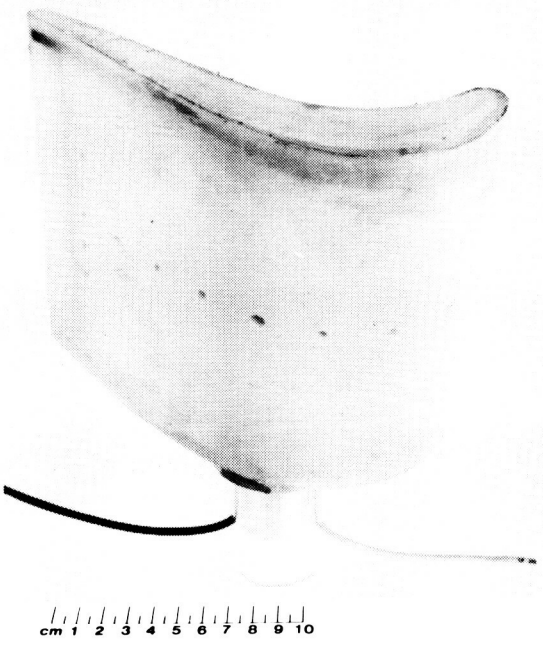

SUCTION SURFACE OF CAST AIRFOIL

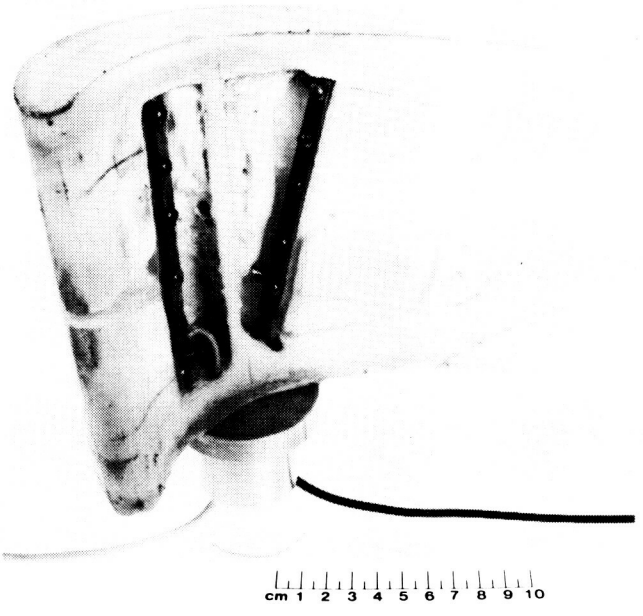

PRESSURE SURFACE OF CAST AIRFOIL

FIG. 7 STAGES OF FABRICATION FOR THE FIRST STAGE ROTOR

84-2-25-2

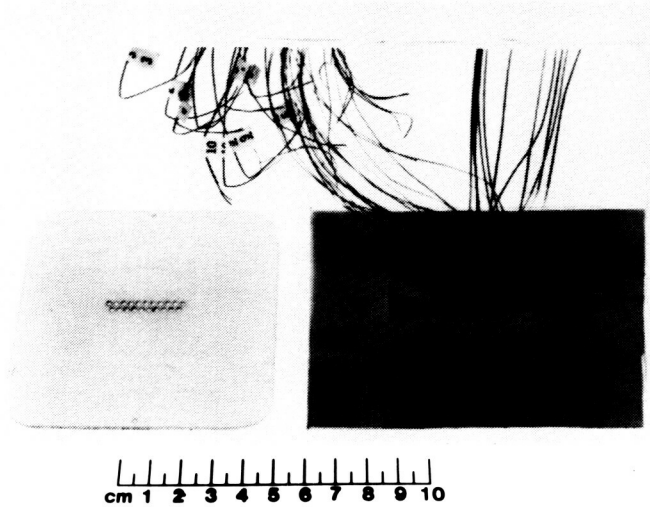

LEADING EDGE THERMOCOUPLE GRID

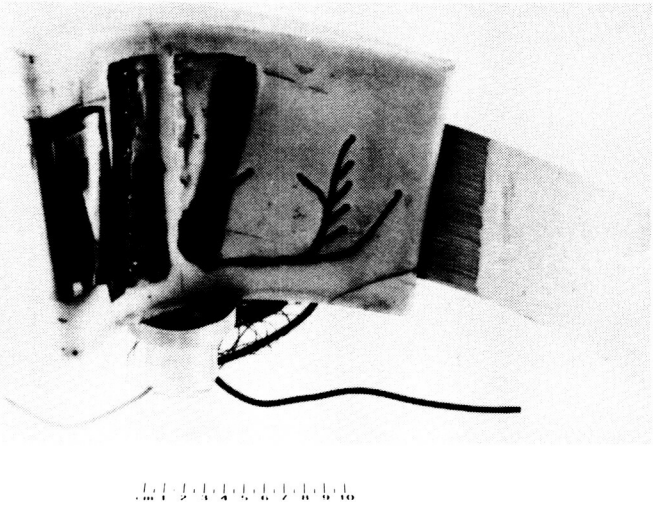

AIRFOIL WITH FOIL PARTIALLY INSTALLED

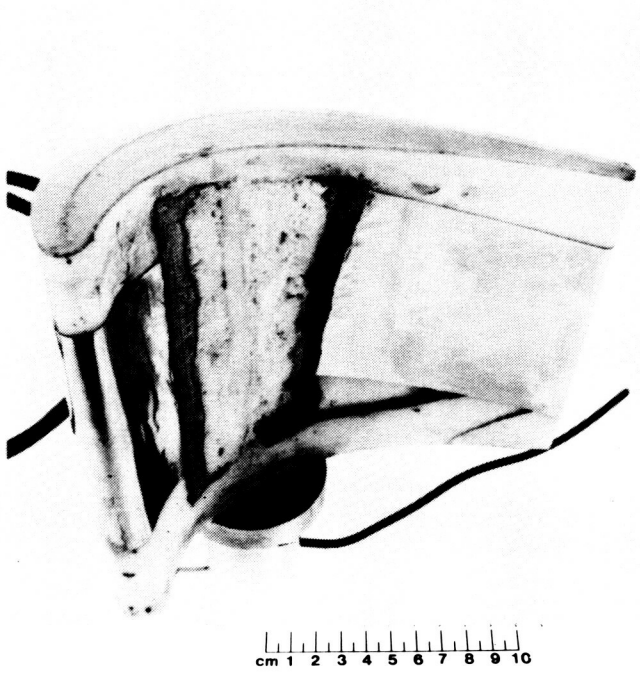

AIRFOIL WITH INSTRUMENTATION CAVITY CLOSED

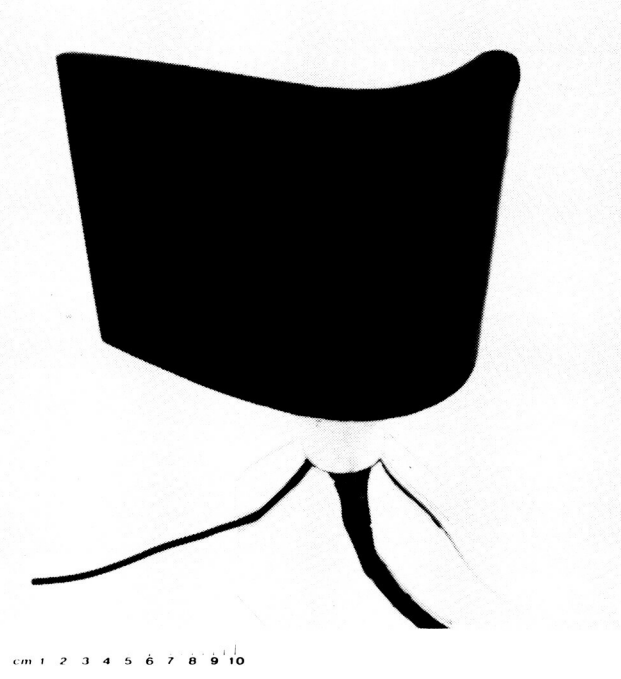

COMPLETED TEST AIRFOIL

FIG. 8 STAGES OF FABRICATON FOR THE FIRST STAGE ROTOR

84-2-25-1

$B_x = 5.932$ in. TOTAL ARC LENGTH = 20.334 in.

S=0 at S'=11.11 in.

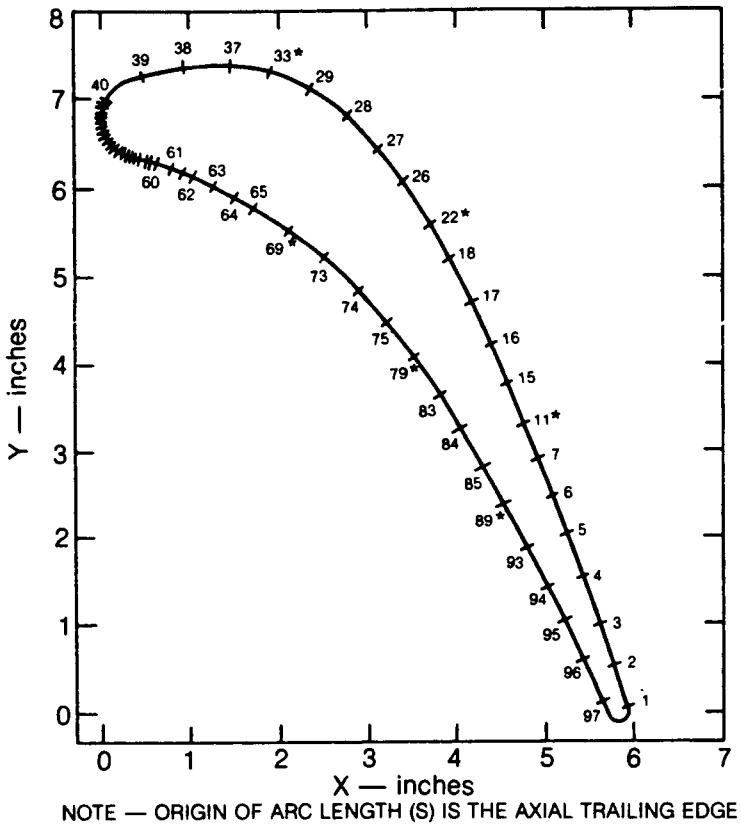

ORIGINAL PAGE IS
OF POOR QUALITY

NOTE — ORIGIN OF ARC LENGTH (S) IS THE AXIAL TRAILING EDGE (MAXIMUM X), S INCREASES MOVING COUNTERCLOCKWISE

SUCTION SURFACE AIRFOIL TC's 1-60
PRESSURE SURFACE AIRFOIL TC's 40-97

T.C.#	X/B_x	S'/B_x
1	0.995	0.012
2	0.968	0.096
3	0.941	0.181
4	0.915	0.265
5	0.887	0.349
6	0.858	0.434
7	0.829	0.518
11*	0.799	0.602
15	0.767	0.686
16	0.735	0.771
17	0.700	0.855
18	0.663	0.939
22*	0.620	1.024
26	0.575	1.108
27	0.524	1.192
28	0.464	1.277
29	0.396	1.361
33*	0.324	1.445
37	0.169	1.529
38	0.155	1.614

T.C.#	X/B_x	S'/B_x
39	0.073	1.698
40	0.007	1.782
41	0.004	1.791
42	0.001	1.799
43	0.000	1.808
44	0.000	1.816
45	0.001	1.824
46	0.002	1.833
47	0.005	1.841
48	0.008	1.850
49	0.013	1.858
50	0.018	1.867
51	0.023	1.875
52	0.030	1.883
53	0.037	1.892
54	0.044	1.900
55	0.052	1.909
56	0.060	1.917
57	0.068	1.926
58	0.076	1.934

T.C.#	X/B_x	S'/B_x
59	0.084	1.942
60	0.092	1.951
61	0.130	1.993
62	0.172	2.035
63	0.209	2.077
64	0.246	2.119
65	0.285	2.162
69*	0.356	2.246
73	0.421	2.330
74	0.484	2.414
75	0.538	2.499
79*	0.590	2.583
83	0.637	2.667
84	0.679	2.752
85	0.723	2.836
89*	0.764	2.920
93	0.802	3.004
94	0.840	3.089
95	0.878	3.173
96	0.914	3.257
97	0.949	3.342

* AT THESE AXIAL STATIONS T.C.s LOCATED AT 50% SPAN AND ±8.3, 16.6 AND 25% AWAY FROM MIDSPAN

FIG. 8 INSTRUMENTATION DIAGRAM FOR THE FIRST STAGE STATOR

84-5-26-1

ORIGINAL PAGE IS
OF POOR QUALITY

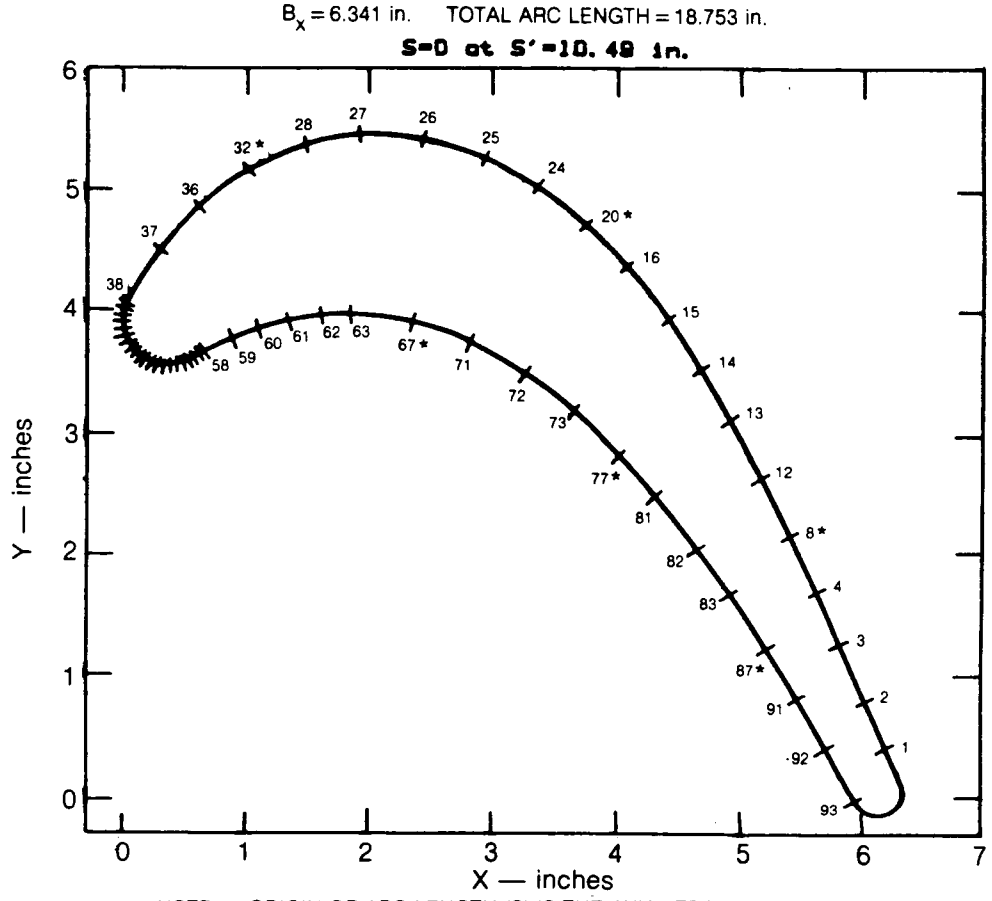

NOTE — ORIGIN OF ARC LENGTH (S) IS THE AXIAL TRAILING EDGE (MAXIMUM X), S INCREASES MOVING COUNTERCLOCKWISE

SUCTION SURFACE AIRFOIL TC's 1-58
PRESSURE SURFACE AIRFOIL TC's 38-93

T.C.#	X/B_x	S'/B_x
1	0.975	0.069
2	0.945	0.148
3	0.912	0.227
4	0.878	0.306
8*	0.845	0.385
12	0.811	0.463
13	0.773	0.542
14	0.735	0.621
15	0.692	0.700
16	0.643	0.779
20*	0.588	0.858
24	0.525	0.936
25	0.456	1.015
26	0.382	1.094
27	0.303	1.173
28	0.226	1.252
32*	0.155	1.331
36	0.095	1.410
37	0.044	1.488
38	0.003	1.567

T.C.#	X/B_x	S'/B_x
39	0.001	1.575
40	0.000	1.583
41	0.000	1.591
42	0.002	1.599
43	0.004	1.607
44	0.007	1.615
45	0.012	1.622
46	0.017	1.630
47	0.023	1.638
48	0.030	1.646
49	0.037	1.654
50	0.044	1.662
51	0.052	1.670
52	0.061	1.678
53	0.068	1.686
54	0.076	1.693
55	0.083	1.701
56	0.090	1.709
57	0.096	1.717
58	0.103	1.725

T.C.#	X/B_x	S'/B_x
59	0.139	1.764
60	0.172	1.804
61	0.211	1.843
62	0.251	1.883
63	0.290	1.922
67*	0.371	2.000
71	0.445	2.080
72	0.513	2.159
73	0.574	2.237
77*	0.629	2.316
81	0.680	2.395
82	0.730	2.474
83	0.774	2.553
87*	0.820	2.632
91	0.858	2.711
92	0.899	2.789
93	0.940	2.868

* AT THESE AXIAL STATIONS T.C.s LOCATED AT 50% SPAN AND ±8.3, 16.6 AND 25% AWAY FROM MIDSPAN

FIG. 10 INSTRUMENTATION DIAGRAM FOR THE FIRST STAGE ROTOR

84-5-26-

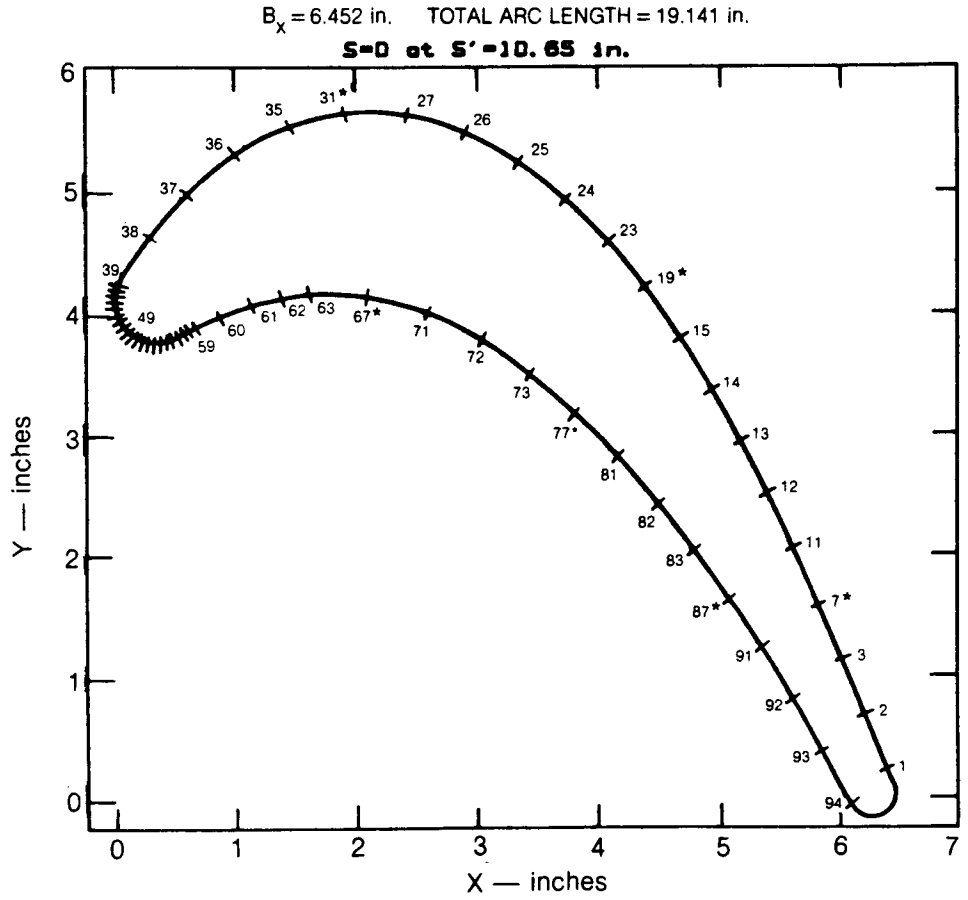

NOTE — ORIGIN OF ARC LENGTH (S) IS THE AXIAL TRAILING EDGE (MAXIMUM X), S INCREASES MOVING COUNTERCLOCKWISE

SUCTION SURFACE AIRFOIL TC's 1-59
PRESSURE SURFACE AIRFOIL TC's 39-94

T.C.#	X/B_x	S^p/B_x
1	0.990	0.023
2	0.962	0.101
3	0.933	0.178
7*	0.904	0.255
11	0.871	0.333
12	0.839	0.411
13	0.804	0.488
14	0.767	0.566
15	0.727	0.643
19*	0.682	0.721
23	0.634	0.798
24	0.580	0.876
25	0.518	0.953
26	0.451	1.031
27	0.377	1.108
31*	0.298	1.186
35	0.226	1.263
36	0.157	1.341
37	0.095	1.418
38	0.047	1.496

T.C.#	X/B_x	S^s/B_x
39	0.002	1.573
40	0.001	1.581
41	0.000	1.589
42	0.000	1.596
43	0.002	1.604
44	0.004	1.612
45	0.008	1.620
46	0.012	1.627
47	0.018	1.635
48	0.024	1.643
49	0.031	1.651
50	0.038	1.658
51	0.044	1.666
52	0.052	1.674
53	0.060	1.682
54	0.067	1.689
55	0.075	1.697
56	0.082	1.705
57	0.089	1.713
58	0.096	1.720

T.C.#	X/B_x	S^s/B_x
59	0.103	1.728
60	0.139	1.767
61	0.177	1.806
62	0.214	1.844
63	0.250	1.883
67*	0.325	1.961
71	0.401	2.038
72	0.471	2.116
73	0.533	2.193
77*	0.592	2.271
81	0.645	2.348
82	0.696	2.426
83	0.742	2.503
87*	0.786	2.581
91	0.828	2.658
92	0.868	2.736
93	0.908	2.813
94	0.945	2.891

*AT THESE AXIAL STATIONS T.C.s LOCATED AT 50% SPAN AND ±8.3, 16.6 AND 25% AWAY FROM MIDSPAN

FIG. 11 INSTRUMENTATION DIAGRAM FOR THE SECOND STAGE STATOR

84-5-26-2

CENTER BODY NOSE REMOVED TO SHOW WENDON SLIP-RING (MODEL W212-101) INSTALLED IN THE LSRR

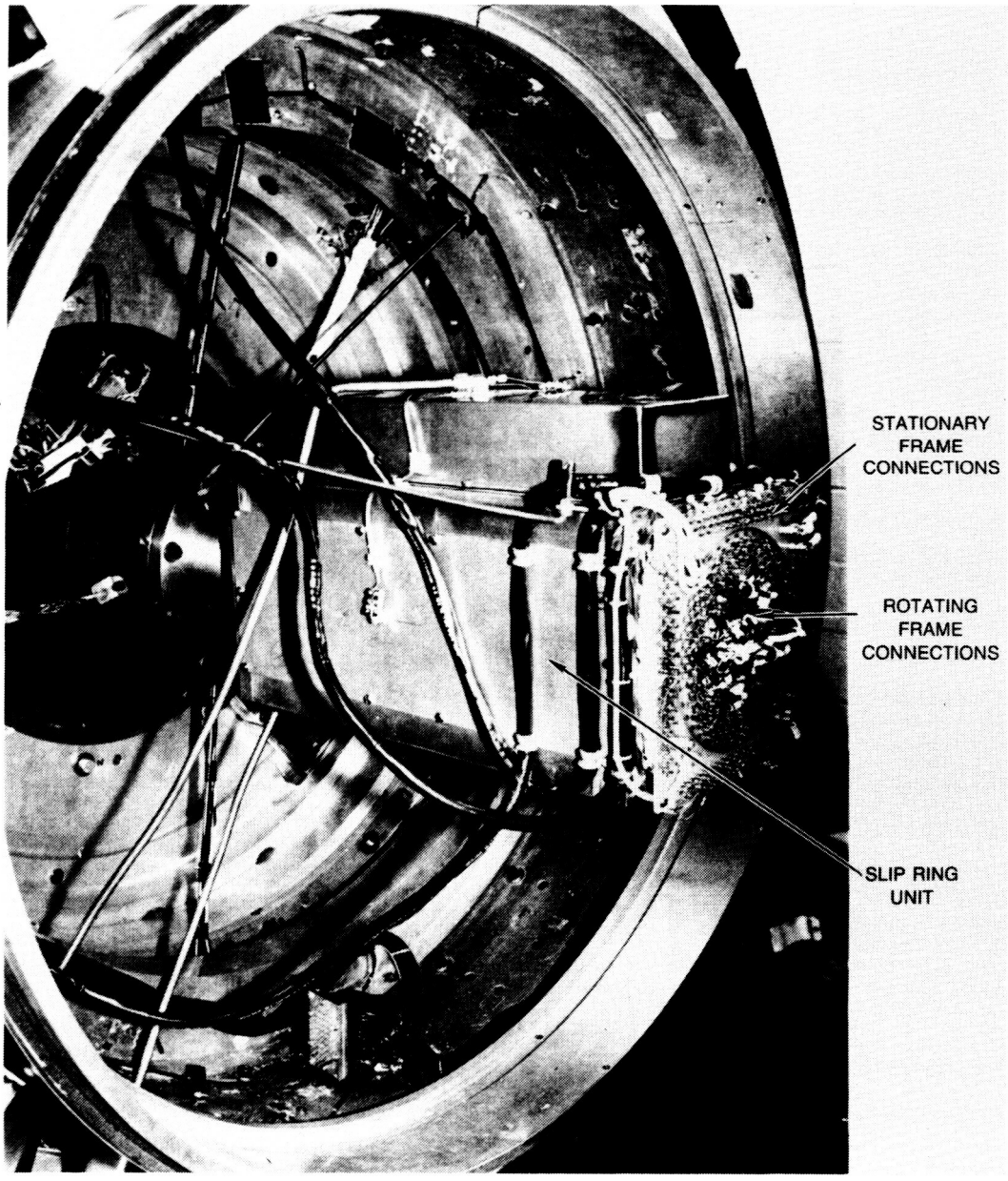

FIG. 12 CENTER BODY NOSE REMOVED TO SHOW WENDON SLIP-RING (MODEL W212-101) INSTALLED IN THE LSRR

86-5-18-5

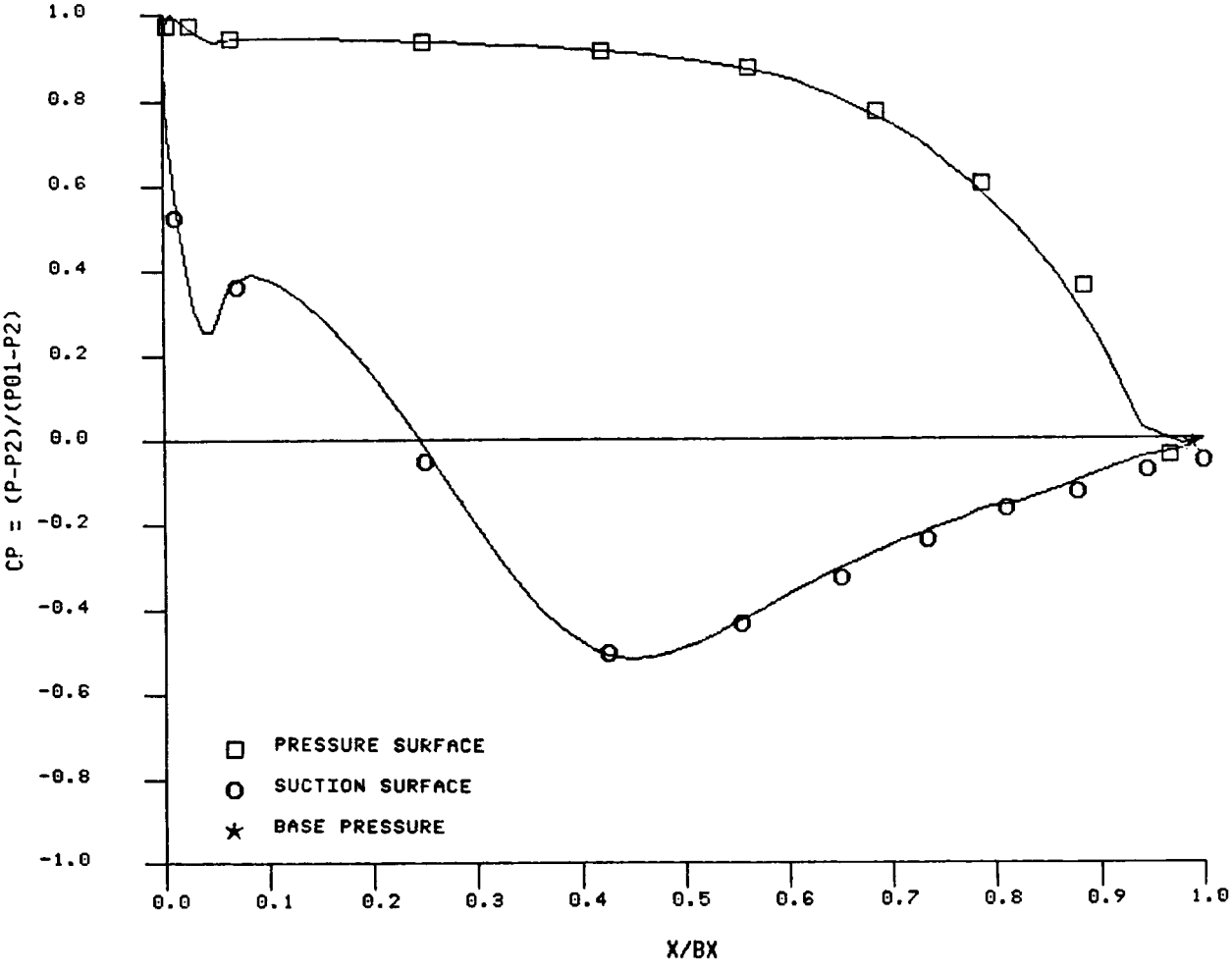

FIG. 13 FIRST STATOR PRESSURE DISTRIBUTION, $\phi = 0.78$

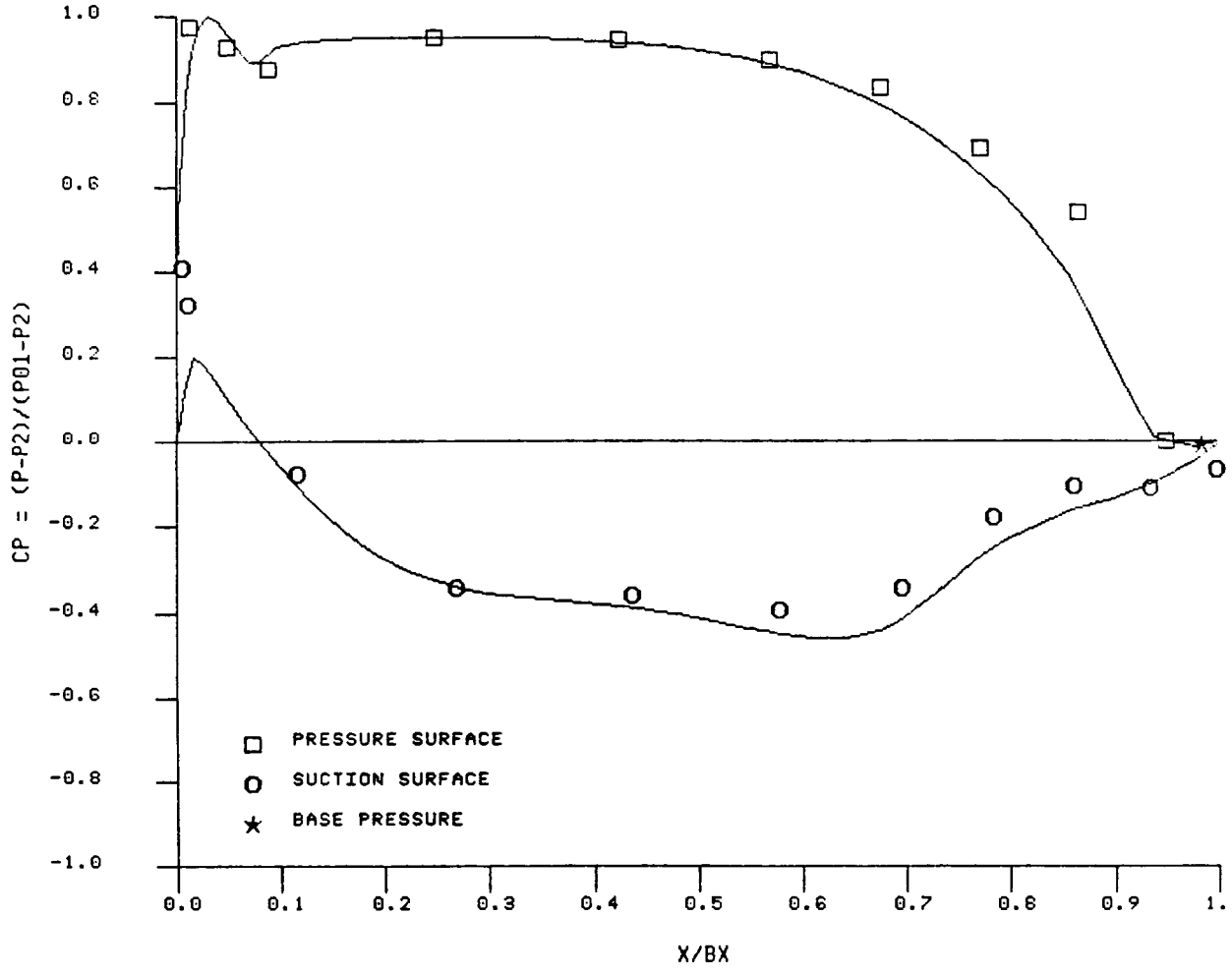

FIG. 14a ROTOR PRESSURE DISTRIBUTION, ϕ = 0.68

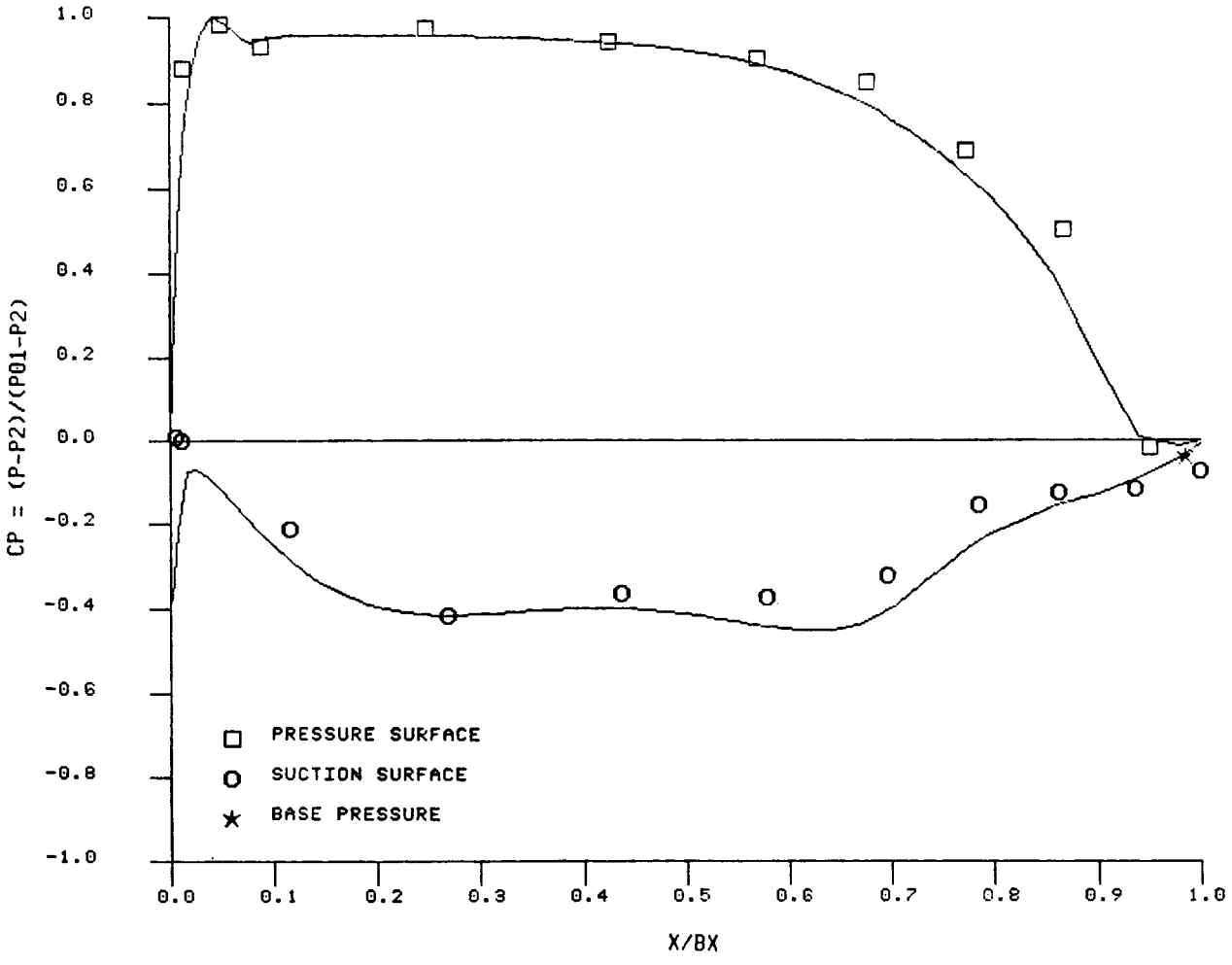

FIG. 14b ROTOR PRESSURE DISTRIBUTION, ϕ = 0.78

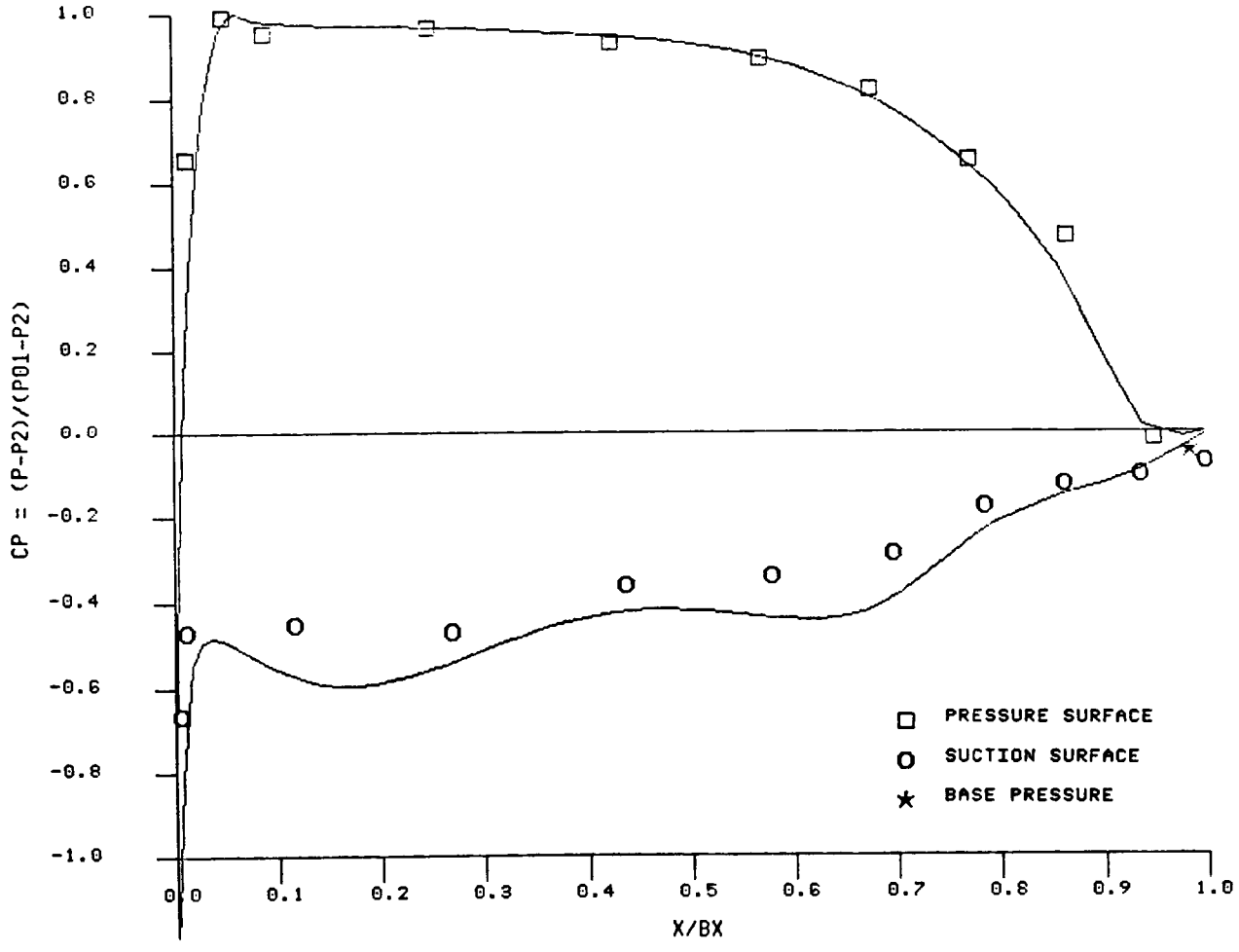

FIG. 14c ROTOR PRESSURE DISTRIBUTION, ϕ = 0.96

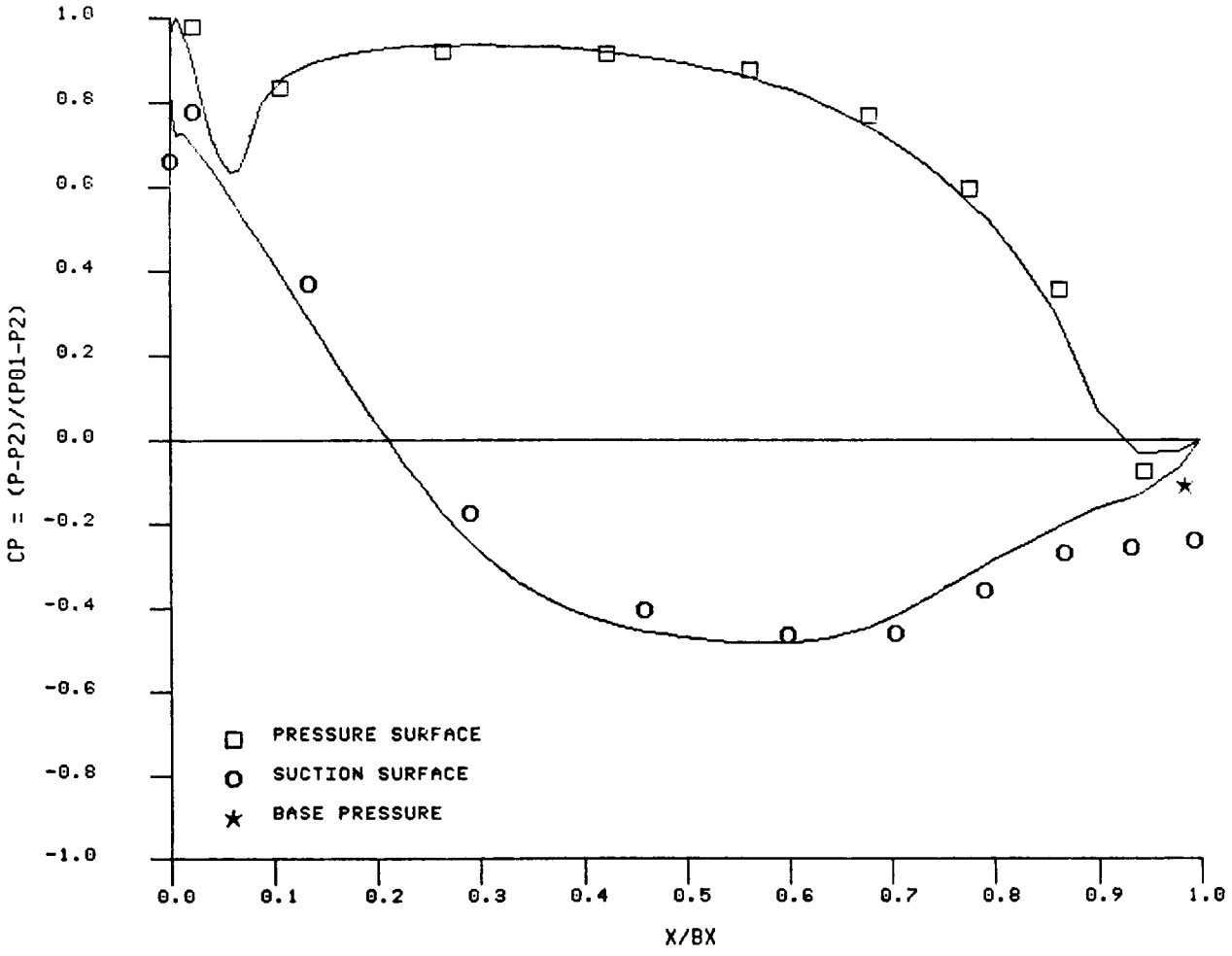

FIG. 15a SECOND STATOR PRESSURE DISTRIBUTION, ϕ = 0.68

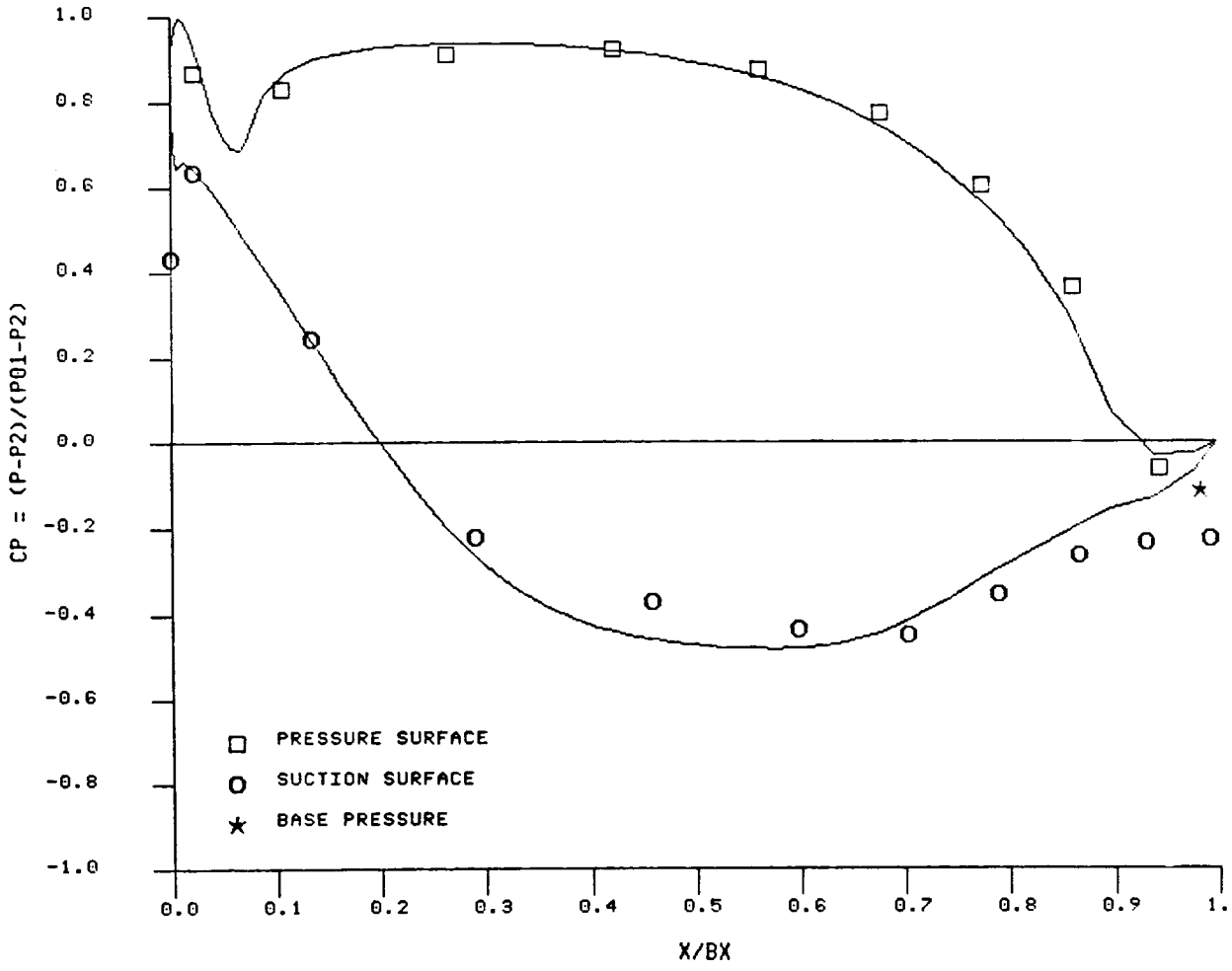

FIG. 15b SECOND STATOR PRESSURE DISTRIBUTION, ϕ = 0.78

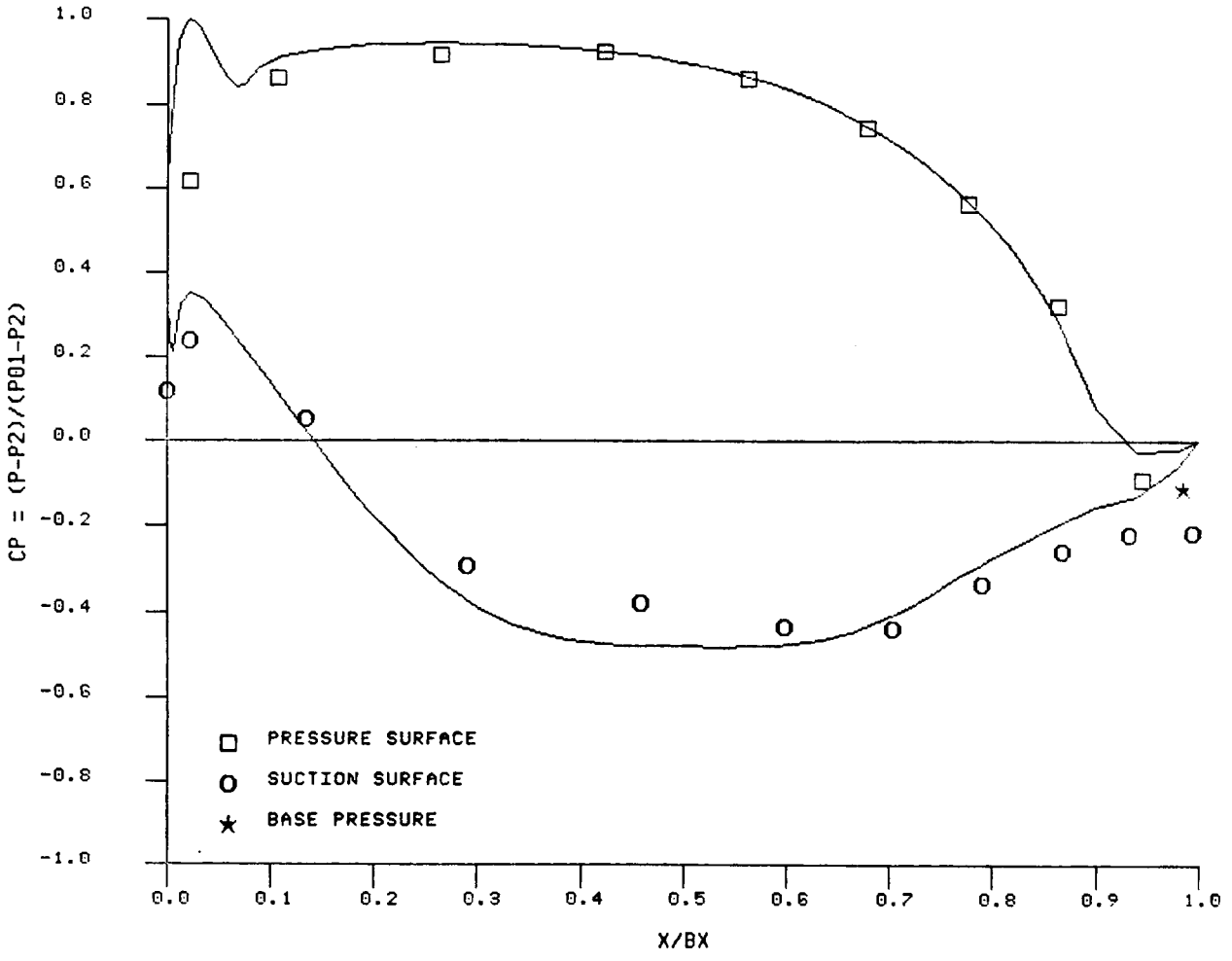

FIG. 15c SECOND STATOR PRESSURE DISTRIBUTION, ϕ = 0.96

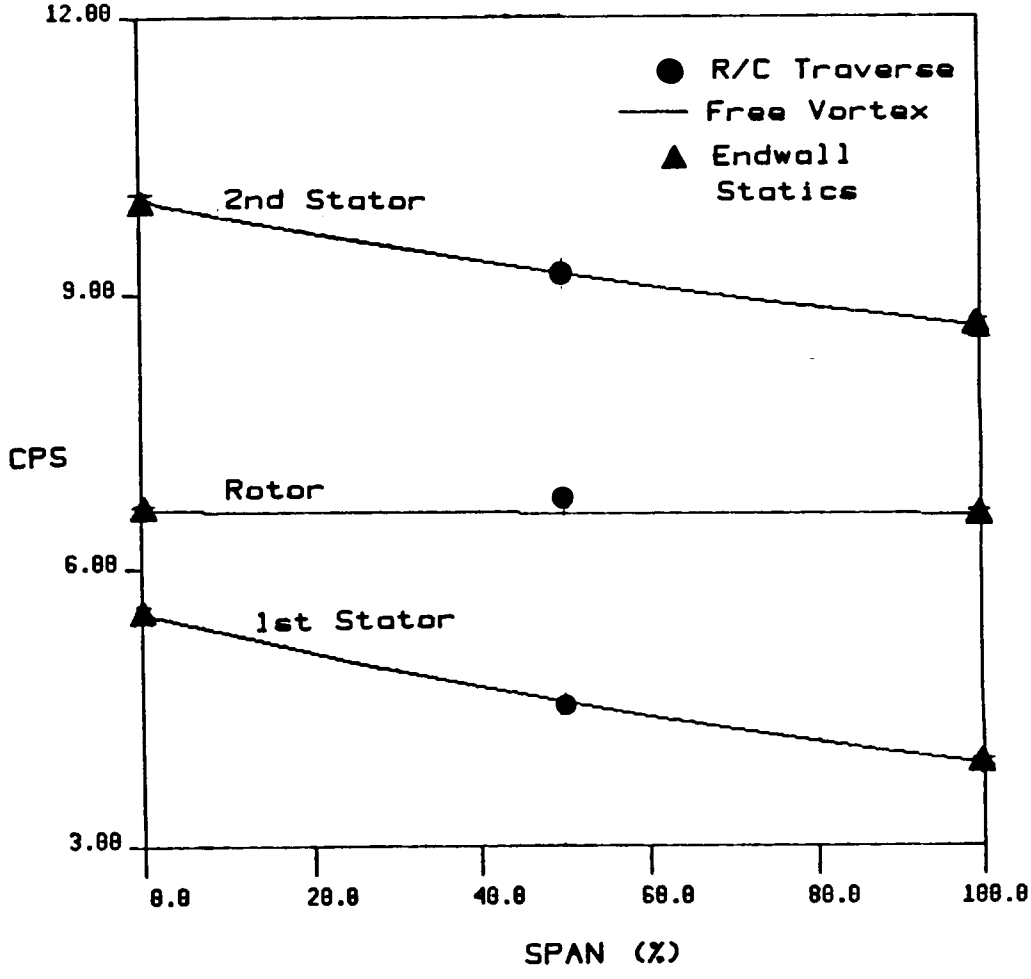

FIG. 16 FLOWPATH HUB AND TIP AND MIDSPAN TRAVERSE STATIC PRESSURES

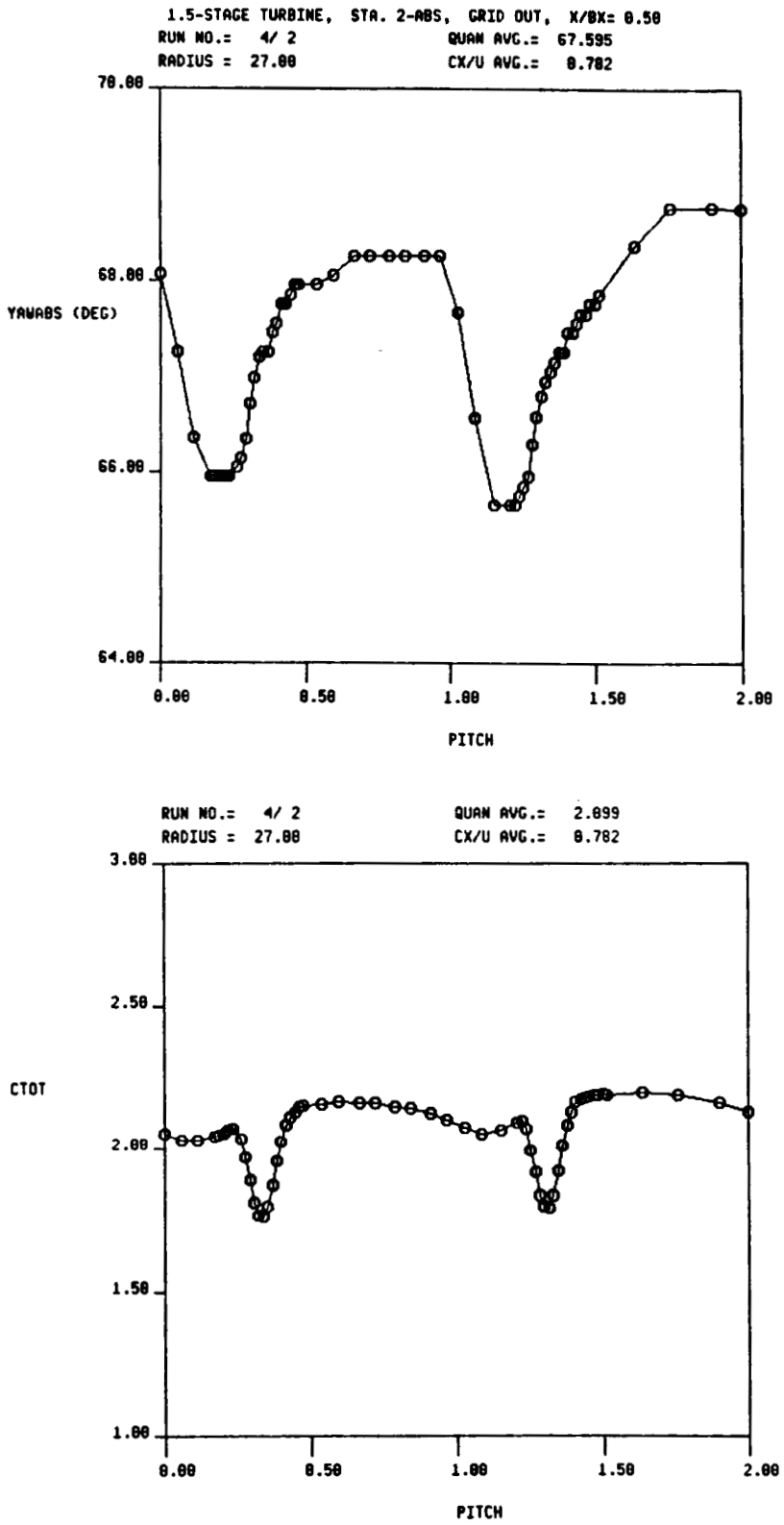

FIG. 17 ABSOLUTE YAW ANGLE AND VELOCITY FROM 5-HOLE PROBE TRAVERSE AT 1ST STATOR EXIT (X/Bx = 0.17)

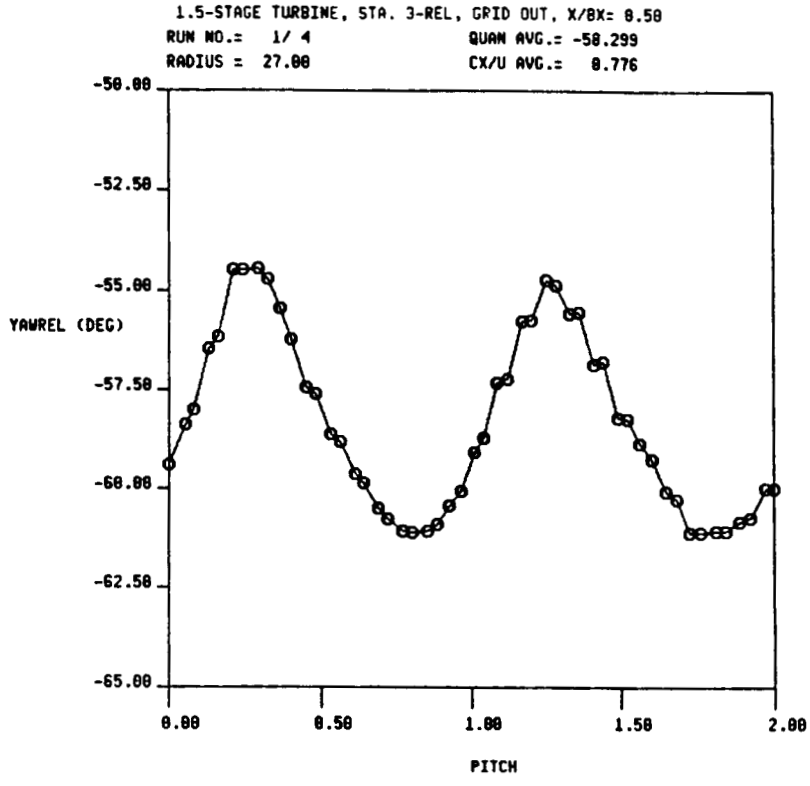

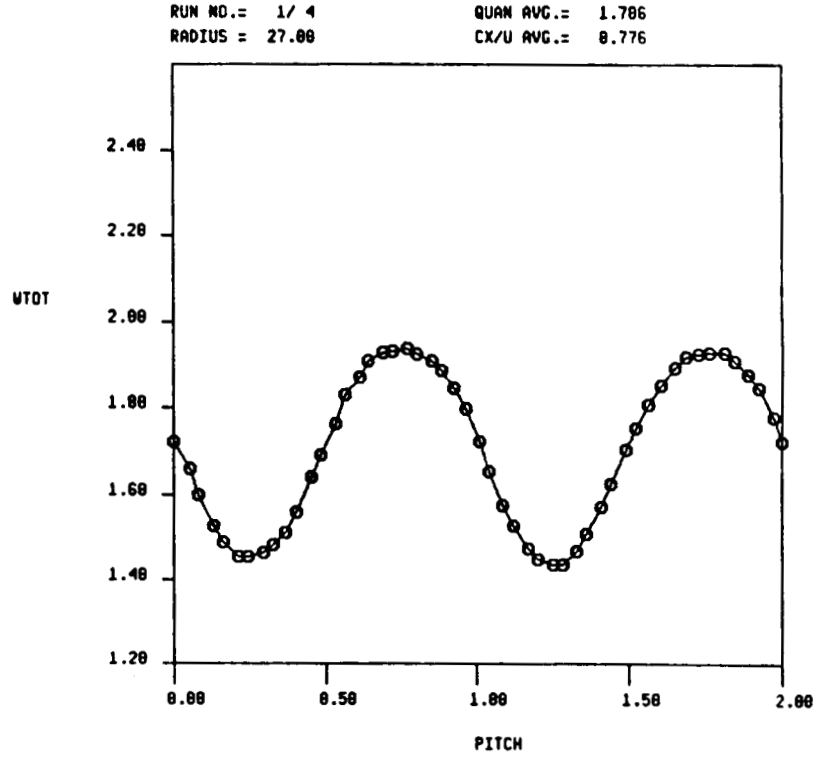

FIG. 18 RELATIVE YAW ANGLE AND VELOCITY FROM 5-HOLE PROBE TRAVERSE AT ROTOR EXIT (X/Bx = 0.36)

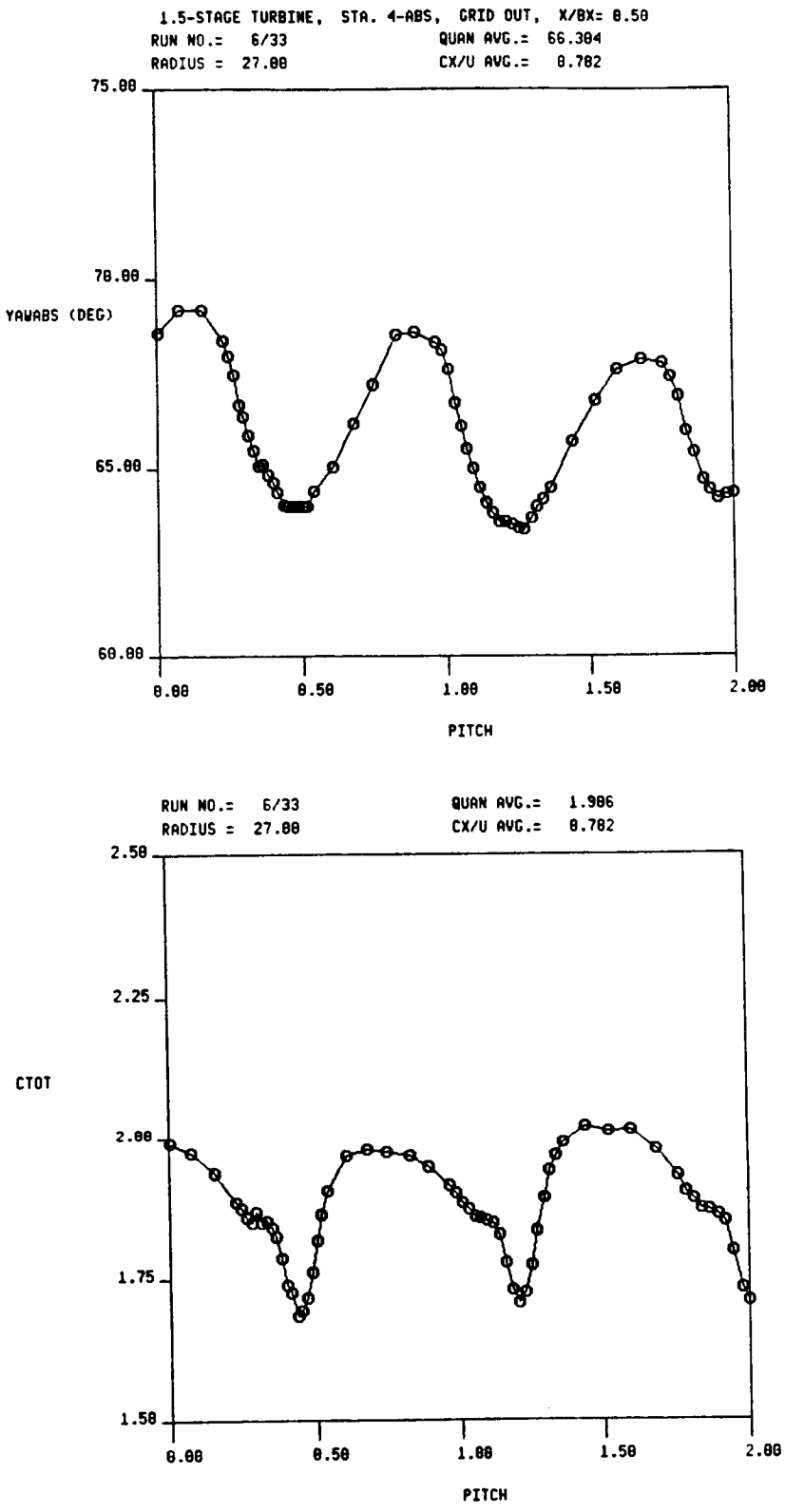

FIG. 19 ABSOLUTE YAW ANGLE AND VELOCITY FROM 5-HOLE PROBE TRAVERSE AT 2ND STATOR EXIT (X/Bx = 0.14)

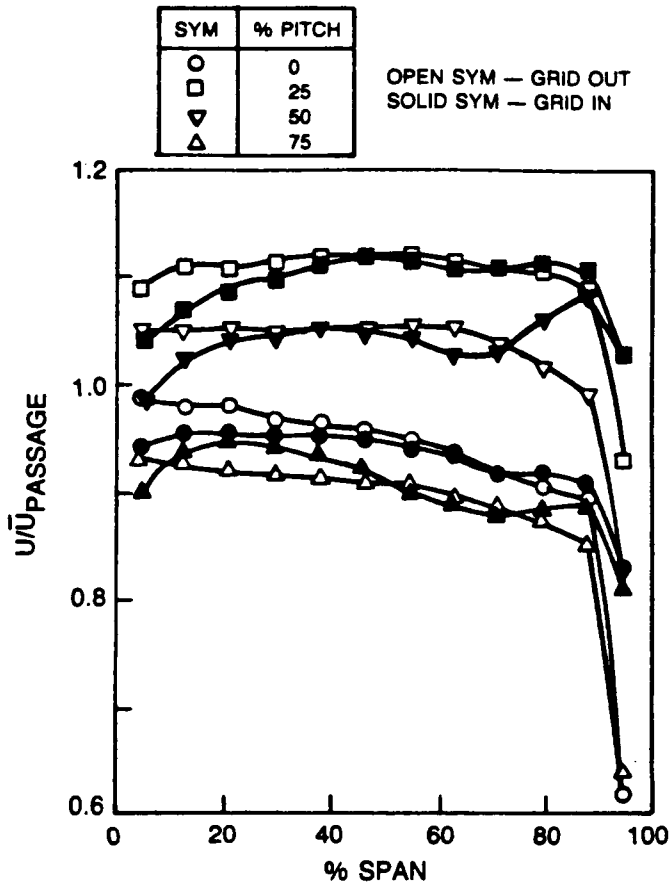

a) SPANWISE DISTRIBUTIONS OF THE TEMPORALLY AVERAGED STREAMWISE VELOCITY AT VARIOUS PITCH LOCATIONS

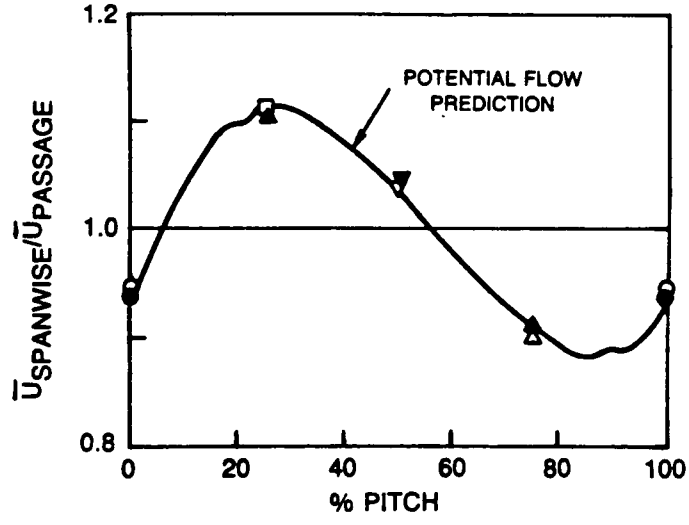

b) SPANWISE AVERAGED STREAMWISE VELOCITIES

FIG. 20 DISTRIBUTIONS OF THE MEAN VELOCITY AT X=-1.35 IN. (6.5 MESH LENGTHS FROM THE GRID)

ACOUSTIC AND VIBRATION CONTRIBUTIONS TO THE TOTAL UNSTEADY HOT-FILM SIGNAL

SYM	f — Hz	SOURCE	% TOTAL POWER SPECTRUM
A	4.6	FLOOR VIBRATION (HOT FILM VIBRATES)	26
B	29.8	MAIN BLOWER SHAFT FREQUENCY	3 1/2
C	40.6	ACOUSTIC STANDING WAVE (REFLECTION BETWEEN INLET HONEYCOMB AND TURBINE MODEL NOSEPIECE) — FUNDAMENTAL FREQUENCY	7 1/2
D	81.2	ACOUSTIC STANDING WAVE — FIRST HARMONIC OF C	< 1/2
E	118	ACOUSTIC STANDING WAVE — FUNDAMENTAL FREQUENCY OF THE CROSS-DUCT MODE OF C (OR POSSIBLY THE SECOND HARMONIC OF C)	< 1/10
F	190.7	TURBINE MODEL ROTOR PASSING FREQUENCY	18
G	328	MAIN BLOWER BLADE PASSING FREQUENCY	< 1/10
H	381.4	FIRST HARMONIC OF F	1/2
I	424	STROUHAL SHEDDING FROM DOWNSTREAM SPARS	< 1/10

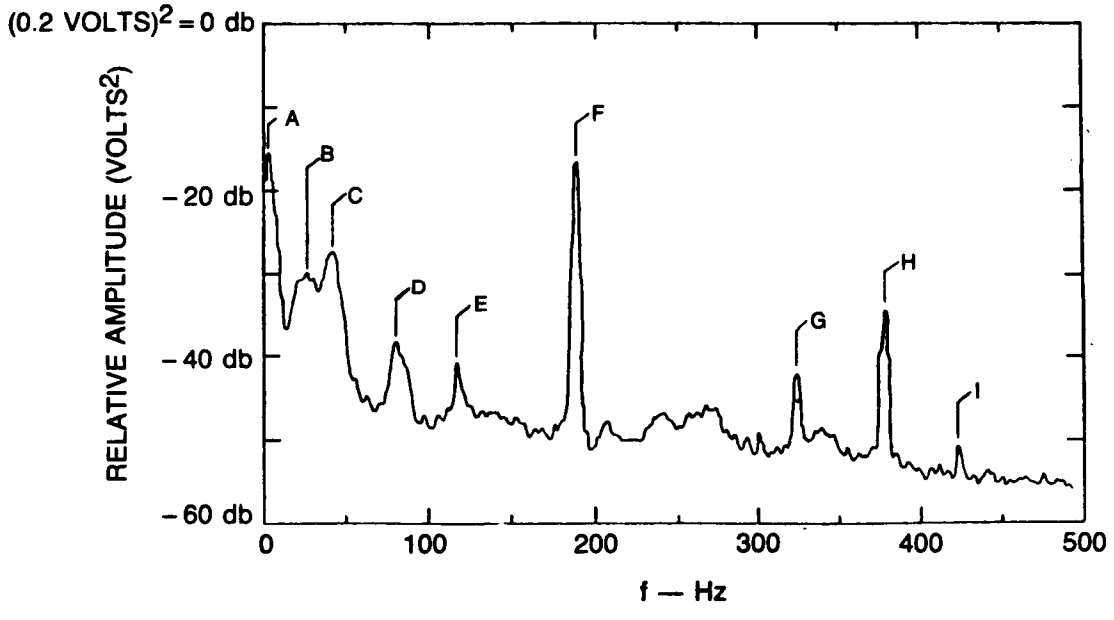

FIG. 21 SPECTRAL DISTRIBUTION OF THE UNFILTERED HOT-FILM SIGNAL UPSTREAM OF THE FIRST STATOR LEADING EDGE FOR THE MINIMUM TURBULENCE (NO GRID) CONFIGURATION

86—6—84 - 2

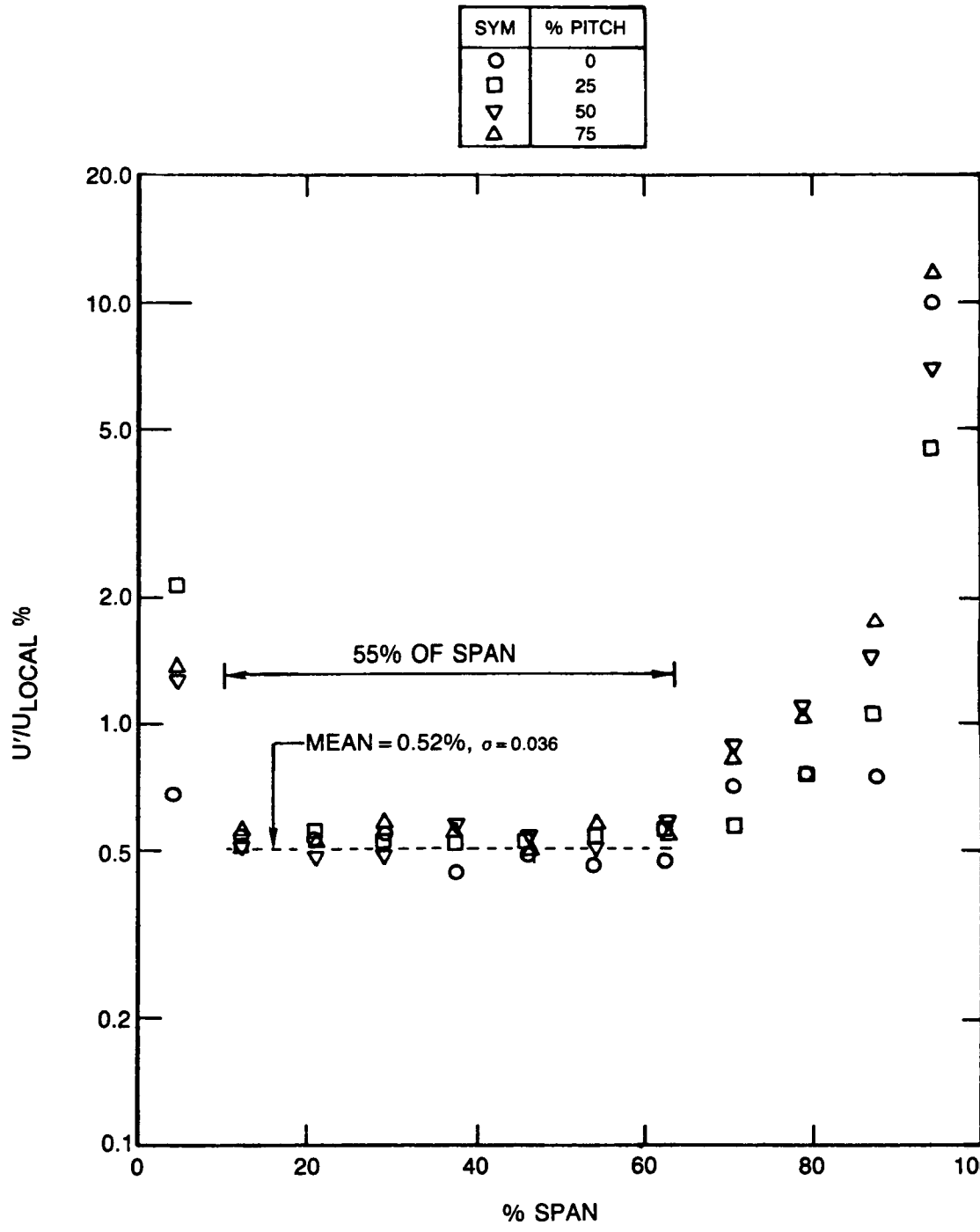

FIG. 22 RMS LEVEL OF THE STREAMWISE COMPONENT OF TURBULENCE AT X=-1.35 IN. AT VARIOUS PITCH LOCATIONS FOR THE MINIMUM TURBULENCE (NO GRID) CONFIGURAITON

86—6—84—1

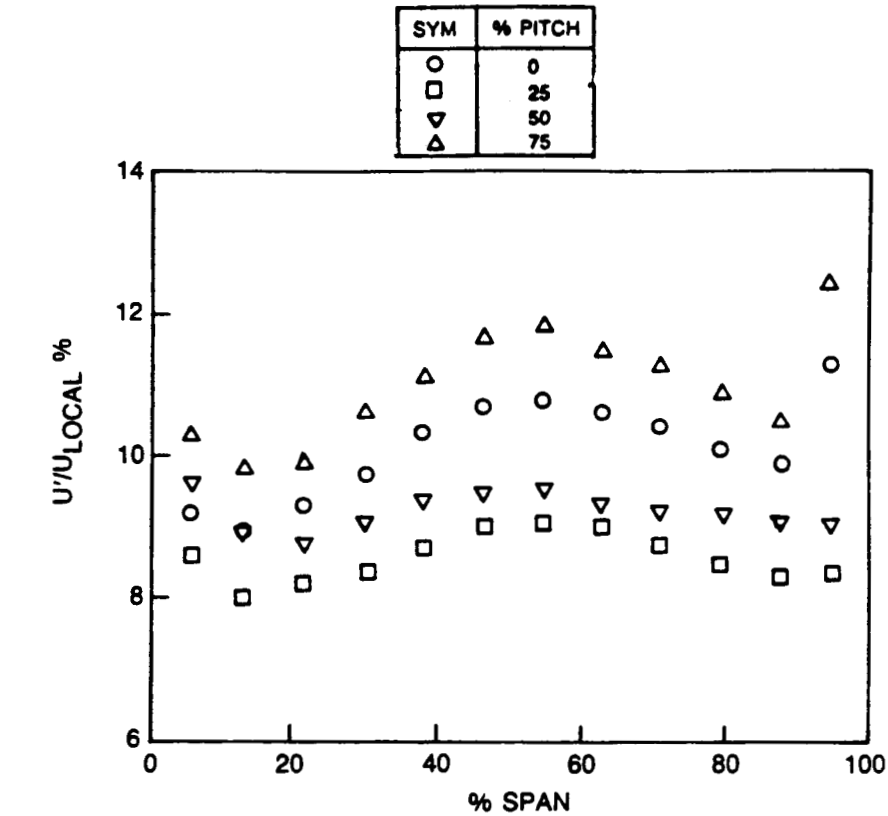

a) X TURBULENCE BASED ON LOCAL VELOCITY

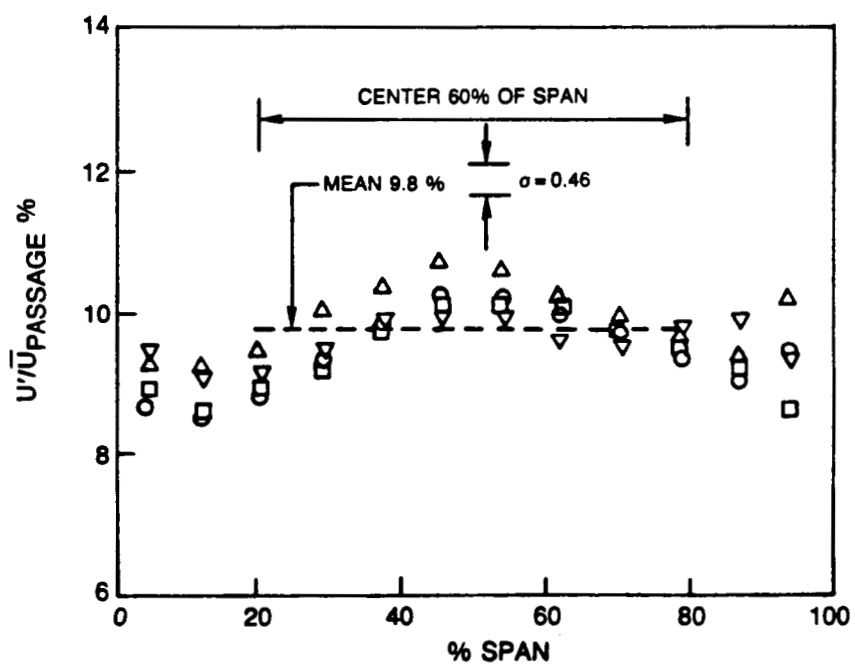

b) X TURBULENCE BASED ON MEAN PASSAGE VELOCITY

FIG. 23 RMS LEVEL OF THE STREAMWISE COMPONENT OF TURBULENCE AT X=-1.35 IN. (6.5 MESH LENGTHS FROM THE GRID) AT VARIOUS PITCH LOCATIONS

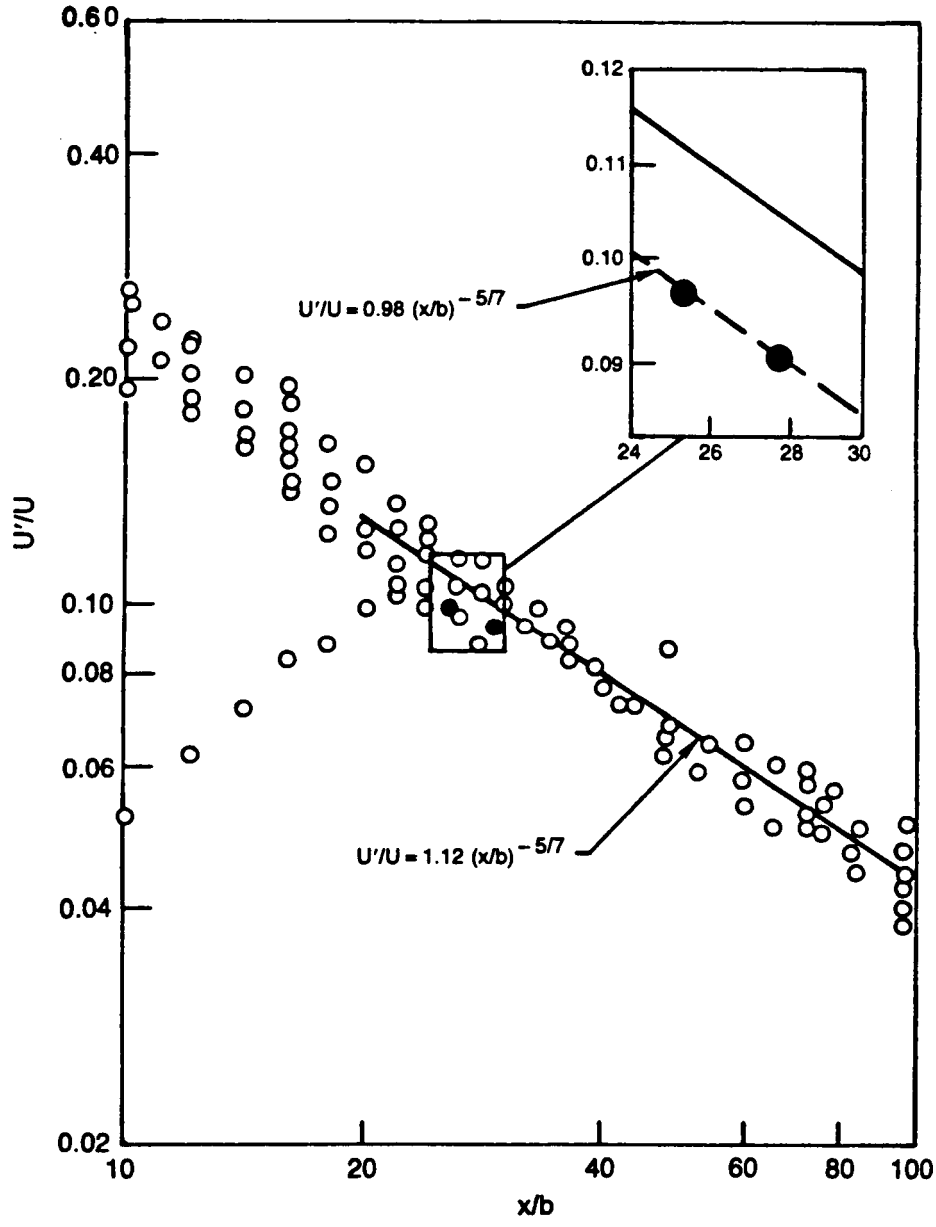

FIG. 24 COMPARISON OF THE MIDSPAN TURBULENCE INTENSITY AND DECAY WITH THE BIPLANE GRID DATA OF BAINES AND PETERSON

86-5-18-4

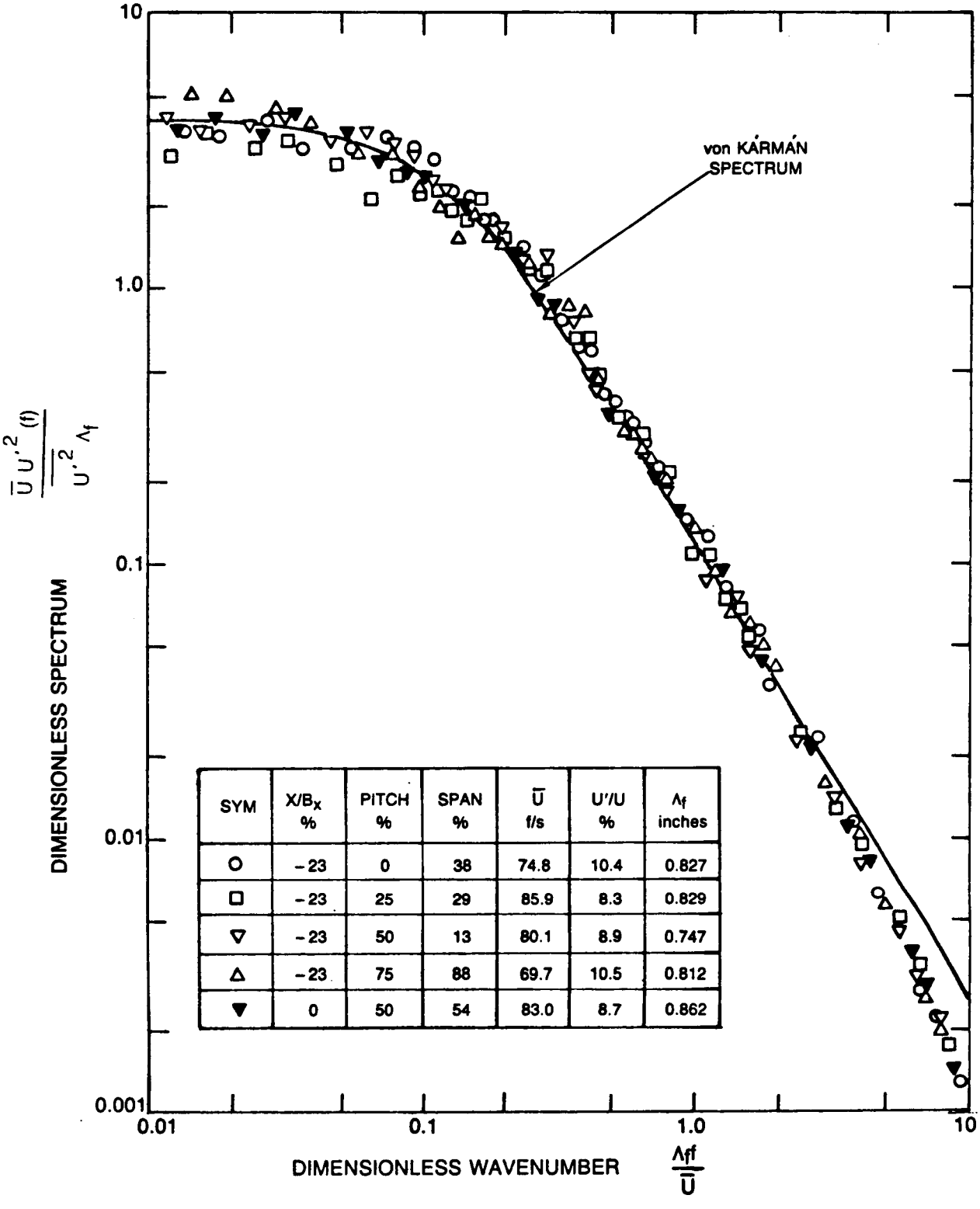

FIG. 25 POWER SPECTRAL DENSITY DISTRIBUTIONS MEASURED AT VARIOUS PITCH, SPAN AND AXIAL LOCATIONS WITH THE TURBULENCE GRID IN

86—6—84—3

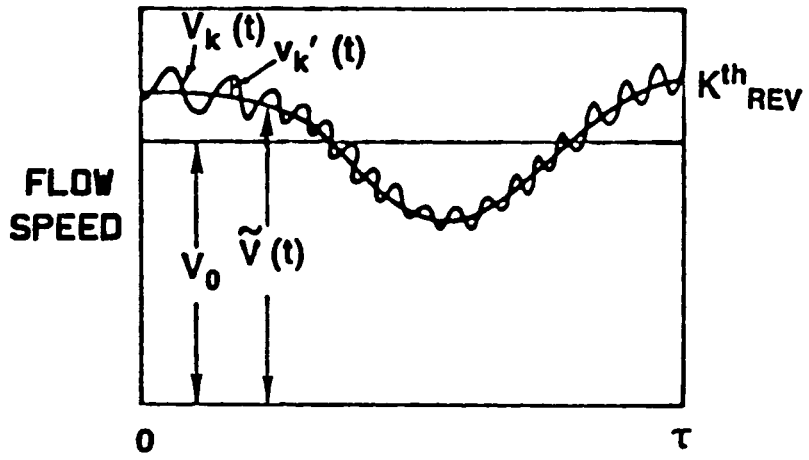

$$\overline{U}_T \cong \frac{1}{N_{REV}} \sum_{K=1}^{N_{REV}} \frac{1}{\tau} \int_0^{\tau} (V_k(t)-V_0)^2 \, dt \Big/ V_{REF}^2$$

$$\overline{U}_T = \frac{1}{\tau} \int_0^{\tau} (\tilde{V}(t)-V_0)^2 dt \Big/ V_{REF}^2 + \frac{1}{N_{REV}} \sum_{K=1}^{N_{REV}} \frac{1}{\tau} \int_0^{\tau} v_k'^2 \, dt \Big/ V_{REF}^2$$

$$\overline{U}_T = \overline{U}_P + \overline{U}_R$$

FIG. 26 DEFINITION OF AVERAGE TOTAL, PERIODIC AND RANDOM UNSTEADINESS

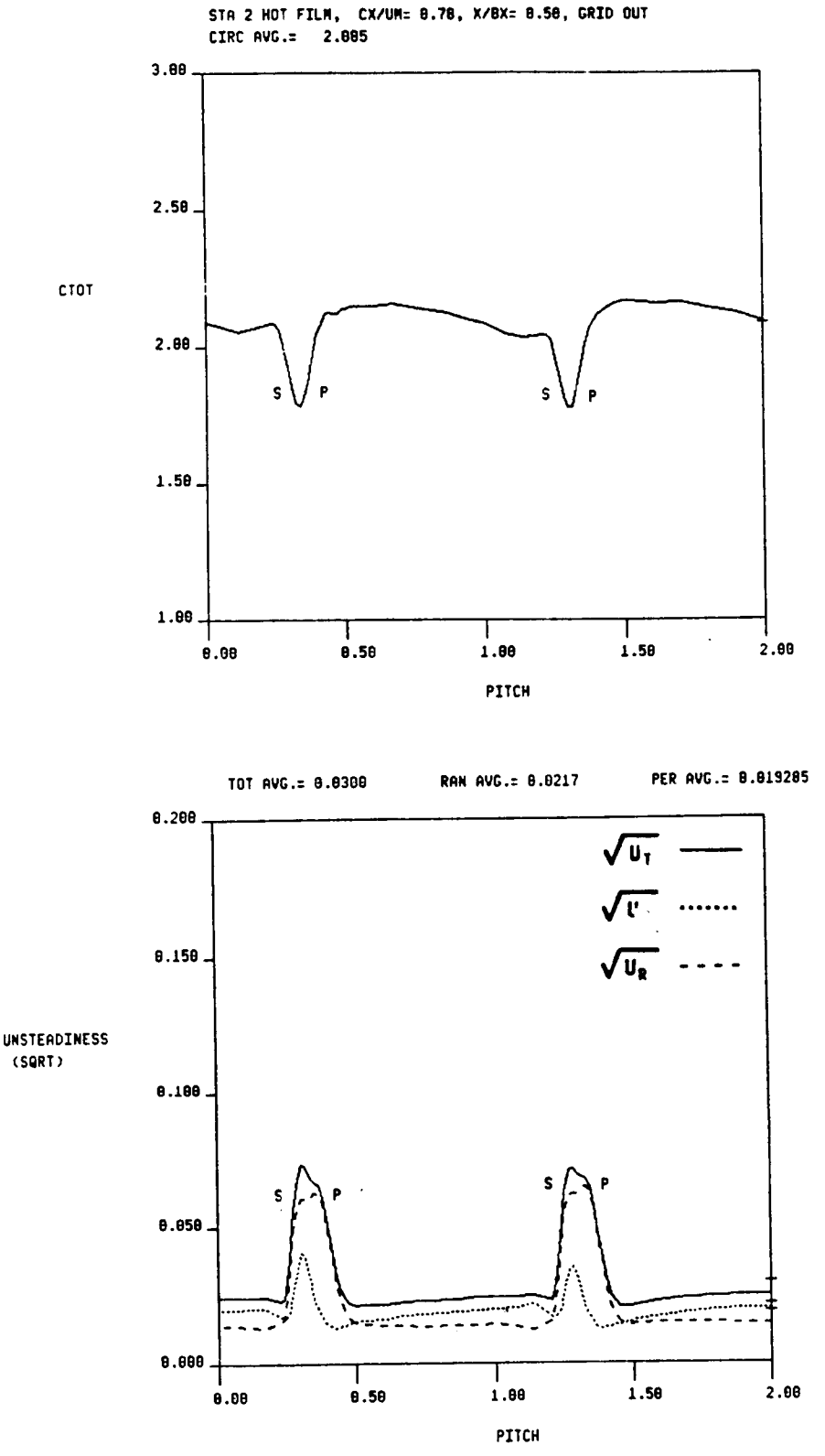

FIG. 27a CIRCUMFERENTIAL DISTRIBUTION OF TIME AVERAGED SPEED AND UNSTEADINESS AT 1ST STATOR EXIT, GRID-OUT

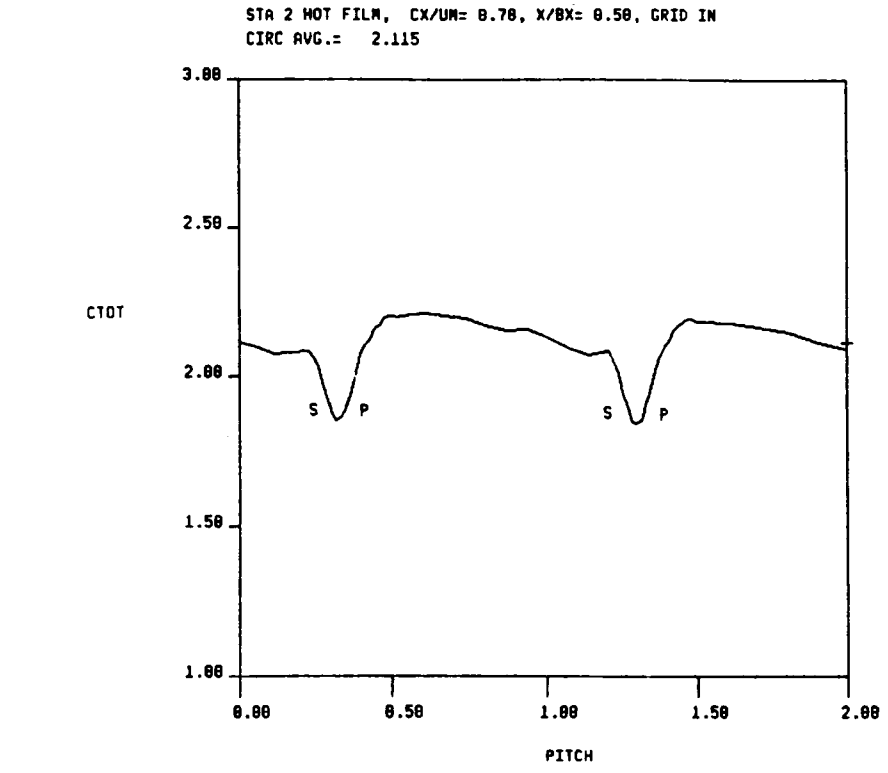

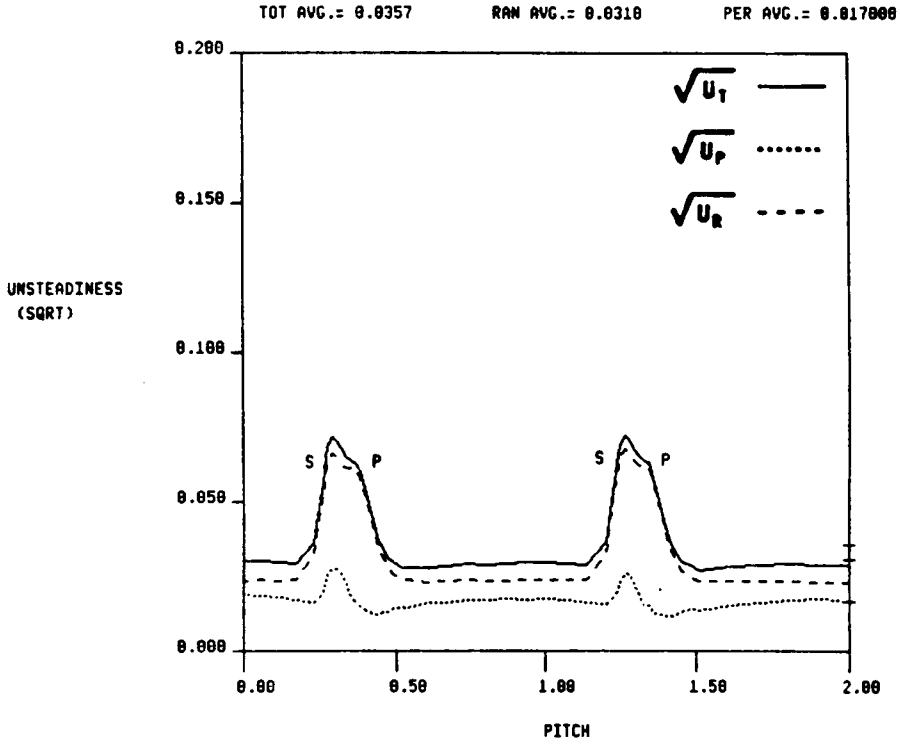

FIG. 27b CIRCUMFERENTIAL DISTRIBUTION OF TIME AVERAGED SPEED AND UNSTEADINESS AT 1ST STATOR EXIT, GRID-IN

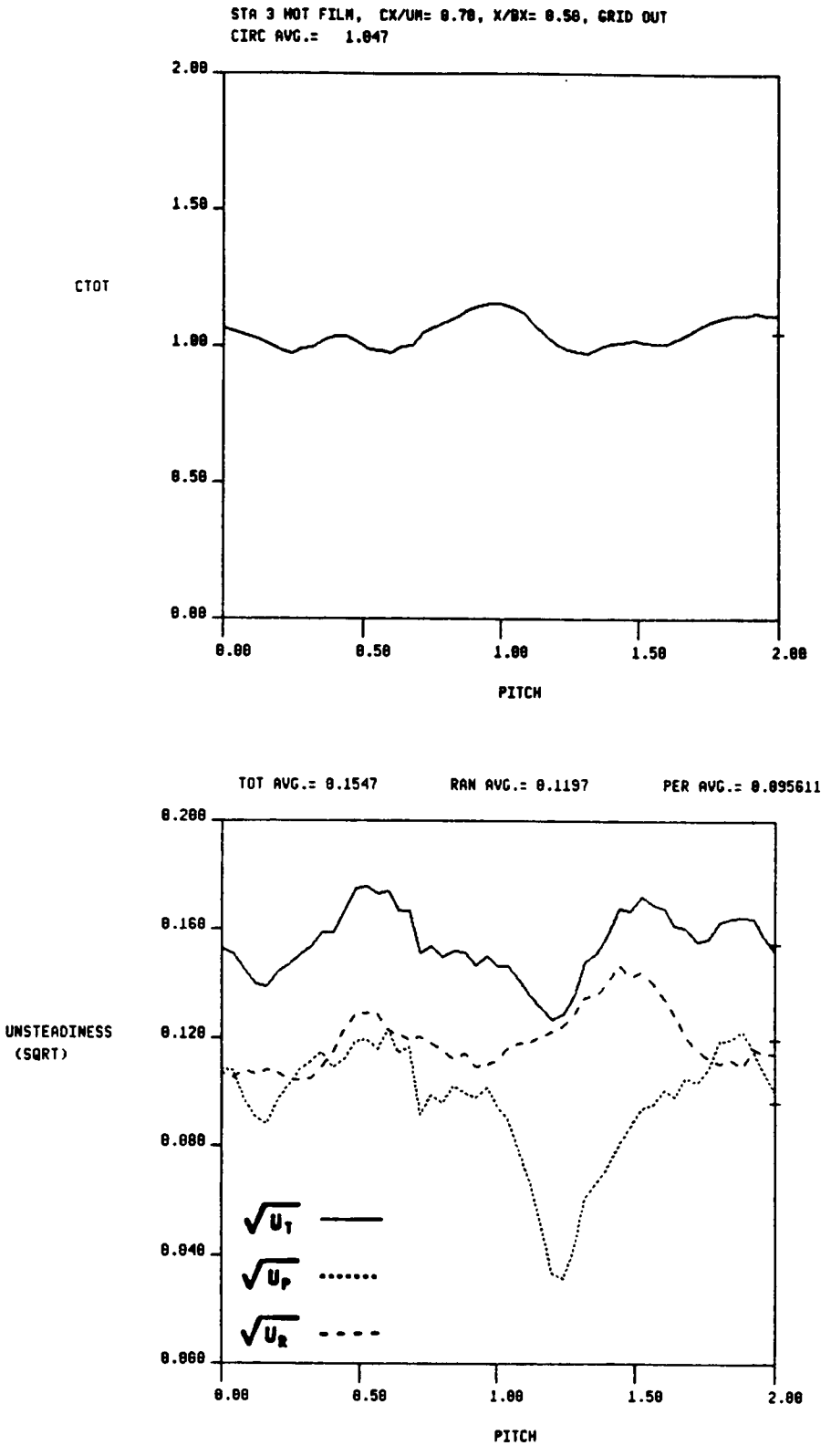

FIG. 28a CIRCUMFERENTIAL DISTRIBUTION OF TIME AVERAGED SPEED AND UNSTEADINESS AT ROTOR EXIT, GRID-OUT

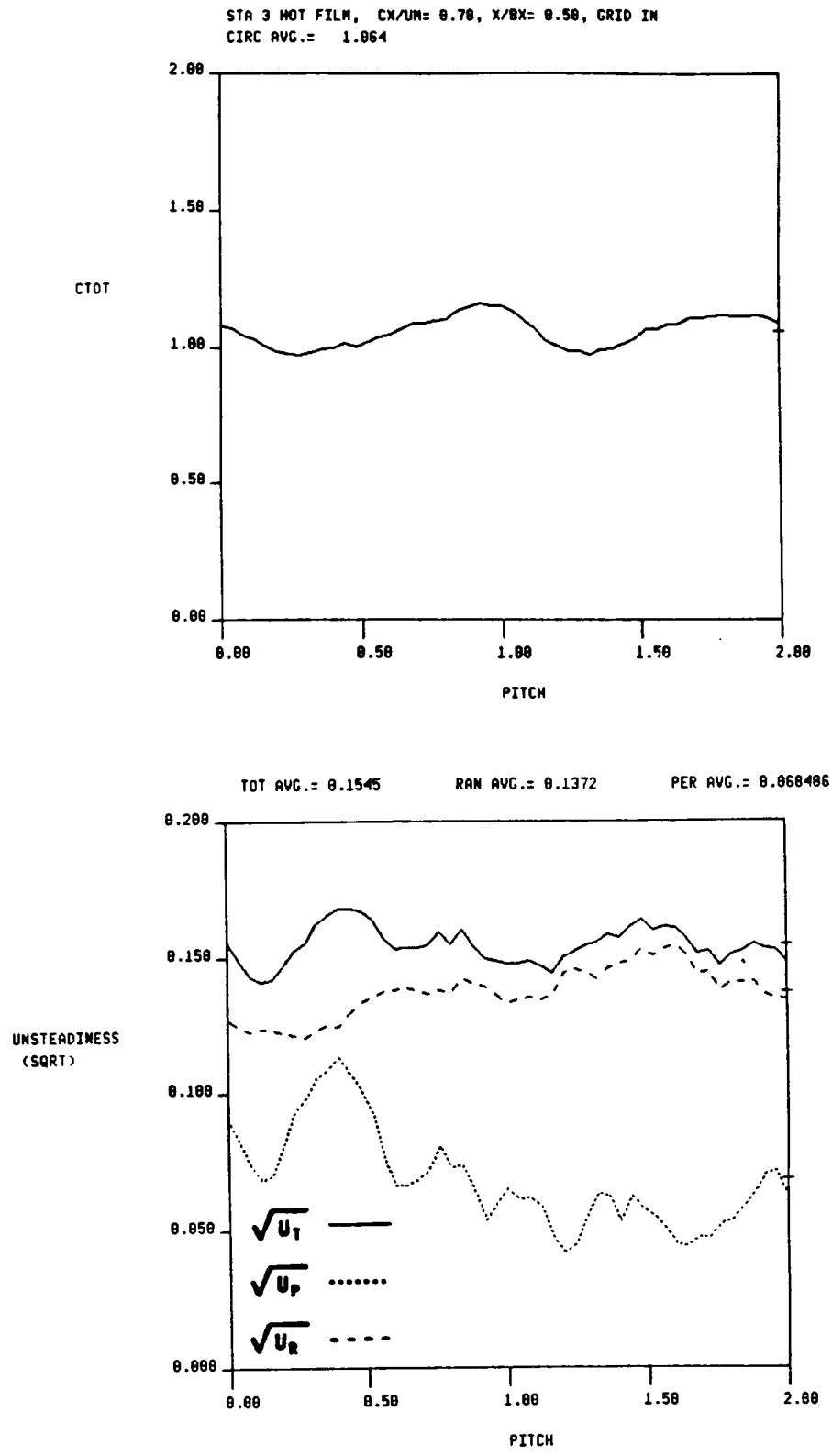

FIG. 28b CIRCUMFERENTIAL DISTRIBUTION OF TIME AVERAGED SPEED AND UNSTEADINESS AT ROTOR EXIT, GRID-IN

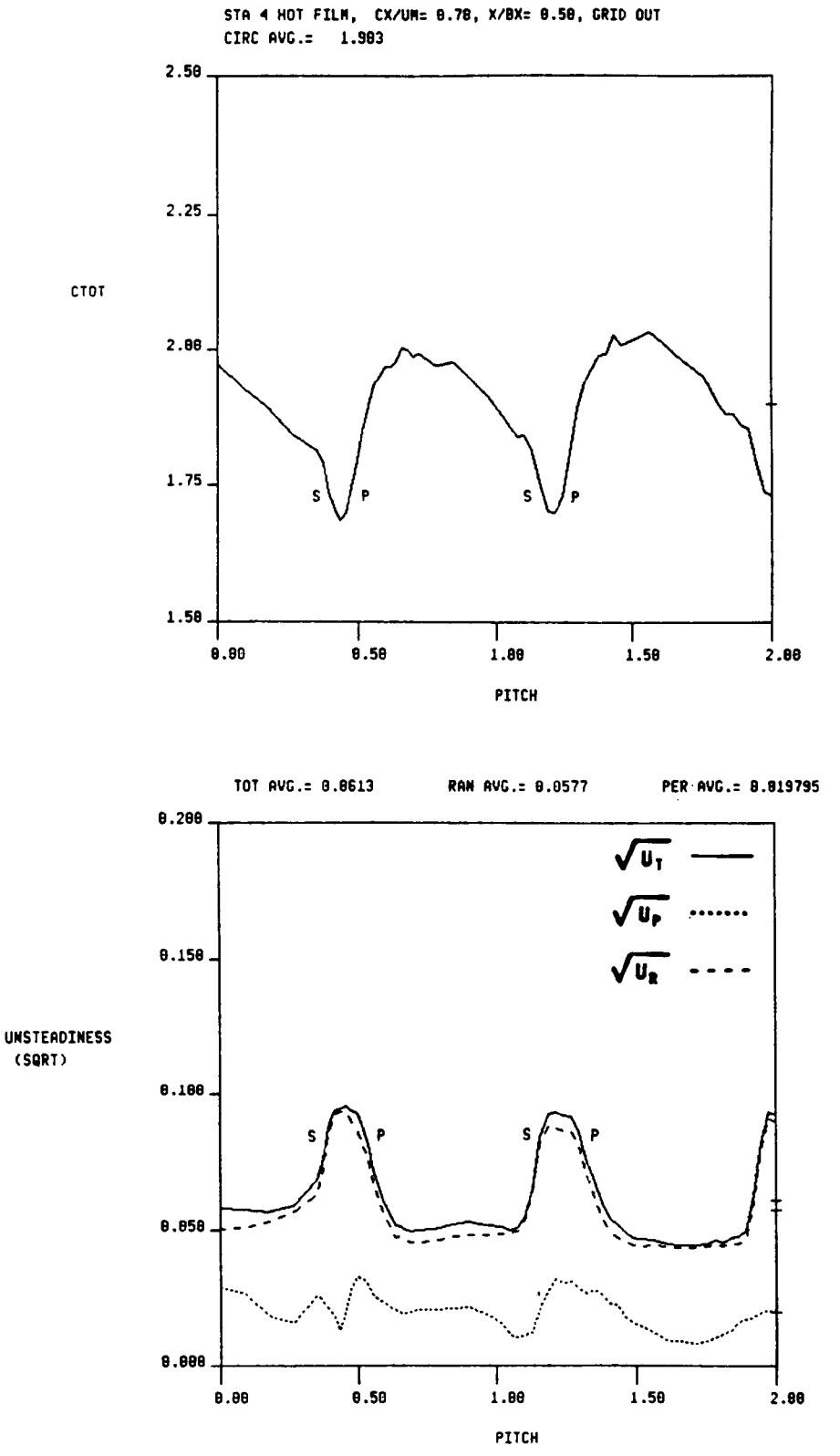

FIG. 29a CIRCUMFERENTIAL DISTRIBUTION OF TIME AVERAGED SPEED AND UNSTEADINESS AT 2ND STATOR EXIT, GRID-OUT

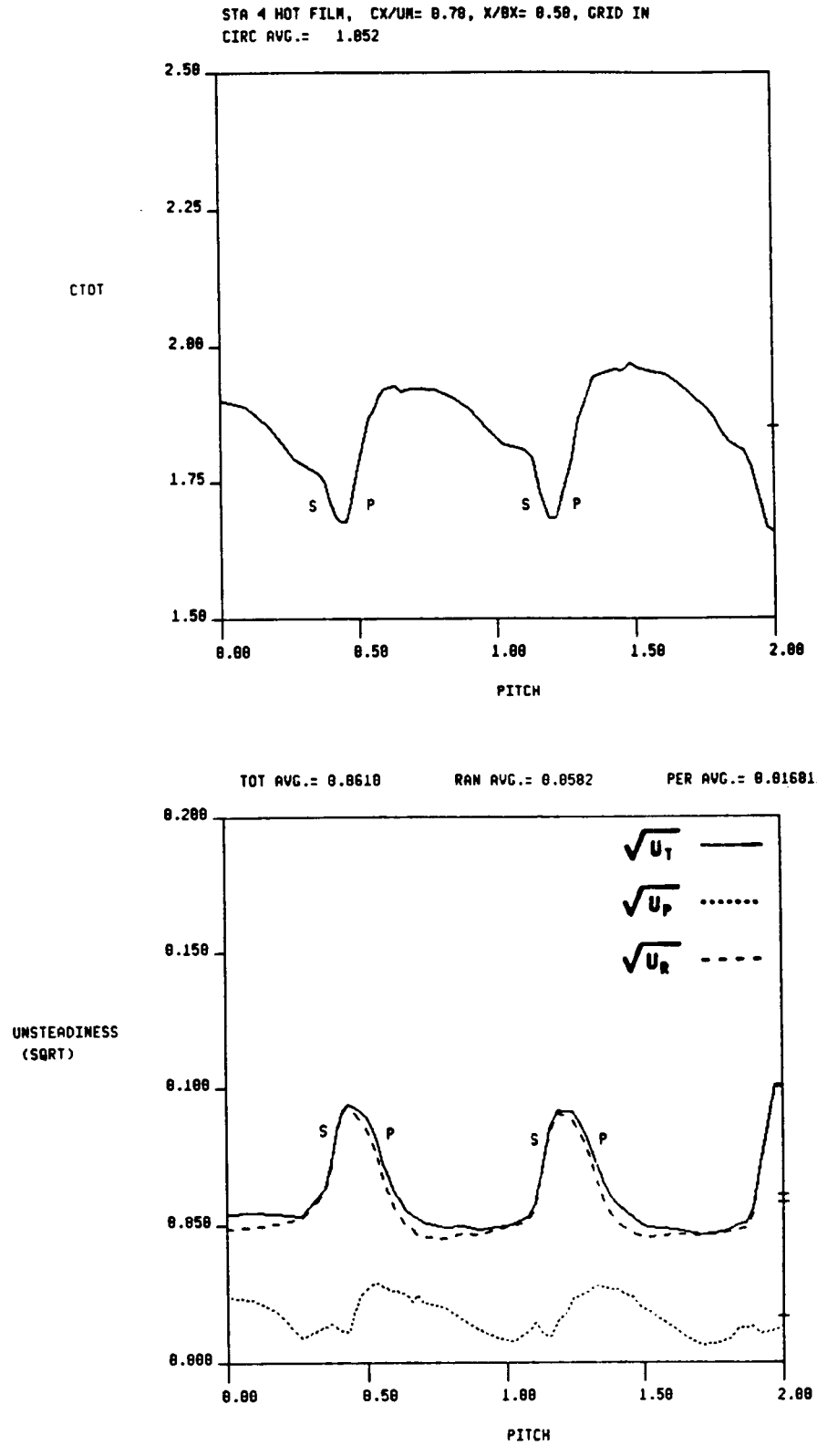

FIG. 29b CIRCUMFERENTIAL DISTRIBUTION OF TIME AVERAGED SPEED AND UNSTEADINESS AT 2ND STATOR EXIT, GRID-IN

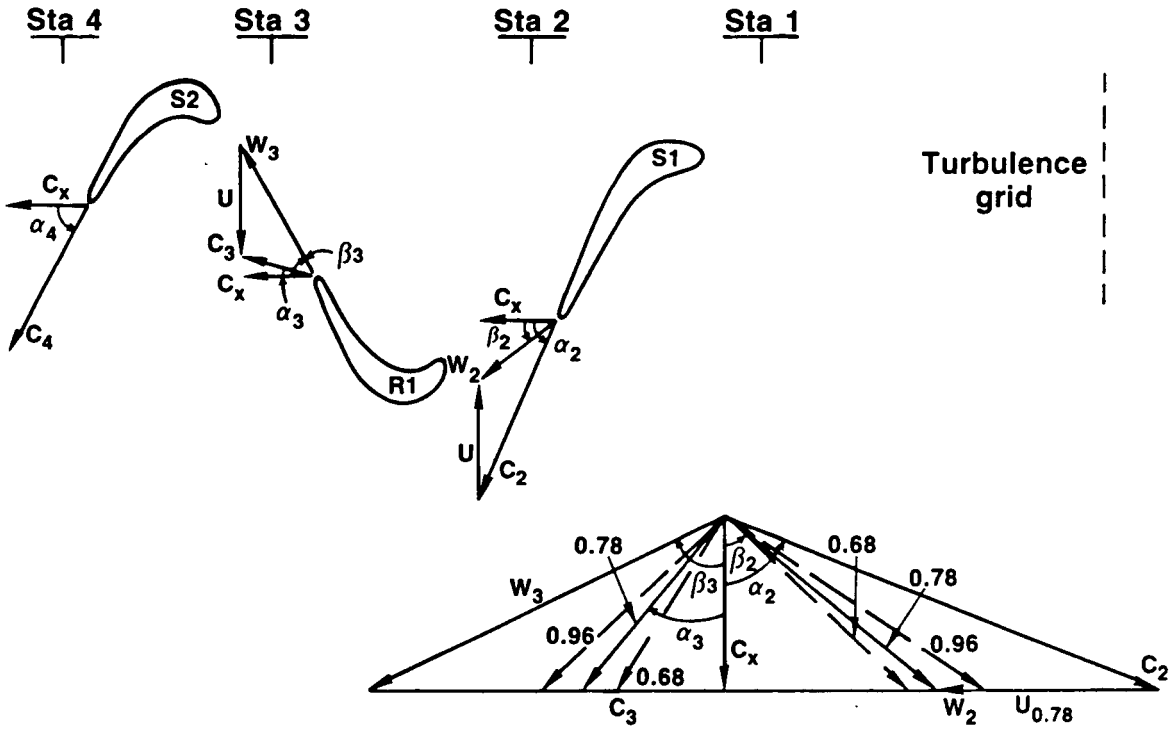

FIG. 30 LSRR TURBINE AIRFOIL MEAN SECTIONS AND VELOCITY TRIANGLES

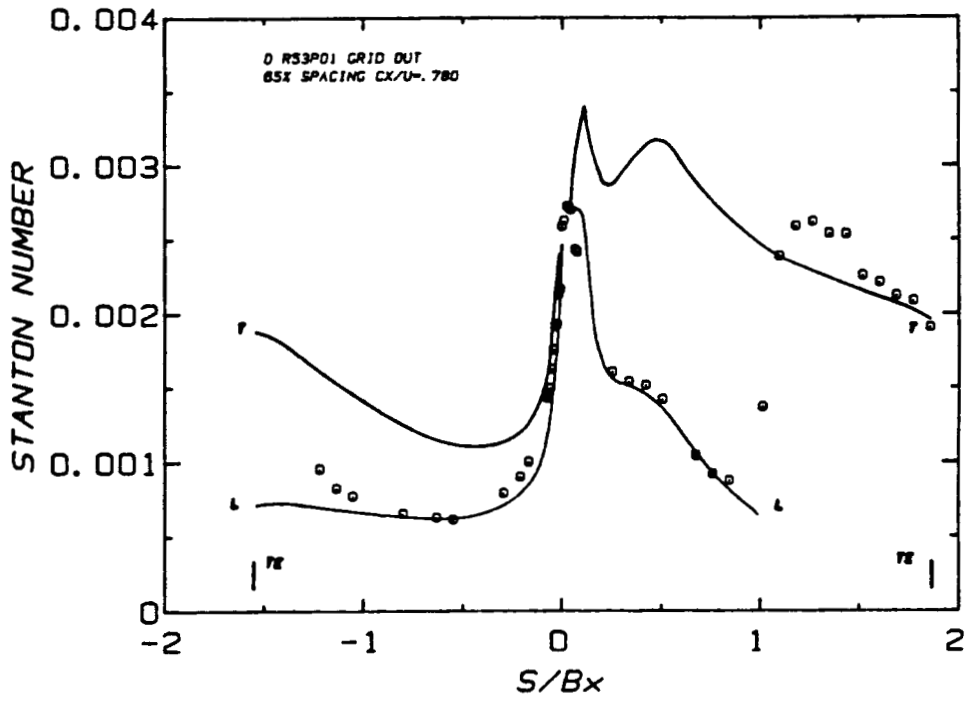

a) SINGLE-STAGE STATOR

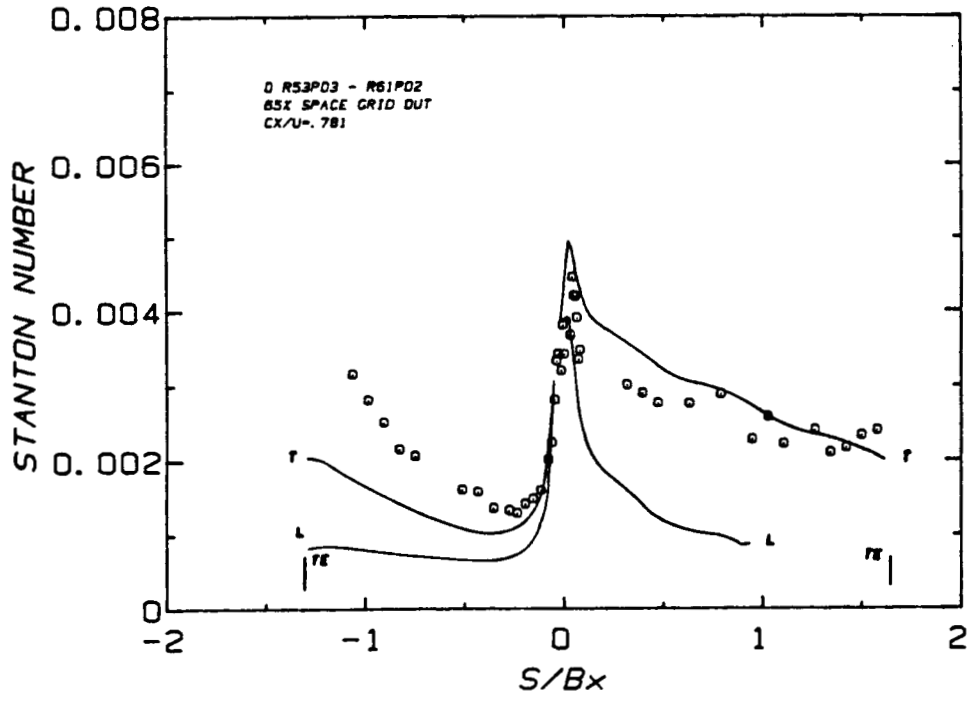

b) SINGLE-STAGE ROTOR

FIG. 31 Measured and Predicted Heat Transfer Distributions for the Single-Stage Configuration, Design Flow Coefficient, 65% Axial Spacing and Grid Out

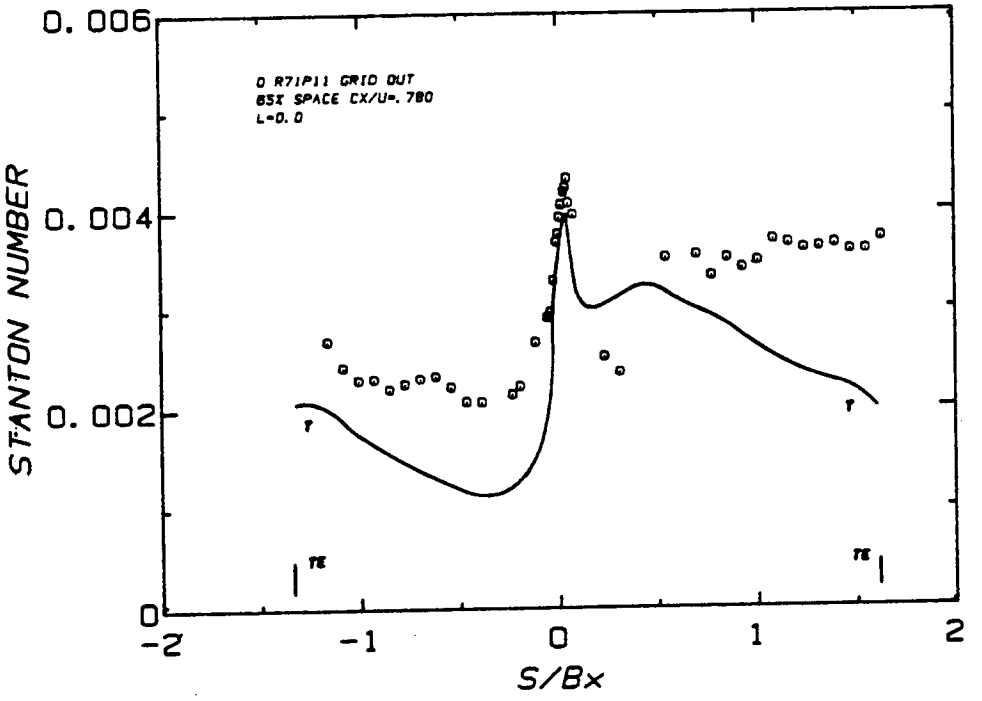

FIG. 32 **Measured and Predicted Heat Transfer Distributions for the Second Stator in the 1 1/2 Stage Configuration, Design Flow Coefficient and Grid Out**

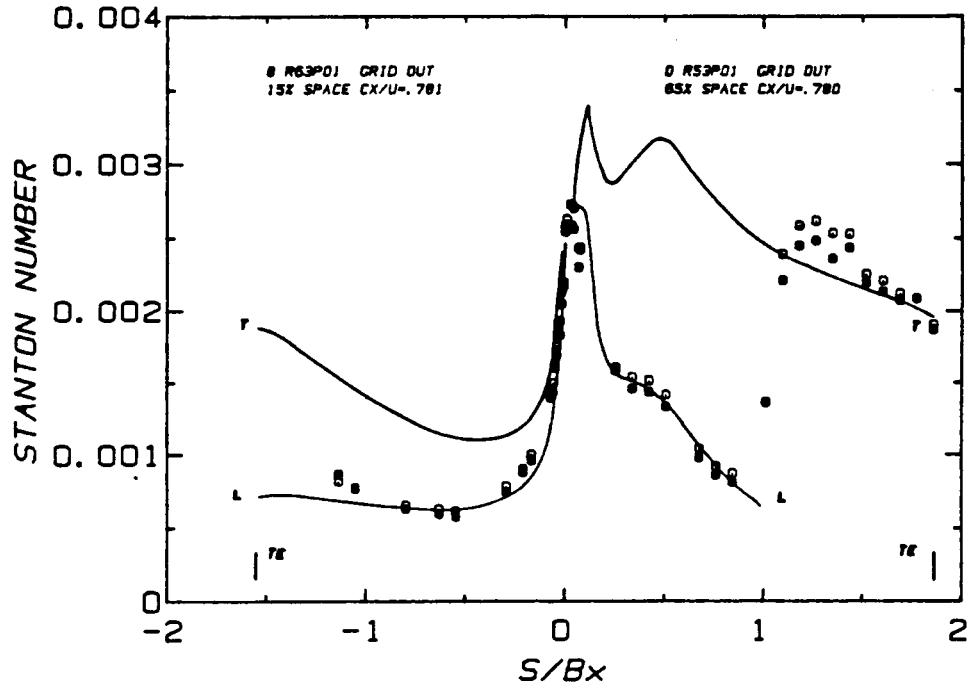

a) SINGLE-STAGE STATOR

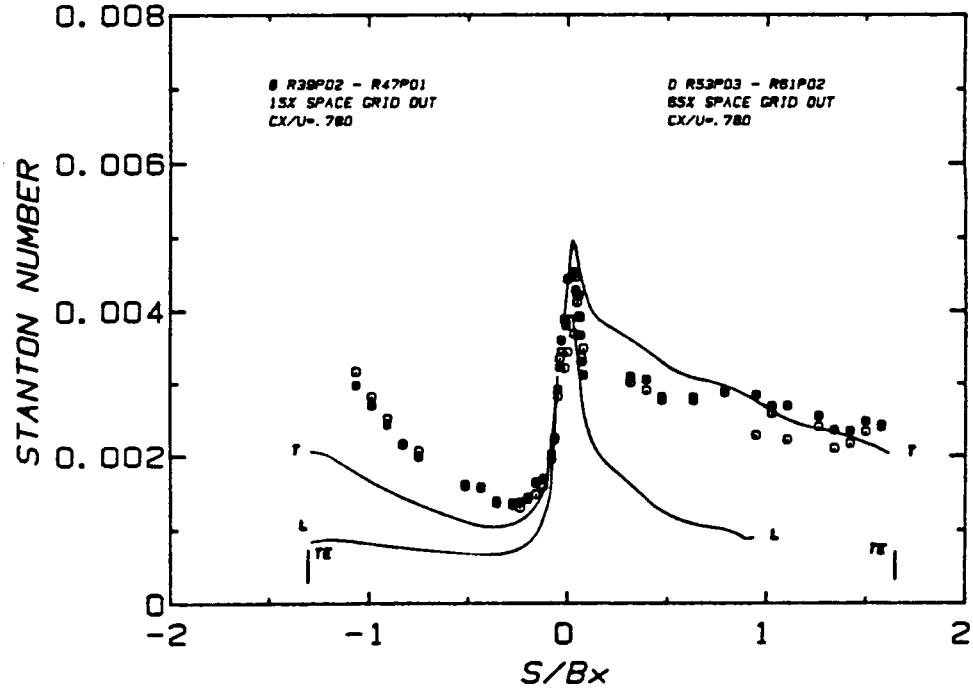

b) SINGLE-STAGE ROTOR

FIG. 33 EFFECT OF AXIAL SPACING ON THE STATOR AND ROTOR HEAT TRANSFER DISTRIBUTIONS FOR THE SINGLE-STAGE CONFIGURATION, DESIGN FLOW COEFFICIENT AND GRID OUT

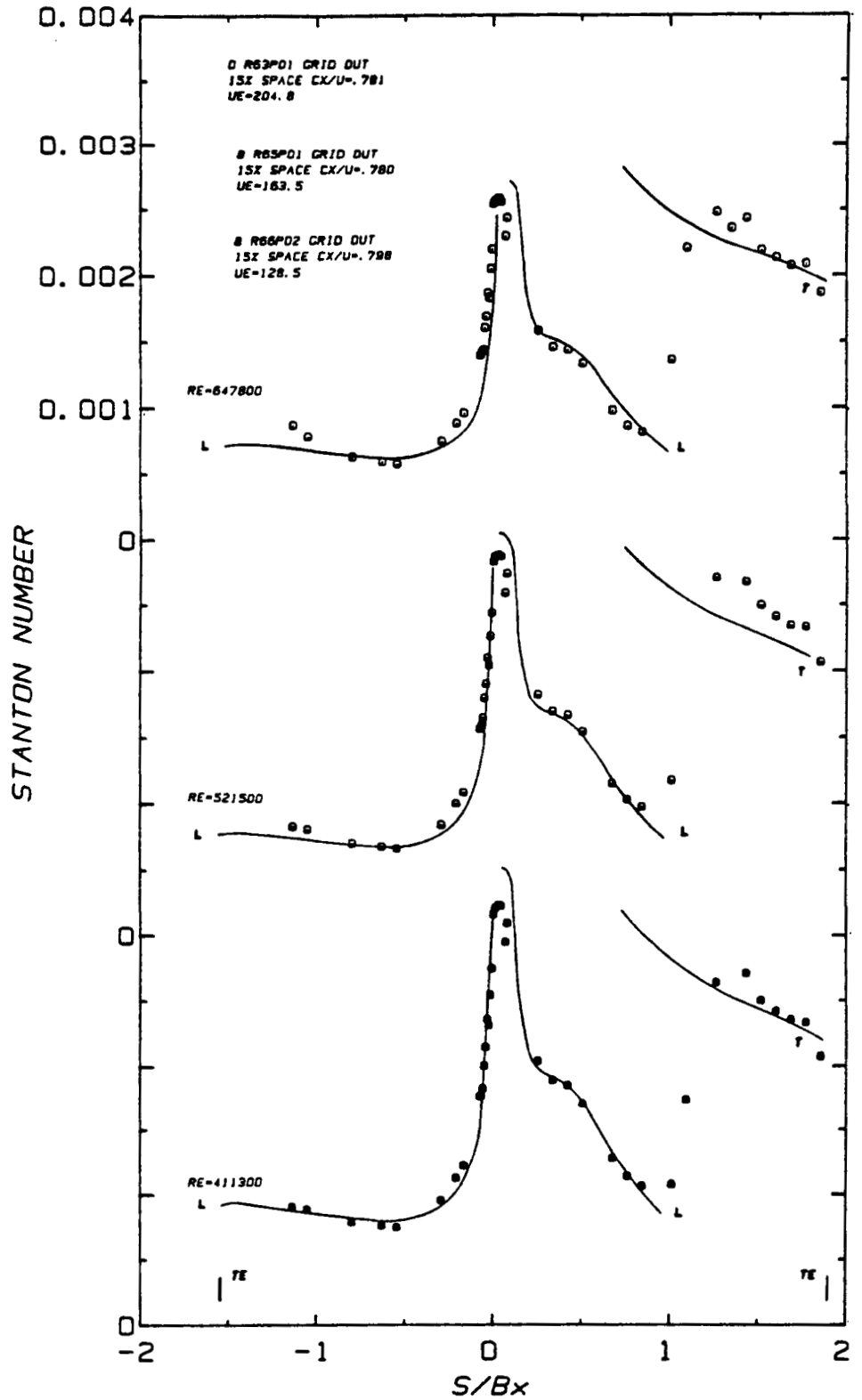

FIG. 34 EFFECT OF REYNOLDS NUMBER ON THE SINGLE-STAGE STATOR HEAT TRANSFER DISTRIBUTION, DESIGN FLOW COEFFICIENT, 15% AXIAL SPACING AND GRID OUT

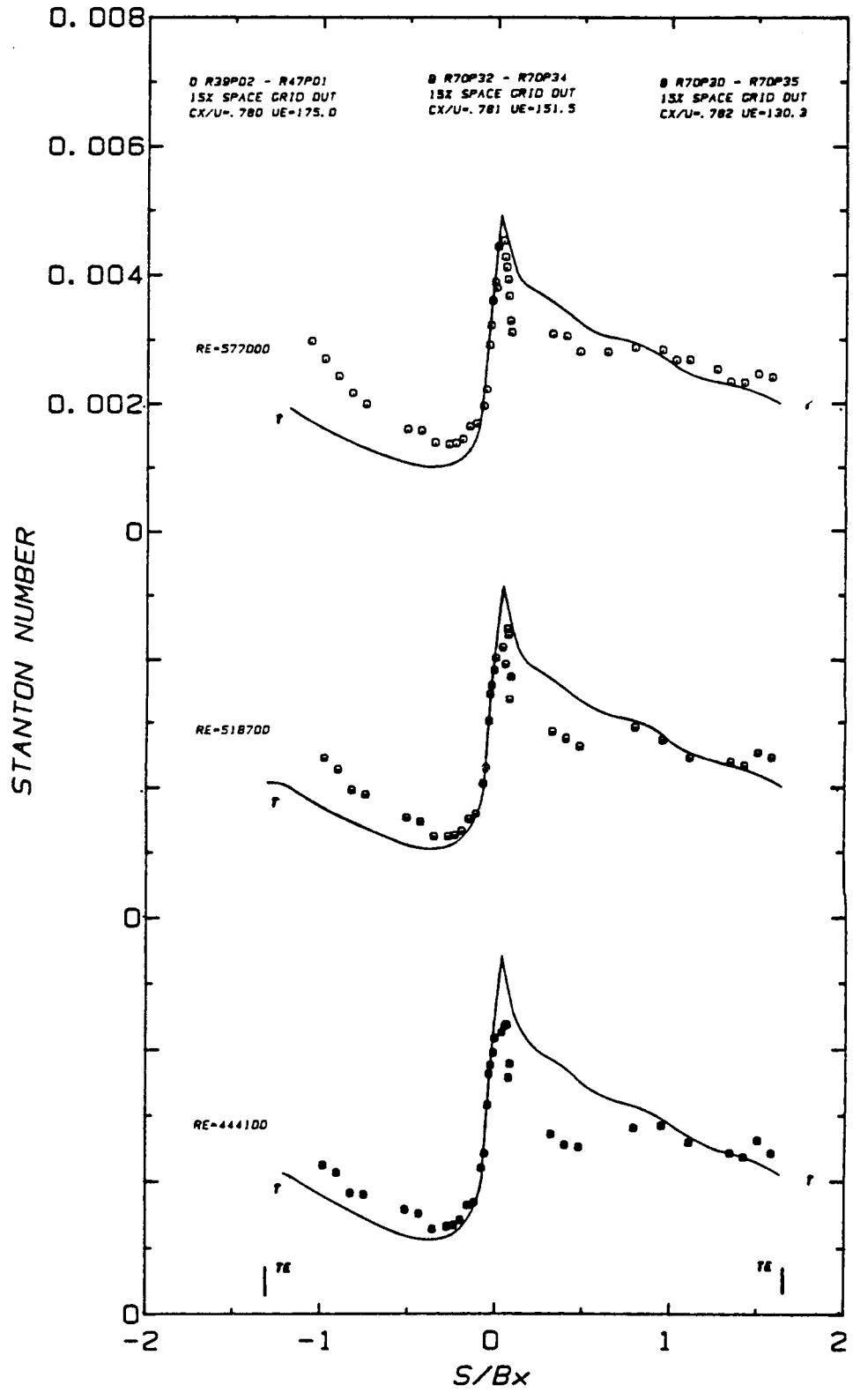

FIG. 35a EFFECT OF REYNOLDS NUMBER ON THE SINGLE-STAGE ROTOR HEAT TRANSFER DISTRIBUTION, DESIGN FLOW COEFFICIENT, 15% AXIAL SPACING AND GRID OUT

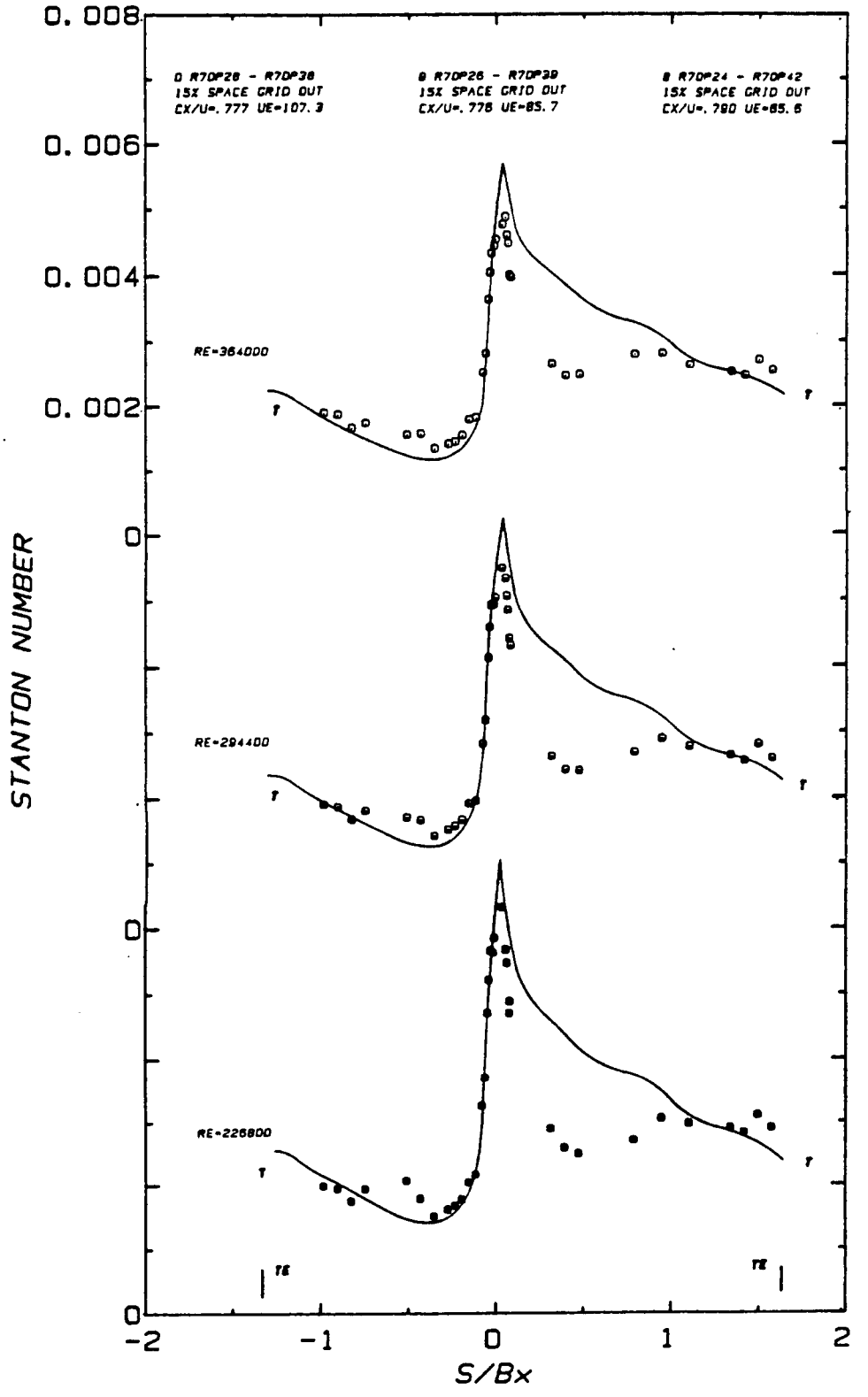

FIG. 35b EFFECT OF REYNOLDS NUMBER ON THE SINGLE-STAGE ROTOR HEAT TRANSFER DISTRIBUTION, DESIGN FLOW COEFFICIENT, 15% AXIAL SPACING AND GRID OUT

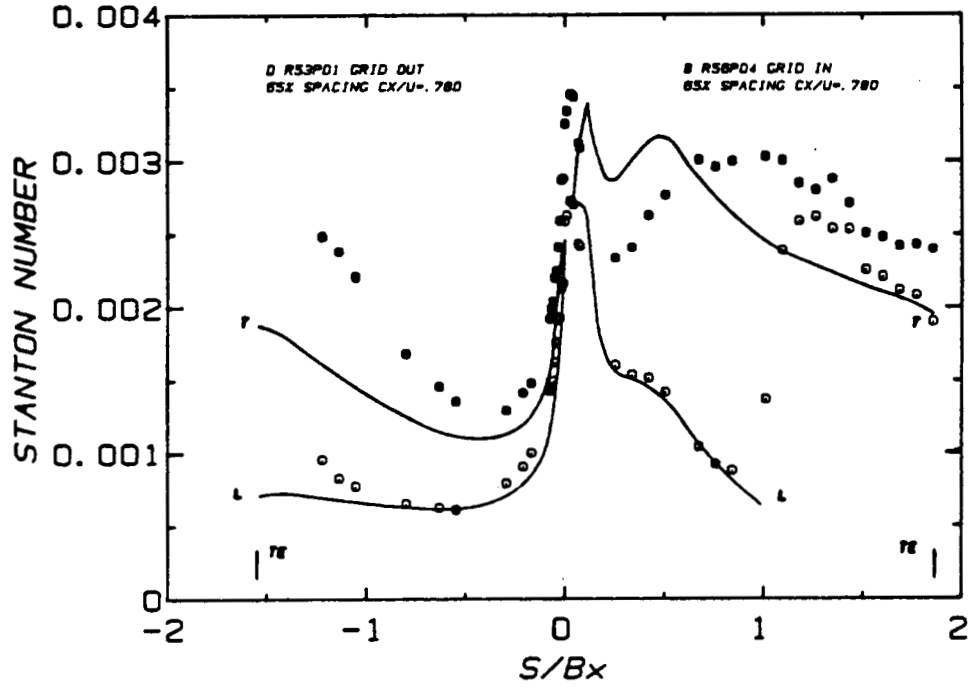

a) SINGLE-STAGE STATOR

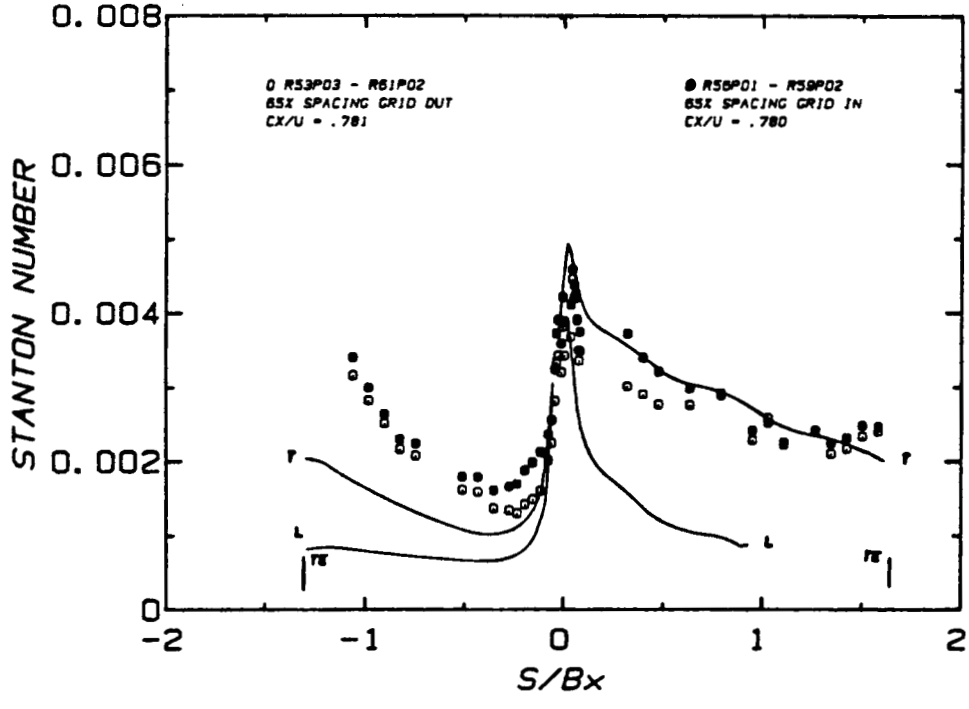

b) SINGLE-STAGE ROTOR

FIG. 36 EFFECT OF FREE-STREAM TURBULENCE ON THE STATOR AND ROTOR HEAT TRANSFER DISTRIBUTIONS FOR THE SINGLE-STAGE CONFIGURATION, DESIGN FLOW COEFFICIENT AND 65% AXIAL SPACING

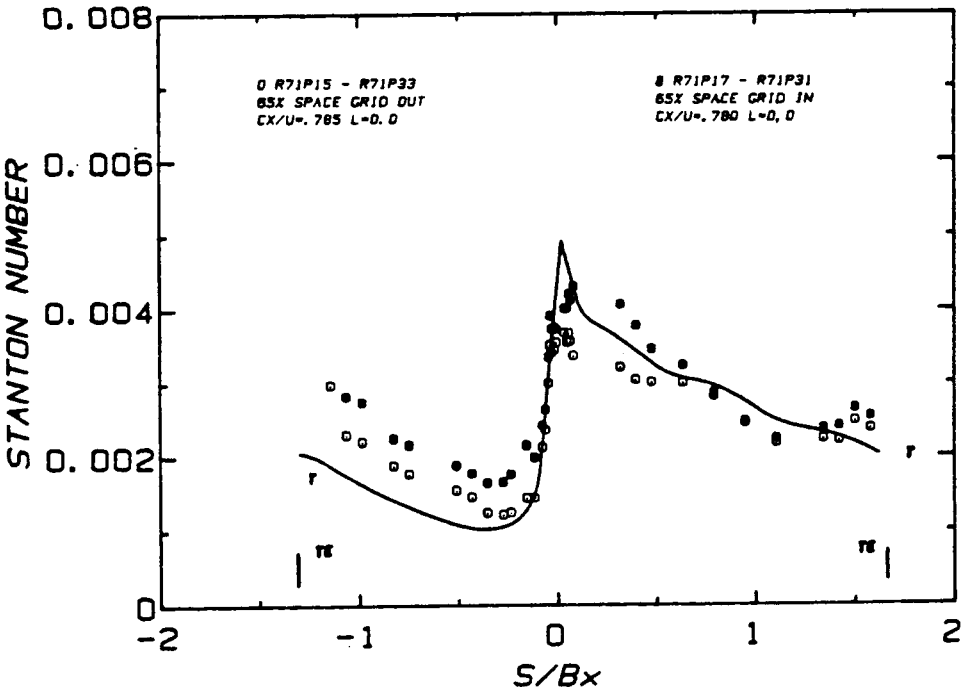

a) 1-1/2 STAGE ROTOR

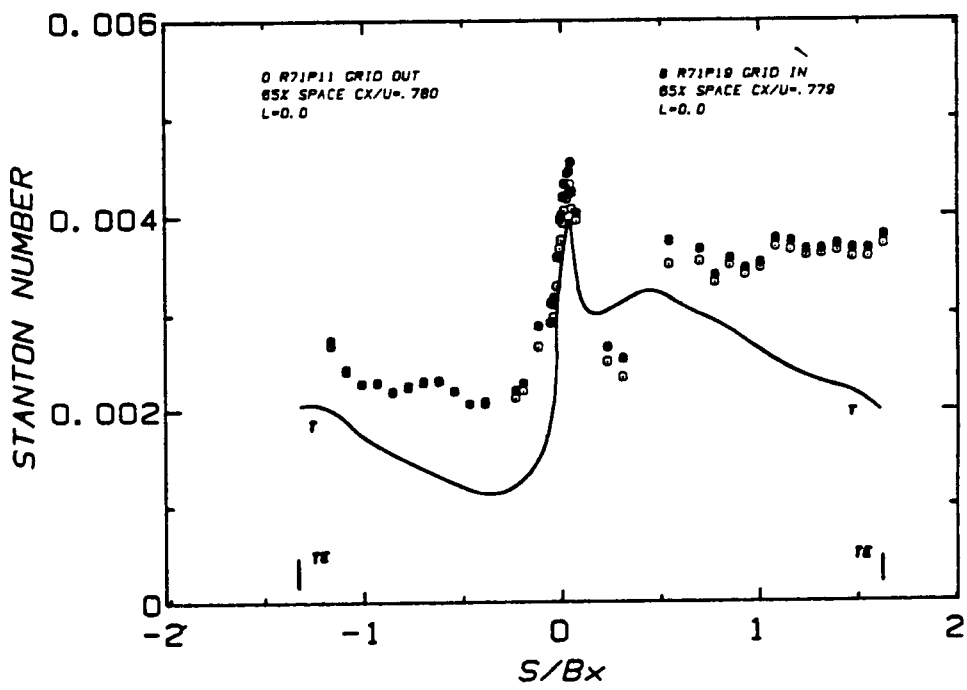

b) 1-1/2 STAGE SECOND STATOR

FIG. 37 EFFECT OF THE UPSTREAM GRID ON THE ROTOR AND SECOND STATOR HEAT TRANSFER DISTRIBUTIONS FOR THE 1-1/2 STAGE CONFIGURATION, DESIGN FLOW COEFFICIENT

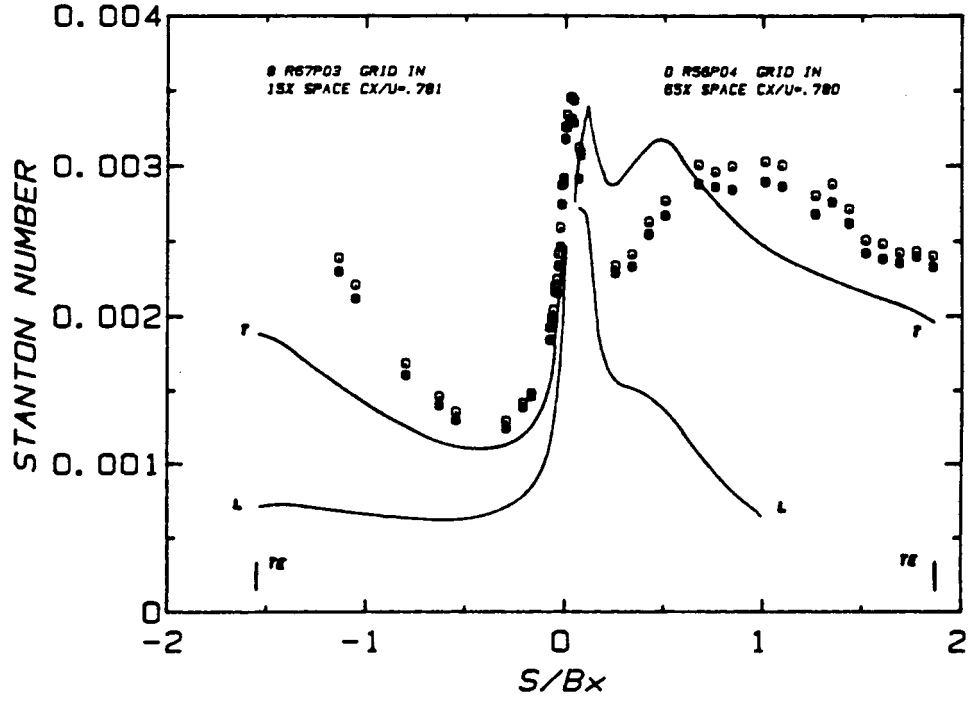

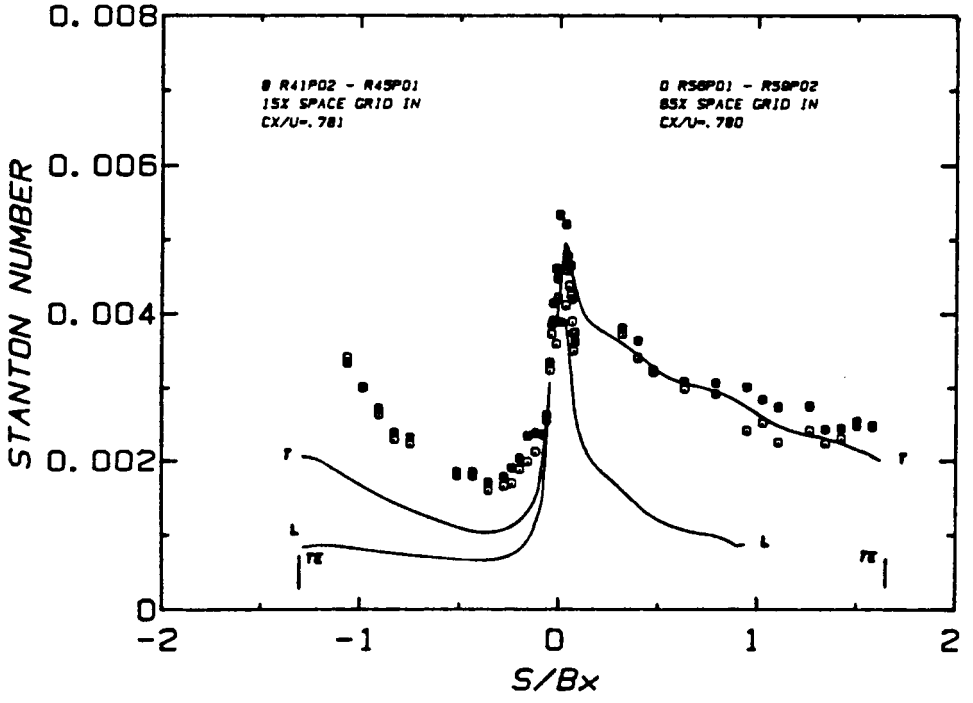

FIG. 38 EFFECT OF AXIAL SPACING ON THE STATOR AND ROTOR HEAT TRANSFER DISTRIBUTIONS FOR THE SINGLE-STAGE CONFIGURATION, DESIGN FLOW COEFFICIENT AND GRID IN

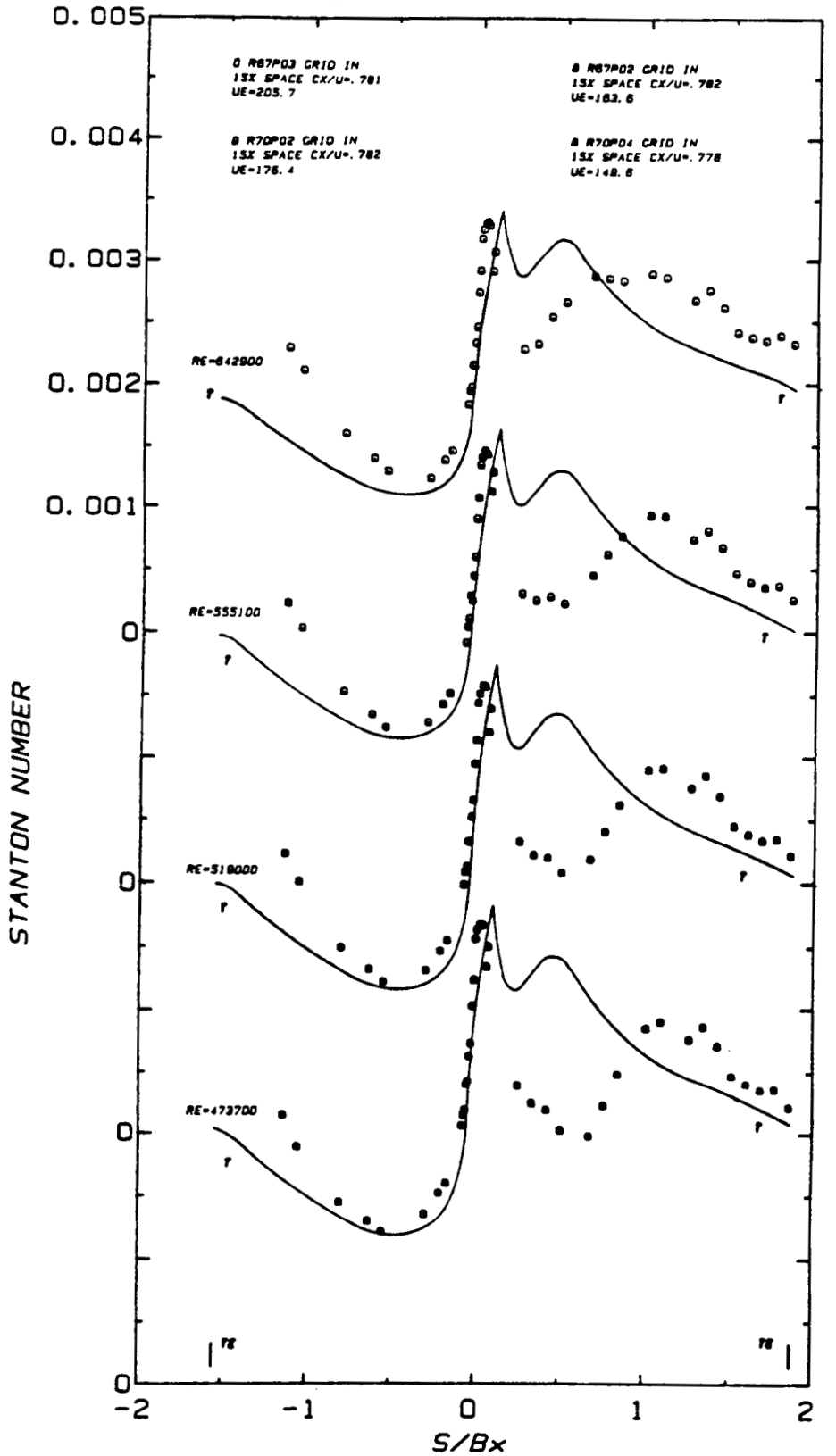

FIG. 39a EFFECT OF REYNOLDS NUMBER ON THE SINGLE-STAGE STATOR HEAT TRANSFER DISTRIBUTION, DESIGN FLOW COEFFICIENT, 15% AXIAL SPACING AND GRID IN

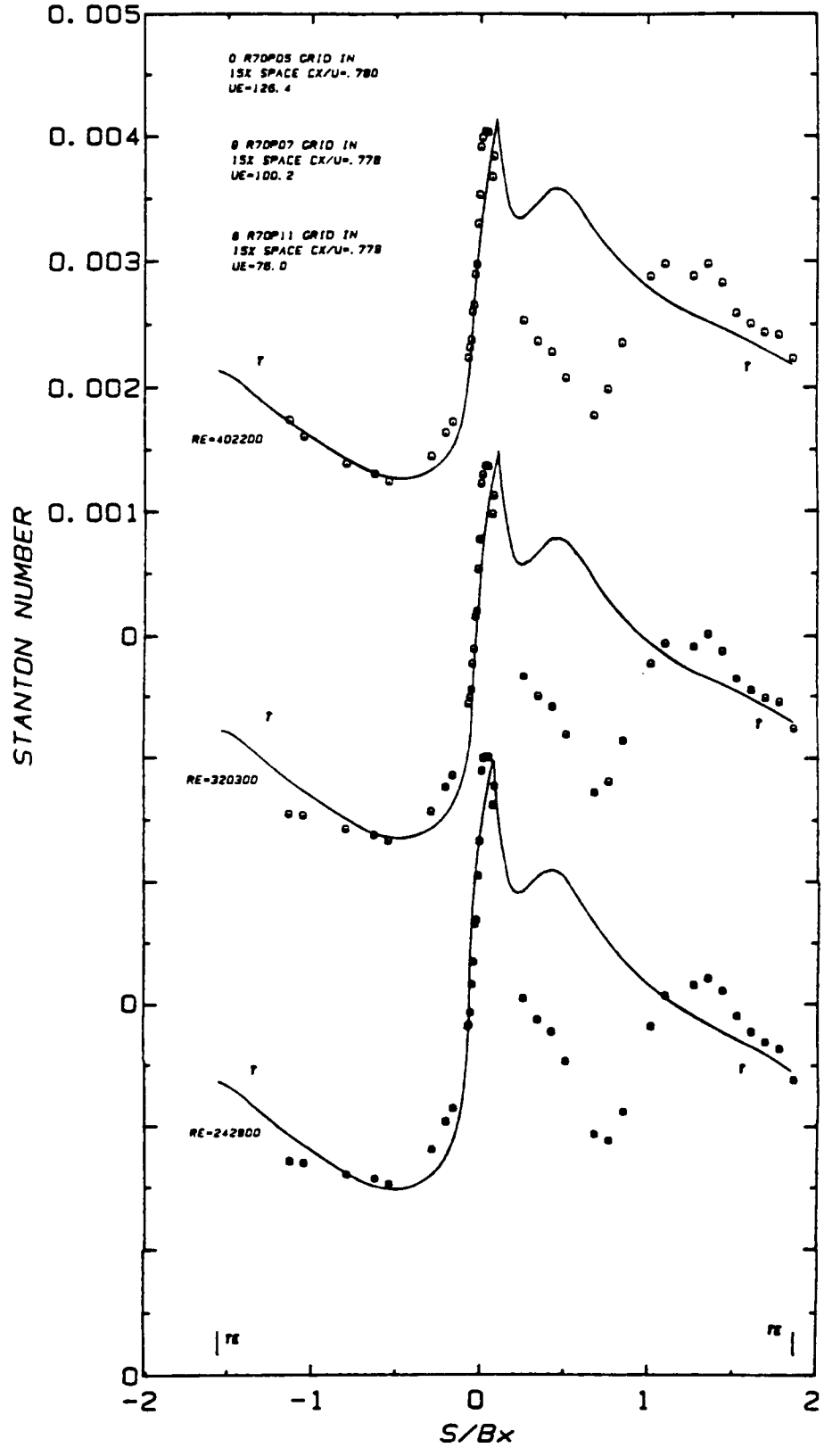

FIG. 39b EFFECT OF REYNOLDS NUMBER ON THE SINGLE-STAGE STATOR HEAT TRANSFER DISTRIBUTION, DESIGN FLOW COEFFICIENT, 15% AXIAL SPACING AND GRID IN

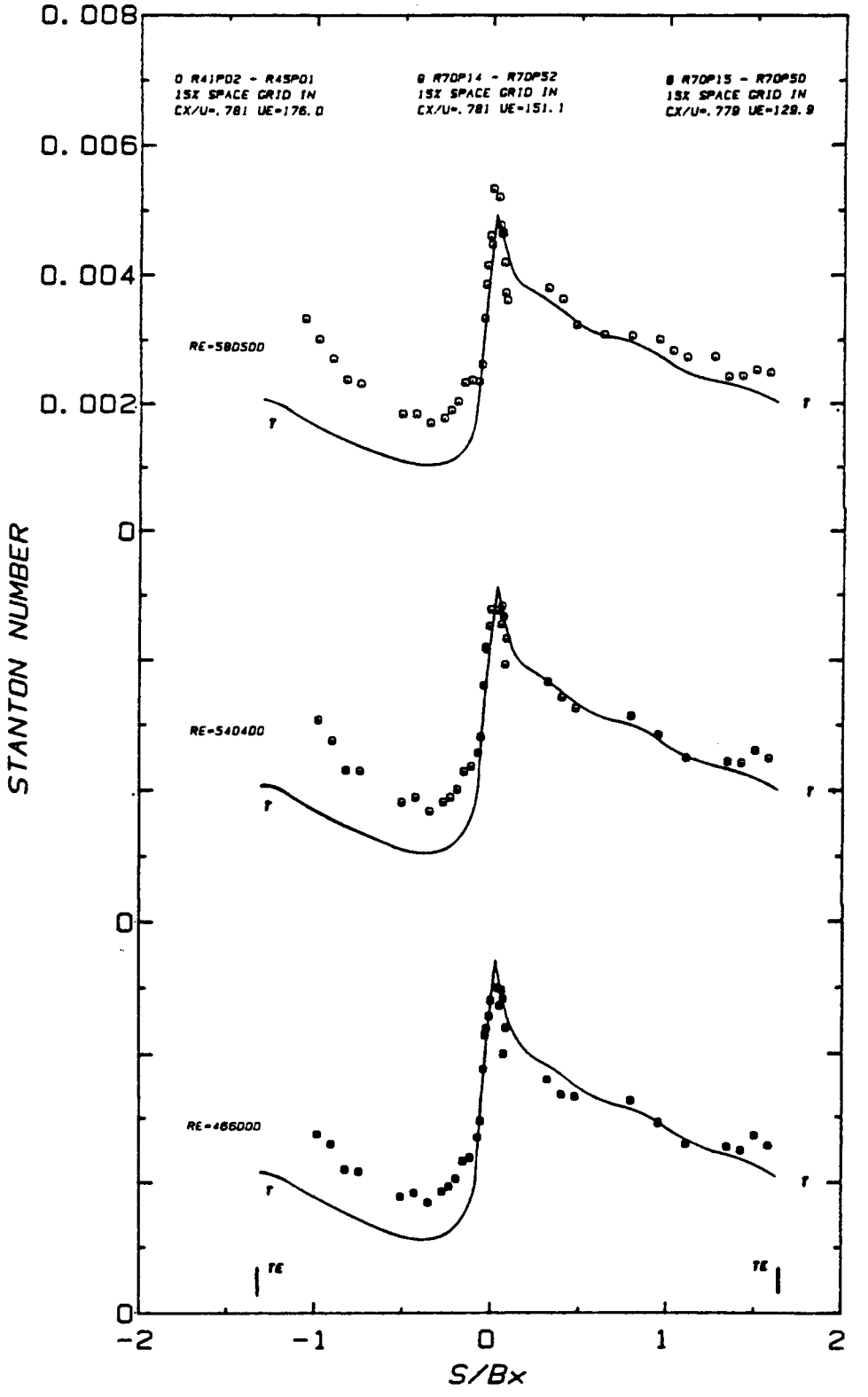

FIG. 40a EFFECT OF REYNOLDS NUMBER ON THE SINGLE-STAGE ROTOR HEAT TRANSFER DISTRIBUTION, DESIGN FLOW COEFFICIENT, 15% AXIAL SPACING AND GRID IN

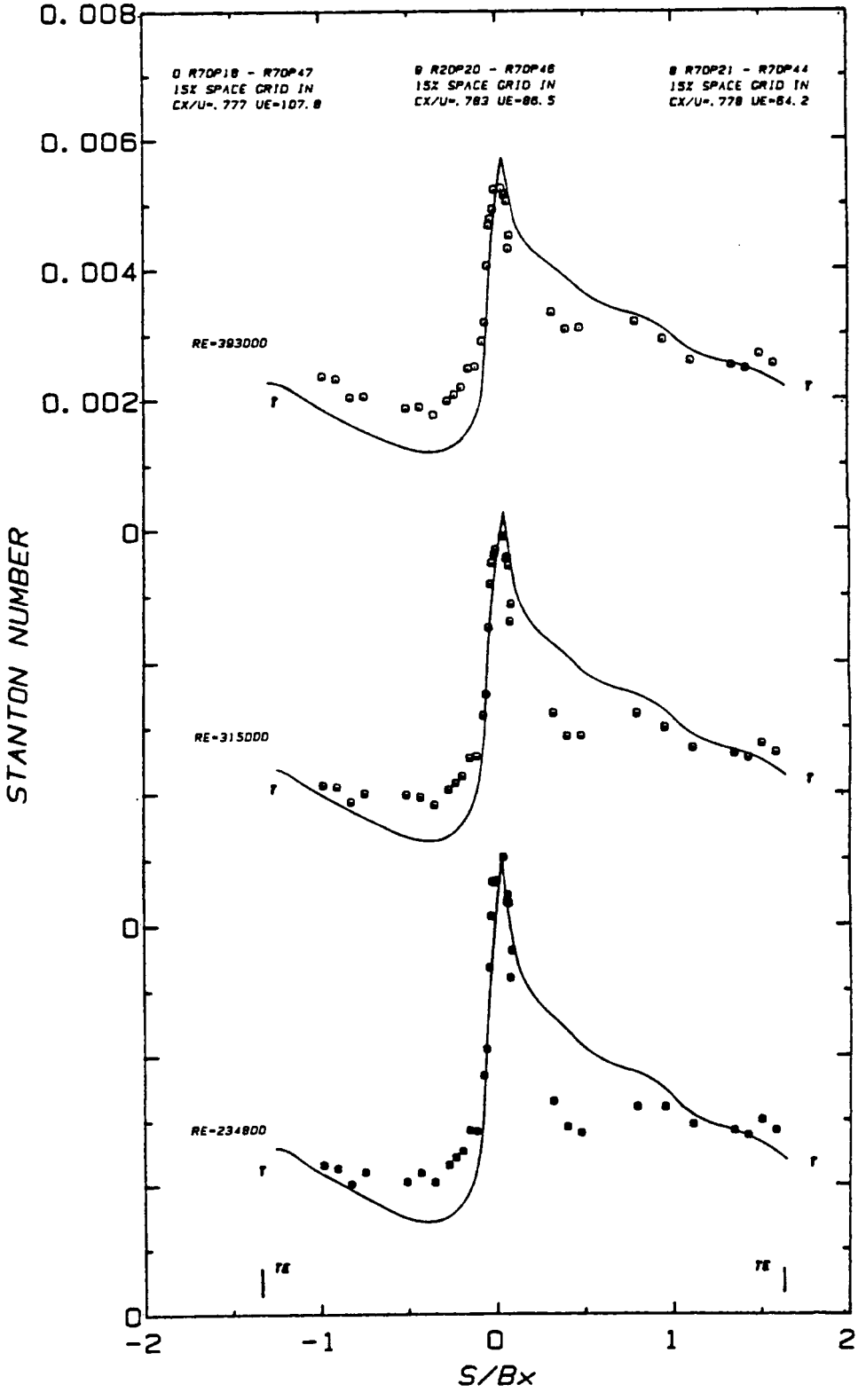

FIG. 40b EFFECT OF REYNOLDS NUMBER ON THE SINGLE-STAGE ROTOR HEAT TRANSFER DISTRIBUTION, DESIGN FLOW COEFFICIENT, 15% AXIAL SPACING AND GRID IN

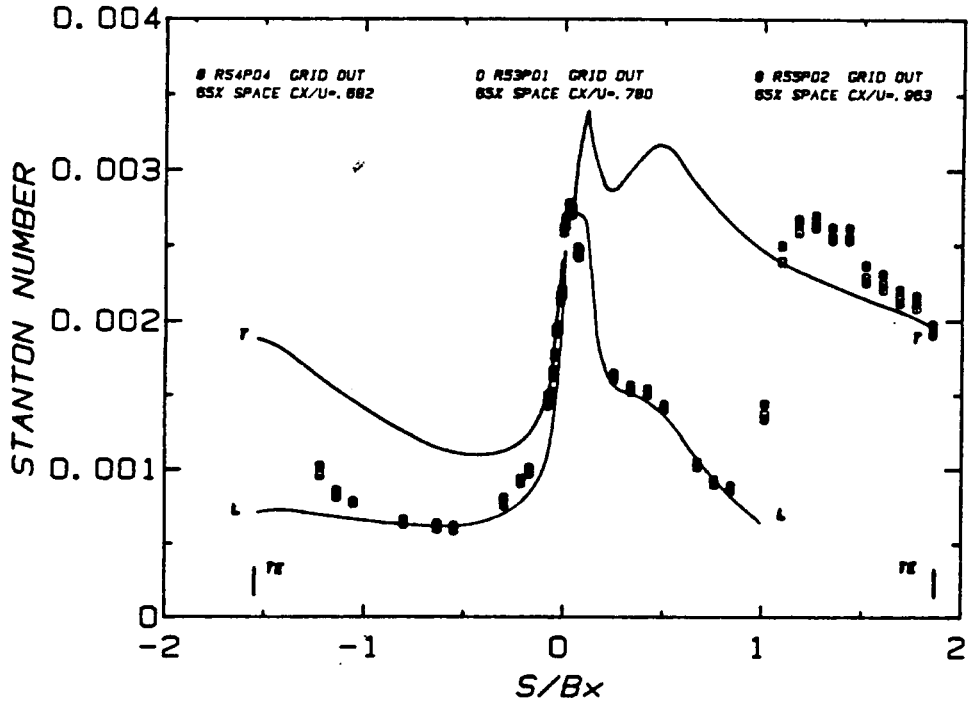

a) SINGLE-STAGE STATOR

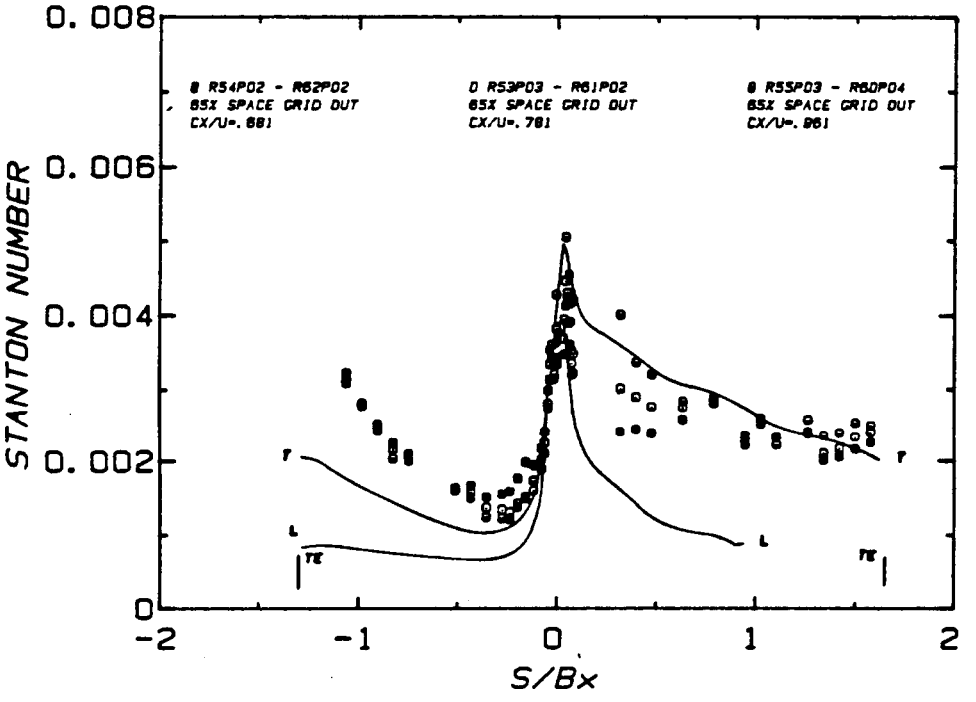

b) SINGLE-STAGE ROTOR

FIG. 41 EFFECT OF FLOW COEFFICIENT ON THE STATOR AND ROTOR HEAT TRANSFER DISTRIBUTIONS FOR THE SINGLE-STAGE CONFIGURATION, 65% AXIAL SPACING AND GRID OUT

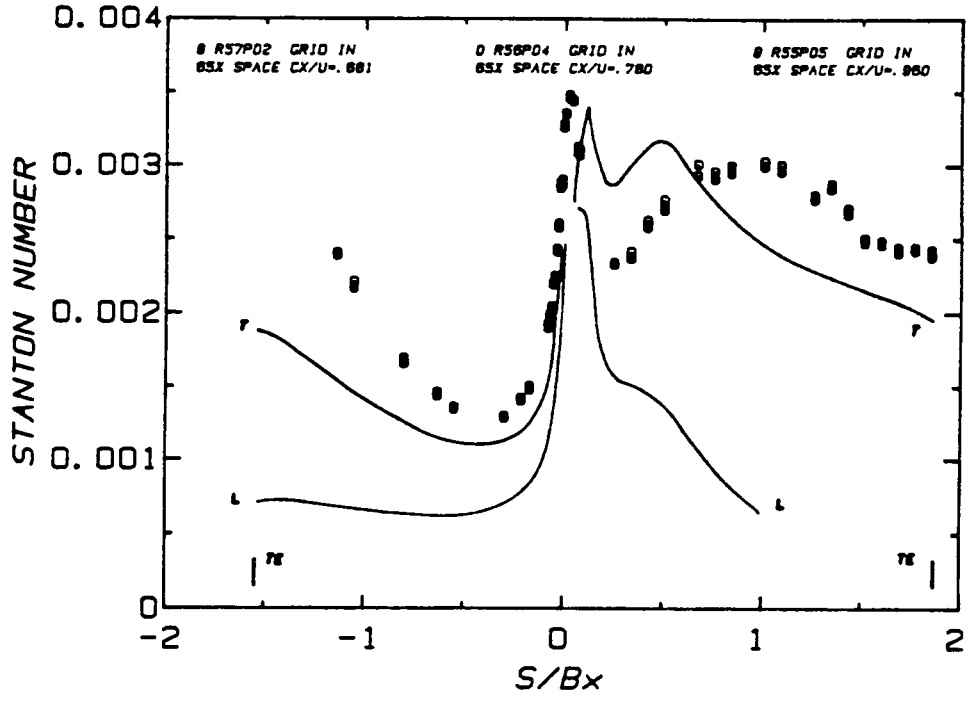

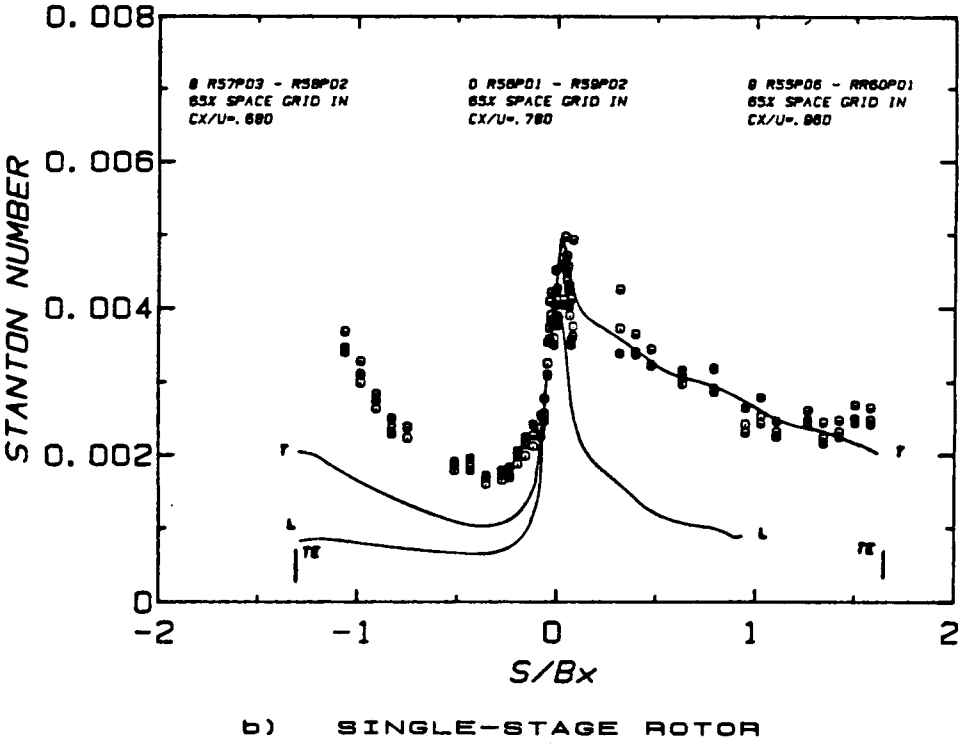

FIG. 42 EFFECT OF FLOW COEFFICIENT ON THE STATOR AND ROTOR HEAT TRANSFER DISTRIBUTIONS FOR THE SINGLE-STAGE CONFIGURATION, 65% AXIAL SPACING AND GRID IN

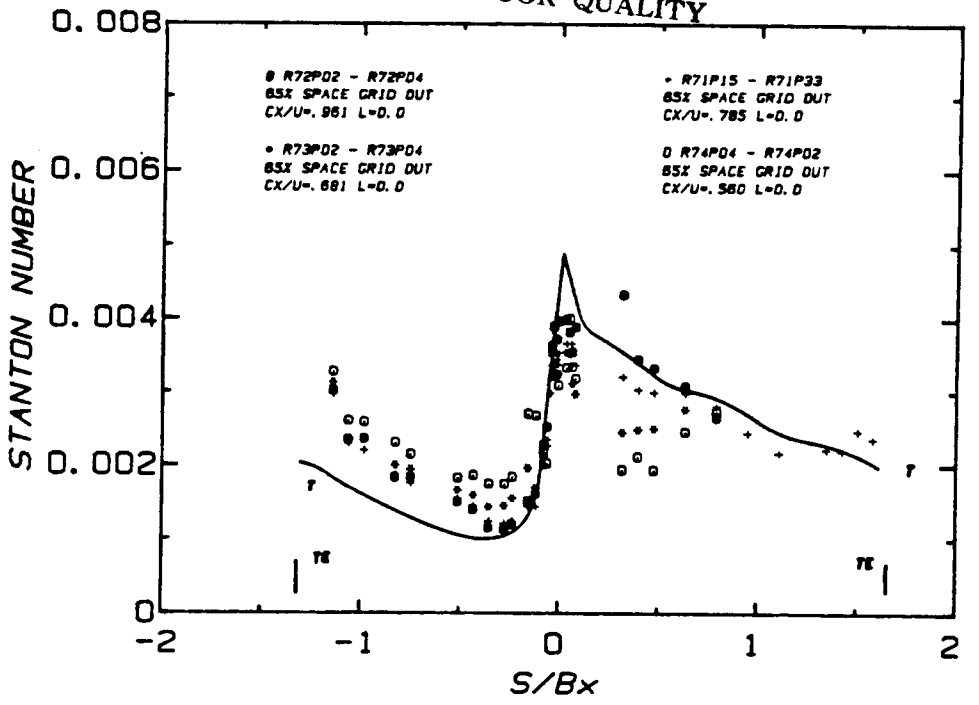

a) Cx/U = 0.96, 0.78, 0.68 and 0.56

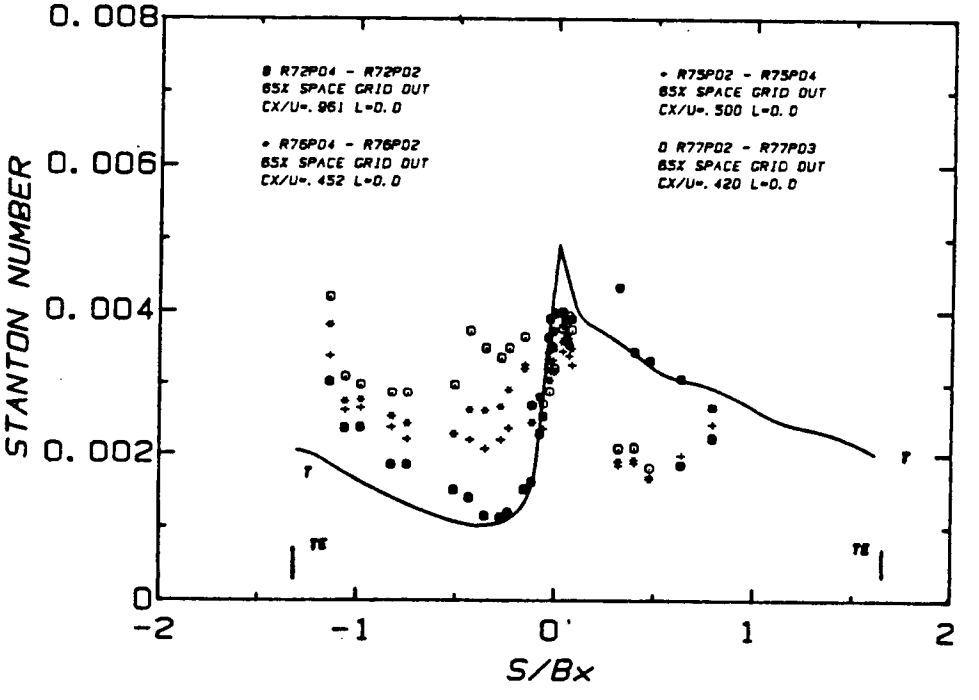

b) Cx/U = 0.96, 0.50, 0.45 and 0.42

FIG. 43 Effect of Extreme Variation of the Flow Coefficient on the Rotor Heat Transfer Distribution, 1 1/2 Stage Configuration, Grid Out

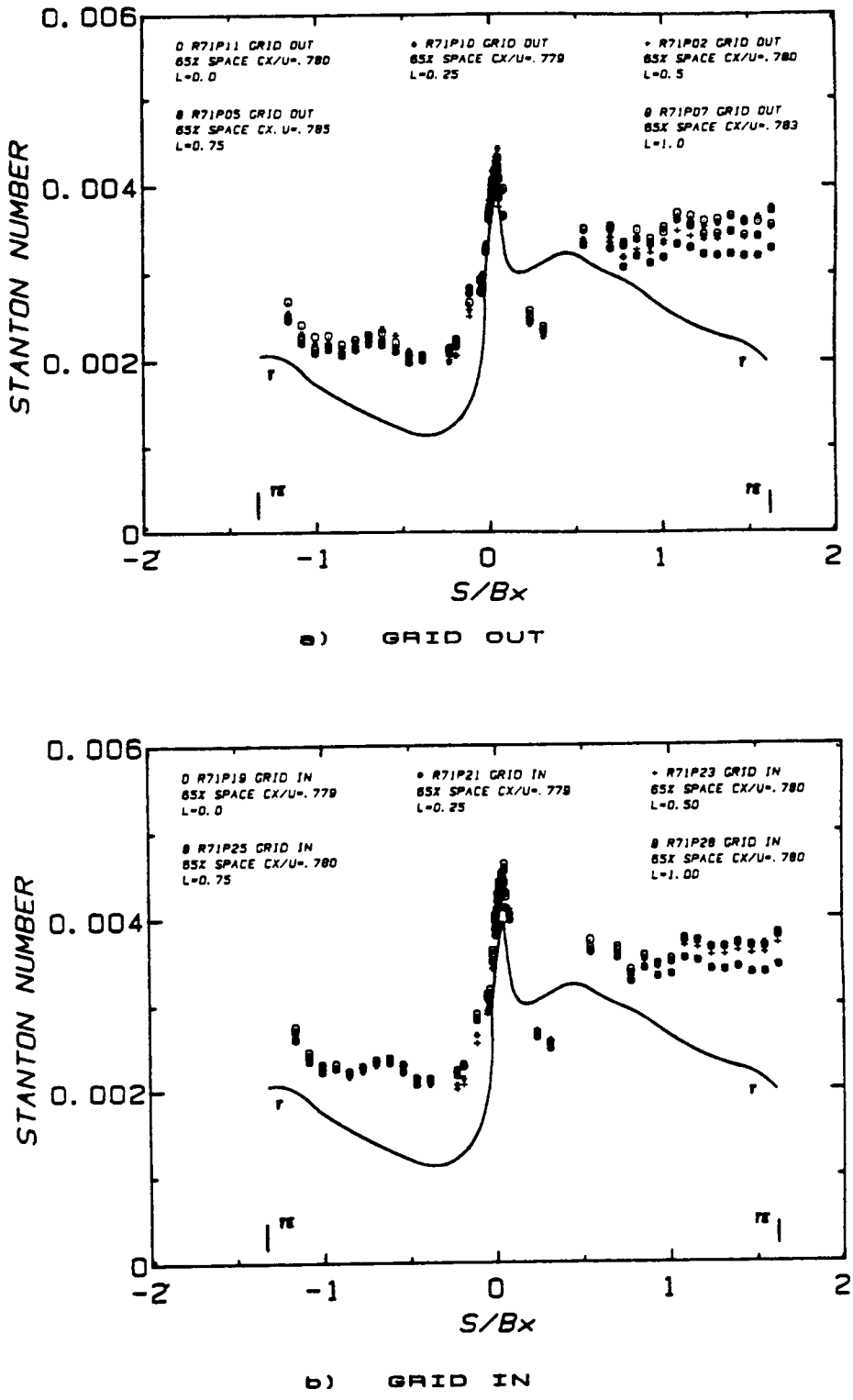

FIG. 44 EFFECTS OF THE UPSTREAM GRID AND THE RELATIVE CIRCUMFERENTIAL POSITIONS OF THE FIRST AND SECOND STATORS ON THE SECOND STATOR HEAT TRANSFER DISTRIBUTION 1-1/2 STAGE CONFIGURATION, DESIGN FLOW COEFFICIENT

DATA SETS	Re_N RANGE	Re_{BX} RANGE
R53P01 R65P01 R66P02	22630-35490	411300-635300

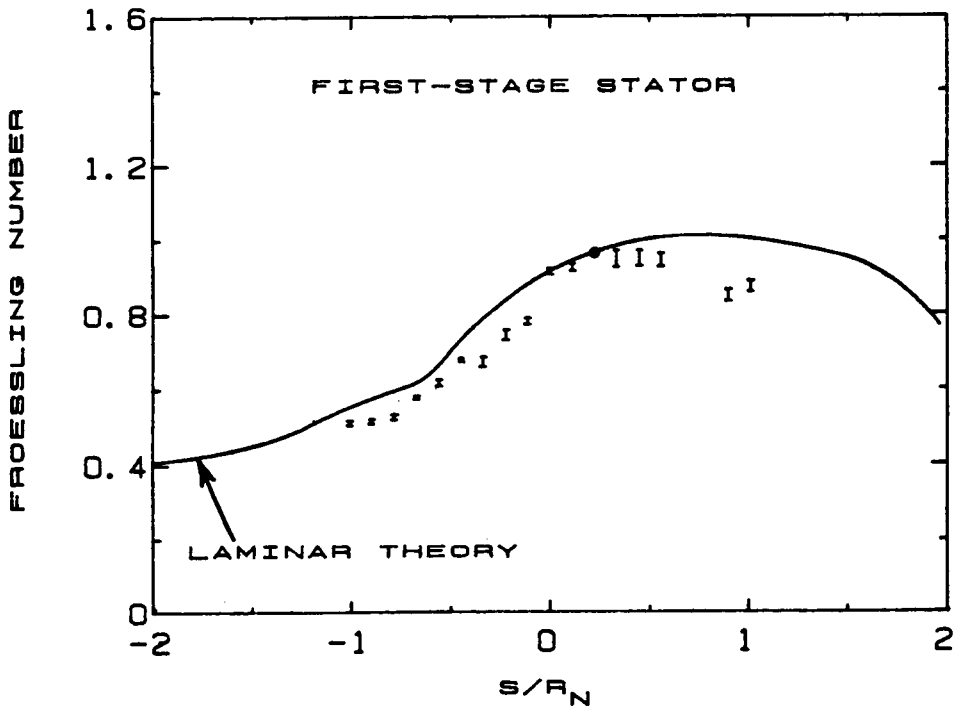

FIG. 45 MEASURED AND PREDICTED HEAT TRANSFER DISTRIBUTIONS FOR THE LEADING EDGE REGION OF THE FIRST-STAGE STATOR. DATA OBTAINED OVER A RANGE OF REYNOLDS NUMBERS WITH THE UPSTREAM GRID OUT

DATA SETS	Re_N RANGE	Re_{BX} RANGE
R66P05 R70P04 R67P02 R70P05 R67P03 R70P07 R70P02 R70P11	13280-36080	242800-542900

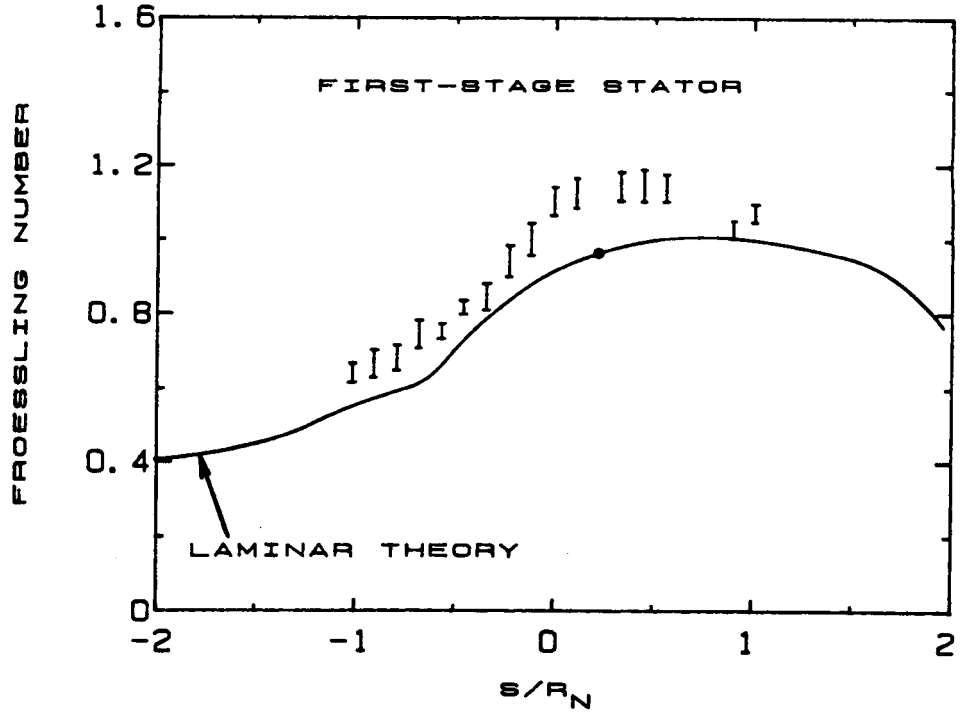

FIG. 46 MEASURED AND PREDICTED HEAT TRANSFER DISTRIBUTIONS FOR THE LEADING EDGE REGION OF THE FIRST-STAGE STATOR. DATA OBTAINED OVER A RANGE OF REYNOLDS NUMBERS WITH THE UPSTREAM GRID IN

DATA SETS	Re_N RANGE	Re_{SX} RANGE	Cx/U RANGE
R46P04 – R38P08 R47P01 – R39P02 R48P02 – R40P01 R70P35 – R70P30 R70P38 – R70P28 R70P39 – R70P26 R70P42 – R70P24	15550–48040	214300–580700	0.680–0.961

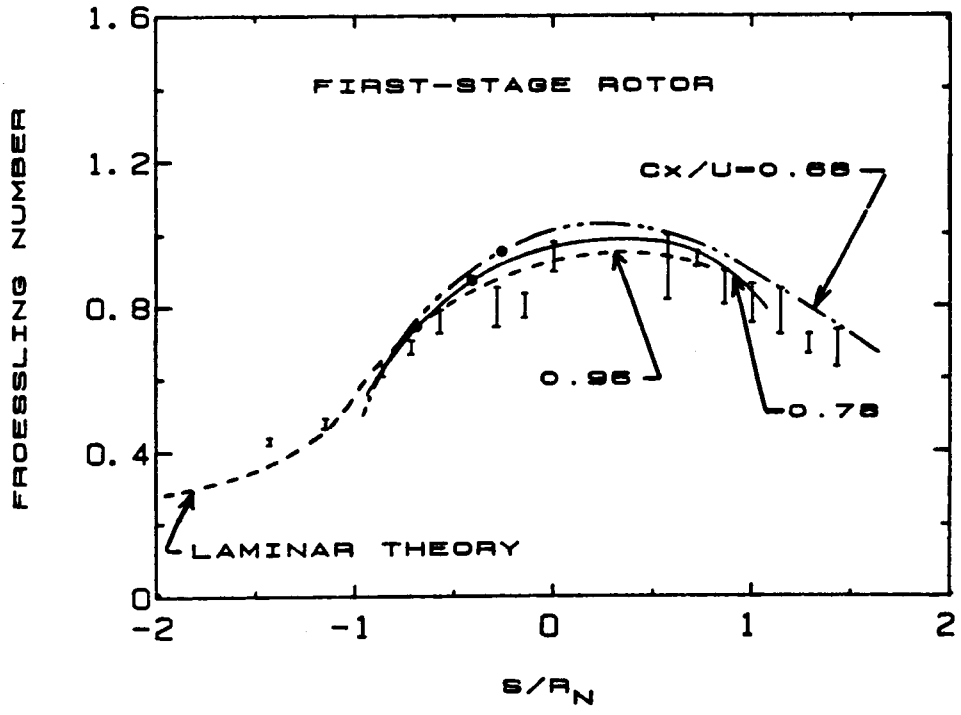

FIG. 47 MEASURED AND PREDICTED HEAT TRANSFER DISTRIBUTIONS FOR THE LEADING EDGE REGION OF THE FIRST-STAGE ROTOR FOR THREE FLOW COEFFICIENTS. DATA OBTAINED OVER A RANGE OF REYNOLDS NUMBERS WITH THE UPSTREAM GRID OUT

DATA SETS	Re_N RANGE	Re_{BX} RANGE	Cx/U RANGE
R46P02 – R42P02 R45P01 – R41P02 R44P04 – R40P04 R70P52 – R70P14 R70P50 – R70P15 R70P47 – R70P18 R70P46 – R20P20 R70P44 – R70P21	16870–48340	233700–565800	0.679–0.960

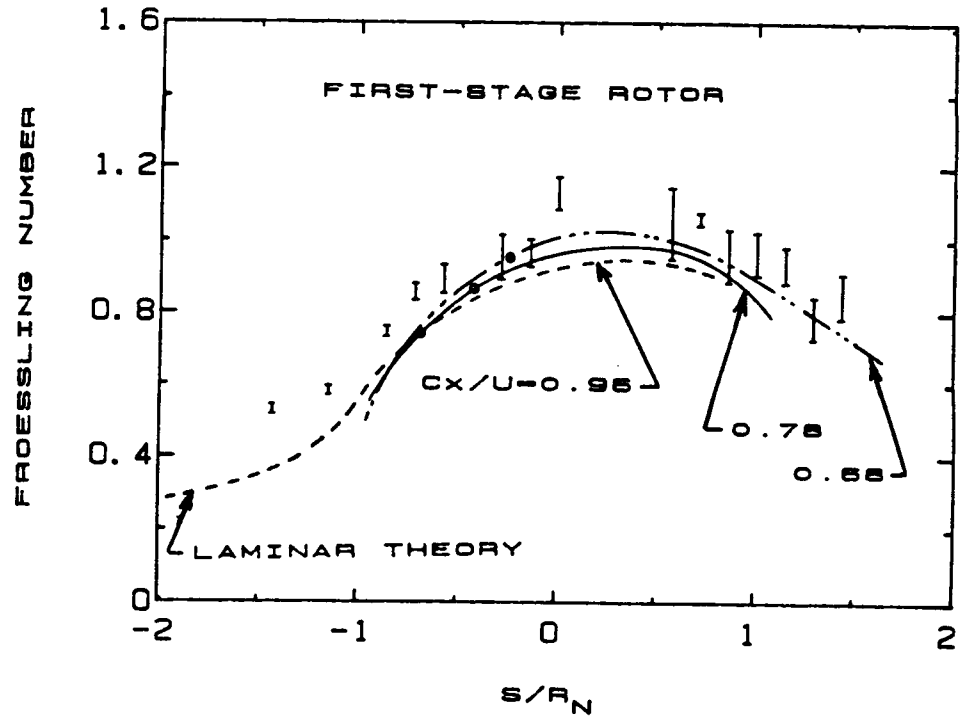

FIG. 48 MEASURED AND PREDICTED HEAT TRANSFER DISTRIBUTIONS FOR THE LEADING EDGE REGION OF THE FIRST-STAGE ROTOR FOR THREE FLOW COEFFICIENTS. DATA OBTAINED OVER A RANGE OF REYNOLDS NUMBERS WITH THE UPSTREAM GRID IN

DATA SETS	Re_N RANGE	Re_{SX} RANGE	L RANGE
R71P02 R71P05 R71P07 R71P10 R71P11	36150-37980	616700-643100	0.0-1.0

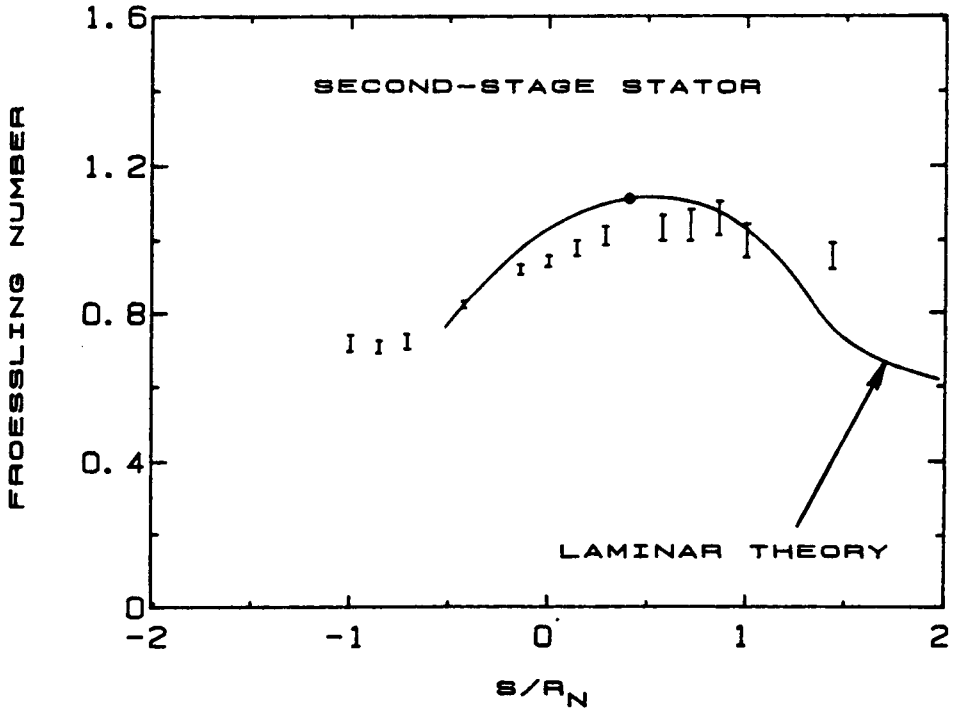

FIG. 49 MEASURED AND PREDICTED HEAT TRANSFER DISTRIBUTIONS FOR THE LEADING EDGE REGION OF THE SECOND-STAGE STATOR. DATA OBTAINED FOR FIVE RELATIVE CIRCUMFERENTIAL POSITIONS OF THE FIRST AND SECOND STATORS AND WITH THE UPSTREAM GRID OUT

DATA SETS	Re_N RANGE	Re_{BX} RANGE	L RANGE
R71P19 R71P21 R71P23 R71P25 R71P28	36650-37410	624500-639000	0.0-1.0

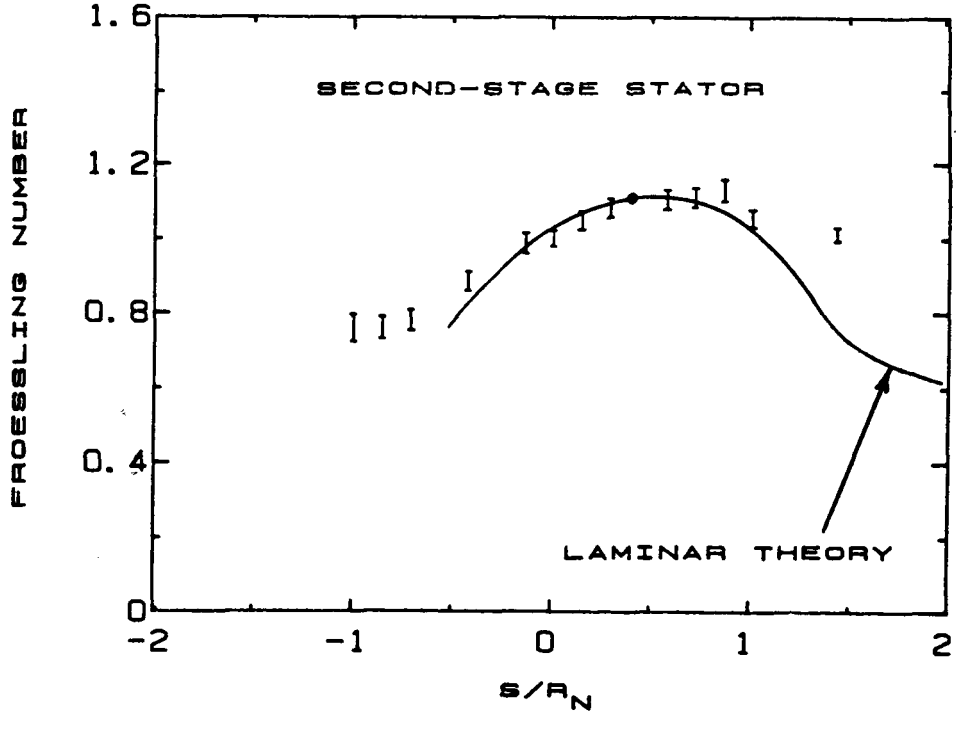

FIG. 50 MEASURED AND PREDICTED HEAT TRANSFER DISTRIBUTIONS FOR THE LEADING EDGE REGION OF THE SECOND-STAGE STATOR. DATA OBTAINED FOR FIVE RELATIVE CIRCUMFERENTIAL POSITIONS OF THE FIRST AND SECOND STATORS AND WITH THE UPSTREAM GRID IN

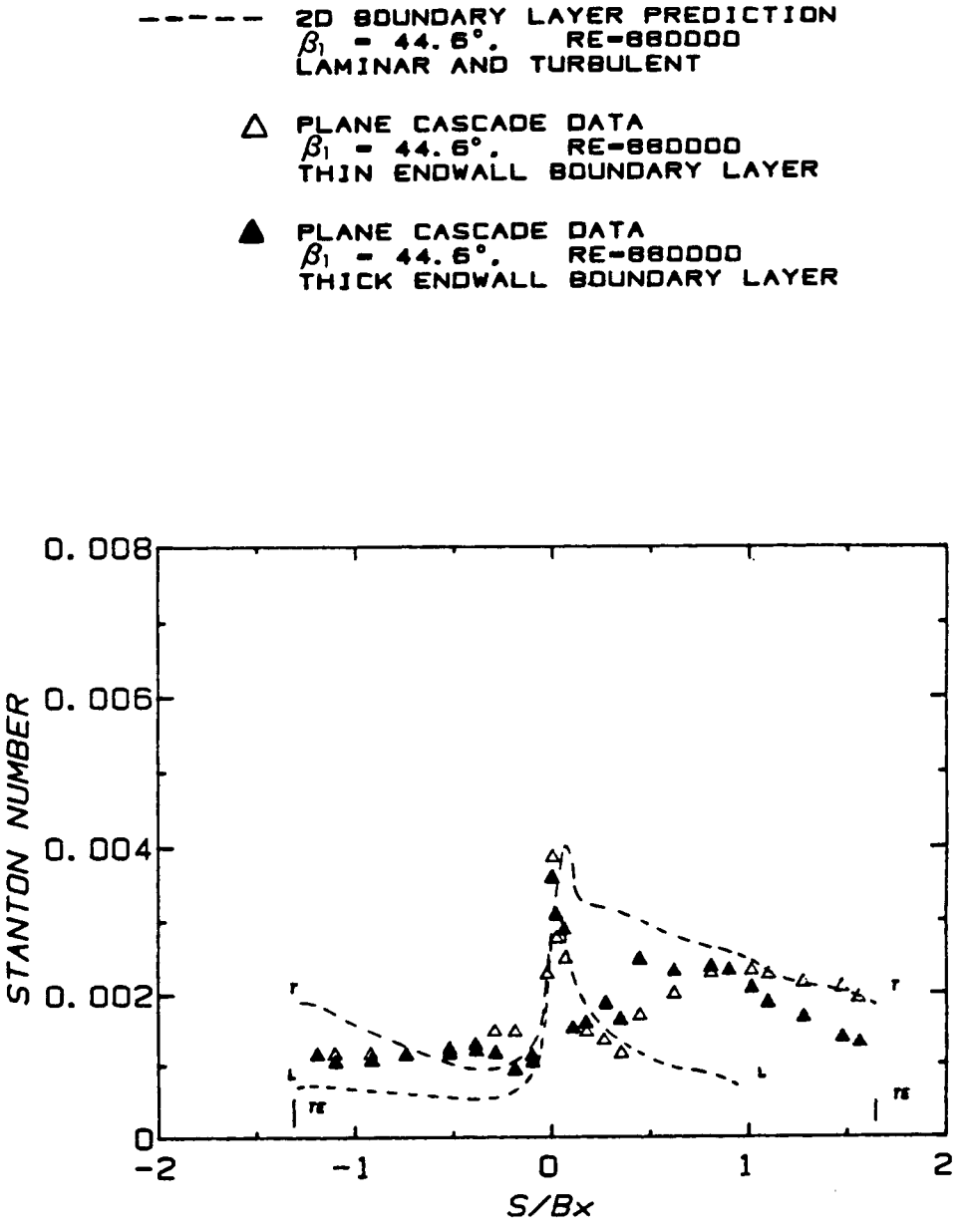

FIG. 51 MEASURED AND PREDICTED HEAT TRANSFER DISTRIBUTIONS FOR THE ROTOR (MIDSPAN SECTION) IN A LARGE-SCALE PLANE CASCADE

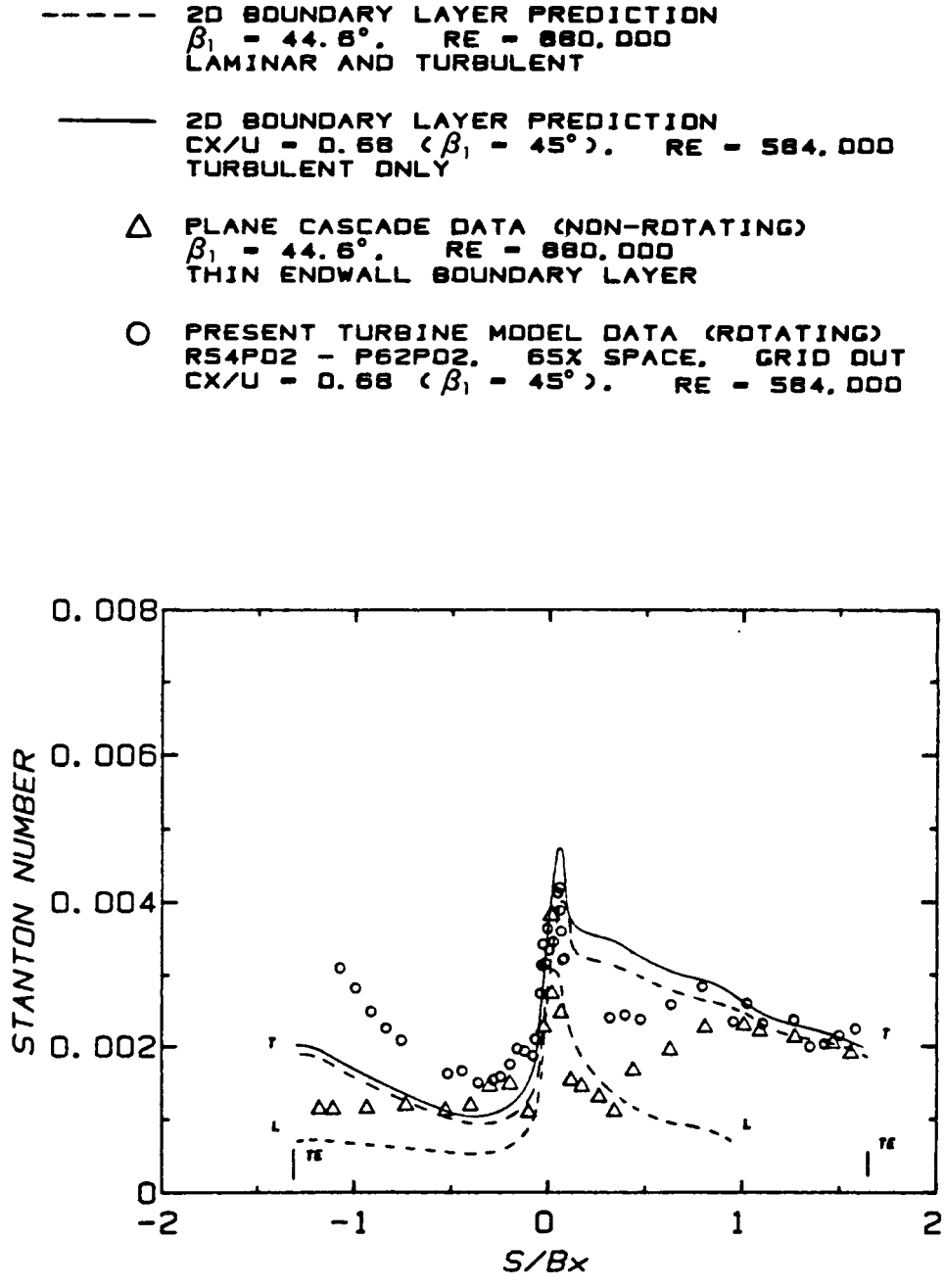

FIG. 52 COMPARISON OF MEASURED AND PREDICTED HEAT TRANSFER DISTRIBUTIONS FOR THE ROTOR IN THE PRESENT ROTATING TURBINE MODEL AND THE SAME AIRFOIL MIDSPAN GEOMETRY INSTALLED IN A PLANE CASCADE (NON-ROTATING)

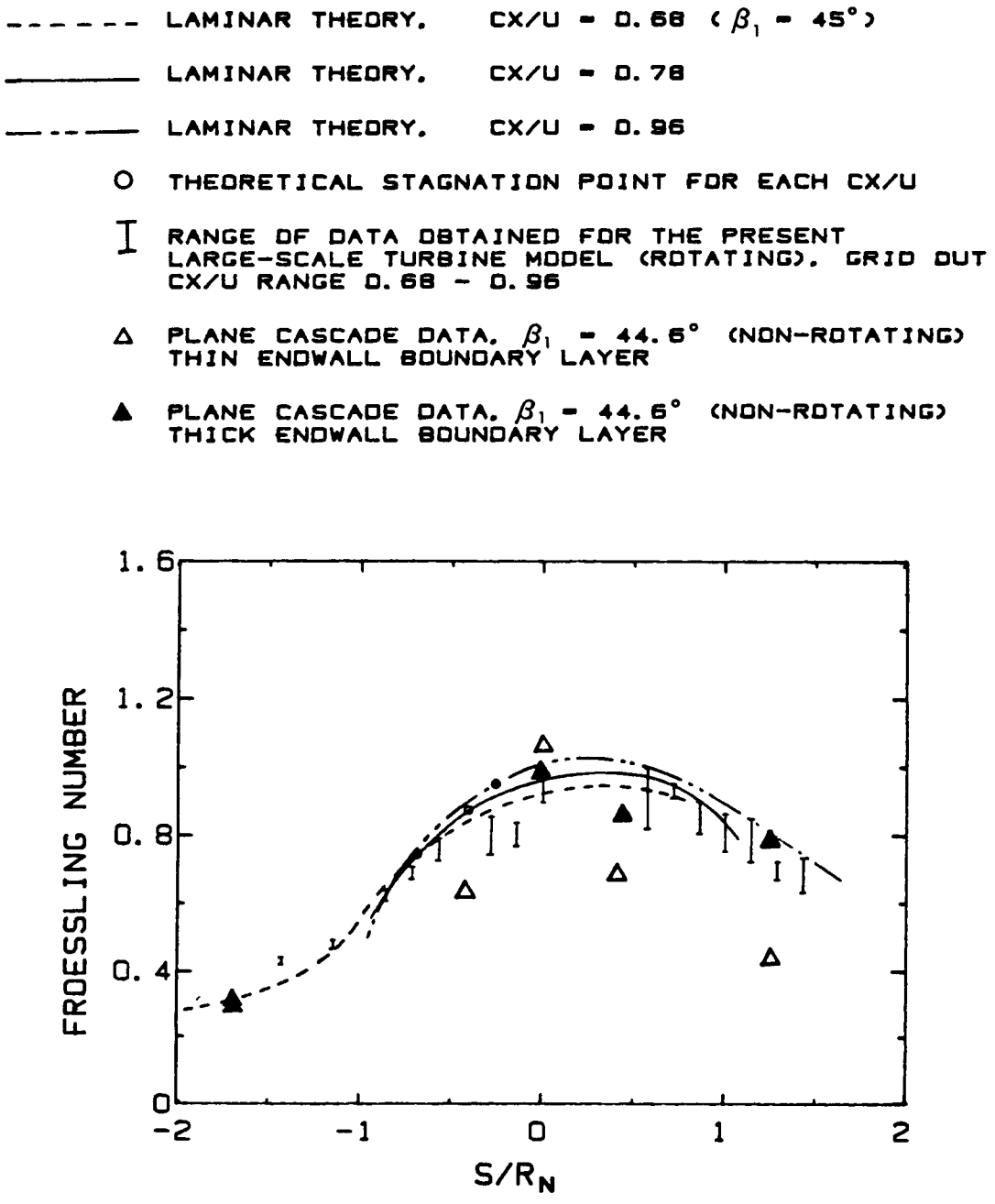

FIG. 53 COMPARISON OF MEASURED AND PREDICTED HEAT TRANSFER DISTRIBUTIONS FOR THE LEADING EDGE REGION OF THE ROTOR. DATA OBTAINED ON THE PRESENT ROTATING TURBINE MODEL AND FOR THE SAME AIRFOIL MIDSPAN GEOMETRY INSTALLED IN A PLANE CASCADE (NON-ROTATING)

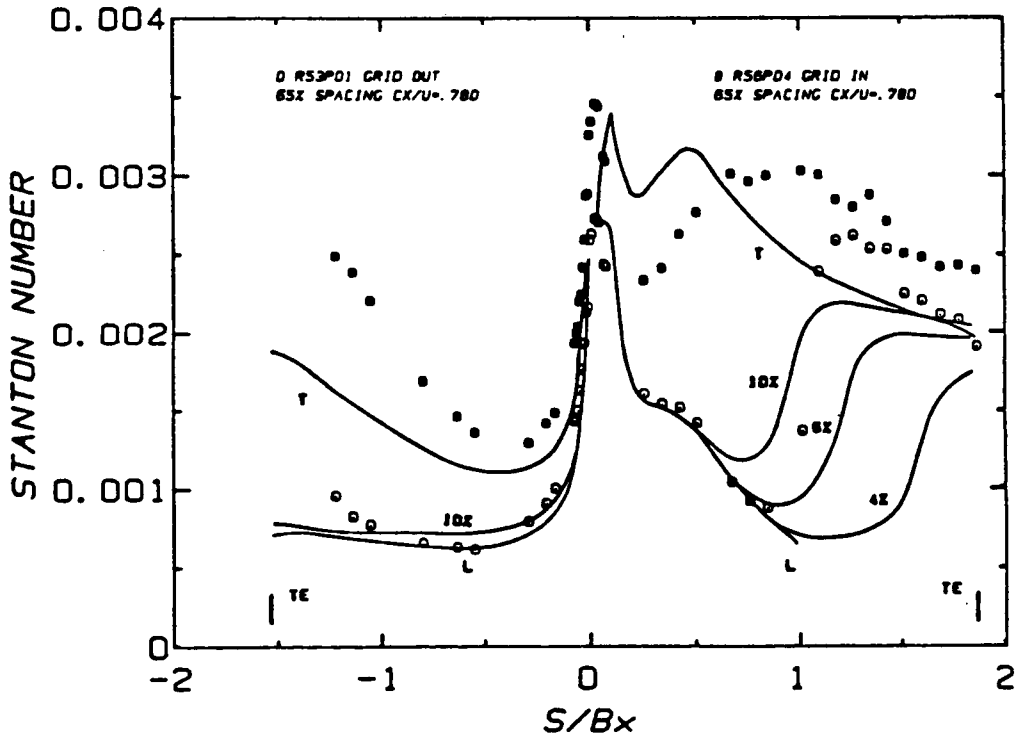

FIG. 54 ANALYTICAL/EXPERIMENTAL COMPARISONS FOR THE FIRST STAGE STATOR, Cx/U = 0.78

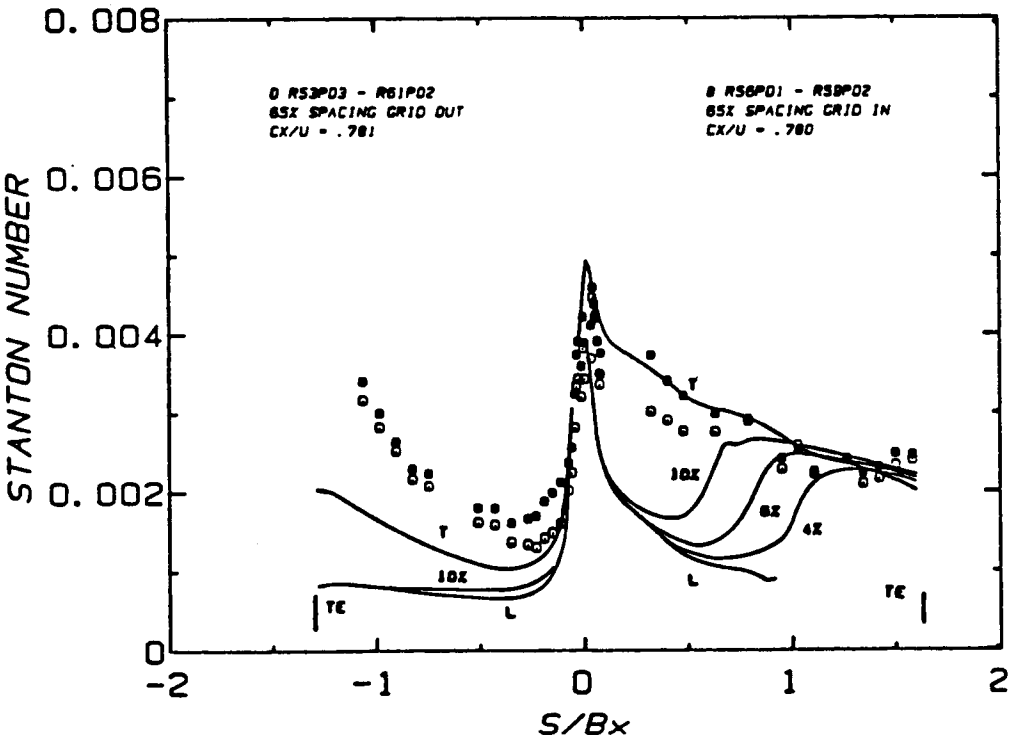

FIG. 55 ANALYTICAL/EXPERIMENTAL COMPARISONS FOR THE FIRST STAGE ROTOR, Cx/U = 0.78

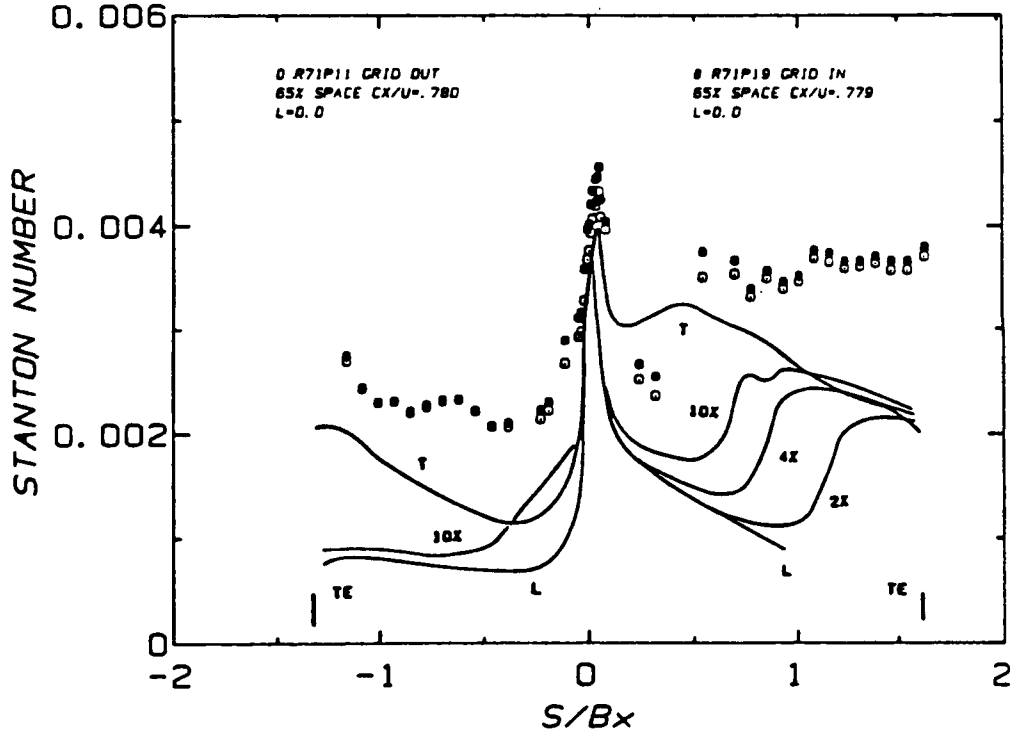

FIG. 56 ANALYTICAL/EXPERIMENTAL COMPARISONS FOR THE SECOND STAGE STATOR, Cx/U = 0.78

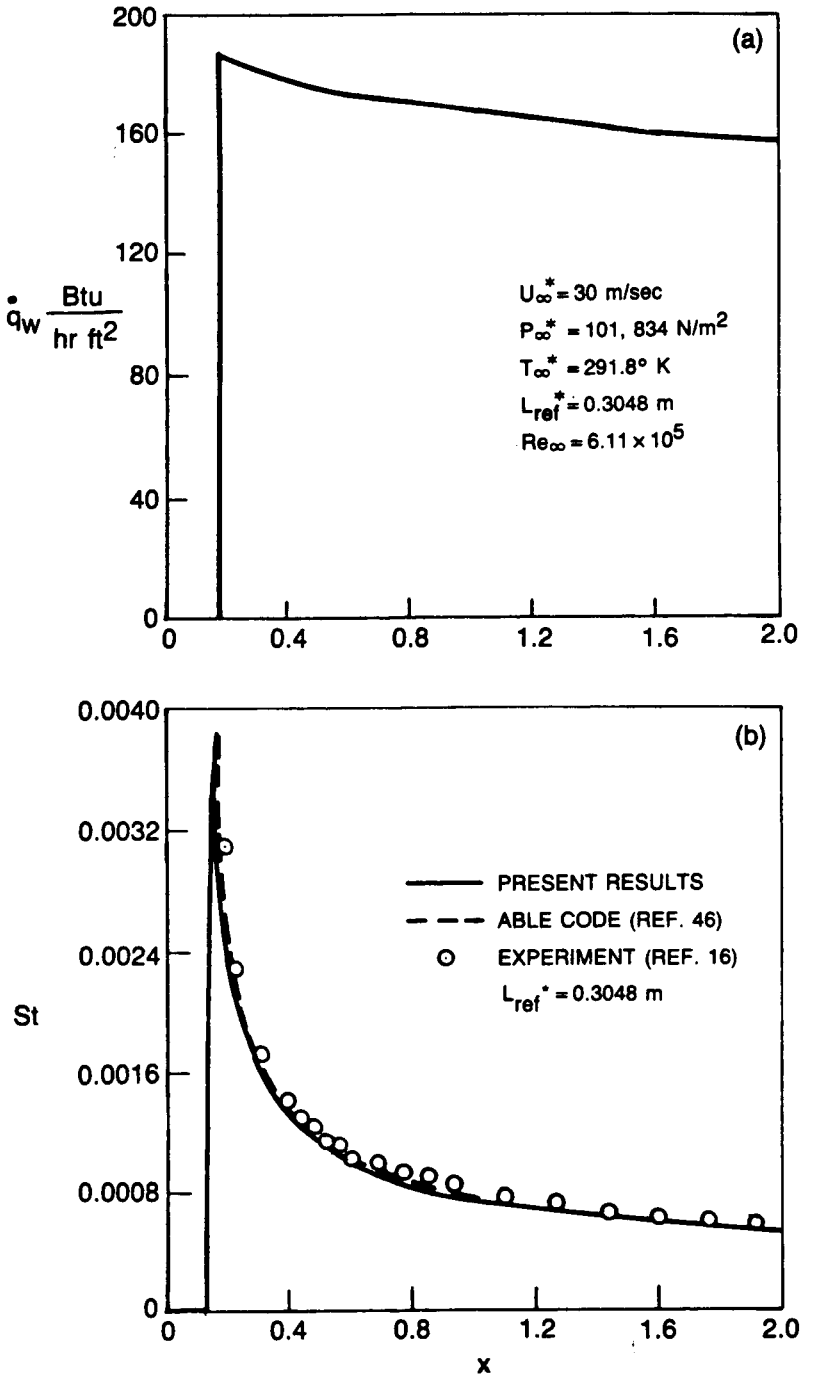

FIG. 57 Steady Laminar Flow Over Heated Flat Plate
a) Prescribed Wall Heat Transfer Distribution
b) Predicted Stanton Number Distribution

86—8—24—1

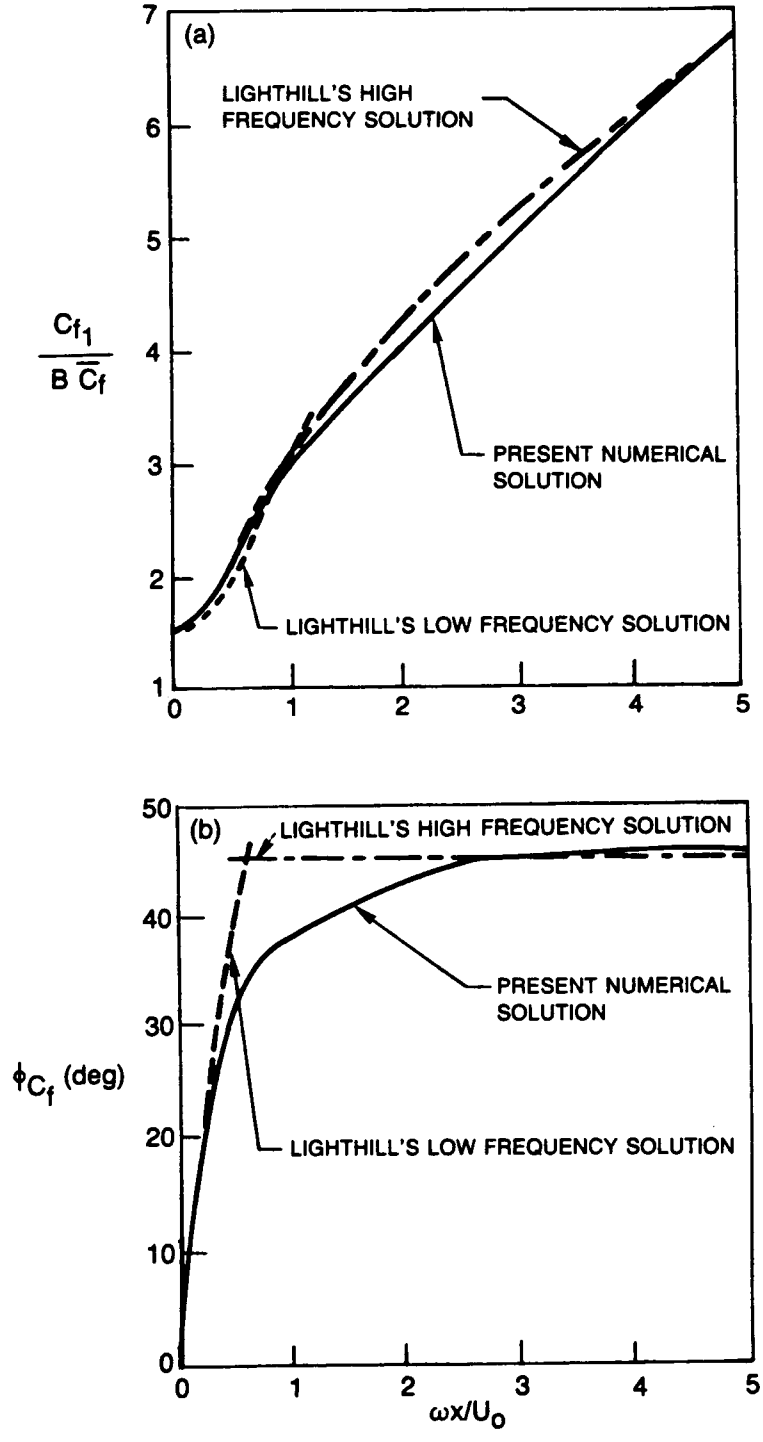

FIG. 58 Laminar Flow Over a Flat Plate in an Oscillating Stream
(a) Amplitude of Skin Friction Fluctuation
(b) Phase Angle of Skin Friction Fluctuation

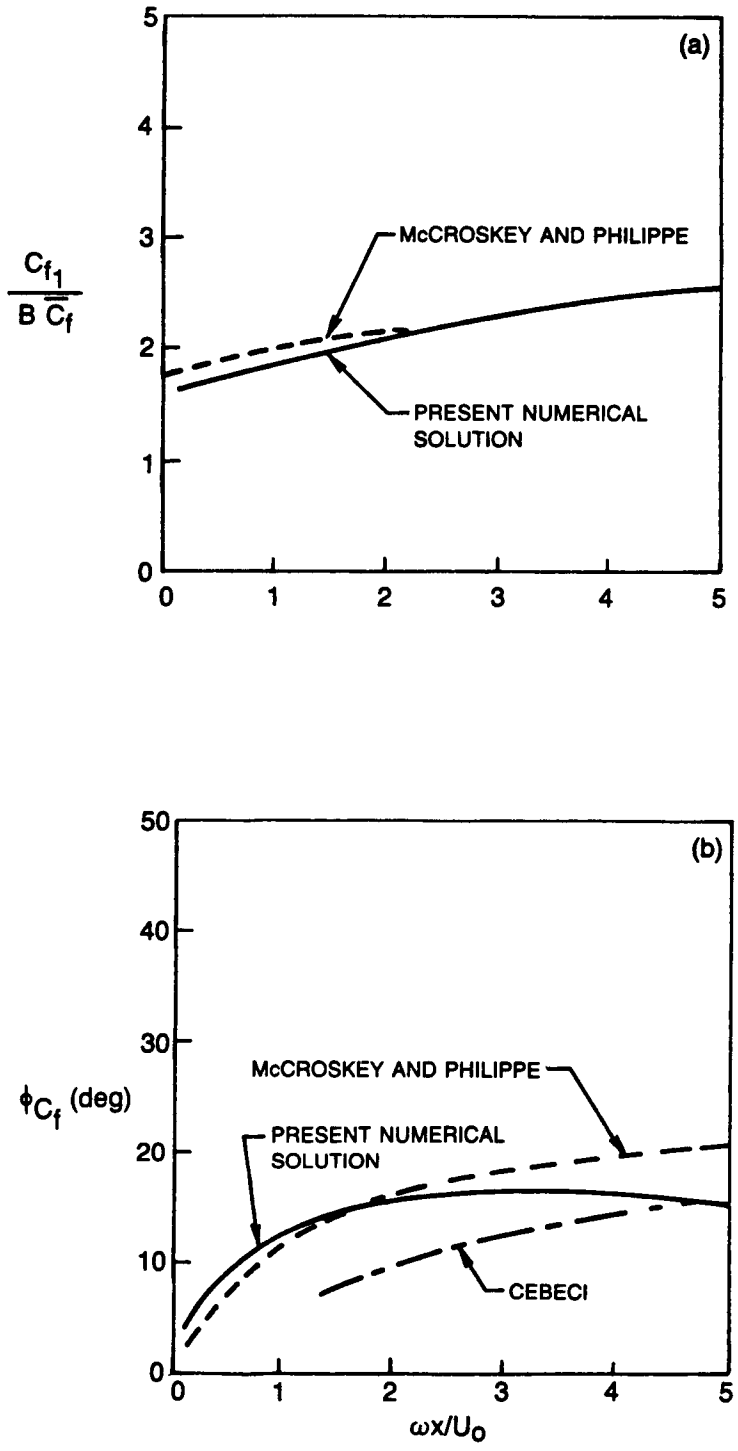

FIG. 59 Turbulent Flow Over a Flat Plate in an Oscillating Stream
(a) Amplitude of Skin Friction Fluctuation
(b) Phase Angle of Skin Friction Fluctuation

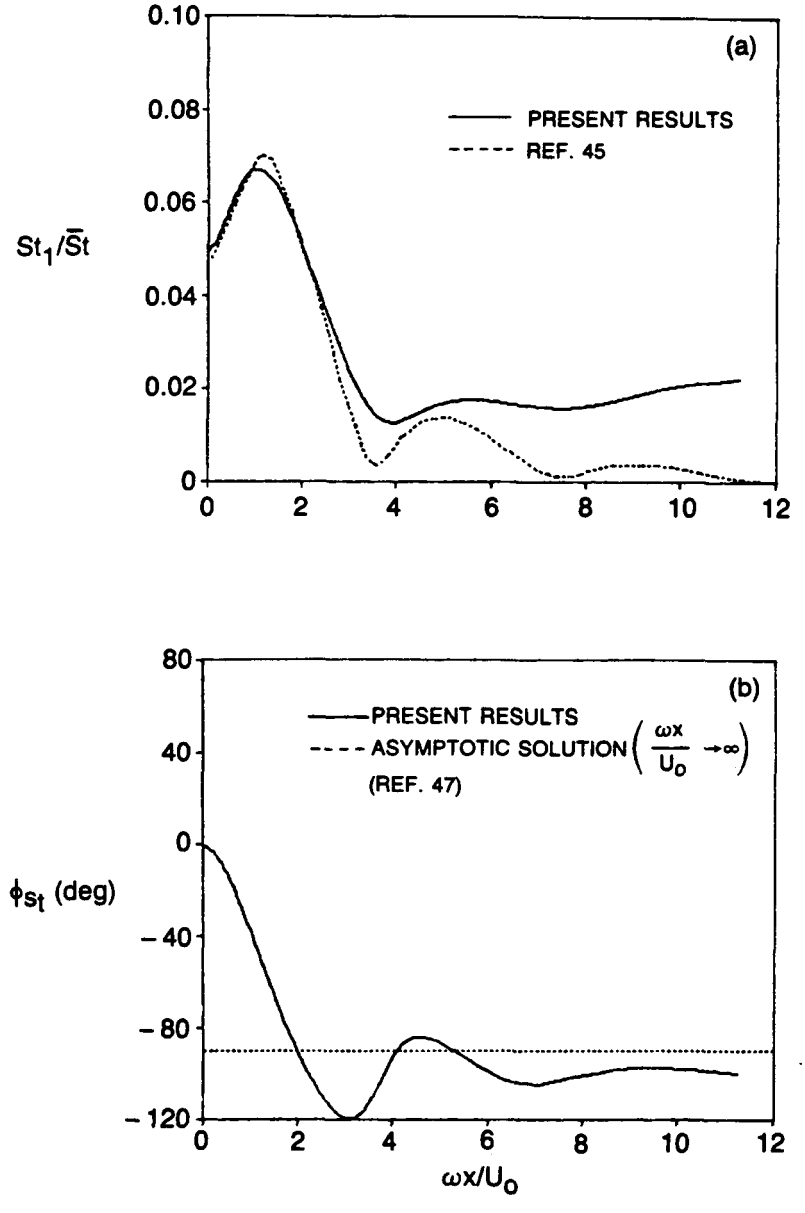

FIG. 60 Laminar Flow Over a Heated Flat Plate in an Oscillating Stream
(a) Amplitude of Stanton Number Fluctuation
(b) Phase Angle of Stanton Number Fluctuation

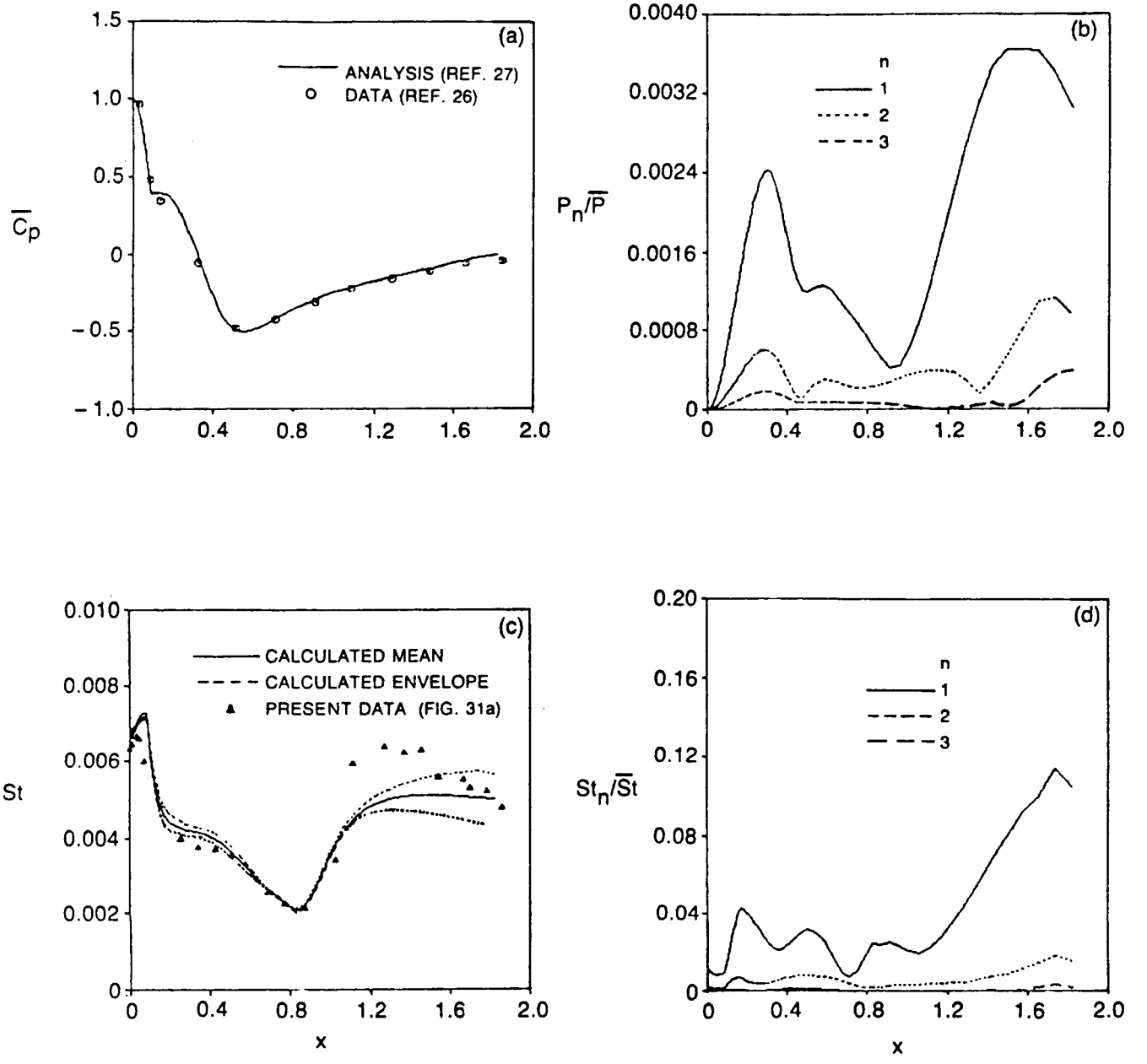

FIG. 61 Flow Over Stator Suction Surface
(a) Mean Pressure Distribution
(b) First Three Fourier Components of Pressure
(c) Mean Stanton Number and Unsteady Evelope
(d) First Three Fourier Components of Stanton Number

86—8—24—5

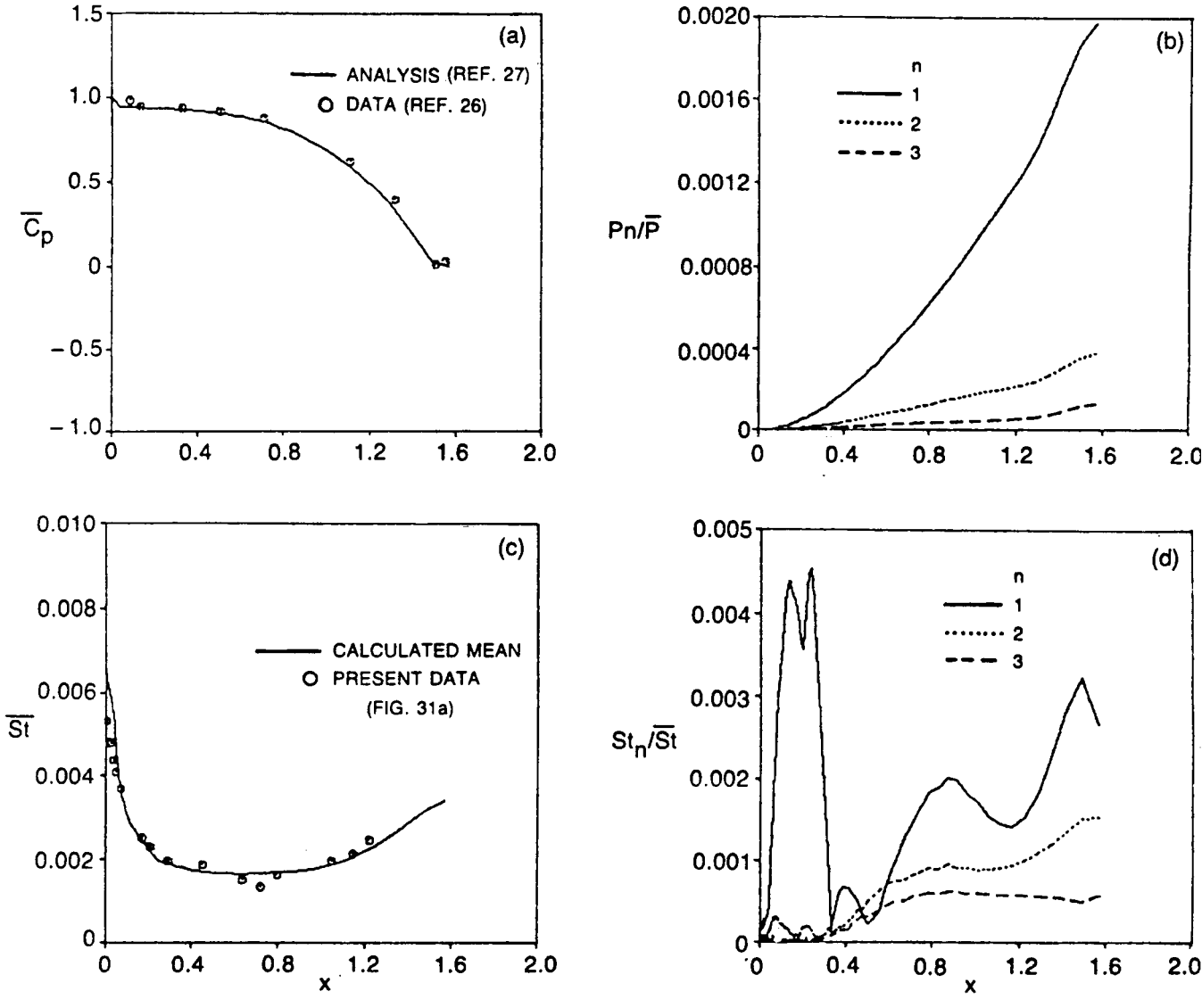

FIG. 62 **Flow Over Stator Pressure Surface**
(a) Mean Pressure Distribution
(b) First Three Fourier Components of Pressure
(c) Mean Stanton Number
(d) First Three Fourier Components of Stanton Number

86—8—24—6

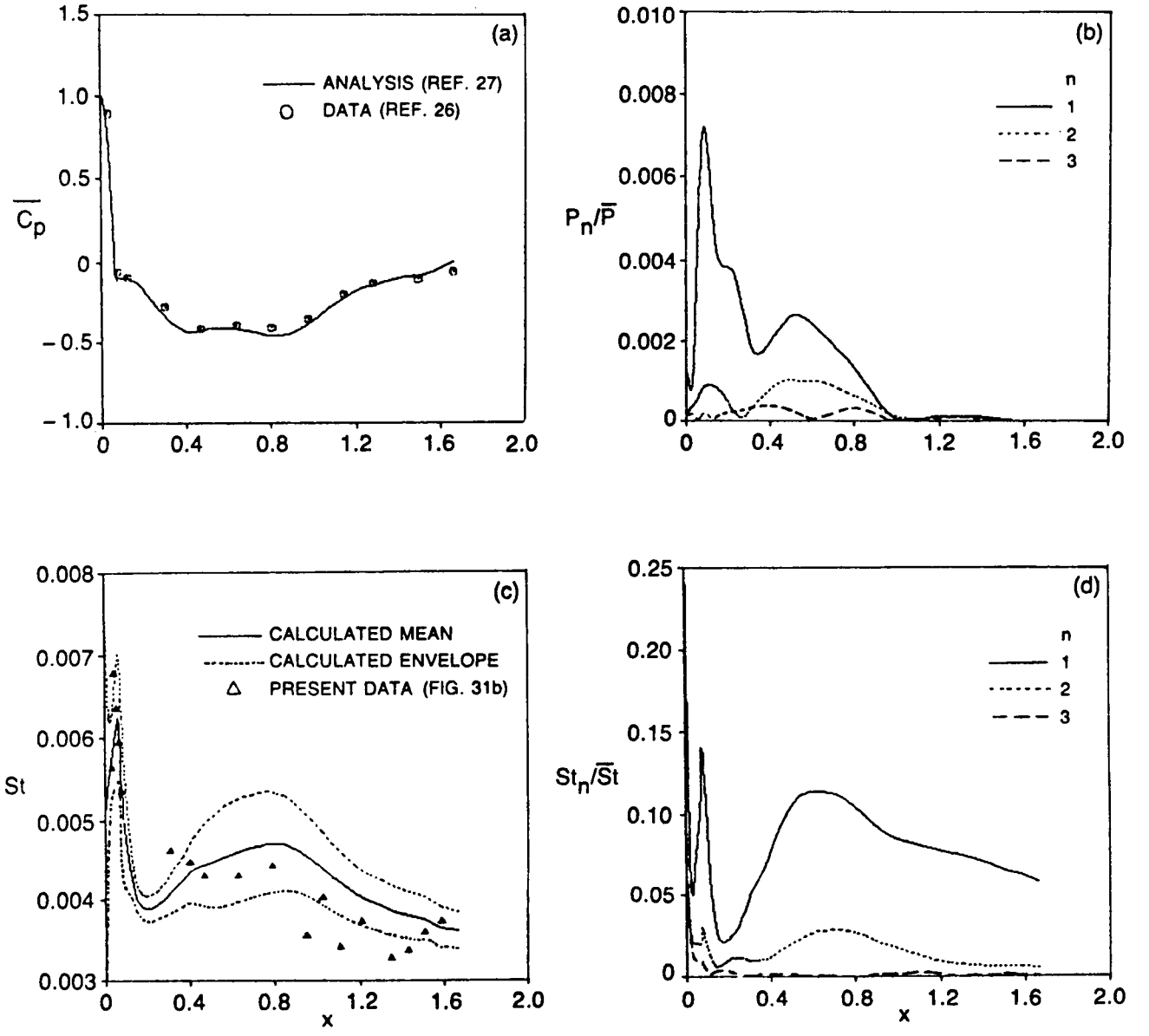

FIG. 63 Flow Over Rotor Blade Suction Surface
(a) Mean Pressure Distribution
(b) First Three Fourier Components of Pressure
(c) Mean Stanton Number and Unsteady Envelope
(d) First Three Fourier Components of Stanton Number

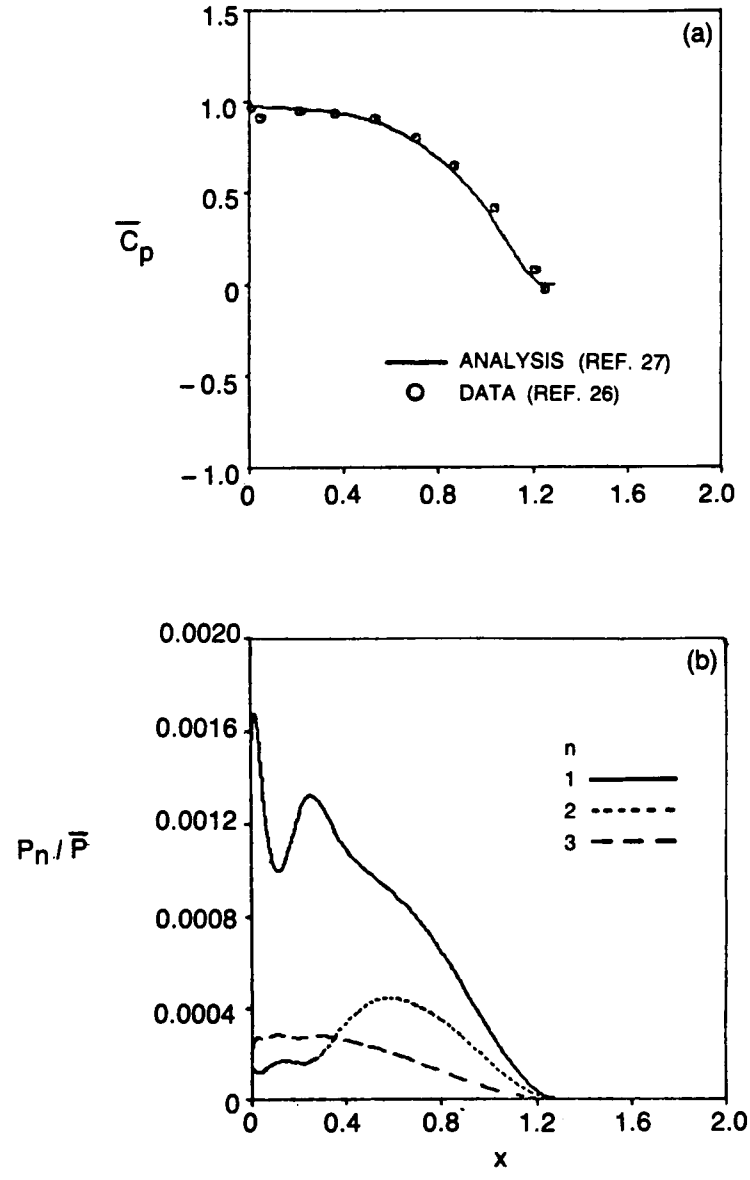

FIG. 64 Flow Over Rotor Pressure Surface
(a) Mean Pressure Distribution
(b) First Three Fourier Components of Pressure

86—8—24—8

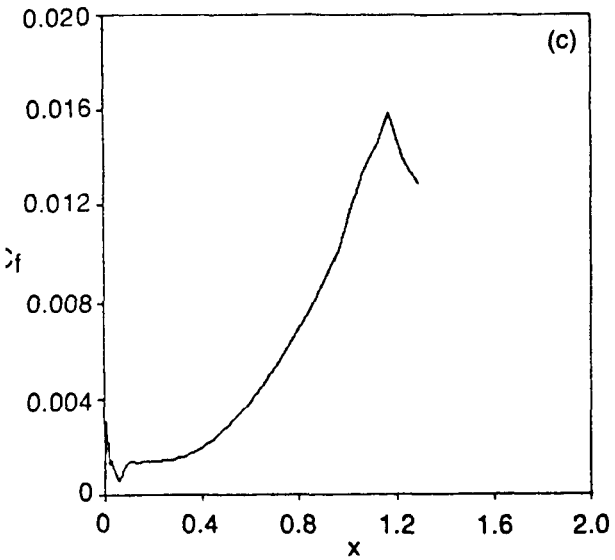

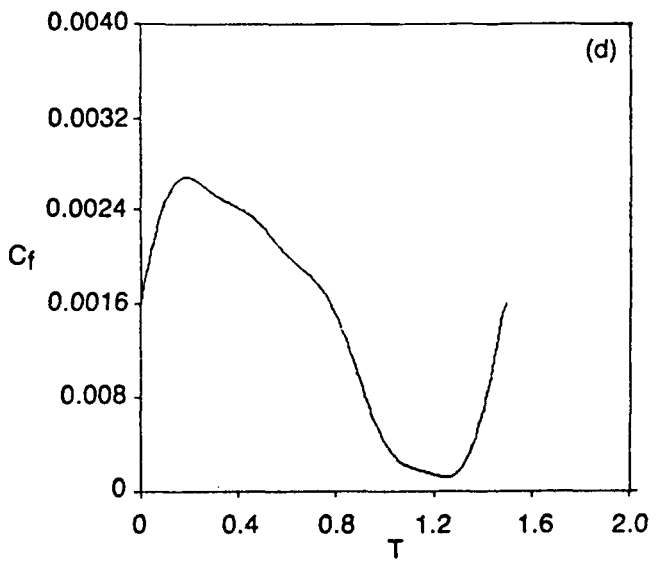

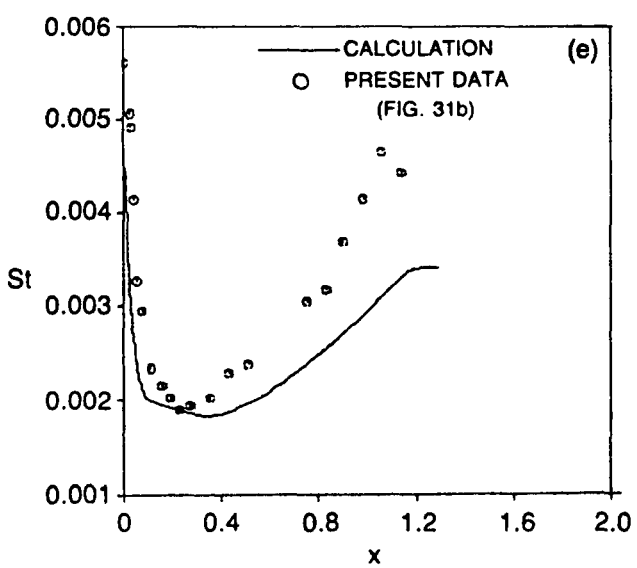

FIG. 64 cont'd. Flow Over Rotor Pressure Surface
(c) Skin Friction Results from Steady Calculation
(d) Skin Friction at Station Upstream of Reverse Flow Region
(e) Stanton Number Based on Steady Calculation

86—8—24—9

NASA
National Aeronautics and Space Administration

Report Documentation Page

1. Report No.	2. Government Accession No.	3. Recipient's Catalog No.
NASA CR-4079		

4. Title and Subtitle

The Effects of Inlet Turbulence and Rotor/Stator Interactions on the Aerodynamics and Heat Transfer of a Large-Scale Rotating Turbine Model I—Final Report

5. Report Date
July 1987

6. Performing Organization Code
533-04-11

7. Author(s)
R. P. Dring, M. F. Blair, H. D. Joslyn, G. D. Power, and J. M. Verdon

8. Performing Organization Report No.
UTRC-R86-956480-1 (E-3536)

10. Work Unit No.

9. Performing Organization Name and Address
United Technologies Research Center
Silver Lane
East Hartford, Connecticut 06108

11. Contract or Grant No.
NAS3-23717

13. Type of Report and Period Covered
Contractor Report
Final

12. Sponsoring Agency Name and Address
National Aeronautics and Space Administration
Lewis Resesarch Center
Cleveland, Ohio 44135

14. Sponsoring Agency Code

15. Supplementary Notes
Project Manager, Robert J. Simoneau, Internal Fluid Mechanics Division, NASA Lewis Research Center, Cleveland, Ohio 44135.

16. Abstract

A combined experimental and analytical program was conducted to examine the effects of inlet turbulence on airfoil heat transfer. The experimental portion of the study was conducted in a large-scale (approximately 5× engine), ambient temperature, rotating turbine model configures in both single-stage and stage-and-a-half arrangements. Heat transfer measurements were obtained using low-conductivity airfoils with miniature thermocouples welded to a thin, electrically heated surface skin. Heat transfer data were acquired for various combinations of low or high inlet turbulence intensity, flow coefficient, first-stator/rotor axial spacing, Reynolds number and relative circumferential position of the first and second stators. Aerodynamic measurements obtained as part of the program include distributions of the mean and fluctuating velocities at the turbine inlet and, for each airfoil row, midspan airfoil surface pressures and circumferential distributions of the downstream steady state pressures and fluctuating velocities. Analytical results included airfoil heat transfer predictions produced using existing two-dimensional boundary layer computation schemes and an examination of solutions of the unsteady boundary layer equations. The results of this program are reported in four separate volumes. All four have a common report title and the following volume subtitles:

Report Title: The Effects of Inlet Turbulence and Rotor/Stator Interactions on the Aerodynamics and Heat Transfer of a Large-Scale Rotating Turbine Model.

Volume Titles:	Volume I:	UTRC-R86-956480-1 (NASA CR-4079)	Final Report
	Volume II:	UTRC-R86-956480-2 (NASA CR-179467)	Heat Transfer Data Tabulation 15% Axial Spacing
	Volume III:	UTRC-R86-956480-3 (NASA CR-179468)	Heat Transfer Data Tabulation 65% Axial Spacing
	Volume IV:	UTRC-R86-956480-4 (NASA CR-179469)	Aerodynamic Data Tabulation

17. Key Words (Suggested by Author(s))

Heat transfer
Aerodynamics
Turbines
Rotor/stator
Turbulence
Unsteady flow
Airfoils

general release — MAY, 1988

Subject Category 34

19. Security Classif. (of this report)	20. Security Classif. (of this page)	21. No of pages	22. Price*
Unclassified	Unclassified	167	